Microstructure, Mechanical Properties and Irradiation Response of CrMnFeCoNi-(Y) High-entropy Alloys



Zhouran ZHANG

St Cross College

Supervisors: Prof Patrick S. Grant & Prof David E. J. Armstrong

11th May 2021

Abstract

CrMnFeCoNi, also known as the Cantor alloy, exhibits attractive mechanical properties at cryogenic temperatures and encouraging irradiation resistance. This thesis uses electron backscatter diffraction (EBSD), (scanning) transmission electron microscopy ((S)TEM), transmission Kikuchi diffraction (TKD), and heavy ion irradiation as well as nanoindentation to investigate the microstructure, mechanical properties and irradiation response of bulk spray-formed CrMnFeCoNi-(Y), where Y is added in low concentration to create a fine dispersion of Y-based oxides.

As-sprayed bulk 15 kg CrMnFeCoNi (CSP) and Y-doped CrMnFeCoNi (YCSP) were swaged and then annealed to form as-swaged and as-annealed CrMnFeCoNi (CSW) and Y-doped CrMnFeCoNi (YCSW). The alloys comprised a single face-centred cubic phase of equiaxed, polygonal grains with a high-level of elemental homogeneity. The average grain size for CSP, YCSP, CSW and YCSW was 48.5, 22.3, 8.2 and 5.4 μm. Y reacted with internal oxygen to form Y-based oxides with size of 425 ± 17 nm and volume fraction of $0.307 \pm 0.02\%$ as well as Y_2O_3 dispersoids of a few nanometers and other Y-based oxides of varying compositions, which significantly refined the grains.

The alloys showed comparable bulk tensile properties at -196℃ and 23℃ to other Cantor alloys produced by different (usually small-scale) methods. Unlike the limited ductility of other ODS-HEAs, YCSW showed

balanced strength and ductility, similar to those of conventional austenitic ODS steels. Grain boundary strengthening was the main strengthening mechanism with only limited precipitation strengthening due to the non-optimum Y-based oxide dispersion. Using EBSD, (S)TEM and TKD, extensive deformation nano-twinning in fractured CSW and YCSW specimens at -196℃ showed a strong crystallographic orientation dependence. Multiple twin variants were activated even in grains where twinning was unfavoured, causing twin-twin intersections. Deformation twinning and profuse nano-stacking faults contributed to higher storage capacity for plastic deformation.

Using 2 MeV V^+ and Ni^+ ion irradiation at 500℃ , at low (0.51 and 0.63 dpa) and high dose (2.33 and 2.84 dpa), radiation-induced segregation (RIS) was observed in grain boundaries only at high dose. Cr-rich, MnNi-rich and FeCo-rich precipitates occurred at grain boundaries, most likely due to thermal annealing occurred during ion irradiation. Irradiated CSW and YCSW contained $1/3\langle 111\rangle$ partial loops and $1/2\langle 110\rangle$ perfect loops. YCSW showed better resistance than CSW in terms of its smaller average size, lower number density and slower growth rate of loops, likely due to oxides acting as sinks for point defects. CSW and YCSW showed no obvious improvement in irradiation resistance over conventional alloys such as 316SS. Irradiation-induced hardening was likely caused by a synergistic effect of defect clusters, RIS, and precipitates. Using TKD, deformation twinning, usually rarely observed in

unirradiated CSW, occurred after irradiation, likely due to the stress concentration effect of irradiation-induced defect clusters.

Declaration of Originality

The work described in this thesis was carried out by the author in the Department of Materials, University of Oxford, under the supervision of Prof. Patrick Grant and Prof. David Armstrong. This thesis is submitted for the degree of Doctor of Philosophy at University of Oxford. I hereby declare that all of the work in this thesis is original and my own, except as specified in the text, and that no part of the thesis has been submitted for a degree at this or any other university.

Acknowledgements

I am sincerely grateful to my supervisors Prof. Patrick Grant and Prof. David Armstrong for their guidance and support throughout the entire project. I really enjoyed all the discussions which are truly insightful and invaluable. Being a student with them has benefited me a lot both academically and personally. Without them my DPhil would not be possible.

I would like to thank Dr. Atsushi Sato who manufactured the spray-formed HEA billets, which no doubt formed the basis of this work. A big thanks to Dr. Jack Haley who has helped me unreservedly with FIB, electropolishing setup, TEM characterisation and analysis. I would also like to thank Dr. Phani Karamched for his help with EBSD and the many random questions I asked. Many thanks to Dr. John Waite, Dr. Bo-Shiuan Li and Dr. Anna Kareer for their help with nanoindentation, EBSD and Wetlab skills. Thank you Dr. Junliang Liu, Dr. Guanze He and Dr. Hongbing Yu for their assistance with characterisation and the useful discussions we had.

I would like to show my gratitude to Dr. Nianhua Peng for conducting ion irradiation experiments in University of Surrey; to my supervisor Prof. David Armstrong for operating the swaging machine; to Robin Vincent and Gideon Ring for their help in sectioning the materials and many trivial technical matters; to Dr. Guillaume Matthews for conducting XRD experiments for me and to Dr. Jicheng Gong for conducting

finite element modeling for me.

To all the member in office 18.02: Dr. John Waite, Dr. Alex Leide, Dr. Matthew Lloyd, Miss Shahnaz Hoque, Miss Bethany Jim, Dr. Carmen Makepeace, Dr. Thomas Davis, Mr Keivan Samani and Mr Robert Kerr, you have made my DPhil a truly wonderful and memorable time and thank you for your companion and support. Many thanks to my lab members in both Patrick and David's group, especially Dr. Yingwei Wu and Dr. Enzo Liotti, for their warm and interesting chat during lunchtime and on the shuttle bus.

Lastly, I would like to express gratitude to my parents for supporting me as always and letting me know you are the anchor no matter how far we are apart and how far I will go.

Journal Publications

Parts of the work in this thesis have been or will be published in peer-reviewed journals:

Z. Zhang, D.E.J. Armstrong, P.S. Grant. The effects of irradiation on CrMnFeCoNi high-entropy alloy and its derivatives. *Progress in Materials Science*, 100807, 2021. (in press)

S. Zhao, Z. Li, C. Zhu, W. Yang, Z. Zhang, D.E.J. Armstrong, P.S. Grant, R.O. Ritchie, M.A. Meyers. Amorphization in extreme deformation of the CrMnFeCoNi high-entropy alloy. *Science advances*, 7(5):eabb3108, 2021.

Z. Zhang, D.E.J. Armstrong, P.S. Grant. Tensile properties and deformation behavior of bulk CrMnFeCoNi high-entropy alloys by spray forming.

Target journal: *Materials Design*, 2021

Z. Zhang, D.E.J. Armstrong, P.S. Grant. Microstructure and mechanical properties of bulk ODS-CrMnFeCoNi high-entropy alloys.

Target journal: *Scripta Materialia*, 2021

Z. Zhang, D.E.J. Armstrong, P.S. Grant. Irradiation effects in CrMnFeCoNi-(Y) high-entropy alloys.

Target journal: *Journal of Nuclear Materials*, 2021

Selected oral and poster presentations

"Microstructure and Mechanical Properties of Bulk CrMnFeCoNi High-entropy Alloys by Spray Forming" Z. Zhang, D.E.J. Armstrong, P.S. Grant.

Oral presentation at MRS Fall Meeting Exhibit, Boston, 2018

"Tensile Properties and Deformation Behaviour of Yttrium Doped Bulk CrMnFeCoNi High entropy Alloys by Spray Forming" Z. Zhang, D.E.J. Armstrong, P.S. Grant.

Invited oral presentation at Scientific meeting in honour of Professor Brian Cantor CBE FREng, Oxford, 2019

"Radiation-induced Segregation, Defect Clusters and Hardening of Y-free and Y-doped Bulk CrMnFeCoNi High-entropy Alloys" Z. Zhang, D.E.J. Armstrong, P.S. Grant.

Poster presentation at TMS World Congress on High Entropy Alloys, Seattle, 2019

Second Prize for best posters

Contents

List of abbreviations **xii**

List of Figures **xvi**

List of Tables **xxxv**

1 Introduction **1**

1.1 High-entropy alloys 1

1.2 Structural materials challenges for advanced nuclear reactors 4

1.3 Motivations for the research 5

1.4 Thesis structure 8

2 Literature Review **9**

2.1 Microstructure and manufacturing of Cantor alloys . . . 9

2.2 Mechanical properties of Cantor alloys 12

2.2.1 Tensile properties of Cantor alloys 13

2.2.2 Temperature and strain-rate dependent mechanical behaviour 16

2.2.3 Hall-Petch relationship 22

2.2.4 Strain-hardening behaviour 23

2.2.5 Twinning behaviour 24

2.3 Oxide dispersion strengthening HEAs 28

2.4 Irradiation response of HEAs 34

2.4.1 Radiation collision cascade 35

2.4.2 Irradiation response of low-activation refractory HEAs 36

2.4.3 Radiation-induced segregation and phase instability 41

2.4.4 Radiation-induced dislocation lines and loops . . 48

2.4.5 Void swelling 54

2.4.6 Gas bubbles 61

2.4.7 Conclusions 64

3 Materials and Methods **67**

3.1 Materials and Manufacturing 67

3.2 X-ray diffraction and Rietveld refinement analysis 69

3.3 Scanning electron microscopy and Energy-dispersive X-ray spectroscopy 71

3.4 Electron backscatter diffraction and transmission Kikuchi diffraction 73

3.5 Transmission electron microscopy and sample preparation 75

3.5.1 Transmission electron microscopy 77

3.5.2 Twin-jet electropolishing 79

3.5.3 Focused ion beam assisted in-situ lift-out for TEM 81

3.5.4 Dislocation loops imaging 84

3.5.5 The counting and sizing of loops 88

3.5.6 Dislocation loops characterisation 89

3.6 Mechanical testing 94

3.6.1 Nanoindentation 94

3.6.2 Tensile testing and finite element analysis 95

3.7 Irradiation facilities and conditions 96

3.7.1 Heavy ion irradiation 96

3.7.2 SRIM simulation 99

3.8 Irradiation-induced hardening by nanoindentation 101

4 Microstructure of CrMnFeCoNi-(Y) **103**

4.1 Chemical composition 103

4.2 Crystal structure 104

4.3 Initial microstructure of CrMnFeCoNi-(Y) 105

4.4 Oxide particles 117

4.5 Conclusions 123

5 Mechanical behaviour of CrMnFeCoNi-(Y) **125**

5.1 Nano-hardness 125

5.2 Tensile properties at -196℃ and 23℃ 128

5.2.1 Grain boundary strengthening 128
5.2.2 Comparison of Cantor alloy tensile properties . . 130
5.2.3 Other strengthening mechanisms 133
5.2.4 Comparison with other ODS HEAs 137
5.3 Deformation behaviour of CrMnFeCoNi-(Y) 139
5.4 Conclusions 151

6 Irradiation response of CrMnFeCoNi-(Y) 153
6.1 Radiation-induced segregation 154
6.2 Radiation-induced dislocation lines and loops 170
6.3 Radiation-induced hardening 181
6.4 Conclusions 188

7 Conclusions 191

8 Future work 195

References 197

List of abbreviations

HEA high-entropy alloy 2

FCC face-centred cubic 2

BCC body-centred cubic 37

VIM vacuum induction melting 5

MLM magnetic levitation melting 9

MA mechanical alloying 9

HPT high-pressure torsion 9

AM additive manufacturing 9

SPD severe plastic deformation 10

SPS spark plasma sintering 10

ASTM American Society for Testing and Materials 14

gs grain size 14

AC as-cast 14

CR cold-rolled 14

HR hot-rolled 14

CF cold-forged 14

HF hot-forged 14

SW swaging 14

SWC shock wave compaction 10

ECAP equal-channel angular pressing 14

YS yield strength 14

UTS ultimate tensile strength 14

Elong fracture elongation 14

TWIP twinning-induced plasticity 23

SFE stacking fault energy 24

TEM transmission electron microscopy 7

CSP as-sprayed CrMnFeCoNi HEA 68

YCSP as-sprayed Y-doped CrMnFeCoNi HEA 68

CSW as-swaged and annealed CSP 68

YCSW as-swaged and annealed YCSP 68

IPF inverse pole figure 27

EBSD electron backscatter diffraction 27

ODS oxide dispersion strengthening 6

PM powder metallurgy 10

APT atom probe tomography 29

HRTEM high-resolution transmission electron microscopy 32

STEM scanning transmission electron microscopy 32

RIS radiation-induced segregation 8

GB grain boundary 154

HAGB high-angle grain boundary 43

EELS electron energy loss spectroscopy 45

BF bright-field 32

MD molecular dynamics 49

DFT density-functional theory 24

TA tensile axis 27

XRD X-ray diffraction 69

FWHM full width at half maximum 70

EDS energy dispersive X-ray spectroscopy 71

SEM scanning electron microscopy 71

TKD transmission Kikuchi diffraction 73

DF dark-field 77

SAED selected area electron diffraction 77

FIB focused ion beam 81

CSM Continuous Stiffness Measuremen 94

SRIM Stopping Ranges of Ions in Matter 99

WBDF weak-beam dark-field 84

KMBF kinematical bright-field 84

CCD charge-coupled device 86

CBED convergent beam electron diffraction 87

ICP-OES induction coupled plasma-optical emission spectroscopy 67

OM optical microscopy 9

ADF annular dark-field 45

FFT Fast Fourier Transform 119

F/M ferritic/martensitic 138

FEM finite element model 96, 140

IQ image quality 139

IASCC irradiation-assisted stress corrosion cracking 42

BSE back-scattered electron 71

CRSS critical resolved shear stress 184

SFT stacking fault tetrahedra 189

List of Figures

2.1 OM images (a) showing the commonly observed dendritic micro-segregated microstructure in as-cast Cantor alloys[77] and (b) showing a homogeneous and equiaxed grain structures for the as-sprayed Cantor alloys.[78] 10

2.2 Ashby diagram showing fracture toughness as a function of yield strength for high-entropy alloys in relation to a wide range of material systems, showing the excellent mechanical damage tolerance (toughness combined with strength) of the Cantor alloy.[9] 13

2.3 The summary of representative tensile properties measured using ASTM standards at -196℃ and 23℃ for Cantor alloys manufactured using different techniques. The following acronyms are used: as-cast (AC), cold-rolled (CR), hot-rolled (HR), cold-forged (CF), hot-forged (HF), swaging (SW), shock wave compaction (SWC), equal-channel angular pressing (ECAP), vacuum induction melting (VIM), mechanical alloying (MA), spark plasma sintering (SPS) and magnetic levitation melting (MLM). The left y-axis represents strength with unit of MPa while the left y-axis represents ductility with unit of %. The data is arranged approximately by different manufacturing methods. The data is taken from Otto et al. (2013),[16] Kim et al. (2018),[36] Zaddach et al. (2015),[56] Joo et al. (2017),[81] Laplanche et al. (2016),[34] Joo et al. (2017),[69] Gali et al. (2013),[89] Eißmann et al. (2017),[70] Gludovatz et al. (2014),[9] Jang et al. (2018),[76] Fu et al. (2017),[82] Jian et al. (2017),[77] Joo et al. (2017),[81] Shahmir et al. (2016,2017),[73,74] Dami et al.(2017),[71] and Sun et al. (2017).[66] 15

2.4 Yield strength σ_y (upper axis) and elongation to fracture ε (lower axis) as a function of $d^{-1/2}$ (d = the average grain size) at room temperature for Cantor alloys fabricated using different techniques. The data is taken from the work of Otto et al. (2013),[16] Kim et al. (2018),[36] Zaddach et al. (2015),[56] Joo et al. (2017),[81] Laplanche et al. (2016),[34] Joo et al. (2017),[69] Gali et al. (2013),[89] Eißmann et al. (2017),[70] Gludovatz et al. (2014),[9] Jang et al. (2018),[76] Fu et al. (2017)[82] and Sun et al. (2017).[66] 17

2.5 Representative tensile properties (a) yield strength, (b) ultimate tensile strength and (c) fracture elongation of Cantor alloys at temperature from -196℃ to 1100℃. Data was obtained from Otto et al.,[16] Gludovatz et al.,[9] Gali et al.[89] and Jang et al.[76] 18

2.6 The temperature dependence of the 0.2% offset yield stress of Ni and equiatomic alloys. The dashed lines are curve fits according to temperature dependent Peierls-barrier-dominated lattice friction relationship.[91] Figure adapted with permission from.[91] 19

2.7 (a) Successive stress-strain curves using repeated load relaxation tests at room temperature for specimens of Cantor alloys and at strain rates of 10^{-5} s^{-1} and 10^{-3} s^{-1}, (b) physical activation volume, obtained at different temperatures, as a function of the true plastic strain. Figure adapted with permission from.[95] 21

2.8 Comparison of strain-hardening rates and corresponding stress curves as a function of true strain for different alloys at RT: TWIP steel ($FeMn_{18}Al_{1.5}C_{0.6}Si_{0.22}$),[112] $Al_{0.3}CrFeCoNi$ HEA,[113] 304 stainless steel,[114] $Cr_{10}Mn_{30}Fe_{50}Co_{10}$ high-entropy steel,[57] and the Cantor alloy.[9] Reprinted with permission from.[29] 24

2.9 Stress vs strain curves for the Cantor alloy at -196℃ and 23℃ with four TEM images corresponding to each point marked on the curves. The tensile stress at which twinning occurs was 720±30 MPa. Reprinted with permission from.[34] 26

2.10 Inverse pole figures (IPFs) calculated from Electron Backscatter Diffraction (EBSD) of different strain levels: (a) 0%, (b) 7%, (c) 13%, (d) 27%, (e) 41%, (f) 51%; Reprinted with permission from.[118] 27

2.11 Stress–strain curves of pristine Cantor powder, pristine Cantor, Cantor+Y_2O_3, and Cantor+Y alloys. Adapted with permission from.[142] 31

2.12 STEM BF images of (a) 0.5 wt.% and (b) 3 wt.% Y_2O_3-CoFeCoNi. HRTEM images of (c,e) monoclinic and (d,f) cubic Y_2O_3 oxides with average size of 6.5 nm in the ODS-HEAs with the addition of 0.5 wt.% and 3 wt.% Y_2O_3 respectively. Adapted with permission from.[146] 33

2.13 Periodic table with the UK 'time-to-low level waste (LLW)' values for each naturally occurring element after irradiation during one full operation cycle in a fusion reactor divertor cassette body. Note that no tritium removal is considered, and is responsible for the long-lived waste of the lighter elements, such as He, and Li. Adapted with permission from.[168] 37

2.14 Bright-field TEM images as a function of dpa for $W_{38}Ta_{36}Cr_{15}V_{11}$ HEA thin film irradiated in situ with 1 MeV Kr^{2+} ions at 800℃ . (a) pristine, (b) 0.2 dpa, (c) 0.6 dpa, (d) 1.0 dpa, (e) 1.6 dpa, (f) 3.2 dpa, (g) 4.8 dpa, (h) 6.4 dpa, and (i) 8 dpa. There were no dislocation loops but slightly enhanced precipitation shown as black spots in some grains. Reprinted with permission from.[52] 40

2.15 (a) Representative irradiation-induced segregation profiles from a STEM-EDS linescan at a random high angle GB in the Cantor alloy irradiated with 3 MeV Ni ions at 500℃ and 2 dpa. (b) Comparison of the compositional change along GBs and the matrix between the Cantor alloy and conventional FCC alloys (304 high and commercial purity,[155] model Ni-Cr alloys,[156,186] model Fe-Ni-Cr alloys[156]). Adapted with permission from Barr et al.[185] . 44

2.16 (a) STEM-BF image of a dislocation loop in the Cantor alloy; (b) high-angle annular dark-field (HAADF) image enlarged from the region marked by the red box showing an interstitial-type Frank loop. Element linescan profiles across the dislocation loops in (c) FeNi, (d) FeCoNi, (e) CrFeCoNi and (f) CrMnFeCoNi. Adapted with permission from Lu et al.[184] 46

2.17 Formation energy of a [100] dumbbell in (a) FeNi, (c) CrCoNi and (e) CrFeCoNi alloys determined by ab initio calculations (upper column); formation energy of a vacancy in (b) FeNi, (d) CrCoNi and (f) CrFeCoNi (lower column). The black dashed lines represent the formation energies of interstitials and vacancies in Ni. The formation energy of interstitials in Ni is beyond the scale of (c) and (e). Adapted with permission from Zhao et al.[189,190] 47

2.18 Cross-sectional TEM images showing the distribution of dislocations, dislocation loops and voids in Ni, CoNi, FeNi, CrFeCoNi and CrMnFeCoNi irradiated with 1.5 or 3 MeV Ni ions at different fluences. Scale bar is 100 nm. Adapted with permission from Lu et al.[30] 50

2.19 (a) Loop density; (b) loop size distribution; (c) average diameter of loops and (d) fraction of $1/3\langle 111\rangle$ faulted loops in FeNi, FeCoNi, CrFeCoNi and CrMnFeCoNi irradiated with 3 MeV Ni ions at 500℃ and up to 38 ± 5 dpa. Reprinted with permission from.[184] 51
2.20 Comparison of loop density versus irradiation temperature in $Cr_{18}Mn_{27}Fe_{27}Ni_{28}$ and conventional Fe-Cr-Ni austenitic alloys,[100,198–210] irradiated at similar conditions. The drawn lines are intended as tendency lines. Reprinted with permission from.[188] 53
2.21 (a) Optical profilometer measurements of void swelling in Ni, CoNi, CrCoNi and CrMnFeCoNi. (b) Step height change of each alloy after irradiation. Cross-sectional TEM images showing different sizes and density of voids in (c) Ni, (d) CoNi, (e) CrCoNi and (f) CrMnFeCoNi. Adapted with permission from Jin et al.[213] 55
2.22 (a) Cross-sectional TEM images of Ni, CoNi, FeNi and CrFeCoNi irradiated with 1.5 MeV Ni ions to $3 \times 10^{15}\text{cm}^{-2}$ at 500℃ with enlarged area marked by a dotted blue box; scale bar in the inset figures is 50 nm. (b) cross-sectional TEM images of Ni, FeNi, FeCoNi and CrMnFeCoNi irradiated with 3 MeV Ni ions to $5 \times 10^{16}\text{cm}^{-2}$ at 500℃ , showing reduced void formation with increasing compositional complexity. Reprinted with permission from.[30] . . 57
2.23 Cross-sectional TEM images of CrCoNi, CrMnFeCoNi and CrFeCoNiPd irradiated with 3 MeV Ni ions at (a) 420, (b) 500 and (c) 580℃ to a fluence of $5 \times 10^{16}\text{cm}^{-2}$, showing dependence of void formation on composition and temperature. Adapted with permission from Lu et al. and Yang et al.[183,214] 58

2.24 Comparison of swelling behaviour for the Cantor alloy, its derivatives, and conventional steels (e.g. 316SS, $FeCr_{15}Ni_{16}$) under similar conditions.[198,199,219,220] Data was obtained from the work of Gan et al.,[198] Okita et al.,[199] Packan et al.[219] and Yang.[220] Average size (nm, square marks) and the number density of voids ($10^{20}m^{-3}$, circles) are displayed as a function of overall swelling (%). The irradiation conditions are included on the right where half hollow marks represented data obtained at irradiation of $\sim$ 10 dpa and solid marks represented data obtained at irradiation of 50-70 dpa. 61

2.25 (a) The migration (E_m^v) and (b) formation (E_f^v) energies of vacancies and (c) and (d) of interstitials (E_m^i and E_f^i) of $Ni_{80}X_{20}$ (X=Cr, Mn, Fe, Co, Ni and Pd) binary alloys from DFT calculations. The dashed lines represent the energies in Ni. Adapted with permission from Fan et al.[223] 64

3.1 Schematic geometry of the as-sprayed billet, and the typical location and size of samples extracted for thermochemical processing. Microstructural investigation was from central region of cross-section specimens. Inset: image of an actual as-sprayed billet (diameter: 150 mm and height: 70 mm). TA in subsequent testing was parallel to the swaging direction. 69

3.2 Schematic setups for (a) conventional EBSD on a bulk sample and (b) on-axis TKD on from TEM thin foil. Figure adapted with permission from Liu.[230] 74

3.3 Schematic diagram of (a) diffraction mode and (b) imaging mode in a TEM operating at parallel beam mode. Reprinted with permission from Williams et al.[233] 78

3.4 Schematic diagram of (a) the setup of the twin-jet process, and (b) a specimen with concave surface from twin-jet electropolishing. This figure was provided by courtesy of Matthew Riding. 80
3.5 (a) SEM top view image and (b) side view image of a TEM specimen made by twin-jet electropolishing. 81
3.6 (a)-(i) The step-by-step in-situ lift-out processes used in this thesis. 82
3.7 A typical weak-beam DF image with inverted contrast for YCSW irradiated using V^+ at 2.33 dpa. 84
3.8 Three different types of diffraction conditions used to image diffraction contrast: (a) two-beam dynamical, (b) KMBF and (c) WBDF. The exaggerated Ewald sphere is shown on the left-hand side with a schematic diffraction pattern (DP) showing the position of Kikuchi lines in the center and an actual corresponding DP on the right-hand side. . 85
3.9 TEM images of irradiation-induced dislocation loops obtained using (a) KMBF and (b) WBDF conditions in the same region of CSW. 86
3.10 (a) Actual diffraction pattern and (b) archived diffraction pattern with the same crystal parameters in the database using SingleCrystal software showing the zone axis is [111]. 87
3.11 WBDF inverted contrast images of two $\frac{1}{3}\langle 111\rangle$ type dislocation loops in YCSW imaged with ±g-vector conditions. (a) Outside contrast and (b) inside contrast. 89
3.12 (a) Kikuchi map from FCC metals and alloys. (b), (c) and (d) Kikuchi lines corresponding to [001], [011] and [112] zone axis in (a) generated by Spherical Kikuchi Maps package provided by Oxford Instrument CHANNEL 5 software. (e), (f) and (g) Corresponding simulated SAED pattern in CSW along [001], [011] and [112] zone axis. 91

3.13 Schematic diagrams showing the basic principle for inside-outside technique for loop nature determination. (a) An interstitial loop with diffracting planes (green lines) and arrows showing the plane rotation in (b). (c) and (d) The case for a vacancy loop. (e) and (f) The position of the image contrast relative to the projection of loops for the diffraction conditions shown in (g) and (h). Figure adapted with permission from Williams et al.[233] 93
3.14 (a) SEM image containing an array of 4 × 4 indents and (b) hardness and modulus as a function of depth for one indent of CSW. 95
3.15 A photograph of the transport rail with samples mounted, showing an irradiation region exposed to ions and an unirradiated region covered by a Cu grid. 98
3.16 Damage profiles calculated by SRIM for all four irradiation conditions with peak damage in dpa marked on the curves. 100
3.17 Hardness curves as a function of depth for unirradiated (shown as black) and irradiated (shown as red) region of CSW irradiated with 2 MeV V^+ at 2.33 dpa. 102
4.1 X-ray diffraction patterns of CSP, CSW, YCSP and YCSW. There was one FCC phase with lattice parameter a = 0.360 nm. 104
4.2 Optical microscopy (OM) images of (a) CSP, (b) YCSP, (c) CSW and (d) YCSW showing an equiaxed, polygonal grain structure. There was a low volume fraction of "white" spots in CSP which are suggested to be non-metallic inclusions. Dispersed white spots in YCSP were possibly Y-based oxides. 106

4.3 False coloured EBSD orientation maps and inverse pole figure texture plots for (a) CSP, (b) YCSP, (c) CSW and (d) YCSW. The swaging direction for (c) and (d) is shown in (a). Orientation maps show polygonal grain structure in all four alloys while annealing twins were observed in CSW and YCSW. There was an effective grain size reduction after yttrium addition. The IPF texture on the left side showed a minor ⟨111⟩ texture in CSW and YCSW. . . . 107
4.4 Composition true maps (by SEM-EDS) from CSP. The alloy was single FCC phase with five principal elements uniformly distributed. A low fraction of fine-scale carbon, oxide, sulfide and silicide inclusions were suggested to derive from the raw materials. 109
4.5 SEM image and the composition true maps (by SEM-EDS) from YCSP with five principal elements uniformly distributed. Scattered Y-oxides had an average size of 3.94 μm. 110
4.6 EDS spectrum with an enlarged spectrum in the inset based on SEM-EDS maps of YCSP. The magenta curve is the fitted spectrum. 111
4.7 Composition true maps (by SEM-EDS) and SEM image of CSW with five principal elements uniformly distributed with a few Si-based oxide inclusions. 112
4.8 SEM image and the composition true maps (by SEM-EDS) from YCSW with five principal elements uniformly distributed. Y-oxides had an average size of 425 ± 17 nm. . 113

4.9 TEM BF images (a) CSP and (b) as-swaged CSP. (c,d) BF and dark-field (DF) images of as-swaged YCSP. (a) shows CSP was largely free of dislocations while (b) shows there were a large number of dislocations in as-swaged CSP and initial grains were sheared into ultrafine grains (a few hundred nanometers). 115
4.10 TEM BF images of the microstructure of (a,b) CSW and (c,d) YCSW. (a) Some dislocations marked by white arrows remained in CSW. (b) Precipitates in CSW both along grain boundaries and in grains. (c) and (d) Dislocation entanglement and dislocation pinning by particles in YCSW. 116
4.11 (a) SAED pattern of the region in Figure 4.10b with a simulated $Cr_{23}C_6$ SAED pattern in the inset. The experiment result was in agreement with $M_{23}C_6$ structure. (b) The line-scan profiles of a $M_{23}C_6$ particle, showing enrichment in Cr. The concentration of Cr and C approximately agreed with $Cr_{23}C_6$. 117
4.12 STEM-ADF image and compositional maps for Cr, Mn, Fe, Co, Ni, Y, C and O in YCSW, indicating Y-based oxides, Cr-rich carbides and Cr-rich precipitates. 119
4.13 (a) STEM-ADF image containing some particles marked by white arrows and (b-e) corresponding STEM-EDS linescan profiles across four particles showing the detailed compositions of Y-based oxides and Cr-rich precipitates. In this figure, linescan 1 to 4 corresponds to (b) to (e) respectively. 119

4.14 (a) STEM-ADF image of YCSW containing several Y-based oxide particles with composition maps for Y and O below. (b) HRTEM image of the region marked by white dotted square in one Y_2O_3 particle with the FFT pattern in the inset showing ring patterns identified as Y_2O_3. . . 120
4.15 (a) TEM image of YCSW, (b) SAED pattern in the region marked by white dotted circle, (c) HRTEM image of the region close to the edge of the specimen with FFT pattern in the inset, showing the existence of nanosized feature, (d) FFT pattern of the region marked by green dotted square and labeled as matrix and (e) FFT pattern of the nanosized feature marked by red dotted square and labeled as Y_2O_3. For clearer illustration, the colour of frame for (d) and (e) was set the same with the colour of marks in (c). 122
5.1 Hardness (GPa) as a function of displacement (nm) for CSP, YCSP, CSW and YCSW with standard error bar. . 126
5.2 Hardness as a function of $d^{-1/2}$ (d = the average grain size) for CSP, YCSP, CSW and YCSW with linear best-fit line. 127
5.3 Modulus (GPa) as a function of displacement (nm) for CSP, YCSP, CSW and YCSW with standard error. . . . 128
5.4 Tensile yield strengh as a function of $d^{-1/2}$ (d = the average grain size) for CSP, CSW and YCSW with best-fit line (red marks) as well as data and best-fit lines for Cantor alloys taken from Otto et al. and Sun et al.[16,66] 130

5.5 Yield strength σ_y (upper axis) and elongation to fracture ε (lower axis) as a function of $d^{-1/2}$ (d = the average grain size) at room temperature for Cantor alloys fabricated using different techniques. The data is taken from the work of Otto et al. (2013),[16] Kim et al. (2018),[36] Zaddach et al. (2015),[56] Joo et al. (2017),[81] Laplanche et al. (2016),[34] Joo et al. (2017),[69] Gali et al. (2013),[89] Eißmann et al. (2017),[70] Gludovatz et al. (2014),[9] Jang et al. (2018),[76] Fu et al. (2017)[82] and Sun et al. (2017).[66] 131

5.6 Average yield strength σ_y, ultimate tensile strength σ_{uts} (left y axis) and elongation to fracture ε (right y axis) as a function of $d^{-1/2}$ (d = the average grain size) of Cantor alloys from the literature and the present study at -196°C. σ_y, σ_{uts} and ε are marked by solid squares, solid circles and half hollow triangles with arrow. Linear best-fit lines to yield strength and ultimate tensile strength as a function of $d^{-1/2}$ are shown in black. AC (as-cast); CR (cold-rolled); HR (hot-rolled); CF (cold-forged); SW (swaging) and VIM (vacuum induction melting). The data is taken from the work of Otto et al. (2013),[16] Gludovatz et al. (2014),[9] Gali et al. (2013)[89] and Laplanche et al. (2016).[34] 133

5.7 Enlarged X-ray diffraction patterns from 40 to 58° for CSP, CSW, YCSP and YCSW. 135

5.8 Elongation to fracture (%) as a function of yield strength (MPa) for CSW, YCSW and other ODS Cantor alloys[140–143] and commercial ODS steels.[147–154] ODS steels with austensitic structure are marked by solid circles whereas ODS steels either with ferritic or ferritic/martensitic structure are marked by solid triangles. ODS Cantor alloys are marked using solid squares and half solid squares whereas the corresponding Cantor alloys without yttrium's addition are marked by diamonds. 138

5.9 (a) SEM image of the longitude section parallel to TA indicated by black arrow of CSW tensile fractured specimen at -196℃ and the necking region was selected by black dotted box. Two regions, marked by black squares, one from the necking region (region N) and one from the region 3 mm away from region N (region M) were further investigated. (b) and (c) EBSD maps of region M and region N shown in (a) with coloured scale bar and stereographic triangle showing a strong ⟨111⟩ and a moderate ⟨001⟩ deformation texture inserted below. (d), (e) and (f) Misorientation profiles (point-to-point) of three white arrows crossing several twin boundaries marked by A, B and C in (b) and (c), which clearly shows deformation nanotwinning within each grain. 140

5.10 Finite element analysis of the von Mises stress stress distribution in the fractured CSW specimen shown in Figure 5.9. 141

5.11 (a) and (b) Orientation maps and band contrast overlay of regions marked by the white squares in Figures 5.9b and 5.9c with TA on the left and colour scale on the right. Grain subdivision by twin-twin intersection was clearly observed in (b). (c) Pole figures and inverse pole figures of several grains, marked by white capital letters A to H in (a) and (b) showing the orientation relation between the matrix (M) and twins (T). In some cases, such as Grain F and G, two twin variants were observed and marked as T1 and T2. The colour of traces are the same with the colour of letters and X0 is in parallel with TA. 143

5.12 (a) Band contrast image perpendicular to TA, indicated on the left corner and (b) orientation map along TA with stereographic triangle in the inset measured by TKD for fractured CSW in the necking region. One grain oriented $\langle 111 \rangle \parallel$ TA is marked by the white dotted box in which multiple twin variants were activated. There were profuse twin-twin intersection in grains oriented close to $\langle 111 \rangle \parallel$ TA, causing severe grain subdivision and reducing the dislocation mean free path. 145

5.13 (a) Bright-field (BF) TEM images and SAED pattern from fractured CSW in the necking region. One primary twin system with width of 10-100 nm intersected the secondary twin system with width of a few nanometers, and the intersection angle is 70. The SAED pattern along the [011] direction shows two twin variants. By selecting pattern from each single twin variant, two DF TEM images framed by corresponding red and green boxes as red and green circles in the SAED pattern are shown in (b) and (c). The second twin variant and primary twin variant are respectively presented in (b) and (c) as bright features due to strong diffraction from twins. 147

5.14 (a) BF TEM image and SAED pattern of fractured CSW at -196℃ in the necking region. There were deformations twins in addition to numerous stacking faults evidenced by streaky pattern along [111] direction in SAED pattern. (b) Enlarged BF TEM image of the region marked by white dotted circle in (a) showing profuse stacking faults embedded in the twin-matrix lamellae. 148

5.15 (a) BF and (b) DF images of a region of twin-matrix lamellae with embedded stacking faults. (c) SAED pattern from the region shown in (a) and (b). Extra spots were observed in addition to those from twins and matrix. By selecting the extra spots, stacking faults diffracted strongly in (b). (d) HRTEM image with Fast Fourier Transformation (FFT) pattern in the inset. FFT pattern contained streaky lines, evidencing numerous nano-stacking faults. (e) Magnified HRTEM image from the region marked by the red box in (d), showing the atomic structure and stacking sequence (a typical one is marked in red), which were identified as intrinsic stacking faults. 150

5.16 Orientation maps of (a) CSW and (b) YCSW fractured at -196℃, along TA indicated in (b) with IPF texture in the inset of (b) showing a strong ⟨111⟩ and a moderate ⟨001⟩ texture. Several twins in grains oriented close to ⟨001⟩ are marked by white arrows. (c) Band contrast image of YCSW showing several microcracks marked by the black dotted ovals. 151
6.1 BSE images of YCSW containing an indent by nanoindentation (a) before and (b) after 2 MeV V^+ irradiation at 2.33 dpa. Some particle inclusions were likely complex Y-based oxides or non-metallic inclusions. There was further segregation to GBs in (b) irradiated YCSW sample. . . . 155
6.2 SEM-EDS linescan profiles of Cr, Mn, Fe, Co and Ni across high-angle GBs in unirradiated and irradiated regions in CSW and YCSW. (a) Unirradiated CSW, (b) unirradiated YCSW, (c) irradiated CSW and (d) YCSW using 2 MeV Ni^+ ions at 0.63 dpa, (e) irradiated CSW and (f) YCSW using 2 MeV Ni^+ ions at 2.84 dpa. 156
6.3 EDS spectrums of two linescan datasets at the range from 0 to 20 KeV where there is an enlarged spectrum at the energy range from 0 to 2.2 KeV in the inset. The magenta curve is the fitted spectrum by subtracting the background and deconvoluting overlapping peaks. (a) Characteristic X-ray peaks from different elements were overlapping at low energy (<3 keV). (b) Peaks from different elements were eaily distinguished. Note that EDS analysis involve all peaks from 0 to 20 keV. 157

6.4 SEM-EDS linescan profiles of Cr, Mn, Fe, Co and Ni across high-angle GBs in unirradiated and irradiated regions in CSW and YCSW. (a) Unirradiated CSW, (b) unirradiated YCSW, (c) irradiated CSW and (d) YCSW using 2 MeV V^+ ions at 0.51 dpa, (e) irradiated CSW and (f) YCSW using 2 MeV V^+ ions at 2.33 dpa. 159

6.5 The average concentration for the principal elements at the point where the concentration of Mn was the lowest, taken from at least three linescan datasets for (a) 2 MeV Ni^+ ion irradiation at 2.84 dpa and (b) 2 MeV V^+ ion irradiation at 2.33 dpa. (c) and (d) Change in concentration (at.%) with standard deviation for the principal elements. . . . 161

6.6 (a) WBDF inverted contrast image of CSW irradiated using V^+ ions at 2.33 dpa with corresponding (b) SAED pattern from the marked region. (c) WBDF inverted contrast image of YCSW irradiated under the same condition with corresponding (d) SAED pattern. 163

6.7 STEM-ADF image of YCSW irradiated using V^+ ions at 2.33 dpa and STEM-EDS maps for Cr, Mn, Fe, Co, Ni, C, O, Y and Si in the irradiated region. 164

6.8 STEM-BF image of YCSW irradiated using 2 MeV V^+ ions at 2.33 dpa and STEM-EDS maps for Cr, Mn, Fe, Co, Ni, C, O, Y and Si from an irradiated region. 165

6.9 STEM-EDS linescan profiles across Y-based oxide particles in the irradiated region of YCSW under irradiation of 2 Mev V^+ ions at 2.33 dpa. In each case, the particle is approximately in the middle of the linescan. 167

6.10 (a) STEM-ADF image of YCSW irradiated using 2 MeV V^+ ions at 2.33 dpa. (b-e) STEM-EDS linescan profiles across the GB marked by white arrows in (a). Linescan 1 to 4 corresponds to (b) to (e) respectively. 168

6.11 STEM-ADF image of YCSW irradiated using 2 MeV V^+ ions at 2.33 dpa and STEM-EDS maps for Cr, Mn, Fe, Co, Ni, C, O, Y and Si in the region marked by the white box. 170
6.12 WBDF images with inverted contrast for CSW and YCSW irradiated using 2 MeV Ni^+ ions at 0.63 dpa and 2.84 dpa. (a) CSW at 0.63 dpa, (b) YCSW at 0.63 dpa, (c) CSW at 2.84 dpa and (d) YCSW at 2.84 dpa. 171
6.13 WBDF images with inverted contrast for CSW and YCSW irradiated using 2 MeV V^+ ions at 0.51 dpa and 2.33 dpa. (a) CSW at 0.51 dpa, (b) YCSW at 0.51 dpa, (c) CSW at 2.33 dpa and (d) YCSW at 2.33 dpa. 172
6.14 A series of WBDF images with inverted contrast for YCSW using 2 MeV V^+ ions at 2.33 dpa using (a) g=[020], (b) g=$[0\bar{2}0]$, (c) g=$[2\bar{2}0]$, (d) g=[200], (e) g=$[\bar{2}00]$, and (f) g=$[31\bar{1}]$. 173
6.15 The number density (10^{20} m^{-3}) as a function of the average size of dislocation loops in CSW and YCSW irradiated at different conditions. 177
6.16 Hardness change (%) as a function of displacement into the surface (nm) in CSW and YCSW before and after irradiation using (a) 2 MeV Ni^+ and (b) 2 MeV V^+ ions at low and high dose. 182
6.17 TKD band contrast images and orientation maps of indented, unirradiated (a,b) CSW and (c,d) YCSW from the cross-section obtained by FIB from the region of plastic deformation around the indent. 184
6.18 TKD band contrast images and orientation maps of indented CSW irradiated using 2 MeV Ni^+ ions at (a,b) 0.63 dpa and (c,d) 2.84 dpa. Note that the irradiated layer is 800-900 nm. 185

6.19 TKD band contrast images and orientation maps of indented YCSW irradiated using 2 MeV Ni^{+} ions at 2.84 dpa. Note here that the irradiated layer is 800-900 nm. . 186
6.20 STEM-ADF images of indented CSW and YCSW irradiated using 2 MeV Ni^{+} ions at 2.84 dpa with corresponding SAED patterns in the region close to the top surface in the inset. 187

List of Tables

2.1 Summary of total void swelling in Ni, FeNi, FeCoNi, CrCoNi, CrFeCoNi, CrMnFeCoNi and CrFeCoNiPd irradiated with 3 MeV Ni ions at 420, 500 and 580℃. Data was from Ref.[30,183,214,218] 60

3.1 Abbreviations and full descriptions of the four alloys. . . 68

3.2 The characteristic X-ray energy (KeV) of elements in the present study. 72

3.3 Summary of conventional EBSD and on-axis TKD setup parameters used in the present study. 76

3.4 $g \cdot b$ table that is used to distinguish $b = \frac{1}{3}\langle 111\rangle$ and $b = \frac{1}{2}\langle 110\rangle$ dislocation loops. 92

3.5 The summary of irradiation conditions. 98

4.1 The nominal composition (wt.%) of CSP and actual composition (wt%) of CSP and YCSP measured using ICP-OES. 103

4.2 The average grain size of CSP, YCSP, CSW and YCSW determined by the linear intercept method. 108

5.1 The average yield strength σ_y, ultimate tensile strength σ_{uts} and fracture elongation ε and standard deviation for CSP, CSW and YCSW at -196℃ and 23℃. 128

6.1 Visibility and inside-outside contrast showing the nature of each type of dislocation loop in YCSW irradiated using 2 MeV V^+ ions at 2.33 dpa. V=visible and I=invisible. . 175

6.2 The foil thickness, the average size with standard deviation, the maximum size and the number density of CSW and YCSW specimens irradiated at different conditions. . 176

6.3 Quantitative data of dislocation loops, i.e. average size and number density of the Cantor alloys including the present study and conventional alloys (316SS and Fe-15Cr-16Ni) irradiated under similar conditions. 180

6.4 Hardening (%) at the depth of 600 nm in irradiated CSW and YCSW using 2 MeV Ni^+ and V^+ ions at different doses.182

1 Introduction

1.1 High-entropy alloys

Traditional alloy design concepts are based on one or two elements mixed with a lower concentration of other minority elements to give an overall composition that is optimised for various aspects of performance and have led to, for example, large families of steels,[1] aluminium alloys,[2,3] titanium alloys[4] and nickel alloys.[5,6] Nonetheless, there is always a drive for alloys with superior mechanical and other properties, such as high strength,[7] good ductility,[8] high fracture toughness,[9] creep resistance,[10] wear resistance,[11] corrosion resistance,[12] recyclability[13] and low cost.[14] These incremental improvements are achieved by tailoring the alloy composition and microstructure, for example, by thermo-mechanical processing,[15] reducing grain size,[16] increasing solid-solution effects[17,18] or precipitation hardening.[7]

A different approach to alloy design was proposed in 2004 and has attracted considerable attention,[19,20] based on equiatomic or near-equiatomic multi-component alloys, typically comprising four or more elements. It was hypothesized that the associated high configurational entropy of equiatomic mixing may promote and stablise the formation of simple solid solutions rather than a "matrix" predominantly of one or two elements filled with a high volume fraction of usually hard and embrittling intermetallic phases. The materials, proposed simultaneously by Cantor

et al.[19] and Yeh et al.,[20] have come to be known as high-entropy alloys (HEAs).[20] Over time it has emerged that single phase solid solutions HEAs were not often achieved[21–25] and many multicomponent alloys that do no exhibit single solid solution (or even close to) were yet still named as HEAs. Some other terminologies, such as 'multi-principal element alloys (MPEAs)'[26] and 'concentrated solid solution alloys (CSAs)',[27] have been proposed subsequently. Nevertheless, the approach opens up largely unknown central regions of multi-principal alloy phase space. Although the stabilising effect of high configurational entropy of mixing has subsequently been shown not to be a critical feature of the alloys,[16,28] the HEA term remains convenient, and some systems have shown promising mechanical and functional properties.[9,29–31] In this thesis, HEA is used as shorthand to describe near-equiatomic, multi-element materials.

Among the many HEAs since studied, the first proposed and one of the foremost systems is the equiatomic, face-centred cubic (FCC) alloy CrMnFeCoNi.[19] This alloy emerged from the original work of Cantor et al.[19] and has become known as the "Cantor" alloy.[32] It is worth pointing out that although the Cantor alloy retains a simple FCC solid solution even after long annealing up to 500 days[21] at relatively high temperatures (over 800℃), it decomposes into multiple phases at intermediate (500-700℃) annealing temperatures after 500 days.[21,22,33] Nonetheless, a solid solution readily arises in most practical solidification (casting) processes, even on the multi-kg scale.[34–36] Considerable efforts have been devoted to

understand the alloy mechanical behaviour, corrosion resistance, intrinsic properties and, more recently, its irradiation response, making it one of the most thoroughly investigated HEA systems.[29,30,37,38]

The Cantor alloy exhibits some intriguing and attractive mechanical properties,[9,34] particularly an exceptional combination of high yield strength (795 MPa), high ultimate tensile strength (1280 MPa), ductility (70%) and fracture toughness (219 MPa·$m^{1/2}$) at cryogenic temperatures.[9] These properties likely result from a relatively low stacking fault energy (approximately 21 mJ/m^2 at room temperature calculated using quantum mechanical first-principles methods[39] and 18.3–27.3 mJ/m^2 measured by X-ray diffraction experiments[40]), a temperature sensitive friction stress and the onset of widespread deformation nano-twinning at low temperatures.[29,38]

Since 2014, growing attention has been paid to the irradiation response of high-entropy alloys, including the Cantor alloy, its sub-systems and derivatives.[27,41] Through experiment and computational investigations, the Cantor alloy has defect energetics that support its improved radiation resistance, such as less pronounced void swelling, smaller size of defect clusters and retarded defect growth, migration and evolution, when compared with its binary and tertiary sub-systems, and some conventional austenitic steels. These attractive mechanical properties and radiation resistance also make it, or its derivatives, potential candidates for high temperature fission or fusion structural applications.

1.2 Structural materials challenges for advanced nuclear reactors

In order to meet rapidly increasing global energy needs, safe, reliable, and economic operation of advanced fission and eventually fusion power plants is generally considered an important element of a lower carbon energy future.[42] One of the key challenges from both scientific and engineering perspectives is how structural materials that are closest to the atomic fission and fusion reactions themselves can retain the required performance under the associated extreme conditions that will involve higher temperatures, higher pressure, a higher irradiation dose and a more corrosive environment for longer periods (up to 80–100 years for key non-replaceable components) than those experienced in current Gen II or Gen III fission reactors.[43] There are a large number of critical requirements for reactor materials including good dimensional stability (good thermal stability and low void swelling),[44,45] favourable mechanical properties (an acceptable combination of tensile strength, ductility, creep resistance, fracture toughness and fatigue resistance),[46,47] acceptable resistance to radiation damage (less pronounced irradiation-induced defect clusters and thus less irradiation-induced hardening and embrittlement)[48,49] and high degree of chemical compatibility with the potentially corrosive environment (less stress corrosion cracking with or without irradiation assistance).[45,50] In addition, low activation elements are preferred to reduce the radiotoxicity of the most active components during

de-commissioning. The harsh service conditions and multiple requirements present significant challenges to current structural materials, and in some cases constrain reactor design and performance. High-entropy alloys are suggested to have potential as structural materials for civil nuclear power generation, principally because they offer more opportunities for combining low-activation elements,[51] and, in some cases, the possibility of improved mechanical properties,[52] improved radiation resistance[30] and related improvement in dimensional stability.[53,54]

1.3 Motivations for the research

Although the Cantor alloy has been investigated for 17 years, there are many aspects that remain unanswered. Arguably, the progress of understanding and potential industrial applications of HEAs has been inhibited because the majority of HEAs have been manufactured only at a relatively small scale (hundreds of grams), most typically by arc melting.[9,16,31,38,55,56] Although large scale processing techniques have been applied, e.g. vacuum induction melting (VIM),[36,57–62] the arising billets have a distinct dendrite microstructure with pronounced micro-segregation that requires long annealing time to achieve acceptable levels of chemical segregation. New manufacturing methods need to be utilised to produce HEAs at a large scale with comparable or better mechanical properties than laboratory investigations. Spray forming has been reported to lead to a high-level of elemental homogeneity with absence of

micro-segregation[63] even in compositionally complex alloys. This thesis uses spray forming to manufacture the Cantor alloy in 15 kg billets, with exceptional microstructural uniformity.

Due to the fact that the Cantor alloy is not particularly strong at room and elevated temperature (similar to 316 stainless steels), strengthening strategies (e.g. precipitation hardening and grain boundary strengthening) might be utilised to improve mechanical properties. Although the concept of oxide dispersion strengthening (ODS) alloy has been introduced to the Cantor alloys, which successfully improved the strength by the addition of very fine scale oxide particles, i.e. Y_2O_3, the ductility was heavily compromised. An investigation into the trade-off between strength (high precipitates and grain boundary density) and ductility may be helpful, potentially using alternative routes to manufacture ODS-HEAs, such as spray forming. This thesis describes the method of adding Y, in the form of a Y-24 wt.% Fe master alloy, into molten Cantor alloy immediately before deposition, and then how "internal oxygen" reacted with Y during precipitation to form Y_2O_3 or other Y-based oxides in-situ.

Although the onset of deformation twinning at low temperatures has been shown to play a significant role in the excellent cryogenic mechanical properties of Cantor alloys, it is still unclear which twin system is activated and how many twin systems are activated under different stages of deformation. This thesis investigates the extent and crystal orientation dependence of twinning in the Cantor alloy.

Research into the irradiation resistance of HEAs is in the nascent stage. This thesis explores the irradiation response of the Cantor alloy at high temperature of 0.35-0.6T_M (T_M = 1270℃ for the Cantor alloy[33]), including detailed cross-section transmission electron microscopy (TEM) studies and nanoindentation tests. Irradiation-induced structural damage was quantitatively studied and compared with conventional alloys to understand if there are any unusual aspects to the mechanisms of reported enhanced resistance. In addition, Y-based oxides in the ODS Cantor alloy are suggested to play a role as an effective sink for radiation-induced defects.

Overall, the microstructure, mechanical properties and irradiation response of yttrium-free and yttrium-doped CrMnFeCoNi high-entropy alloys (CrMnFeCoNi-(Y)) manufactured by spray forming are discussed. The objectives of the work are:

1. To investigate the microstructure of bulk CrMnFeCoNi-(Y) with particular focus on the nature of the oxide particles;

2. To assess the mechanical behaviour of bulk CrMnFeCoNi-(Y) with particular focus on grain refinement strengthening, precipitation strengthening and twinning mechanisms at low temperature; and

3. To investigate the effect of irradiation on bulk CrMnFeCoNi-(Y), including irradiation-induced segregation, defects clusters and hardening at elevated temperature using high resolution electron microscopy and nanoindentation.

1.4 Thesis structure

A literature review is given in Chapter 2. The materials and manufacturing details of spray forming are given in Chapter 3, which also covers a brief introduction and the typical setup of characterisation techniques used. Details about mechanical testing, heavy ion irradiation experiments and the methods used in irradiation-induced damage characterisation are described. The microstructure of bulk CrMnFeCoNi-(Y) is presented in Chapter 4. Chapter 5 firstly reports the mechanical properties, including hardness and tensile properties at -196℃ and 23℃, of bulk CrMnFeCoNi-(Y) and then investigates the deformation behaviour at -196℃. In Chapter 6, the effect of irradiation in CrMnFeCoNi-(Y) is presented, including radiation-induced segregation (RIS), dislocation loops and radiation-induced hardening. Throughout Chapter 5 and Chapter 6 the mechanical properties and irradiation response of bulk CrMnFeCoNi-(Y) are compared with other Cantor alloys and more traditional alloys (e.g. 316SS). Finally, the results are summarised in Chapter 7, with suggestions for further work given in Chapter 8.

2 Literature Review

2.1 Microstructure and manufacturing of Cantor alloys

Since the proposal of materials tetrahedron in 1989,[64] the development of materials have been closely related to the four basic elements: the structure and composition, the synthesis and processing, the properties (e.g. mechanical and functional properties) and the performance of the material.[65] The properties and performance of Cantor alloys depend on the microstructure, which is derived from the manufacturing processes.

Though different kinds of methods have been used, Cantor alloys have mainly been produced on a laboratory scale (tens of to hundreds of grams),[9,16,31,38,55,56] which is also true for the majority of HEAs. Other techniques have also been applied in fabricating Cantor alloys, including vacuum induction melting (VIM),[35,36,57,58,60–62] magnetic levitation melting (MLM),[66,67] mechanical alloying (MA),[68–72] high-pressure torsion (HPT)[73,74] and additive manufacturing (AM).[75]

The as-cast Cantor alloys usually exhibit very large grain sizes (typically $>$ 1000 μm) and dendritic micro-segregated microstructure, as shown in the optical microscopy (OM) images in Figure 2.1a, that needs homogenisation by annealing at 1000–1200°C for 24–48 h.[36] Due to coarse grains and some extent of porosity in as-cast Cantor alloys, they

are typically strengthened by mechanical processing, such as hot rolling,[76] cold rolling,[9,16] hot forging,[73] and cold swaging,[35] followed by thermal treatment which leads to recovery, recrystallisation and grain growth. These thermomechanical processing techniques usually produced single-phase equiaxed microstructure with average grain size ranging from a few to hundreds of μm[9,16,35,76] whereas Cantor alloys processed by severe plastic deformation (SPD), displayed much finer grains with size of 10 to 500 nm.[73,74] Cantor alloys fabricated by powder metallurgy (PM) have been further consolidated by shock wave compaction (SWC)[71] and spark plasma sintering (SPS).[68,69,72]

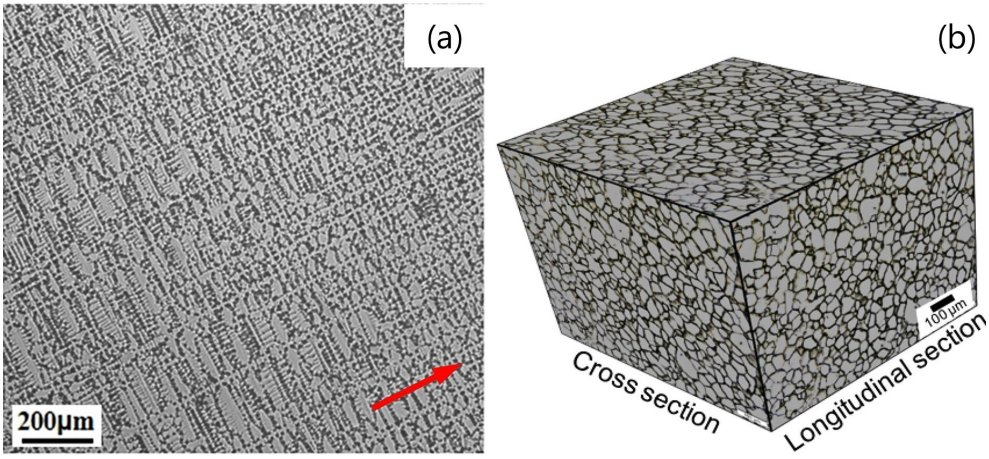


Figure 2.1: OM images (a) showing the commonly observed dendritic micro-segregated microstructure in as-cast Cantor alloys[77] and (b) showing a homogeneous and equiaxed grain structures for the as-sprayed Cantor alloys.[78]

Increasing efforts have been devoted to making bigger billets. Laplanche et al. produced a 1 kg ingot of Cantor alloy by VIM[58] and Sousa et al. manufactured a 2.8 kg billet by spray forming.[78] One of the largest Cantor alloy billet weighing 30 kg was reported by Jang et al. using

VIM.[76] However, as mentioned in Chapter 1.3, the arising billets have a distinct dendrite microstructure with pronounced micro-segregation that requires long annealing time to achieve acceptable levels of chemical segregation. Spray forming has been shown[63,79] to offer the advantages of both casting (high mass flow rate) and powder metallurgy (refined microstructural scale and reduced macro-segregation) and is thus well-suited for manufacturing of complex compositional or multicomponent alloys. The advantageous spray-formed microstructure typically comprises equiaxed/polygonal grains of 20-50 μm without columnar/dendritic morphologies and there are only low levels of microsegregation regardless of position in the billet.[63] It was suggested by Grant[63] that the reduced microsegregation by spray forming is likely aroused from the large amounts of reheating, remelting, mixing, and equilibration constantly occurring at the surface during spray forming. In the meantime, the reheating and remelting of the depositing solid and droplets leads to the destabilisation of any dendritic/cellular microstructure as well as significant grain multiplication effect (grain refinement).

Sousa et al. reported Cantor alloys fabricated using spray forming weighed 2.8 kg and exhibited equiaxed grains with average grain size of 25 μm[78] as shown in Figure 2.1b. A dense deposit, with low levels of macrosegregation and refined equiaxed grains were obtained using spray forming.

2.2 Mechanical properties of Cantor alloys

The attention drawn to Cantor alloys may be attributed to its often described "unusual" mechanical behaviour, in particular an attractive and unusual combination of high cryogenic fracture toughness, strength and ductility. At tensile strength of 730 to 1280 MPa, the fracture toughness exceeds 200 MPa $\cdot$ $m^{1/2}$ at crack initiation and rises to $>$ 300MPa $\cdot$ $m^{1/2}$ for stable crack growth[9] at cryogenic temperatures down to -196℃, which is comparable to the very best cryogenic steels, specifically certain austenitic stainless steels and high-Ni steels. Figure 2.2 shows the Ashby diagram of fracture toughness as a function of yield strength for HEAs and other classes of materials at room temperature. The excellent mechanical damage tolerance of HEAs than most of metallic alloys has triggered a large quantity of research on mechanical properties of Cantor alloys.

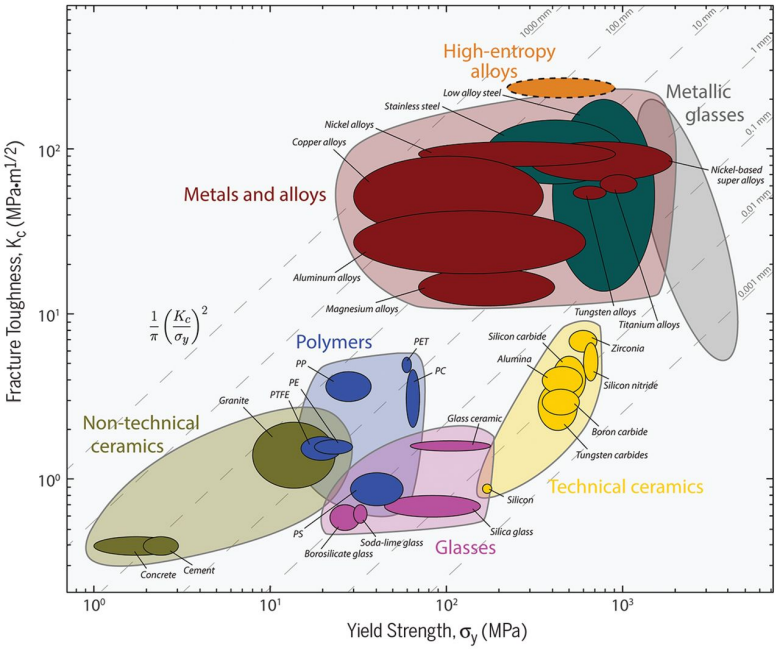


Figure 2.2: Ashby diagram showing fracture toughness as a function of yield strength for high-entropy alloys in relation to a wide range of material systems, showing the excellent mechanical damage tolerance (toughness combined with strength) of the Cantor alloy.[9]

2.2.1 Tensile properties of Cantor alloys

As-cast Cantor alloys[36] usually have a low yield strength σ_y of 205 MPa but ultimate tensile strength σ_{uts} of 450 MPa with an elongation to failure of 50% at room temperature (RT), indicating an excellent uniform deformation and high work hardening capability. Such features make it an potential attractive base alloy for further strengthening. Tensile properties of Cantor alloys produced from different manufacturing and post thermomechanical methods have been reported at temperatures from -258℃ to 1100℃ .[9,16,34,36,56,66,69–71,73,74,76,76,77,80–82] Mechanical response of Cantor alloys at a strain rate from 10^{-5} to 10^{5} s^{-1} were reported.[83–85] Strain-rate sensitivity of Cantor alloys was reported to be greater than

that of pure metals and binary alloys.[85,86] Adiabatic shear bands are usually formed due to heavy plastic flow and abrupt temperature rise in a narrow and localised region, especially under high strain-rate deformation when there is not enough time for heat diffusion.[87] The Cantor alloy has been reported to exhibit high resistance to adiabatic shear band formation under dynamic loading.[84]

Figure 2.3 presents the summary of representative tensile properties measured using American Society for Testing and Materials (ASTM) standards[88] at -196℃ and 23℃ for Cantor alloys manufactured using different techniques. In this figure, grain size (gs) and manufacturing methods are also included. The following acronyms are used: as-cast (AC), cold-rolled (CR), hot-rolled (HR), cold-forged (CF), hot-forged (HF), swaging (SW), shock wave compaction (SWC), equal-channel angular pressing (ECAP), vacuum induction melting (VIM), mechanical alloying (MA), spark plasma sintering (SPS) and magnetic levitation melting (MLM). Yield strength (YS, blue bar) and ultimate tensile strength (UTS, red bar) follow the upper y-axis while fracture elongation (Elong, green bar) follows the lower y-axis. The data is arranged approximately by different manufacturing methods and taken from Otto et al. (2013),[16] Kim et al. (2018),[36] Zaddach et al. (2015),[56] Joo et al. (2017),[81] Laplanche et al. (2016),[34] Joo et al. (2017),[69] Gali et al. (2013),[89] Eißmann et al. (2017),[70] Gludovatz et al. (2014),[9] Jang et al. (2018),[76] Fu et al. (2017),[82] Jian et al. (2017),[77] Joo et al. (2107),[81] Shahmir et al.

(2016,2017),[73,74] Dami et al.(2017),[71] and Sun et al. (2017).[66]

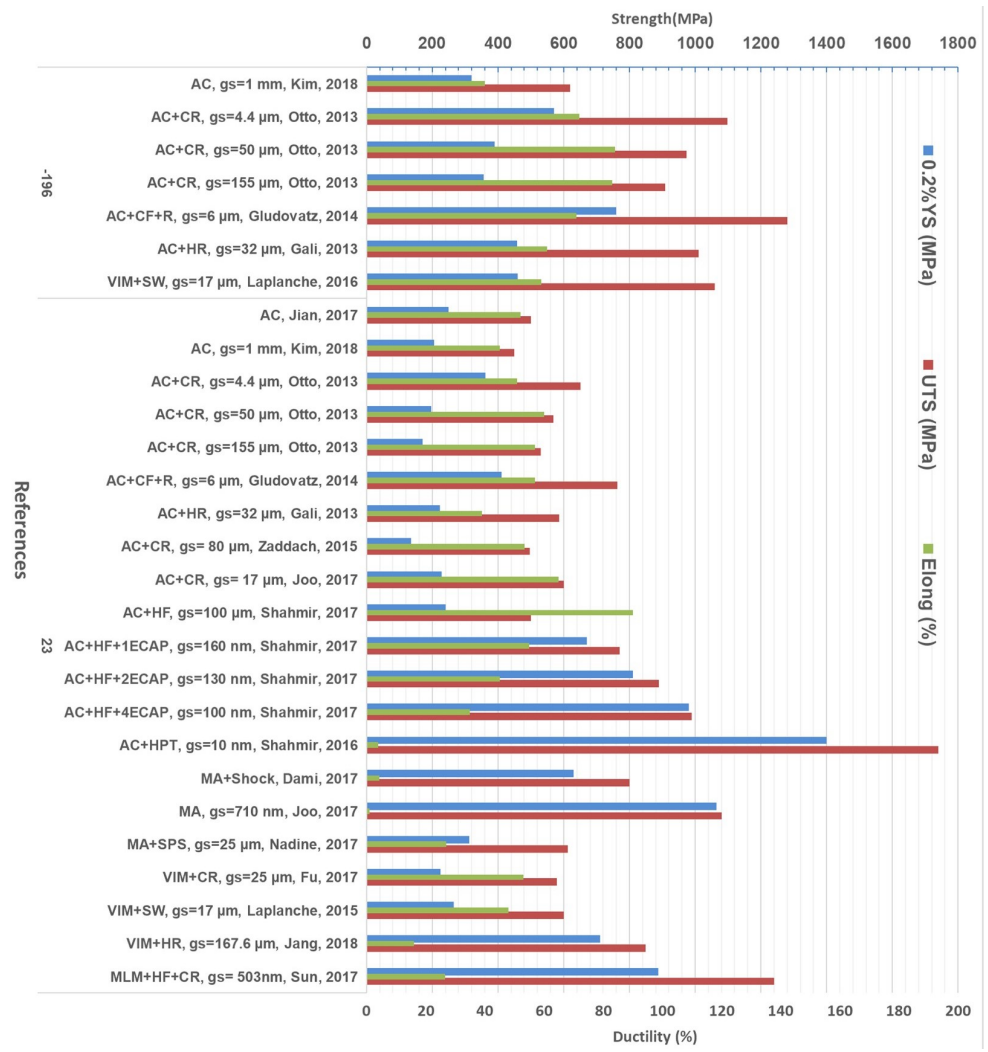


Figure 2.3: The summary of representative tensile properties measured using ASTM standards at -196°C and 23°C for Cantor alloys manufactured using different techniques. The following acronyms are used: as-cast (AC), cold-rolled (CR), hot-rolled (HR), cold-forged (CF), hot-forged (HF), swaging (SW), shock wave compaction (SWC), equal-channel angular pressing (ECAP), vacuum induction melting (VIM), mechanical alloying (MA), spark plasma sintering (SPS) and magnetic levitation melting (MLM). The left y-axis represents strength with unit of MPa while the left y-axis represents ductility with unit of %. The data is arranged approximately by different manufacturing methods. The data is taken from Otto et al. (2013),[16] Kim et al. (2018),[36] Zaddach et al. (2015),[56] Joo et al. (2017),[81] Laplanche et al. (2016),[34] Joo et al. (2017),[69] Gali et al. (2013),[89] Eißmann et al. (2017),[70] Gludovatz et al. (2014),[9] Jang et al. (2018),[76] Fu et al. (2017),[82] Jian et al. (2017),[77] Joo et al. (2017),[81] Shahmir et al. (2016,2017),[73,74] Dami et al.(2017),[71] and Sun et al. (2017).[66]

Figure 2.4 shows yield strength σ_y (upper axis) and elongation to fracture ε (lower axis) as a function of $d^{-1/2}$ (d = the average grain size) at room temperature for Cantor alloys fabricated using different techniques. In general, there is a dependence of yield strength on grain size whereas ε scattered significantly. Considering studies with grain sizes of approximately a few to hundreds of μm, σ_y is approximately 250-400 MPa, σ_{uts} is 600-800 MPa while ε is 40-60% at room temperature. In comparison, 316 and 304 stainless steels with average grain size of 30 μm showed σ_y of 150-200 MPa, σ_{uts} of 400-500 MPa and ε of 45-55% at room temperature,[90] which are similar to those of Cantor alloys. It has been summarised in several reviews[29,37] that the tensile properties of Cantor alloys and austenitic stainless steels are similar at temperatures from 23℃ to 900℃ . Cantor alloys produced by severe plastic deformation methods usually possess much finer grains[73,74] and exhibit high yield strengths due to grain boundary strengthening but very limited ductility because of their poor capacity for accommodating dislocations in the small grains and thus a lack of work hardening.[39] The σ_y and σ_{uts} at room temperature reached 1400 and 1740 MPa but with $\varepsilon \approx$4%.[73]

2.2.2 Temperature and strain-rate dependent mechanical behaviour

As shown in Figure 2.5, the yield strength and ultimate tensile strength of Cantor alloys both decrease continuously with increasing temperature from -196℃ to 1100℃. The drop in strength is steepest from -196℃ to

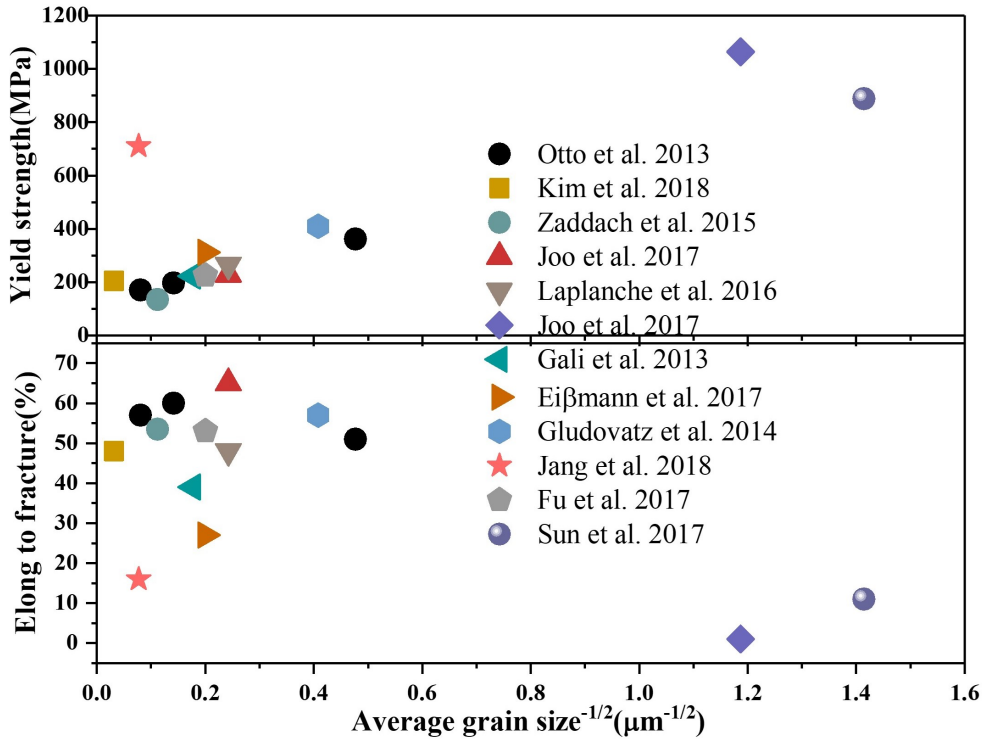


Figure 2.4: Yield strength σ_y (upper axis) and elongation to fracture ε (lower axis) as a function of $d^{-1/2}$ (d = the average grain size) at room temperature for Cantor alloys fabricated using different techniques. The data is taken from the work of Otto et al. (2013),[16] Kim et al. (2018),[36] Zaddach et al. (2015),[56] Joo et al. (2017),[81] Laplanche et al. (2016),[34] Joo et al. (2017),[69] Gali et al. (2013),[89] Eißmann et al. (2017),[70] Gludovatz et al. (2014),[9] Jang et al. (2018),[76] Fu et al. (2017)[82] and Sun et al. (2017).[66]

23℃, relatively gentle from 23℃ to 600℃, and then more noticeable, relative to the rate of decrease from 23℃ to 600℃, up to 1100℃. Tensile ductility ε generally increases from -196℃ to 200℃ but rate of change differs with different grain sizes in the range from 200℃ to 1100℃.

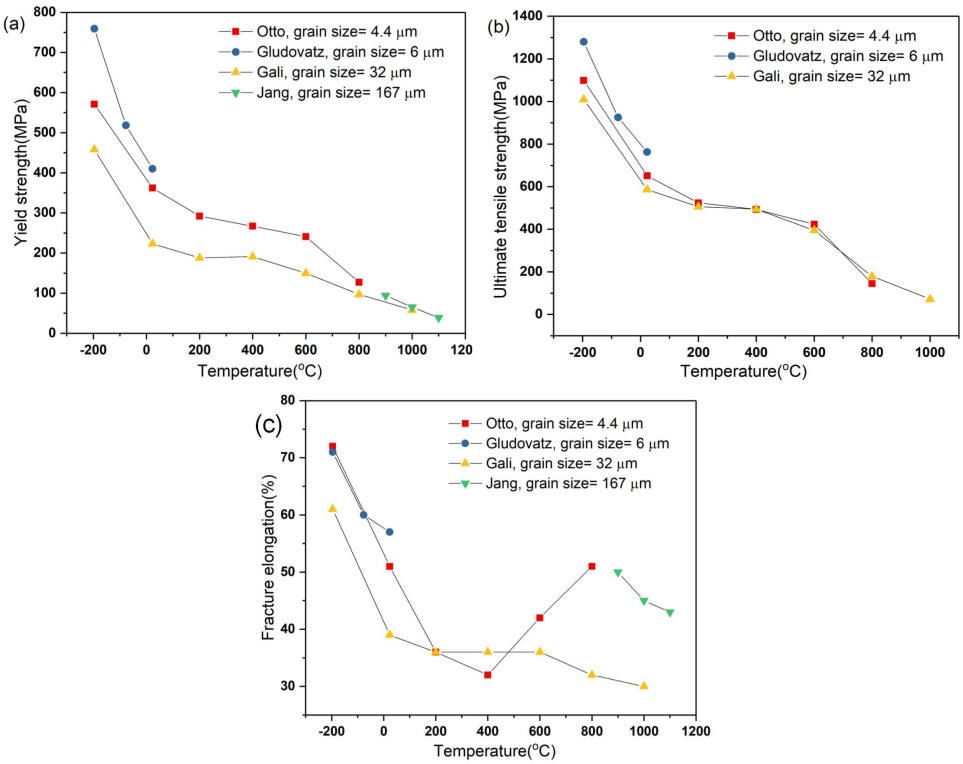


Figure 2.5: Representative tensile properties (a) yield strength, (b) ultimate tensile strength and (c) fracture elongation of Cantor alloys at temperature from -196℃ to 1100℃. Data was obtained from Otto et al.,[16] Gludovatz et al.,[9] Gali et al.[89] and Jang et al.[76]

As shown in Figure 2.6, Wu et al. reported that a family of single-phase equiatomic binary, ternary and quaternary subsets with FCC structures of the Cantor alloy also showed temperature dependence of tensile properties.[91] The temperature dependent yield strength trend is typical in FCC alloys, such as austenitic stainless steels which to some extent share similar compositions with Cantor alloys.[92] It has been demon-

strated that the temperature dependence of the shear modulus is not the dominant factor[93] for this behaviour, which may be instead determined by Peierls-barrier-dominated lattice friction.[91] The Peierls barrier is usually defined as energy per unit length of the dislocation line.[94] In other words, the increase of temperature led to the increase of dislocation width, which makes the dislocation glide easier and thus lower yield strength.[91]

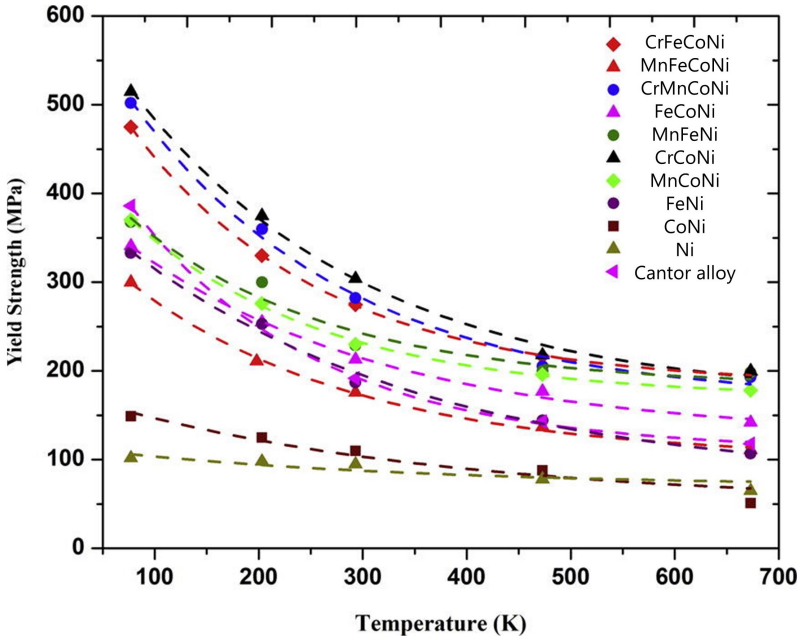


Figure 2.6: The temperature dependence of the 0.2% offset yield stress of Ni and equiatomic alloys. The dashed lines are curve fits according to temperature dependent Peierls-barrier-dominated lattice friction relationship.[91] Figure adapted with permission from.[91]

Apart from the temperature dependence, plastic deformation of alloys, as mentioned earlier, is also strain rate sensitive and affected by thermally activated processes. Thermal activation in the lattice at high temperatures assists dislocations in overcoming the Peierls barrier. The thermal part of shear flow stress can be described by the activation vol-

ume V, which represents the volume of matter involved in the thermally activated processes driven by a resolved shear stress and is defined as:

$$V = bA = -\frac{\delta \triangle G(\tau)}{\delta \tau}\bigg|_T = MkT\frac{\delta ln\dot{\epsilon}}{\delta \sigma}\bigg|_T \tag{2.1}$$

where b=0.255 nm is the magnitude of the Burgers vector (the magnitude and direction of the lattice distortion resulting from a dislocation),[34] A is the activation area, $M = 3.06$ is the Taylor factor relating normal stress σ and shear stress τ, $\triangle G(\tau)$ is the free energy barrier, k is the Boltzmann's constant, T the absolute temperature, and $\dot{\epsilon}$ is the strain rate.

Hong et al.[62] and Wu et al.[91] reported a strong strain-rate dependence of Cantor alloys using strain rate jump tests whereas Laplanche et al.[95] reported negligible effect of strain rate on the flow stress for Cantor alloys using stress relaxation experiments at engineering strain rates of 10^{-5} s^{-1} and 10^{-3} s^{-1} from -196℃ to 150℃ shown as the room temperature stress-strain curves in Figure 2.7a.[95] Figure 2.7b presents the activation volume as a function of true plastic strain at different temperatures for the Cantor alloy.[95] It is suggested by Laplanche et al.[95] that the measured activation volume agreed well in magnitude with the calculated results using a recent theory of solid solution strengthening for HEAs.[96] Thus it was claimed by Laplanche et al. that the Cantor alloy deformed by mechanisms common in conventional FCC solid solution alloys, such as Cu-Mn,[97] Cu-Al,[98] Al-Mg alloys[99] and austenitic

stainless steels[100–102] and no new intrinsic mechanisms were introduced due to being compositionally complex.

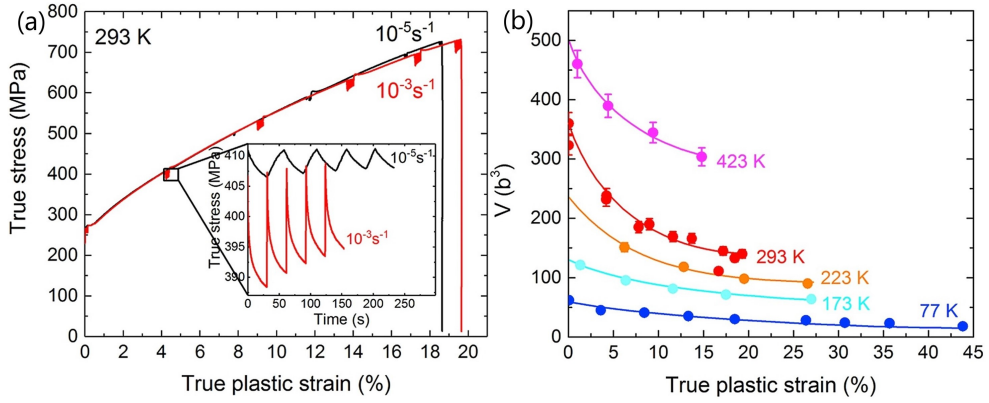


Figure 2.7: (a) Successive stress-strain curves using repeated load relaxation tests at room temperature for specimens of Cantor alloys and at strain rates of 10^{-5} s^{-1} and 10^{-3} s^{-1}, (b) physical activation volume, obtained at different temperatures, as a function of the true plastic strain. Figure adapted with permission from.[95]

Although there are some arguments regarding the thermally-activated deformation mechanism and the strain-rate sensitivity of Cantor alloys, a stronger dependence of yield strength on temperature than conventional dilute FCC solid solutions has been widely reported[62,86,89,95] and the activation volume was measured as 15-500 b^3 at -196-600℃.[103] In general, the activation volume for Cantor alloys at room temperature is lower than those of dilute FCC solid solutions[86] (100-1000 b^3) and higher than those of pure BCC metals ($\sim 10b^3$).

It is still a controversial issue regarding to whether or not Cantor alloys deform by mechanisms common in conventional FCC solid solution alloys. Although some researchers suggested that the overcoming of short-range orders in solid solution HEAs can contribute to higher activation volume,[103] the interaction between short-range orders[104,105] if

existed and dislocations is yet to be established and warrants further analysis.

2.2.3 Hall-Petch relationship

This grain size dependence is given by the well-known Hall-Petch relationship:

$$\sigma_y = \sigma_0 + k_{hp} \cdot d^{-1/2} \tag{2.2}$$

where σ_y is the yield stress, σ_0 is the friction stress value, k_{hp} is Hall–Petch coefficient which represents the effectiveness of grain boundaries in restricting dislocation slip and d is the grain size. Otto et al.[16] reported that in uniaxial tensile tests σ_0 and k_{hp} at room temperature were 125 MPa and 494 MPa·μm$^{1/2}$ respectively for Cantor alloys with grain size ranging from 4.4 μm to 155 μm. Sun et al.[66] extended the grain size to a wider range from 500 nm to 90 μm and similar values of σ_0 (194 MPa) and k_{hp} (490 MPa·μm$^{1/2}$) were observed.

The values of k_{hp} for 304 and 316 steels[101,102,106–109] were in the range of 280-410 MPa·μm$^{1/2}$, which adequately covered grain sizes ranging from micrometers to hundreds of micrometers, equiaxed structure and low density of defects. The value of k_{hp} for Cantor alloys also with equiaxed structure and low density of defects are slightly higher than those of 304 and 316 steels, indicating higher resistance for slip transfer at grain boundaries in Cantor alloys, but the underlying mechanisms are still unclear.

2.2.4 Strain-hardening behaviour

As discussed earlier, the significant decrease in strength with increasing temperature from -196℃ to 1100℃ has been observed in some FCC solid-solutions alloys.[28,110] Nonetheless, what is intriguing in the Cantor alloy is that the increase in yield stress at lower temperatures is accompanied by significant increases in ductility, toughness and ultimate-tensile strength, which has been attributed by many authors[9,16,39,76,111] to a high and steady work-hardening rate caused by a combination of planar dislocation slip and high levels of deformation nano-twinning at cryogenic temperatures. Prevalent occurrence of deformation twinning was suggested to derive from low stacking fault energy, which to some extent resembles twinning-induced plasticity (TWIP) steels.[112]

Figure 2.8 shows the comparison of RT strain-hardening rates and corresponding stress curves as a function of strain for TWIP steel ($FeMn_{18}Al_{1.5}C_{0.6}Si_{0.22}$),[112] $Al_{0.3}CrFeCoNi$ HEA,[113] 304 stainless steel,[114] $Cr_{10}Mn_{30}Fe_{50}Co_{10}$ high-entropy steel,[57] and the Cantor alloy.[9] Unlike other alloys, the Cantor alloy shown as red curve exhibited three different stages which was similar to that of TWIP Steel.[115] After the initial drop, the strain-hardening rate increased for TWIP alloy and there was a plateau for the Cantor alloy, which indicated the activation of twining during this stage.

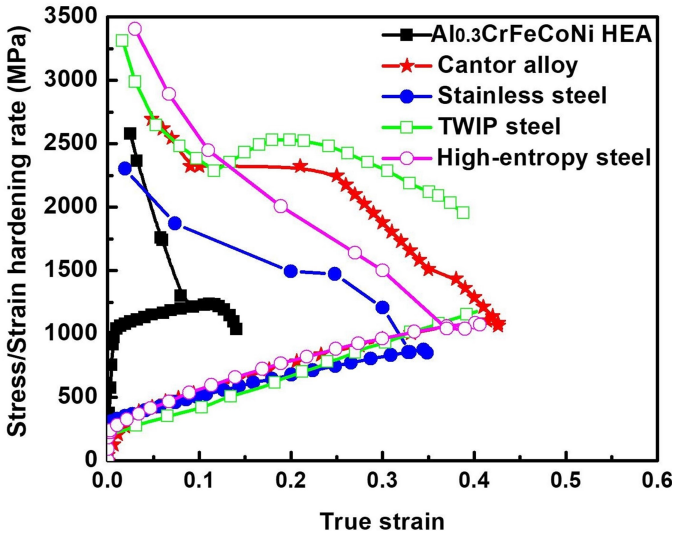


Figure 2.8: Comparison of strain-hardening rates and corresponding stress curves as a function of true strain for different alloys at RT: TWIP steel ($FeMn_{18}Al_{1.5}C_{0.6}Si_{0.22}$),[112] $Al_{0.3}CrFeCoNi$ HEA,[113] 304 stainless steel,[114] $Cr_{10}Mn_{30}Fe_{50}Co_{10}$ high-entropy steel,[57] and the Cantor alloy.[9] Reprinted with permission from.[29]

2.2.5 Twinning behaviour

The incidence of deformation twins depends on the stacking fault energy (SFE) and their frequency increases with the decrease in SFE. Zaddach et al. calculated the SFE for Cantor alloys as 18-27 mJ/m^2 based on measurement of microstrain and stacking fault probability through X-ray diffraction analysis as well as elastic constants calculated using density functional theory (DFT).[39] Okamoto et al. reported 30 ± 5 mJ/m^2 through measuring the separation distance of two coupled Shockley partial dislocations at room temperature.[111] Ab initio calculation[39] calculated the SFE as 20-27 mJ/m^2 at room temperature. The SFE is significantly lower compared with those of pure FCC metals (e.g. Cu, Ni and Al)[29] and similar or slightly higher than other low SFE alloys,

such as AISI 304L (18 mJ/m^2), Cu-30%Zn (14 mJ/m^2) and Cu-12.1%Al-4.1%Zn (7 mJ/m^2).[39] Simulations using first-principles methods[40] also confirm the temperature dependent behaviour of SFE in the Cantor alloy. It was found that SFE decreased dramatically to $\sim$3.4 mJ/m^2 at 0 K[40] and a later investigation reported that SFE actually became negative at 0 K.[116] These results are consistent with the easier formation of deformation twins at cryogenic temperature in Cantor alloys.

Deformation mechanisms for Cantor alloys at low and room temperature were investigated using in-situ TEM on interrupted tensile specimens. A transition between dislocation slip and nano-twinning deformation was frequently observed.[16] Deformation in early stages (up to 2%) resulted from planar dislocation glide in typical FCC slip systems $\{111\}\langle 110\rangle$. Many stacking faults were frequently observed, suggesting the splitting of some $1/2\langle 110\rangle$ dislocations into $1/6\langle 112\rangle$ Shockley partials,[16] as is normal for FCC materials.

In the later stage of plastic deformation (plastic strains $>$ 20%), plasticity occurred only by the aforementioned dislocations which organised into dislocation cells at room temperature whereas extensive deformation via nanotwinning was seen at -196℃ .[16,34] Prolific nanotwinning introduced continuous grain fragmentation by continually introducing new interfaces and decreasing the mean free path of dislocations, which is also called "dynamic Hall-Petch" effect.[58] This effect produces a high degree of work hardening, leads to a significant increase in σ_{uts} and prevents the

early onset of necking instability.

Figure 2.9 shows stress vs strain curves for the Cantor alloy at -196℃ and 23℃ [34] with four TEM images corresponding to each point marked on the curves. As mentioned earlier, only planar dislocations were observed in early stages of deformation, shown as Figure 2.9① where dislocation cells as shown in Figure 2.9③ formed at at 20% at 23℃ . Nanotwins were first observed after true strain of 7.4% at -196℃ (Figure 2.9②) but at 25% at 23℃ (Figure 2.9④). The tensile stress at which twinning occurred was 720 ± 30 MPa, approximately independent of temperature, from which the critical resolved shear stress for twinning was deduced to be 235 ± 10 MPa. The reason why extensive twinning was observed at low temperature instead of room temperature is likely because the specimens did not experience a high enough stress to the "critical" stress.[16,34]

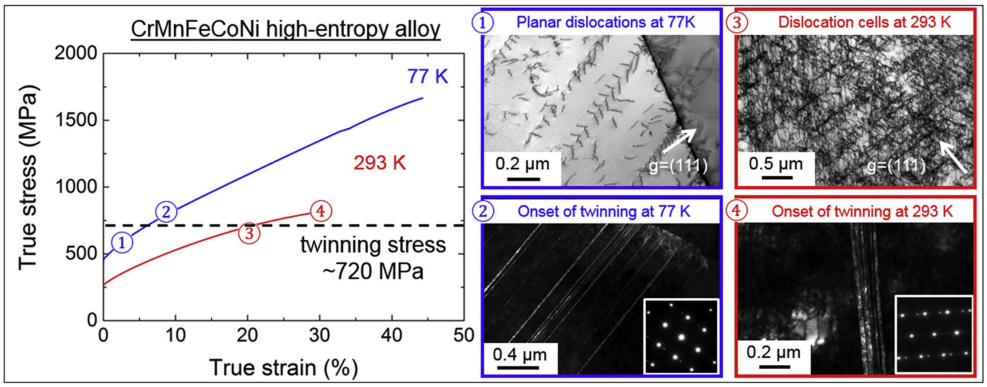


Figure 2.9: Stress vs strain curves for the Cantor alloy at -196℃ and 23℃ with four TEM images corresponding to each point marked on the curves. The tensile stress at which twinning occurs was 720 ± 30 MPa. Reprinted with permission from.[34]

Joo et al.[81] reported a strong dependence on grain orientation of twinning in the Cantor alloy at cryogenic temperature and deformation

twinning was favoured in grains rotating towards the ⟨111⟩ ∥ tensile axis (TA) which resembles TWIP steels.[117] As shown in the inverse pole figures (IPFs) by electron backscatter diffraction (EBSD) in Figure 2.10, Liu et al.[118] revealed a strong ⟨111⟩ ∥ TA and weak ⟨001⟩ ∥TA tensile texture after severe plastic deformation, typical in conventional FCC materials. The presence of 115⟨552⟩ texture component from twinning did not significantly contribute to overall texture.

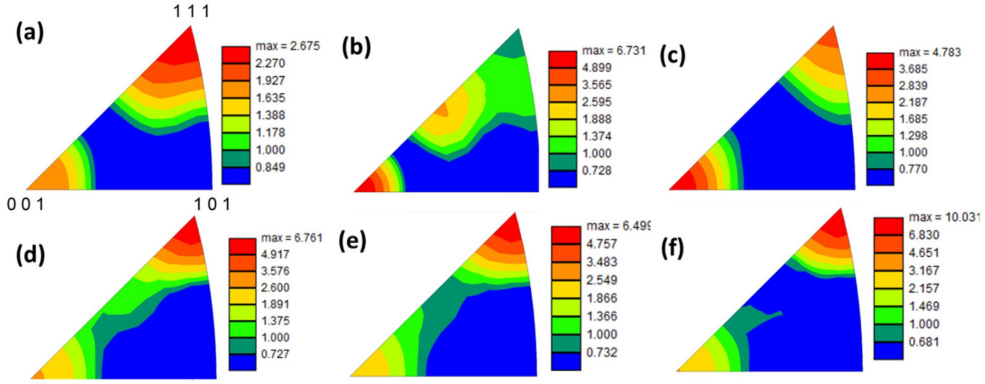


Figure 2.10: Inverse pole figures (IPFs) calculated from Electron Backscatter Diffraction (EBSD) of different strain levels: (a) 0%, (b) 7%, (c) 13%, (d) 27%, (e) 41%, (f) 51%; Reprinted with permission from.[118]

Wu et al.[119] reported that in single crystalline Cantor alloys, the activation of multiple twin systems contributed to their interaction and caused pronounced strain hardening. The self hardening modulus of an isolated twin system was smaller than the twinning self hardening moduli when multiple twin systems were present due to residual Burgers vectors. They also demonstrated that the latent hardening moduli for the observed twin-twin interactions were at least one order of magnitude higher than those for slip-slip and slip-twin/twin-slip interactions, which indicated the significance of twin-twin interactions to the overall material

strengthening.

2.3 Oxide dispersion strengthening HEAs

Advanced fission and fusion power production presents a number of challenges, for their components, which are expected to experience high-energy neutrons and high temperatures for prolonged periods.[43–50] By the addition of a low volume fraction dispersed nano-scale oxide particles into a majority engineering alloy "matrix", ODS steels have improved high-temperature properties and better radiation resistance than non-ODS equivalents. The sub-micron oxide particles act as sinks for point defects produced by irradiation damage, and act as He trapping sites, thus protecting grain boundaries and suppressing macroscopic swelling.[120] Another potential contributing feature of fine oxide particles is to improve creep strength, permitting longer periods of operation at elevated temperature.[121]

Powder metallurgy/mechanical alloying (PM/MA) is the well-established route to fabricate ODS alloys.[122] A prolonged powder milling step is used to disperse and dissolve typically Y_2O_3 particles into steel powders. However, the PM/MA route is often time-consuming, prone to contamination and scaling up to industry (e.g. 10 kg or 100 kg) is difficult.[123] Alternative manufacturing methods, including those based on melt processing and casting, have shown some encouragement to produce ODS alloys at an industrial scale[1,124,125] in the future, but are at an early stage.

In the PM/MA route, elemental or usually pre-alloyed powders are firstly mechanically alloyed by ball milling with Y_2O_3 (or ZrO_2, CeO_2, HfO_2, etc.) under an inert gas environment in an attempt to produce a homogeneous mixture. In order to consolidate the powder, the powder is then cold-pressed, degassed and sintered under pressure (e.g. hot isostatic pressing in a sealed can or spark plasma sintering under uniaxial load), followed by elevated temperature thermomechanical processing such as forging or extrusion to re-precipitate/coarsen the oxide-based dispersoids and to enhance properties.[126]

To achieve the desired mechanical properties and irradiation resistance, a dispersion of fine (1-10 nm) oxides with a fraction of typically 0.25-0.5 wt.% in a single phase matrix is required. There have been many studies and reviews covering this topic, which is beyond the scope of this thesis and can be found elsewhere.[123,127] Using advanced characterisation techniques, such as atom probe tomography (APT) and TEM, the re-precipitated Y-O and Y-Ti-O nanoclusters were shown as comparatively stable under both neutron and ion irradiation at temperatures between 300-700℃ and doses of 15 to 150 dpa.[128–130]

In Ti-free ODS alloys, cubic and monoclinic Y_2O_3 have been frequently identified as 10–40 nm particles[131,132] and smaller Y-Cr oxides have also been observed in ODS alloys with higher chromium content alloys.[133] Precipitates in Ti-containing ODS alloys are usually categorised as large, medium and small particles of diameters 300–50 nm, 50–10 nm

and < 5nm respectively.[134] Larger particles normally have a low number density and varying composition depending on alloy chemistry, but are commonly Cr-Ti oxides,[134] nitrides[133] and carbides.[135] A summary of the characterisation of various ODS particles can be found elsewhere.[136]

One of the disadvantages of single phase HEAs such as the Cantor alloy, is that there are no second phases present to stabilise the grain structure, for example by Zener pinning.[137] In details, a dispersion of fine particles can act to prevent the motion of low- and high-angle grain boundaries by exerting a pinning pressure which counteracts the driving force pushing the boundaries.[138] Consequently, the idea of introducing oxide dispersoids into HEAs has started to be explored.[139] Liu et al.[140] manufactured Y_2O_3-containing CrMnFeCoNi by MA followed by SPS. The addition of 0.25 wt.% Y_2O_3 increased the ultimate tensile strength from 868 MPa to 1001 MPa and the strain to fracture increased from 5.4% to 6.1%. However, when the concentration of Y_2O_3 increased to 0.5 wt.%, both yield strength and strain to fracture decreased. Hadraba et al.[141] reported a SPS processed powdered Cantor alloy reinforced with nano-oxides by adding O_2 gas, Y and Ti to the blend during MA. The introduction of nano-oxides resulted in 50% grain size reduction and an increase in yield strength from 971 MPa to 1269 MPa. However, there was only 0.74% elongation to fracture.

Chung et al.[142] manufactured cryo-mill and SPS pristine Cantor, Cantor $+Y_2O_3$, and Cantor+Y alloys. The Cantor+Y alloy showed a

refined crystallite size, higher dislocation density and high number density of in-situ Y-based nano dispersoids after MA compared with pristine Cantor alloy and Cantor+Y_2O_3 alloy. The Cantor+Y alloys average grain size increased with increasing sintering temperature with an average grain size of 170 ± 140nm at 700℃ compared with 340 ± 270nm at 900℃. Figure 2.11 shows the stress-strain curves of pristine Cantor powder, pristine Cantor, Cantor+Y_2O_3, and Cantor+Y alloys. Yield strength of Cantor+Y alloy increased from 835 MPa to 1460 MPa compared with the pristine Cantor alloy. However, this increase was accompanied by a loss in ductility, with only 1.5% strain to fracture for Cantor+Y alloy.

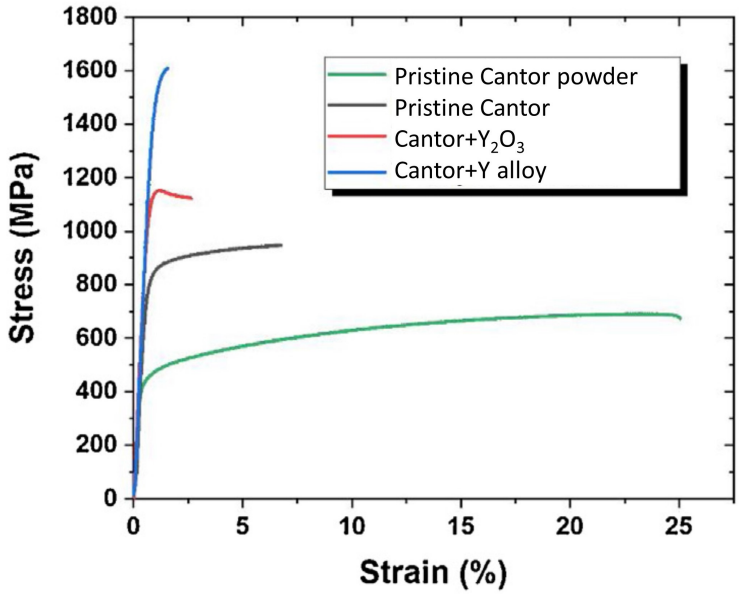


Figure 2.11: Stress–strain curves of pristine Cantor powder, pristine Cantor, Cantor+Y_2O_3, and Cantor+Y alloys. Adapted with permission from.[142]

Fine-scale Y_2O_3 has also been introduced to the ternary and quaternary sub-systems of Cantor alloys. Guo et al.[143,144] found that nano-sized Y_2O_3 (monoclinic structure) with average size of 13.1 ± 7.8 nm and

$Y_2Ti_2O_7$ (pyrochlore structure) particles with average size of 10.6 ± 5.2 nm were uniformly distributed in FeCoNi-$1.5Y_2O_3$ and FeCoNi-1.2Ti-$1.5Y_2O_3$ MA/SPS alloys respectively. Yield strength increased from 559 MPa (FeCoNi) to 981 MPa (FeCoNi-$1.5Y_2O_3$) and 1050 MPa (FeCoNi-1.2Ti-$1.5Y_2O_3$), but again with the compromise of ductility ($2.9\pm0.8\%$ in FeCoNi-$1.5Y_2O_3$ and $1.2\pm0.8\%$ in FeCoNi-1.2Ti-$1.5Y_2O_3$). Similarly, Jia et al.[145] found that compressive yield strength increased from 657 MPa for FeCrCoNi to 1754 MPa for MA/SPS 5 wt.%Y_2O_3 FeCrCoNi but with a reduction in elongation to fracture from $> 50\%$ to 5.8%. Peng et al.[146] added Y_2O_3/Ti/Zr in CoFeCoNi powder and produced a MA/SPS ODS-CrFeCoNi. Figures 2.12a and 2.12b show scanning transmission electron microscopy (STEM) bright-field (BF) images of 0.5 wt.% and 3 wt.% Y_2O_3-CoFeCoNi, revealing high-density nanoscale oxides and a few large precipitates (Cr_2O_3 and Cr_7C_3). Figures 2.12c,e and 2.12d,f show representative high-resolution transmission electron microscopy (HRTEM) images of monoclinic and cubic Y_2O_3 oxides with average size of 6.5 nm in the ODS-HEAs on the addition of 0.5 wt.% and 3 wt.% Y_2O_3 respectively. Complex Y-Ti-O and Y-Zr-O oxides of larger size were observed when Ti/Zr was also added.

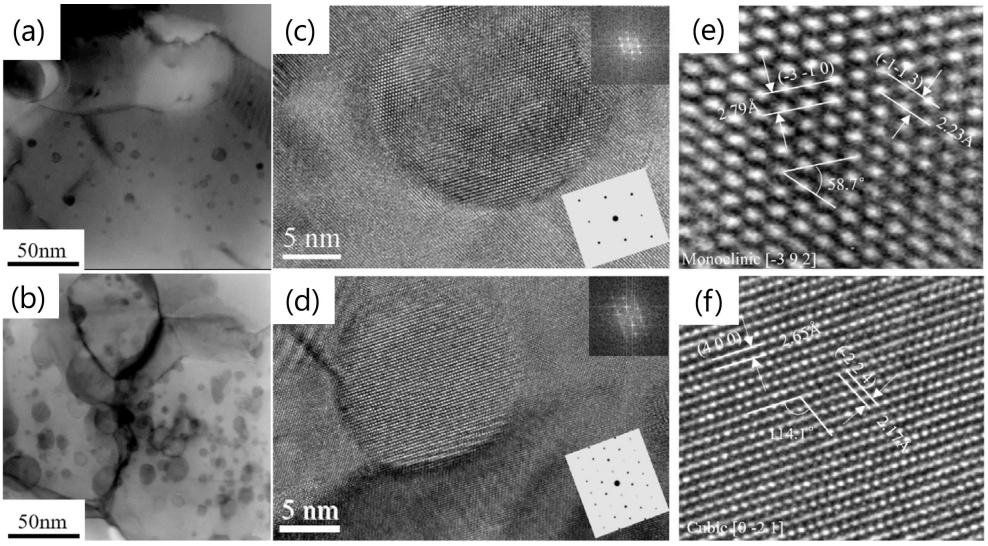


Figure 2.12: STEM BF images of (a) 0.5 wt.% and (b) 3 wt.% Y_2O_3-CoFeCoNi. HRTEM images of (c,e) monoclinic and (d,f) cubic Y_2O_3 oxides with average size of 6.5 nm in the ODS-HEAs with the addition of 0.5 wt.% and 3 wt.% Y_2O_3 respectively. Adapted with permission from.[146]

Overall, studies of ODS-HEAs have mainly focused on the Cantor alloy and its subsystems and the MA/SPS route has been applied in the majority of studies, although there have been different approaches in introducing Y to HEAs. Most commonly, Y_2O_3 was directly added during MA whereas in other studies a minority of Y was pre-alloyed with HEA powder before MA with the intention that Y-based oxides would be formed subsequently. Under optimum conditions, both routes could provide a high-density of nanoscale oxides < 50 nm. These nanoscale oxides led to a reduction in grain size by grain boundary pinning during thermomechanical processing, and contributing significantly to grain boundary strengthening. Combined with precipitate hardening effects, yield strength (tensile and compressive) increased significantly but in general at the expense of ductility. Most ODS-HEAs exhibited an elon-

gation of $< 5\%$, which in general was smaller than current commercial ODS steels[147–154] and likely insufficient for structural materials in nuclear applications. However, this field is much more immature than ferritic ODS steels and there appears no intrinsic reasons why better balanced properties of ODS HEAs might not be achieved as optimisation. As with ODS steels, the challenges will be minimising embrittling contamination, promoting very fine scale dispersion, and establishing processing routes capable of multi-kgs's manufacturing.

2.4 Irradiation response of HEAs

The structural materials used in current nuclear reactors are exposed to energetic particle irradiation at elevated temperature, up to ∼300℃, and structural materials in future nuclear reactors are forecast to be exposed to even higher irradiation doses and temperatures,[45,47,50] i.e. up to 200 dpa and 1000℃. During irradiation damage at elevated temperature, the spatial redistribution of solute and impurity elements by diffusion is enhanced, which may lead to localised enrichment or depletion of alloying elements at dislocation loops, voids, grain boundaries and phase boundaries, and more stable (lower free energy) phases may form.[155–157] Together with irradiation induced dislocation lines and dislocation loops, elevated temperature can accelerate changes in macroscopic properties, leading to hardening and embrittlement.[158,159] The formation and growth of voids and gas bubbles are also well-known for their negative influence

on material performance in radiation environments at elevated temperature.[160–162]

The majority of research for irradiation response of HEAs focused on the Cantor alloy and its sub-systems, derivatives,[28,163–165] usually with FCC structure. Investigations of the irradiation resistance of other HEAs (e.g. body-centred cubic structure) with no relation to the Cantor alloy system have also started, particularly low-activation refractory HEAs, but are at an earlier - although quickly advancing - stage. In this section, radiation damage mechanism, particularly collision cascade is discussed first. Investigations of irradiation response of low-activation refractory HEAs are reviewed. Then due to the significant body of literature, the state-of-the-art experimental and computational results relating to the irradiation response of the Cantor alloy, its sub-systems and derivatives at elevated temperature (300-700℃) are reviewed.

2.4.1 Radiation collision cascade

Irradiated particles lose energy as they propagate through a material. If the energy transferred overcomes the displacement threshold energy E_d, then the atom will be knocked off its lattice site, which is the primary knock-on atom (PKA).[166] If the kinetic energy of PKA is greater than E_d, it continues displacing other atoms in the lattice. Eventually, a cascade of displaced atoms (collisional phase < 1 ps) is formed consisting of energetic displaced atoms and vacancies.[167] The cascade continues to evolve. The collision energy of the displaced atoms distributed to other

neighbouring atoms in the region with highly deposited energy and atoms are similar to molten material. With energy being transferred to the atoms in the surrounding, the molten regions return to the quenched stage where thermodynamic equilibrium is established and stable lattice defects form as point defects or defect clusters. The last stage of cascade is the annealing stage in which the energy of the cascade is decreasing. Following this, defect diffusion, clustering and destruction begin to take over, causing irradiation-induced microstructural changes.[167]

2.4.2 Irradiation response of low-activation refractory HEAs

The radioactivity derived from the activation of elements by neutron irradiation is a concern for nuclear applications. The use of low activation elements is desired to minimise the exposure of plant operators and decommissioners, and to minimise the radioactivity of waste. For example, considerable efforts have been devoted to avoid Co-containing materials in primary circuit water pumps.[164] Specifically, elements used in plants should ideally decay to UK low level waste (LLW) level or below in 100 years or less. Figure 2.13 shows the 'time-to-LLW' values for all possible naturally-occurring elements after neutron exposure predicted in the divertor of a typical fusion reactor.

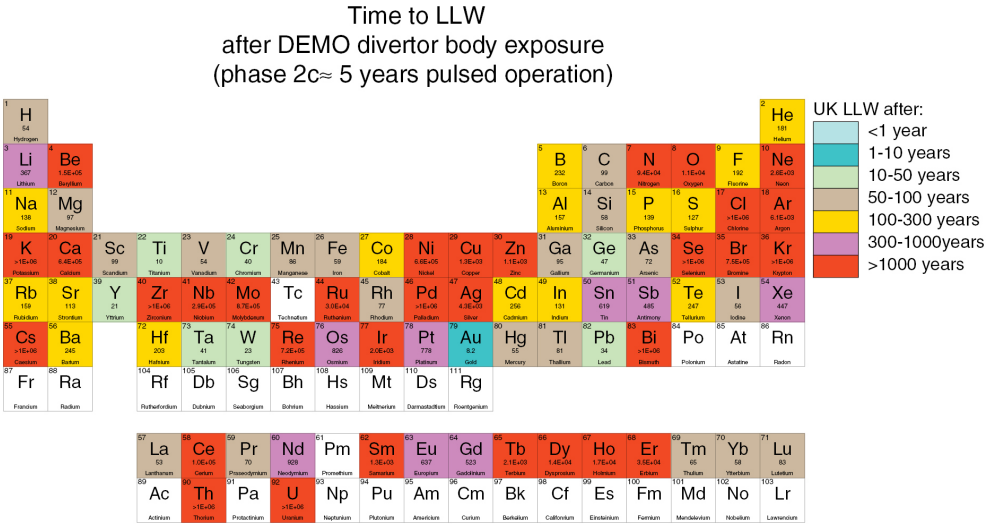


Figure 2.13: Periodic table with the UK 'time-to-low level waste (LLW)' values for each naturally occurring element after irradiation during one full operation cycle in a fusion reactor divertor cassette body. Note that no tritium removal is considered, and is responsible for the long-lived waste of the lighter elements, such as He, and Li. Adapted with permission from.[168]

Most of the studies on irradiation response of low-activation refractory HEAs have been limited to the initial microstructure of HEAs and irradiation-induced hardening assessed using micro-mechanical testing. Investigations of radiation-induced defects, segregation, phase instability, swelling and gas bubbles using advanced electron microscopy are scarce. Studies on initial microstructure of HEAs without investigations of irradiation behaviour were not included in this review, such as W_xTaTiVCr,[169] TiVZrTaHf and TiVZrTaW,[170] CrMnVTi[171] and CrFeTiV.[172]

Kareer et al.[51] reported that TiVZrTa and TiVCrTa consisted of one body-centred cubic (BCC) main phase and minor secondary phases. Using nano-indentation, there was only negligible hardening after 2 MeV V^+ ion irradiation at 500℃ to a fluence of 2.26×10^{15}cm^{-2} compared

with 8% hardening in TiVNbTa and 37% hardening in a V control sample. Sadeghilaridjani et al.[173] reported that after 4.4 MeV Ni^{2+} ion irradiation at RT to a fluence of $1.08 \times 10^{17} cm^{-2}$, TiVZrHfTa exhibited 20% hardening using nano-indentation compared with 50% hardening in 304SS. There was a 28% increase in average yield strength for HfTaTiVZr after irradiation and a 54% increase for 304SS measured by in-situ micro-pillar compression tests.

Moschetti et al.[174] reported a nanocrystalline TiZrNbTaHf irradiated with 5 MeV He^{2+} ions to a fluence of $4.4 \times 10^{17} cm^{-2}$ with a 14% increase in average yield strength from 1833 MPa to 2088 MPa without reduction in strain to failure assessed using micro-tensile testing. There were agglomerated He bubbles in the irradiated TiZrNbTaHf, preferentially located on grain boundaries. The increase in strength without compromising elongation was attributed by Moschetti et al. to a change in deformation mechanism. He bubbles were suggested to weaken grain boundaries which were easier to move compared with unirradiated materials. Waseem et al.[175] irradiated $W_{0.5}(TaTiVCr)_{0.5}$ using 200 keV He^{+} ions at a maximum fluence of $1 \times 10^{17} cm^{-2}$. The hardness increased from 11.6 GPa to 14.9 GPa after irradiation and there was no clear indication of He bubbles and dislocation loops but only small circular-shaped features in some irradiated STEM specimens, which were suspected as precursors of He bubbles.

El-Atwani et al.[52] reported a single-phase BCC $W_{38}Ta_{36}Cr_{15}V_{11}$ HEA

thin film produced using magnetron sputtering deposition. Figure 2.14 shows bright-field TEM images as a function of dpa irradiated in situ by 1 MeV Kr^{2+} ions at 800℃ . There were no radiation-induced dislocation loops even after irradiation of up to 8 dpa at 800℃ and only negligible irradiation hardening using nanomechanical testing. Black dots in Figure 2.14 were determined by TEM and APT to be Cr and V-rich second-phase precipitates and their intensity increased slightly with increasing irradiation dose. Theoretical predictions using ab initio and Monte Carlo modeling showed that good irradiation resistance was attributed to relatively equal mobilities of point defects.

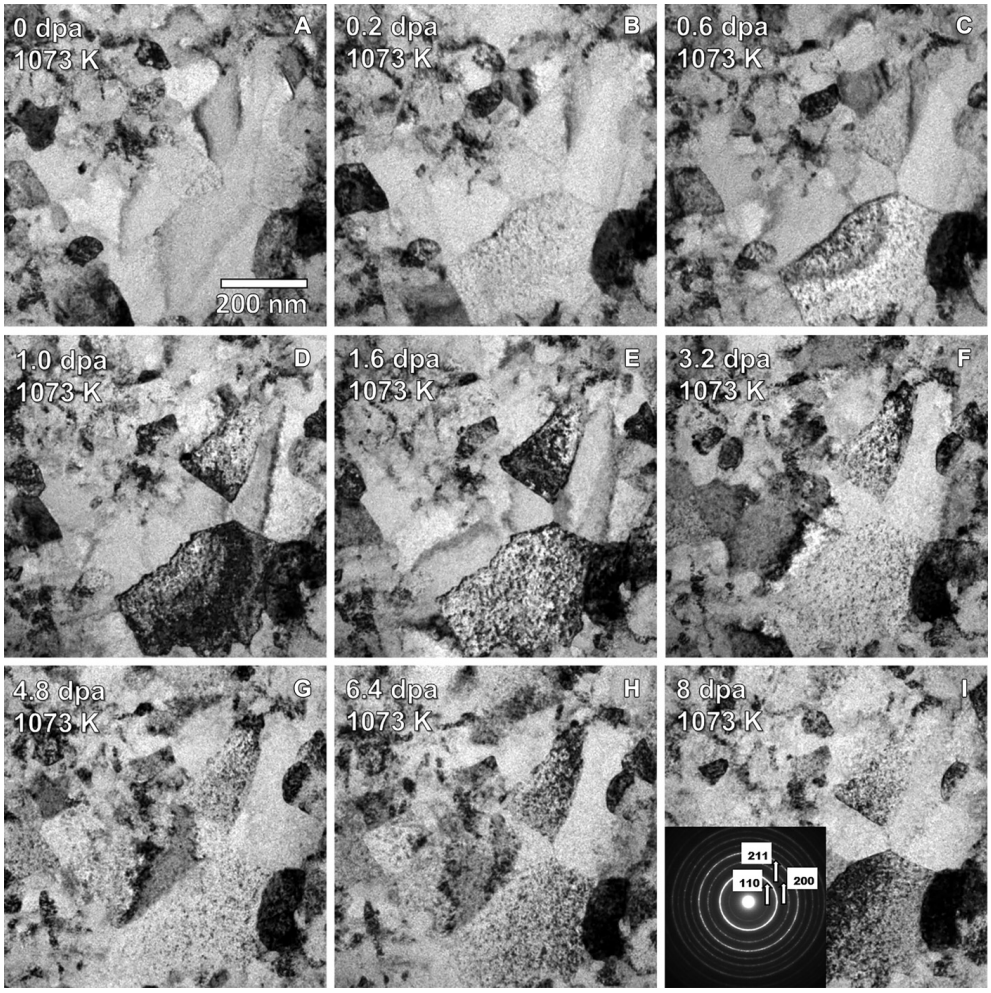


Figure 2.14: Bright-field TEM images as a function of dpa for $W_{38}Ta_{36}Cr_{15}V_{11}$ HEA thin film irradiated in situ with 1 MeV Kr^{2+} ions at 800℃ . (a) pristine, (b) 0.2 dpa, (c) 0.6 dpa, (d) 1.0 dpa, (e) 1.6 dpa, (f) 3.2 dpa, (g) 4.8 dpa, (h) 6.4 dpa, and (i) 8 dpa. There were no dislocation loops but slightly enhanced precipitation shown as black spots in some grains. Reprinted with permission from.[52]

Zhao[176] calculated the point defect properties of BCC-VCrTaW using first-principles modeling. Interstitial dumbbells containing V and Cr were shown to posses lower formation energies, which will likely result in an enrichment of V and Cr and a depletion of Ta and W in the vicinity of defect sinks, agreeing well with experiment results.[52] The distribution of migration energies for vacancies and interstitials exhibited a much

wider overlap region in VCrTaW compared with FCC HEAs, which was suggested to lead to better irradiation resistance than FCC HEAs by enhancing defect recombination.

Overall, low-activation refractory HEAs have been developed at small scale and the effect of irradiation on these HEAs has been investigated using TEM, APT, micro- and nano-mechanical testing as well as simulations. Due to limited data available, no generic conclusions can be made with certainty. It is worth noting that although it has been claimed that some of the HEAs remained single-phase BCC structure after annealing, research on thermal stability over a long period and at elevated temperature for these low-activation refractory HEAs is scarce. The introduction of refractory elements (e.g. Ta and W) into low-activation but not refractory elements (e.g. Ti, V, Cr, and Fe) to form HEAs may be problematic in terms of the tendency to form complex and usually very hard, brittle intermetallics, such as C15 Laves phase, which is likely detrimental to tensile properties and long term mechanical stability.

2.4.3 Radiation-induced segregation and phase instability

Radiation-induced segregation (RIS) is caused by preferential association between the flux of vacancy and interstitial point defects and the flux of solutes to point defect sinks,[177] such as grain boundaries, dislocations and voids. Enrichment or depletion of solute can lead directly to highly localised precipitation if local solute concentrations exceed the solubility limit. RIS behaviour is affected by many factors, including size

difference, temperature, impurities, change of local composition, dose rate etc.[167] For example, size difference between solute atoms plays an important role in determining the direction and magnitude of segregation.[178] It is suggested by Was[167] that oversize solute atoms tend to migrate away from the vacancy flux whereas undersize solute atoms migrate preferentially as interstitials in order to reduce the overall strain energy in the lattice.

RIS can result in the degradation of macroscopic properties, for instance, it has been know for decades that radiation-induced depletion of Cr at grain boundaries contributes to irradiation-assisted stress corrosion cracking (IASCC) in austenitic stainless steels.[179,180]

In nanocrystalline CrFeCoNiCu,[181] the FCC solid solution remained the main phase under fast MeV electron irradiation of up to 40 dpa at 500℃, although there was some minor fraction of transformed BCC and B2-type FeCo and FeNi $L1_0/L1_2$ ordering. Phase separation and $L1_0$ (NiMn)-type ordering also took place in CrMnFeCoNi and CrFeCoNiPd irradiated with 1250 keV electrons of up to 1 dpa at 400℃ but there was no detectable phase separation/decomposition in CrFeCoNi.[182] In contrast, no phase separation/decomposition was observed in either CrMnFeCoNi or CrFeCoNiPd,[183,184] in this case irradiated with 3 MeV Ni ions at 380, 500 and 580℃ to a fluence of $5 \times 10^{16}\text{cm}^{-2}$. When compared with ion irradiation, relatively low primary knock-on atom energies were produced from electron irradiation, which likely contributed to the

different observed microscopic changes in nominally the same alloy. The role of far from equilibrium states generated by ion irradiation on the thermodynamic balance between enthalpy and entropy effect on phase stability must also be considered.

It is worth pointing out that although the Cantor alloy retained a simple FCC solid solution even after long annealing up to 500 days[21] at relatively high temperatures (over 800℃), it decomposed into multiple phases, i.e. $L1_0$-type NiMn, BCC Cr-rich solid solution and B2-type FeCo[21] at intermediate (500-700℃) annealing temperatures after 500 days.[21,22,33] Note that these intermediate temperatures (500-700℃) are likely to be the service temperature for structural materials in advanced nuclear reactors, such as lead-cooled fast reactors (LFR), sodium-cooled fast reactors (SFR) and super critical water-cooled reactors (SCWR) with core outlet temperatures of 550-1000℃, 550℃ and 350-720℃ respectively.[43,47]

Barr et al. explored the RIS behaviour of the Cantor alloy under 3 MeV Ni^{2+} ion irradiation at 500℃ and a fluence up to 3×10^{15} cm^{-2}.[185] Figure 2.15a shows representative RIS profiles at a random high-angle grain boundary (HAGB) at 2 dpa using STEM-EDS linescan, while Figure 2.15b compares the compositional change along GBs to regions away from GBs for the Cantor alloy and conventional FCC alloys (304 high and commercial purity,[155] model Ni-Cr alloys,[156,186] and model Fe-Ni-Cr alloys[156]). There was a substantial depletion of Mn and enrichment of Co and Ni along HAGBs at both 2 and 3 dpa, which followed similar trends

to the RIS behaviour in conventional Fe-Ni-Cr alloys. Self-diffusion radiotracer diffusion coefficient measurements at high temperature[187] showed that the fastest and slowest diffuser were Mn and Co respectively, leading to corresponding a depletion of Mn and enrichment of Co based on the vacancy dominated inverse Kirkendall mechanism (the preferential coupling of solutes to the vacancy flux).[157] The magnitude of segregation was similar for the Cantor alloy and for conventional Fe-Ni-Cr alloys under similar irradiation conditions.

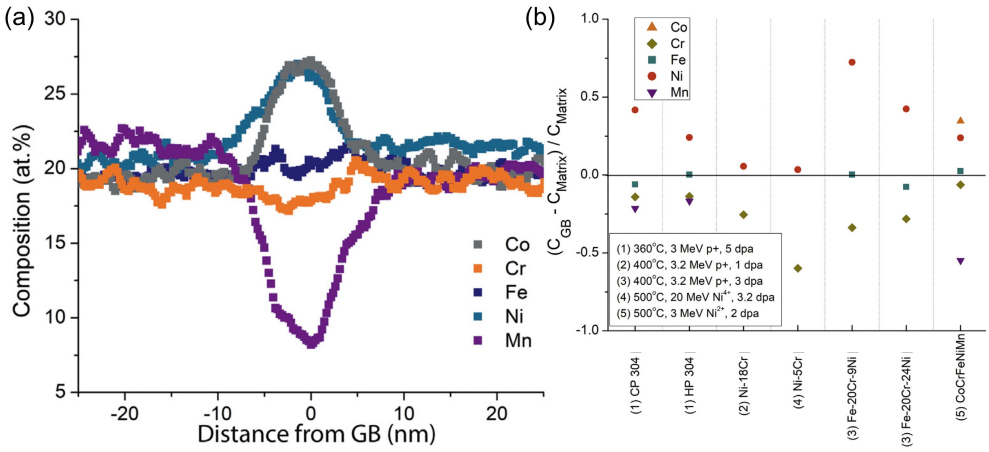


Figure 2.15: (a) Representative irradiation-induced segregation profiles from a STEM-EDS linescan at a random high angle GB in the Cantor alloy irradiated with 3 MeV Ni ions at 500℃ and 2 dpa. (b) Comparison of the compositional change along GBs and the matrix between the Cantor alloy and conventional FCC alloys (304 high and commercial purity,[155] model Ni-Cr alloys,[156,186] model Fe-Ni-Cr alloys[156]). Adapted with permission from Barr et al.[185]

Kumar et al. studied the irradiation behaviour of Co-free $Cr_{18}Mn_{27}Fe_{27}Ni_{28}$ single-phase alloy irradiated with 3 or 5.8 MeV Ni ions at temperatures ranging from room temperature to 700℃, and up to 10 dpa. There were no phase changes according to X-ray diffraction but there was enrichment of Ni and depletion of all other three elements at GBs based on

STEM-EDS linescan measurements. When compared with a more conventional $FeCr_{20}Ni_{24}$ alloy, the solute segregation in $Cr_{18}Mn_{27}Fe_{27}Ni_{28}$ was significantly reduced.[188]

Chemical segregation along defect clusters can also occur. RIS behaviour at defect clusters in FeNi, FeCoNi, CrFeCoNi and CrMnFeCoNi was investigated using electron energy loss spectroscopy (EELS).[184] Figure 2.16a shows a STEM-BF image and Figure 2.16b shows an enlarged high-angle annular dark-field (HAADF) image of an interstitial-type dislocation loop in irradiated Cantor alloy with corresponding compositional linescan profiles across dislocation loops in the four alloys (Figures 2.16c-d). Frank dislocation loops were enriched with Ni and Co, and depleted in Cr and Fe in FeNi, FeCoNi, CrFeCoNi, whereas there was no obvious segregation in the Cantor alloy.

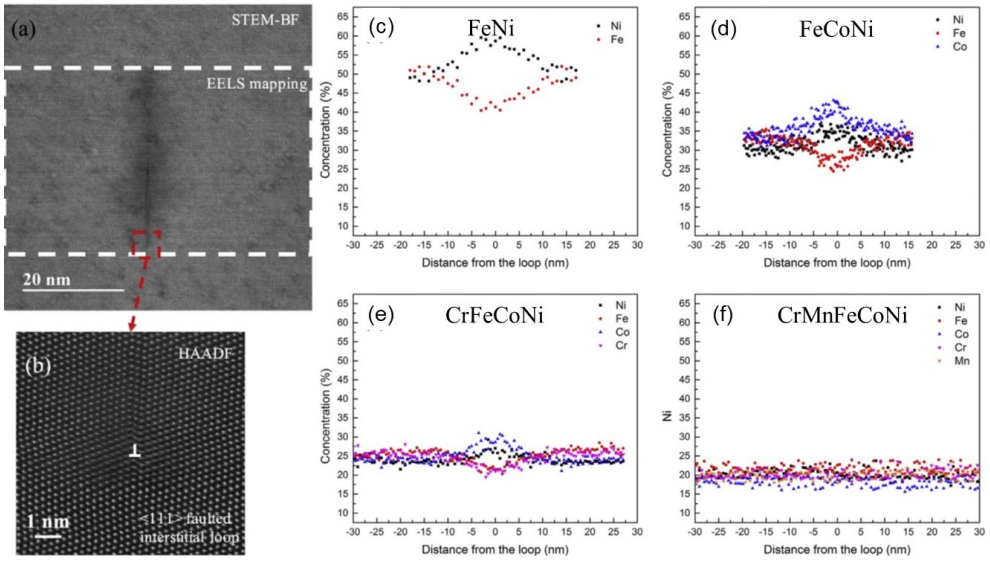


Figure 2.16: (a) STEM-BF image of a dislocation loop in the Cantor alloy; (b) high-angle annular dark-field (HAADF) image enlarged from the region marked by the red box showing an interstitial-type Frank loop. Element linescan profiles across the dislocation loops in (c) FeNi, (d) FeCoNi, (e) CrFeCoNi and (f) CrMnFeCoNi. Adapted with permission from Lu et al.[184]

RIS at defects will depend upon the propensity to form such defects and the extent of the equilibrium concentration of vacancies and interstitials at a given temperature will be determined by the associated point defect formation energies. Using ab initio calculations and empirical potentials, Zhao et al. calculated the formation energy of interstitials and vacancies in FeNi, CrCoNi and CrFeCoNi, which are shown in Figure 2.17, with the formation energy for Ni marked by a black dashed line. The defect formation energies presented as a distribution, with an overlap of interstitial and vacancy formation energies. Generally, the formation energy of preferred [100] interstitial dumbbells (E_f^i) in alloys was lower than that in Ni (3.96 eV[189] and 4.27 eV[190]) while the formation energy of vacancies (E_f^v) was higher than that in Ni ($E_f^v \approx$1.45 eV)[189,190]).

Considering various possible dumbbell interstitials in HEAs, preferable diffusion channels due to lower formation energies of certain types of dumbbells were observed, which can be expected to affect the RIS behaviour along defect clusters. For example, in FeNi, the lower formation energy of a [100] Ni–Ni dumbbell than a [100] Fe–Fe dumbbell suggested that interstitial defects will preferentially diffuse in Ni and not Fe.[190] In contrast, Co-containing (e.g. Co-Co, Co-Fe and Co-Cr) dumbbells in CrFeCoNi had, in general, a lower formation energy than Ni-Ni dumbbells, leading to preferable binding of Co interstitials,[189] which agreed well with the interstitial-dominated RIS behaviour along intersitial loops for Ni/Co enrichment and Fe depletion in FeNi and CrFeCoNi discussed above.

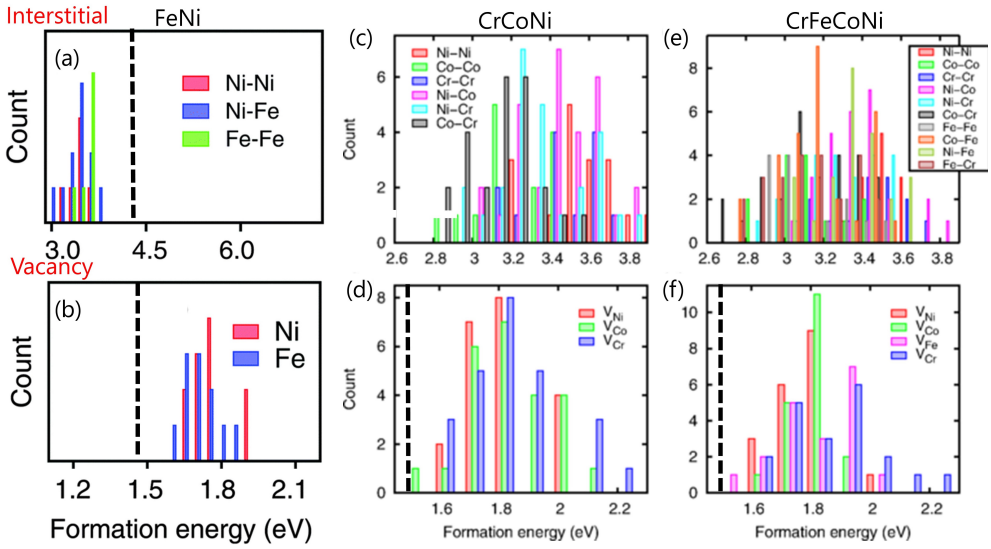


Figure 2.17: Formation energy of a [100] dumbbell in (a) FeNi, (c) CrCoNi and (e) CrFeCoNi alloys determined by ab initio calculations (upper column); formation energy of a vacancy in (b) FeNi, (d) CrCoNi and (f) CrFeCoNi (lower column). The black dashed lines represent the formation energies of interstitials and vacancies in Ni. The formation energy of interstitials in Ni is beyond the scale of (c) and (e). Adapted with permission from Zhao et al.[189,190]

With regard to vacancy formation energy, in both CrCoNi and CrFeCoNi, vacancies will likely favour a Ni-rich as well as Co/Cr-depleted environment because more Ni atoms in the first-nearest-neighbor shell surrounding vacancies lead to a lower formation energy for vacancies[190] while higher Co and Cr atoms in the first-nearest-neighbour shell lead to an increase in vacancy formation energy. It is then expected that Ni will enrich at vacancy-type defect clusters in FeNi, CrCoNi and CrFeCoNi. This trend has also been observed in $FeCr_{20}Ni_{10}$ austenitic steel due to strong binding interactions between Ni and vacancies.[191]

2.4.4 Radiation-induced dislocation lines and loops

A Frenkel pair (vacancy and interstitial pair) can form during irradiation-induced collision cascades, where a portion of such pairs survive and then contribute to the overall defect and defect cluster population. Dislocation loops may disappear by annihilation with vacancies or encountering sinks but may also grow by the absorption/influx of interstitials. Dislocation lines and loops are known to have significant impact on macroscopic properties, for example causing hardening and embrittlement.[192,193]

He et al. showed that there were $1/3\langle 111\rangle$ type interstitial, either elliptical Frank loops or $1/2\langle 110\rangle$ type polygonal (mostly rhombus) perfect loops in CrFeCoNi under 400, 500 and 1250 kV in situ electron irradiation at 400℃ and up to 1 dpa.[182,194] Loops in CrFeCoNi exhibited non-linear power law growth that was more than 40 times slower than the near-linear defect growth behaviour for Ni. Two forms of loops were produced

simultaneously, in a number ratio close to 3 (faulted): 1 (perfect), and no faulted loop was observed to transform to a perfect loop, and vice versa.

CrMnFeCoNi and CrFeCoNiPd were also irradiated under the same conditions as CrFeCoNi (1250 kV electrons, 400℃ and 1 dpa). The density of loops was much lower while the loop sizes were larger in the quinary alloys compared with CrFeCoNi.[182,194] Although there were both type of loops in three alloys, the fraction of perfect loops was lower in the quinary alloys. He et al. suggested this may arise due to the reduced stacking fault energy of the quinary alloys compared with CrFeCoNi,[182] although other work has suggested that the SFE of CrFeCoNiPd may be the highest among these alloys.[116,195]

Ni, FeNi, CoNi, FeCoNi, CrFeCoNi and CrMnFeCoNi were irradiated with 1.5 or 3 MeV Ni^+ ions at 500℃ [30,196] and both voids and dislocation loops were readily observed. Figure 2.18 shows the distribution of dislocations, dislocation loops and voids in Ni and the five alloys. There were dislocation networks in irradiated Ni, FeNi, CoNi and CrFeCoNi and long dislocation lines and larger dislocation loops formed at greater sub-surface depth than voids in Ni and CoNi. In FeNi and CrFeCoNi, dislocation loops formed near the sample surface, extending to a depth of 600 nm, followed by a region containing a comparatively low density of small voids. Interstitials were shown through molecular dynamics (MD) simulations to move in 1D in Ni for relatively long distances without encountering and annihilating with vacancies whereas interstitials

migrated randomly in 3D in FeNi, producing a high proportion of annihilation events with neighboring mono-vacancies and vacancy clusters, leading to a much smaller concentration of residual voids.

In addition, the energy barrier to small vacancy cluster migration is calculated to be smaller than that of a single vacancy in FeNi (di-vacancy migration energy is 0.515 eV). Di- and tri-vacancy clusters had migration energies similar to that of a single interstitial, so that interstitials and vacancies can migrate simultaneously, encouraging a higher recombination rate and lower concentration of surviving defects in FeNi than in CoNi or Ni.[30,197]

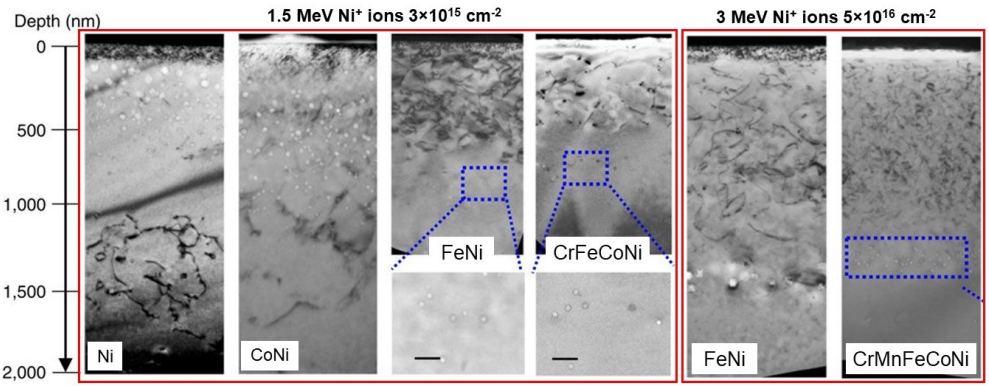


Figure 2.18: Cross-sectional TEM images showing the distribution of dislocations, dislocation loops and voids in Ni, CoNi, FeNi, CrFeCoNi and CrMnFeCoNi irradiated with 1.5 or 3 MeV Ni ions at different fluences. Scale bar is 100 nm. Adapted with permission from Lu et al.[30]

Figure 2.19 shows the loop density, loop size distribution, average diameter of loops and fraction of faulted loops in FeNi, FeCoNi, CrFeCoNi and CrMnFeCoNi irradiated with 3 MeV Ni ions at 500℃ and up to 38 ± 5 dpa.[184] The trend in loop density was CrMnFeCoNi > CrFeCoNi = FeCoNi > FeNi, where the loop density was approximately one

order of magnitude higher in CrMnFeCoNi than in FeNi and two times higher in CrFeCoNi and FeCoNi than in FeNi. In contrast, the average diameter of loops in FeNi, FeCoNi, CrFeCoNi and CrMnFeCoNi was 76 nm, 42 nm, 51 nm and 24 nm respectively, and large loops with a diameter of over 150 nm were only present in FeNi. There was a higher fraction of faulted loops in more compositionally complex alloys (52%, 34%, 17% and 8% respectively in CrMnFeCoNi, CrFeCoNi, FeCoNi and FeNi), which was likely attributed to the restrained evolution of faulted to perfect loops due to a lower stacking fault energy.[116,184]

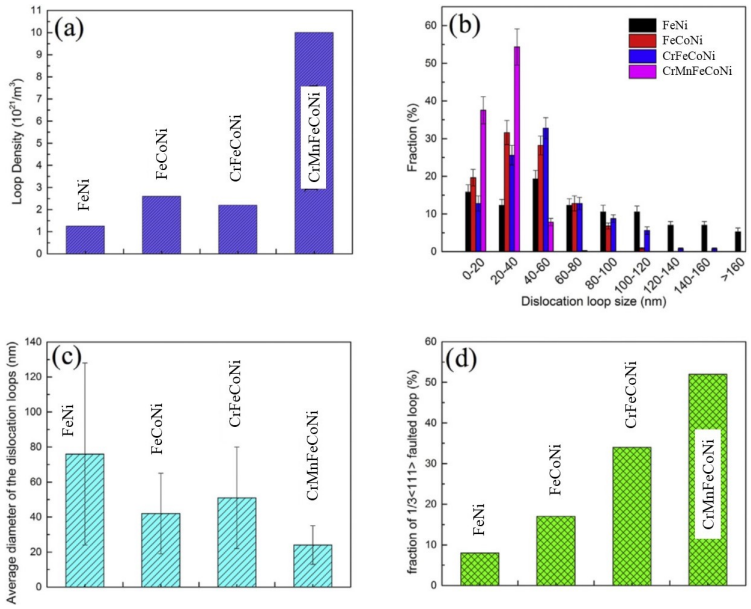


Figure 2.19: (a) Loop density; (b) loop size distribution; (c) average diameter of loops and (d) fraction of $1/3\langle 111\rangle$ faulted loops in FeNi, FeCoNi, CrFeCoNi and CrMnFeCoNi irradiated with 3 MeV Ni ions at 500℃ and up to 38 ± 5 dpa. Reprinted with permission from.[184]

There are some discrepancies relating to characteristic dislocation loops and their evolution. For example, in some reports, the density of loops in CrMnFeCoNi and CrFeCoNiPd was lower, and the loop sizes

larger, when compared with CrFeCoNi after high energy electron irradiation[182,194] and both perfect loops with $b = 1/2\langle 110\rangle$ and Frank loops with $b = 1/3\langle 111\rangle$ formed simultaneously.[182,194] In contrast, elsewhere[30,184] it is reported that the density of loops in CrMnFeCoNi was approximately 5 times higher than that in CrFeCoNi while the average diameter of loops was only one half that of CrFeCoNi after heavy ion irradiation. Moreover, the higher fraction of faulted loops in ion irradiated CrMnFeCoNi was attributed to a lower tendency for the transformation of faulted loops to perfect loops, which apparently is at odds with the finding that no such transition was needed for perfect loop formation under in-situ electron irradiation. It should be noted that there are significant challenges in comparison of findings from different experiments due to the challengens in keeping consistent materials, comparable irradiation conditions and imaging techniques, and that quantification is sensitive to sample preparation, surface contamination and complex imaging conditions.

In $Cr_{18}Mn_{27}Fe_{27}Ni_{28}$ irradiated with 3 or 5.8 MeV Ni ions at temperatures ranging from room temperature to 700℃ up to 10 dpa,[188] there were a high-density of small dislocation loops at all temperatures. The loop density was nearly independent of dose at low temperatures whereas the loop density monotonically decreased and loop sizes monotonically increased with increasing temperature. Figure 2.20 shows the loop density as a function of irradiation temperature in $Cr_{18}Mn_{27}Fe_{27}Ni_{28}$ and conventional austenitic alloys irradiated at similar conditions.[100,198–210] The

overall loop densities were significantly higher in irradiated $Cr_{18}Mn_{27}Fe_{27}Ni_{28}$, for instance, the loop density in $Cr_{18}Mn_{27}Fe_{27}Ni_{28}$ was nearly 50 times greater than that of $FeCr_{15}Ni_{20}$ when irradiated at 675℃ and up to 30 dpa (Note that dislocation lines and tangled dislocations were not included in the counting).[201] The Cantor alloy also exhibited an order of magnitude higher loop density than its ternary sub-systems, but also much smaller average diameter of loops due to the slower defect growth dynamics described earlier.

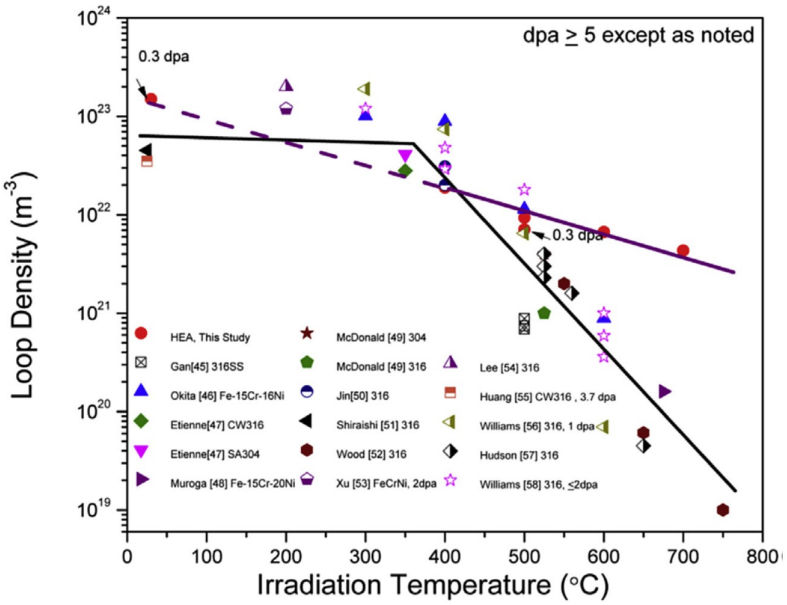


Figure 2.20: Comparison of loop density versus irradiation temperature in $Cr_{18}Mn_{27}Fe_{27}Ni_{28}$ and conventional Fe-Cr-Ni austenitic alloys,[100,198–210] irradiated at similar conditions. The drawn lines are intended as tendency lines. Reprinted with permission from.[188]

Overall, there were interstitial-type, either elliptical Frank loops ($1/3\langle 111\rangle$) or rhombus perfect loops ($1/2\langle 110\rangle$), in the Cantor alloy and its derivatives under both electron and heavy ion irradiations at elevated temperature. Although there were some discrepancies in terms of the size and

density of loops, as well as loop evolution of faulted to perfect loops, possibly due to different primary knock-on energy and errors introduced from counting procedures, a simplified trend was obtained. The Cantor alloy shows a higher number density but much smaller size of dislocation loops compared with its binary and tertiary sub-systems, and conventional FCC alloys. Complex dislocation networks and long dislocation lines formed in less compositionally complex alloys, but not in the Cantor alloy, which could suggest an extended incubation period and retarded defect growth kinectics.

2.4.5 Void swelling

At temperatures between 0.3 T_M and 0.6 T_M, the agglomeration of irradiation-induced vacancies and the growth of voids can cause pronounced volume swelling, degrade material performance, and thus have a significant deleterious impact on allowable lifetime and reactor operations.[47,202,208,211] Earlier studies have shown that void formation is expected in conventional Fe-Cr-Ni alloys for ion irradiation doses above 1-10 dpa at 350℃ to 650℃,[212] and swelling in Fe-Cr-Ni alloys can be modified by varying the Ni and Cr concentration.

Figure 2.21 shows the extent of swelling measured using an optical profilometer and corresponding cross-sectional TEM images of voids in Ni, CoNi, FeNi, CrCoNi, FeCoNi, CrFeCoNi and CrMnFeCoNi irradiated with 3 MeV Ni ions to $5 \times 10^{16} cm^{-2}$ (peak dose 53 dpa) at 500℃.[213] All six alloys exhibited significantly lower void swelling than Ni. For exam-

ple, the void swelling of Ni was 6.7%, whereas CrMnFeCoNi and FeCoNi showed the lowest void swelling of $< 0.2\%$. Fe additions were more effective in reducing void swelling than Co, and the void swelling was not simply related to the extent of alloying only. For example, FeNi showed lower void swelling than CrCoNi and CoNi, and FeCoNi exhibited similar void swelling to CrMnFeCoNi, which suggests that the intrinsic irradiation resistance of alloying elements should be considered in searching for HEAs with high irradiation tolerance,[213] although comparable data for all elements of interest are not easily available.

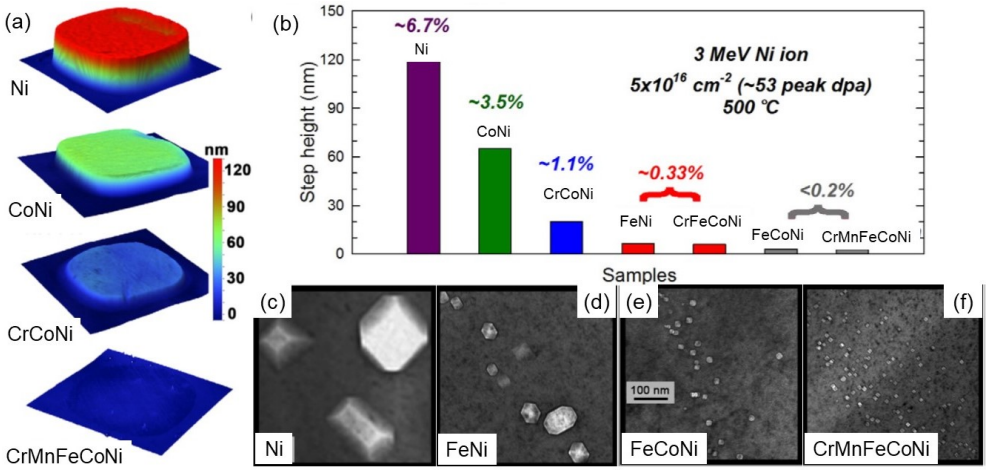


Figure 2.21: (a) Optical profilometer measurements of void swelling in Ni, CoNi, CrCoNi and CrMnFeCoNi. (b) Step height change of each alloy after irradiation. Cross-sectional TEM images showing different sizes and density of voids in (c) Ni, (d) CoNi, (e) CrCoNi and (f) CrMnFeCoNi. Adapted with permission from Jin et al.[213]

Figure 2.22 shows cross-sectional TEM images of CoNi, FeNi, FeCoNi, CrFeCoNi and CrMnFeCoNi irradiated with 1.5 MeV Ni ions ($3 \times 10^{15}\text{cm}^{-2}$) and/or 3 MeV Ni ions ($5 \times 10^{16}\text{cm}^{-2}$) at 500°C.[30] The void swelling of Ni was 1.8% while CrMnFeCoNi had a swelling of 0.02%. The overall void swelling resistance can be ranked in the order Ni<CoNi<

FeNi≤CrFeCoNi<FeCoNi≤CrMnFeCoNi. As discussed earlier, the vacancy cluster migration energy barrier in FeNi was lower than that of a single vacancy, which can result in a higher recombination rate of interstitials and vacancies and thus a lower concentration of surviving defects.[30,197] Furthermore, with increasing size of clusters, MD simulations showed that the diffusion coefficient of vacancy clusters decreased rapidly and clusters containing more than 7-13 vacancies migrated much slower in NiFe, $Ni_{80}Fe_{20}$, $Ni_{80}Cr_{20}$ and $Ni_{40}Fe_{40}Cr_{20}$ than in Ni.[54] This finding is consistent with the observed trend in void swelling behaviour in Ni, FeNi and CrFeCoNi.

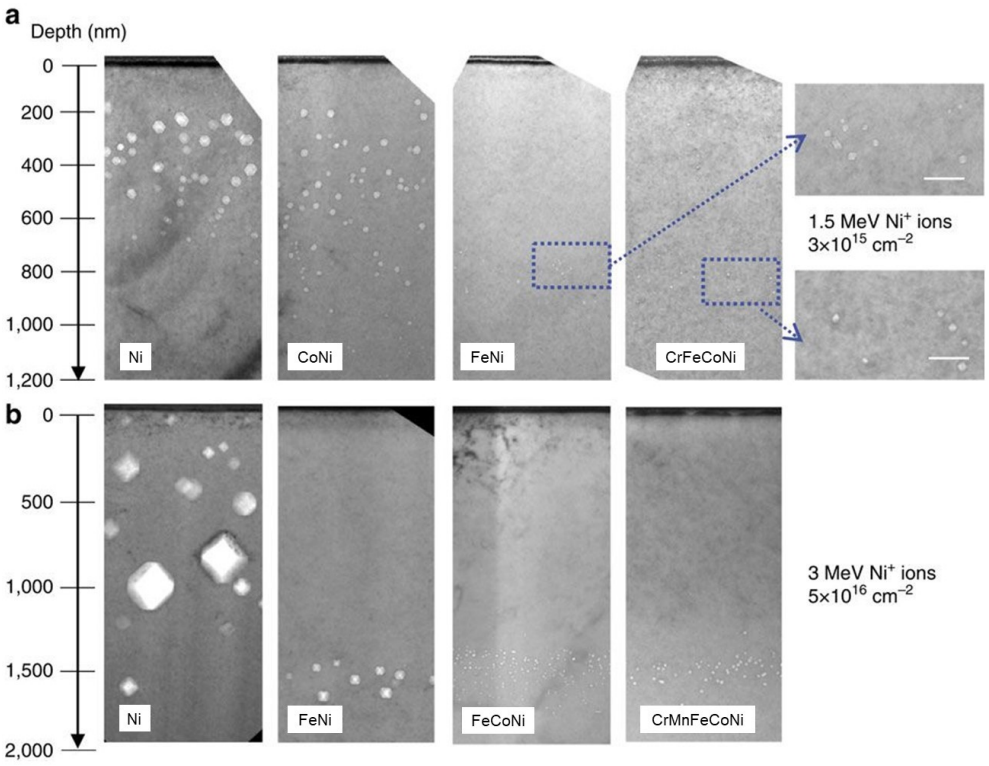


Figure 2.22: (a) Cross-sectional TEM images of Ni, CoNi, FeNi and CrFeCoNi irradiated with 1.5 MeV Ni ions to 3×10^{15}cm^{-2} at 500℃ with enlarged area marked by a dotted blue box; scale bar in the inset figures is 50 nm. (b) cross-sectional TEM images of Ni, FeNi, FeCoNi and CrMnFeCoNi irradiated with 3 MeV Ni ions to 5×10^{16}cm^{-2} at 500℃ , showing reduced void formation with increasing compositional complexity. Reprinted with permission from.[30]

There was an obvious dependence of void swelling on irradiation temperature in CrCoNi, CrMnFeCoNi and CrFeCoNiPd[183,214] irradiated with 3 MeV Ni ions at 420, 500 and 580℃ and at a fluence of 5×10^{16}cm^{-2}. An additional irradiation temperature of 650℃ ($0.61T_M$) was also applied to the Cantor alloy, but no voids were observed. Figure 2.23 shows the cross-sectional TEM images of three alloys irradiated at different temperatures. At 420℃, the highest swelling was in CrCoNi (0.24%) while CrMnFeCoNi and CrFeCoNiPd had only 0.02% and 0.003% swelling. The average void size in CrCoNi was nearly 4 times and 6 times higher

than CrMnFeCoNi and CrFeCoNiPd, while the void number density in CrCoNi was more than one magnitude higher than the two quinary alloys. At 500 and 580℃, there were no zones denuded of voids in CrCoNi whereas there was only a comparatively small fraction of smaller voids in CrMnFeCoNi beyond 1000 nm depth from the surface, as shown in Figure 2.23b and 2.23c. There were voids in all regions of CrFeCoNiPd at all temperatures. Although the void number density in CrMnFeCoNi was nearly 4 times higher than in CrFeCoNiPd, the average void size was ∼2 times smaller, contributing to slightly less void swelling in CrMnFeCoNi(0.07%).

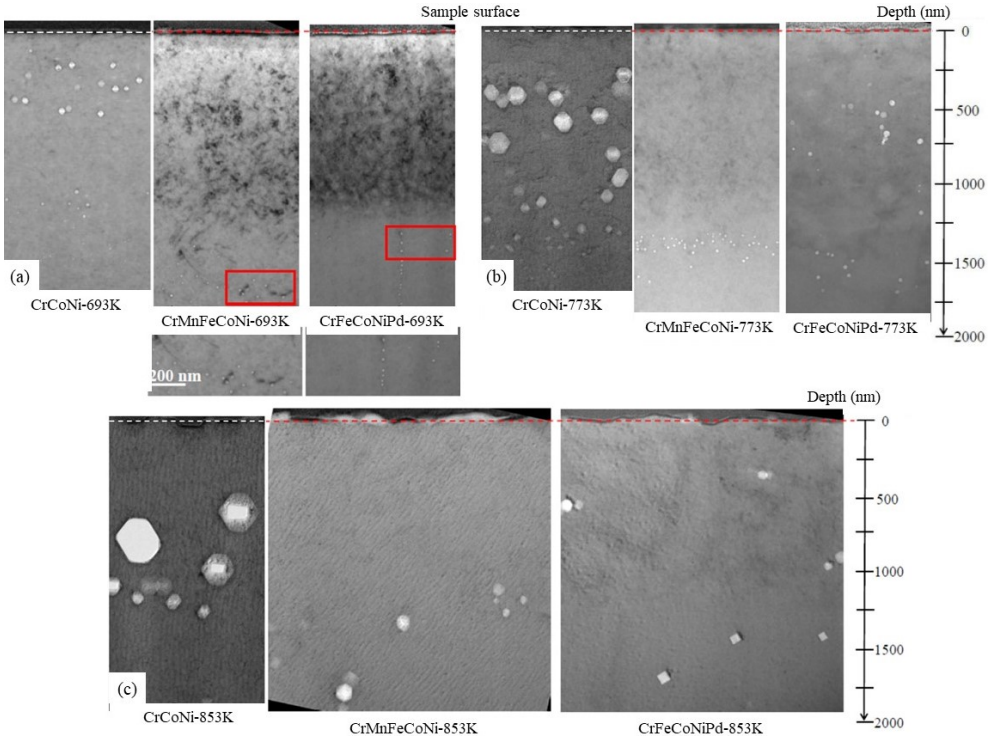


Figure 2.23: Cross-sectional TEM images of CrCoNi, CrMnFeCoNi and CrFeCoNiPd irradiated with 3 MeV Ni ions at (a) 420, (b) 500 and (c) 580℃ to a fluence of 5×10^{16}cm^{-2}, showing dependence of void formation on composition and temperature. Adapted with permission from Lu et al. and Yang et al.[183,214]

Table 2.1 summarises the void swelling behaviour of Ni and FeNi, FeCoNi, CrCoNi, CrMnFeCoNi and CrFeCoNiPd irradiated with 3 MeV Ni ions to a peak dose of $\sim$ 60 dpa at a depth of 0-1800 nm from the surface, at 420, 500 and 580℃. In general, CrCoNi exhibited very poor swelling resistance, even worse than FeNi, which again showed that alloying with Fe was more effective than Cr in terms of voids swelling resistance, and that increasing compositional complexity does not always lead to higher void swelling resistance. Yang et al.[183] suggested that slightly less pronounced void growth in CrFeCoNiPd compared with CrMnFeCoNi may be related to higher lattice distortion and a stronger binding energy between vacancies and constituent atoms in CrFeCoNiPd, which restricts vacancy mobility, promotes a higher recombination rate and leaves fewer free point defects. The mean local lattice distortion has been suggested to be in the order: CrFeCoNi $<$ CrMnFeCoNi $<$ CrFeCoNiPd using X-ray total scattering experiments.[215] DFT calculations also show less than 5% local distortion in CrFeCoNi and CrMnFeCoNi but $\sim$ 8% lattice distortion in CrFeCoNiPd due to comparatively large bond distance of Pd-Pd neighbours. Modeling of $Ni_{80}Mn_{20}$ and $Ni_{80}Pd_{20}$ also showed that vacancy migration energies and the gap between vacancy and interstitial migration energy were surprisingly similar, suggesting that an alloying strategy based on the introduction of elements with larger atomic size differences into HEAs to increase local lattice distortion as a means to modify vacancy mobility alone (and here irradiation resistance), may

not be effective. Moreover, larger atomic size mismatch may contribute to a tendency for the decomposition of any solid-solution phases that themselves are suggested to contribute to the irradiation resistance of HEAs.[216,217]

Table 2.1: Summary of total void swelling in Ni, FeNi, FeCoNi, CrCoNi, CrFeCoNi, CrMnFeCoNi and CrFeCoNiPd irradiated with 3 MeV Ni ions at 420, 500 and 580℃. Data was from Ref.[30,183,214,218]

T/℃	Ni	FeNi	CrCoNi	CrFeCoNi	CrMnFeCoNi	CrFeCoNiPd
420	/	/	0.24%	/	0.02%	0.003%
500	9.4%	0.45%	7.01%	0.02%	0.07%	0.1%
580	/	/	9.34%	/	0.37%	0.3%

No detectable void formation at any of the ion irradiation conditions studied were observed in $Cr_{18}Mn_{27}Fe_{27}Ni_{28}$ irradiated with 3 or 5.8 MeV Ni ions at temperatures from room temperature to 700℃ and up to 10 dpa.[188] Figure 2.24 presents the comparison of swelling behaviour between the Cantor alloy, its derivatives, and conventional steels (e.g. 316SS, $FeCr_{15}Ni_{16}$) under similar conditions.[198,199,219,220] Average size (nm, square marks) and the number density of voids ($10^{20}m^{-3}$, circles) are displayed as a function of overall swelling (%) in different materials. The irradiation conditions corresponding to each data point were included on the right where half hollow marks represented data obtained at the irradiation of $\sim$ 10 dpa and solid marks represented data obtained at the irradiation of 50 or 60 dpa. The Cantor alloy and CrFeCoNi exhibited nearly one magnitude lower overall swelling (0.017% and 0.072% respectively) than conventional alloys (0.45% for 316SS[198] and 1.1% for $FeCr_{15}Ni_{16}$[199]) under similar or even harsher conditions. Smaller aver-

age size of voids for the Cantor alloy and CrFeCoNi accounts for lower overall swelling than other derivatives and conventional steels even with relatively similar or even higher number density of voids.

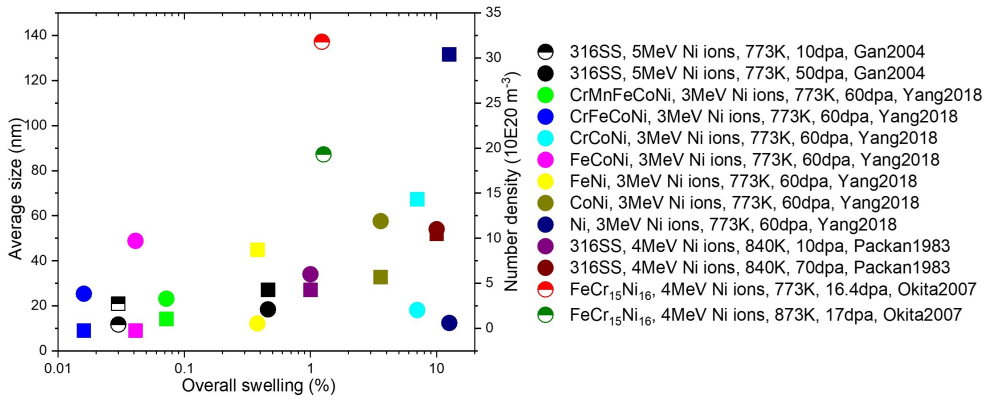


Figure 2.24: Comparison of swelling behaviour for the Cantor alloy, its derivatives, and conventional steels (e.g. 316SS, $FeCr_{15}Ni_{16}$) under similar conditions.[198,199,219,220] Data was obtained from the work of Gan et al.,[198] Okita et al.,[199] Packan et al.[219] and Yang.[220] Average size (nm, square marks) and the number density of voids ($10^{20}m^{-3}$, circles) are displayed as a function of overall swelling (%). The irradiation conditions are included on the right where half hollow marks represented data obtained at irradiation of $\sim$ 10 dpa and solid marks represented data obtained at irradiation of 50-70 dpa.

2.4.6 Gas bubbles

Extensive He production and retention from neutron induced transmutation reactions is a significant issue for materials to be applied in fast neutron reactors. He atoms can diffuse rapidly, and may bond with vacancies, to form bubbles due to the limited intrinsic solubility of He in most metallic systems. Hence, point defect behaviour, including mobility and concentration, are intimately linked with the problems that arise from He retention, and bubble formation, such as pronounced degradation in some macroscopic properties.

The temperature dependence on bubble formation in CrFeCoNi was investigated by implantation of 275 keV He ions at up to 5.14×10^{16}cm^{-2} fluence[221] at 250, 300 and 400℃, and by 2 MeV He ions at 500, 600 and 700℃ and at up to 1.52×10^{16}cm^{-2} fluence.[222] Generally, grain boundaries acted as sink traps for He to aggregate into He bubbles and there was a He-depleted zone beside the grain boundary. The average size of He bubbles increased whereas the He bubble density decreased with increasing temperature. At low temperatures (250, 300 and 400℃), He accumulation was slightly suppressed in the CrFeCoNi. At 500, 600 and 700℃, there was a narrower distribution of He bubbles near the region with the highest concentration of incident He ions in CrFeCoNi than in Ni. He bubbles had a smaller diameter, larger number density and smaller volume fraction in CrFeCoNi compared with Ni, consistent with previous descriptions of the differences in the energy barrier for point defect migration in Ni and CrFeCoNi.

The effect of specific elements in Ni-based binary alloys on He bubble formation behaviour has also been investigated. $Ni_{80}X_{20}$ (X=Cr, Mn, Fe, Co, Ni and Pd) alloys were irradiated under 200 keV He ions at 500℃ and 1×10^{16}cm^{-2} fluence. Figure 2.25 displays the migration (E_m^v, Figure 2.25a) and formation (E_f^v, Figure 2.25b) energies of vacancies and interstitials (E_m^i, Figure 2.25c and E_f^i, Figure 2.25d) of the binary alloys respectively. The combined experiments and DFT calculations show that alloying elements have a significant effect on He cavity formation. As seen

in Figure 2.25a and 2.25c, $Ni_{80}Mn_{20}$ exhibited the smallest energy gap between interstitial (E_m^i, mean value $\approx$ 0.3 eV) and vacancy migration energies (E_m^v, mean value $\approx$ 0.9 eV) of the binary alloys studied, which is likely to enhance vacancy-interstitial recombination rates and thus reduce bubble or cavity size in $Ni_{80}Mn_{20}$. In contrast, $Ni_{80}Co_{20}$ had the highest migration energy for vacancies (E_m^v, mean value $\approx$ 1.15 eV) and the lowest migration energy for interstitials (E_m^i, mean value $\approx$ 0.15 eV) and correspondingly $Ni_{80}Co_{20}$ showed the largest cavity size. The lower vacancy formation energy for $Ni_{80}Pd_{20}$ could result in a relatively wide and flat He cavity distribution over the irradiated range, and consistent with wider distribution of voids in CrFeCoNiPd, as shown in Figure 2.23.

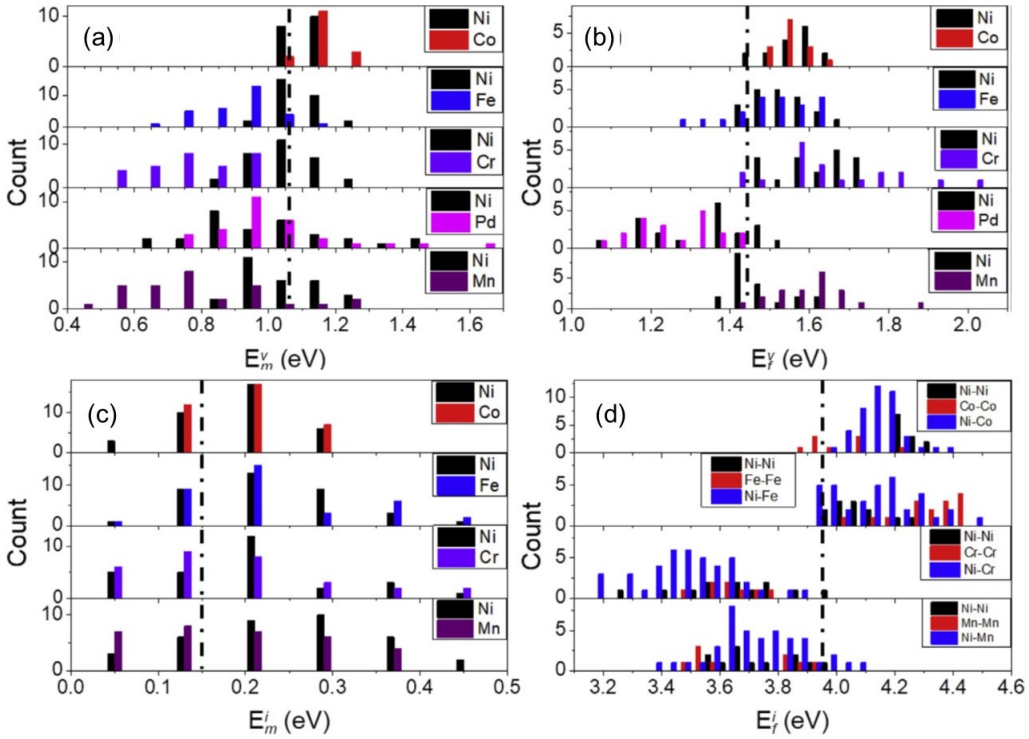


Figure 2.25: (a) The migration (E^v_m) and (b) formation (E^v_f) energies of vacancies and (c) and (d) of interstitials (E^i_m and E^i_f) of $Ni_{80}X_{20}$ (X=Cr, Mn, Fe, Co, Ni and Pd) binary alloys from DFT calculations. The dashed lines represent the energies in Ni. Adapted with permission from Fan et al.[223]

2.4.7 Conclusions

Most studies of the effect of irradiation on HEAs have focused on the Cantor alloy as a model system because it is a simple solid solution, unlike many HEAs that are often much more micro-structurally complex. The research methods have typically involved irradiation analogues (electrons, heavy ions and He) to neutron bombardment. Sophisticated microstructural analyses and computations have focused on comparative behaviour of single elements, binary alloys and the inter-related medium and high-entropy alloys. However, computational results including defect energies have been mostly limited to binary alloys, which may make

it difficult to extrapolate findings to HEAs. Nonetheless, much of the trend-wise calculations of defect migration and formation energies are consistent with experimental investigations. Some key observations are:

Calculated point defect formation and migration energies are described as a statistical distribution instead of the single values typically used in dilute alloys. There is a relatively small gap or even overlap between interstitial and vacancy migration energies, which will likely induce relatively high recombination rates and increase the possibility of defect annihilation, thus leaving less surviving defects.

Comparatively retarded diffusion of interstitials and slightly faster migration of vacancies are expected in binary, CrCoNi and CrFeCoNi than in Ni due to higher interstitial migration energies and slightly lower vacancy migration energies.

The Cantor alloy has excellent phase stability against high dose heavy ion irradiation. RIS along grain boundaries at elevated temperature in the Cantor alloy and its derivatives shows strong depletion of Mn and enrichment of Ni/Co, the magnitude of which is comparable to RIS in some FCC commercial alloys (304 stainless steels and Fe-Ni-Cr alloys). RIS along dislocation loops is significantly suppressed in the Cantor alloy, which may arise from retarded interstitial diffusion. Chemically biased diffusion may lead to Ni/Co enrichment and Fe depletion in FeNi and CrFeCoNi alloys due to the lower formation energy of Ni-Ni dumbbell defect and Co-containing dumbbell defect.

Interstitial-type, either elliptical Frank loops ($1/3\langle 111\rangle$) or rhombus perfect loops ($1/2\langle 110\rangle$), are observed in the Cantor alloy and its derivatives under both electron and heavy ion irradiations at room and elevated temperature. There are some discrepancies regarding the size and density of loops as well as loop evolution, possibly due to different primary knock-on energy and errors introduced from counting procedures. Nonetheless, the Cantor alloy typically has a higher number density but much smaller size of dislocation loops compared with its binary and tertiary sub-systems, and conventional FCC alloys, which could suggest an extended incubation period for loop formation and retarded defect growth kinectics.

The Cantor alloy shows significantly enhanced resistance against void swelling compared with its derivatives and conventional FCC alloys, with only 0.2% void swelling under Ni ion irradiation up to 53 dpa. Large vacancy clusters were calculated to migrate much slower in binary and tertiary alloys than in Ni, which may suggest this is the mechanism for underpinning swelling resistance in the Cantor alloy.

CrFeCoNi was more resistant to growth of He bubbles and bubble coarsening during post-annealing than Ni. There was a narrower distribution of He bubbles of smaller size, higher number density and smaller volume fraction in CrFeCoNi compared with Ni, which likely resulted from suppressed He diffusion.

3 Materials and Methods

3.1 Materials and Manufacturing

Vacuum induction melted master ingots of the nominally equiatomic Cantor alloy were supplied by Baosteel, Shanghai, China. The ingots were then re-melted using VIM in an alumina-based crucible at 1560℃ under vacuum ($< 3 \times 10^{-1}$ Pa) and poured under Ar gas though a ZrO_2 nozzle into a two-stage N_2 atomiser and spray formed in the Advanced Processing Lab at Oxford University at an average mass flow rate of 0.58 kg $\cdot$ s^{-1} and an average gas flow rate of 0.27 kg $\cdot$ s^{-1} into cylindrical billets at a spray distance of 600 mm. The spray forming experiments were led and operated by Atsushi Sato. Nominally "pure" Y (Goodfellow Cambridge Ltd) was arc melted with Fe to form Y-24 wt.% Fe eutectic and then dropped into the molten Cantor alloy, just before spray forming. It was essential to minimise the time available for Y to react with residual O or founding materials.

Figure 3.1 displays the schematic geometry of the as-sprayed billet with an image of an actual billet in the inset, together with the size of cylindrical samples cut from the billet by water-jet cutting for subsequent swaging and microstructural investigation. The composition of as-sprayed billets was measured by AMG Superalloys (UK) using induction coupled plasma-optical emission spectroscopy (ICP-OES). The cylinders with $\phi \times l = 9 \times 150$ mm^2 (ϕ is the diameter and l is the length of the

cylinder respectively) were swaged using a four-die swaging machine with diameter reducing progressively from 9 mm to 5 mm (45% reduction in diameter). The cylindrical cross-section rods were then annealed at 800℃ for 1 hour in air followed by furnace cooling. The swaging process was operated by David E.J. Armstrong, other machining procedures were undertaken by Robin Vincent and heat treatments were performed by Tony Wheeler. As the CrMnFeCoNi HEA is also termed as "Cantor" alloy, for more concise expression, the as-sprayed CrMnFeCoNi HEA is denoted as CSP and the as-swaged and annealed CSP is denoted as CSW. Similarly, as-sprayed Y-doped CrMnFeCoNi HEA and as-swaged and annealed YCSP are denoted as YCSP and YCSW. The abbreviations and full descriptions of the four alloys were shown in Table 3.1.

Table 3.1: Abbreviations and full descriptions of the four alloys.

Abbreviations	Full descriptions
CSP	as-sprayed CrMnFeCoNi
YCSP	as-sprayed Y-doped CrMnFeCoNi
CSW	as-sprayed, as-swaged and annealed CrMnFeCoNi
YCSW	as-sprayed, as-swaged and annealed Y-doped CrMnFeCoNi

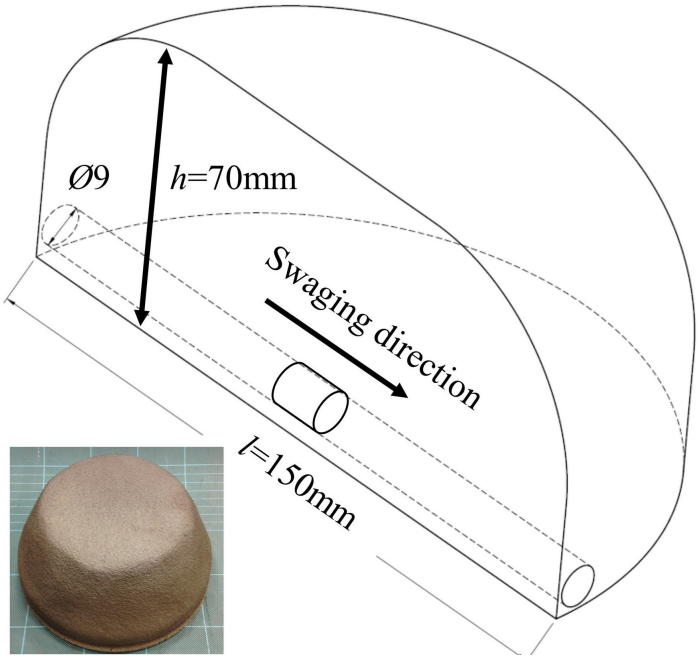


Figure 3.1: Schematic geometry of the as-sprayed billet, and the typical location and size of samples extracted for thermochemical processing. Microstructural investigation was from central region of cross-section specimens. Inset: image of an actual as-sprayed billet (diameter: 150 mm and height: 70 mm). TA in subsequent testing was parallel to the swaging direction.

3.2 X-ray diffraction and Rietveld refinement analysis

X-ray diffraction (XRD) is based on constructive interference of monochromatic X-rays and crystalline samples. The X-rays are first generated by a cathode ray tube, filtered to produce monochromatic radiation, collimated to concentrate, and then directed toward the sample. The interaction of the incident rays with the sample produces constructive interference when Bragg's Law is satisfied. The Bragg's law[224] is expressed

as:

$$n\lambda = 2d \sin\theta \tag{3.1}$$

where d is the spacing between diffracting planes, θ is the incident angle, n is an integer, and λ is the beam wavelength. The Bragg's law relates the wavelength of electromagnetic radiation to the diffraction angle and the lattice spacing in a crystalline sample, which can be used for phase identification and for estimating the lattice parameters and crystallite size.

All XRD measurements were performed by Guillaume Matthews using a Panalytic Empyrean machine operating with Cu $K\alpha 1$ monochromatic radiation in a 2θ (diffraction angle) range from 20° to 100° at 40 kV and 40 mA. Peak identification was achieved by comparing experimental data with simulated XRD traces from Inorganic Crystal Structure Database (ICSD) provided by FIZ Karlsruhe GmbH using the CrystalDiffract software provided by CrystalDiffract Software Ltd, Oxford, England (www.crystalmaker.com). The sample was mounted onto a goniometer and placed within the X-ray beam. The resulting X-ray intensity spectrum over the range of angles was plotted and the Bragg reflection peaks identified.

Full width at half maximum (FWHM) was calculated from XRD patterns after Rietveld refinement analysis following the procedure described in Ref[225] using FullProf software.[226]

3.3 Scanning electron microscopy and Energy-dispersive X-ray spectroscopy

Scanning electron microscopy (SEM) was used to analyse microstructural features in polished materials, using secondary electrons (SE), back-scattered electrons (BSE), and electron induced X-ray emission. Secondary electrons are inelastically scattered from the sample atoms by the beam, which are sensitive to the angle between the beam and the surface, thus showing good topographic contrast. Back-scattered electrons originate due to elastic scattering by nuclei in the material, which provides compositional contrast as well as channelling contrast (whereby different crystallographic directions have different interaction volumes). In general, an accelerating voltage of 5 or 10 keV was used, at a working distance of 8.5 mm and probe current of 200 pA.

Energy Dispersive X-ray spectroscopy (EDS) was used for elemental analysis of samples. An incident X-ray on the sample causes excitation of the surface atoms, stimulating the emission of further X-rays with wavelengths characteristic of individual elements – each element has a unique atomic structure giving a unique set of peaks in its X-ray spectrum. An Oxford Instruments EDS detector was used to capture elemental information in the energy range from 0 to 20 KeV, using an accelerating voltage of 10 keV and probe current of 500 pA. All SEM images and EDS measurements were collected using a Zeiss Merlin SEM.

EDS analyses were performed using Oxford Instruments AZtec soft-

ware (https://nano.oxinst.com/products/aztec/) that allows for several analytical modes: PointID for quantitative spectra analysis at a point or within an area; Linescan for quantitative analysis along a specified line, usually cross a grain boundary or a precipitate; and Mapping for qualitative information over a region. TruLine or TruMap method was selected for all EDS measurements in this thesis, which is suitable for overlapping peaks from different elements, and based on algorithms predicting the peak shape of each element and deconvoluting overlapping peaks from one another and the background signal. Table 3.2 shows the characteristic X-ray energy for possible elements in this thesis. There are several overlapping peaks, such as Cr and O, Cr and Mn, Mn and Fe, Fe and Co, Co and Ni, and Si and Y. In order to obtain quantitative information, QuantLine or QuantMap method was selected to give concentrations in either weight or atomic percent. It is worth noting that the quantitative measurements of lighter elements, such as C and O, are less accurate due to low energy artifacts from the system and surface contamination derived from C buildup during testing, and oxidized surface layer.[227]

Table 3.2: The characteristic X-ray energy (KeV) of elements in the present study.

	Cr	Mn	Fe	Co	Ni	Y	C	O	Si	S
$K\alpha 1$	5.41	5.90	6.40	6.93	7.48	14.96	0.28	0.52	1.74	2.31
$K\beta 1$	5.95	6.49	7.06	7.65	8.27	-	-	-	-	-
$M\alpha 1$/L series	0.58	0.64	0.71	0.78	0.85	1.92	-	-	-	-

Note that the identification of small particles is affected by the spatial resolution of SEM-EDS.[228] It is known that reducing the acceler-

ating voltage can decrease the interaction volume, increase the analysis sensitivity of near-surface features, such as small particles, and thus increasing the spatial resolution.[229] However, some drawbacks arise due to low-voltage, such as the limited analytical flexibility due to low X-ray emission.[229] In this case, if a lower accelerating voltage (<10 kV) was used, the intensity of K series X-ray lines for Cr, Mn, Fe, Co, Ni would be rather low or even close to 0 (if <5 kV), which means that only low energy X-ray lines which severely overlap, are the main source for analysis and thus, in many situations, undermines the accuracy. Therefore, 10 kV was used throughout in order to achieve a balance between spatial resolution and analytical flexibility.

3.4 Electron backscatter diffraction and transmission Kikuchi diffraction

Electron Backscatter Diffraction (EBSD) is an SEM technique capable of identifying the local grain orientation and crystal structure. When the incident backscatter electrons leave at the Bragg angle and undergo diffraction, a Kikuchi line comprised of bands containing information about the system geometry, the crystal structure, and the underlying orientation of the crystal is formed. A detector with a phosphor screen is then used to collect the Kikuchi lines. Two geometric setups shown in Figure 3.2 were used in the thesis, including conventional EBSD and on-axis transmission Kikuchi diffraction (TKD). In order to maximise the

backscattered signal the sample was highly tilted in conventional EBSD, typically to 70°. In TKD measurements, the TEM foil was mounted with the TKD head positioned beneath the sample.

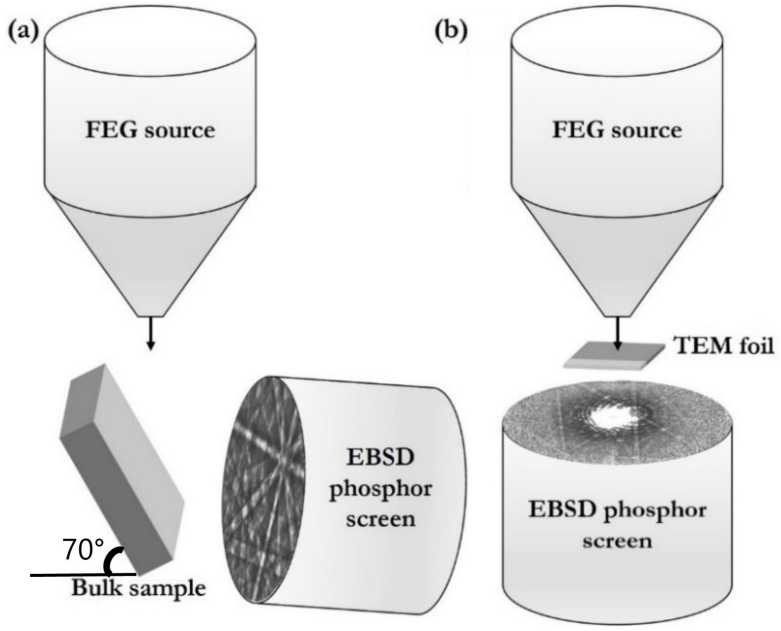


Figure 3.2: Schematic setups for (a) conventional EBSD on a bulk sample and (b) on-axis TKD on from TEM thin foil. Figure adapted with permission from Liu.[230]

A spatial resolution of 20-90 nm can be achieved given optimum measuring parameters and sample preparation.[231] In on-axis TKD measurements, the electron beam passes through the thin TEM foils, leading to a significant decrease of the interaction volume and an increase in spatial resolution to a few nanometers.[232] Thus it is suitable to characterise nano-sized feature, such as nano-crystalline materials, nanoscale particles and twins.

In this thesis, conventional EBSD was used generally, and on-axis TKD was used to investigate nanoscale twins and subgrains in highly de-

formed CSW and YCSW. All EBSD measurements were collected using a Zeiss Merlin FEG-SEM system equipped with a Bruker e-flash high resolution EBSD detector. The detailed setup parameters for conventional EBSD and on-axis TKD are given in Table 3.3.

Since the diffraction signal in conventional EBSD comes from the upper nanometers of the specimen, the surface roughness affects the quality of EBSD data. The specimens used in XRD, SEM and EBSD characterisations were sectioned using a slow saw and ground step-by-step using 600, 1200, 2500 and 4000 grit SiC grinding papers and subsequently with diamond suspensions (3 μm and 1 μm), followed by chemical polishing using colloidal silica suspension with a particle size of 0.25 μm. All grinding and polishing materials were purchased from Struers Ltd.

3.5 Transmission electron microscopy and sample preparation

In this section, the initial TEM characterisation approach is summarised. TEM-based investigations of irradiation-induced damage is introduced later. A JEOL 2100L microscope with a LaB_6 electron source operated at 200 kV was used to carry out the majority of work. HRTEM, STEM imaging and EDS measurements were performed using a JEOL 3000F microscope operating at 300 kV.

Table 3.3: Summary of conventional EBSD and on-axis TKD setup parameters used in the present study.

Mode	Sample tilt(°)	HT (kV)	Probe Current (nA)	Working distance (mm)	Step size (nm)	Pattern resolution
EBSD	70	20	15/20	18	50/20	320×240
TKD	0	30	1.5/2	5	3-5	320×240

3.5.1 Transmission electron microscopy

In TEM, electrons emitted from the electron gun are focused by a set of electromagnetic lenses and apertures to form either a convergent or a parallel beam. In this study, parallel beam illumination mode was used for the majority of micrographs, such as BF images, dark-field (DF) images, selected area electron diffraction (SAED) and HRTEM because the parallel beam provides nearly parallel illumination at low intensity with high coherency. Figure 3.3 shows a simplified schematic diagram of the two TEM modes: diffraction mode (Figure 3.3a) and imaging mode (Figure 3.3b).[233]

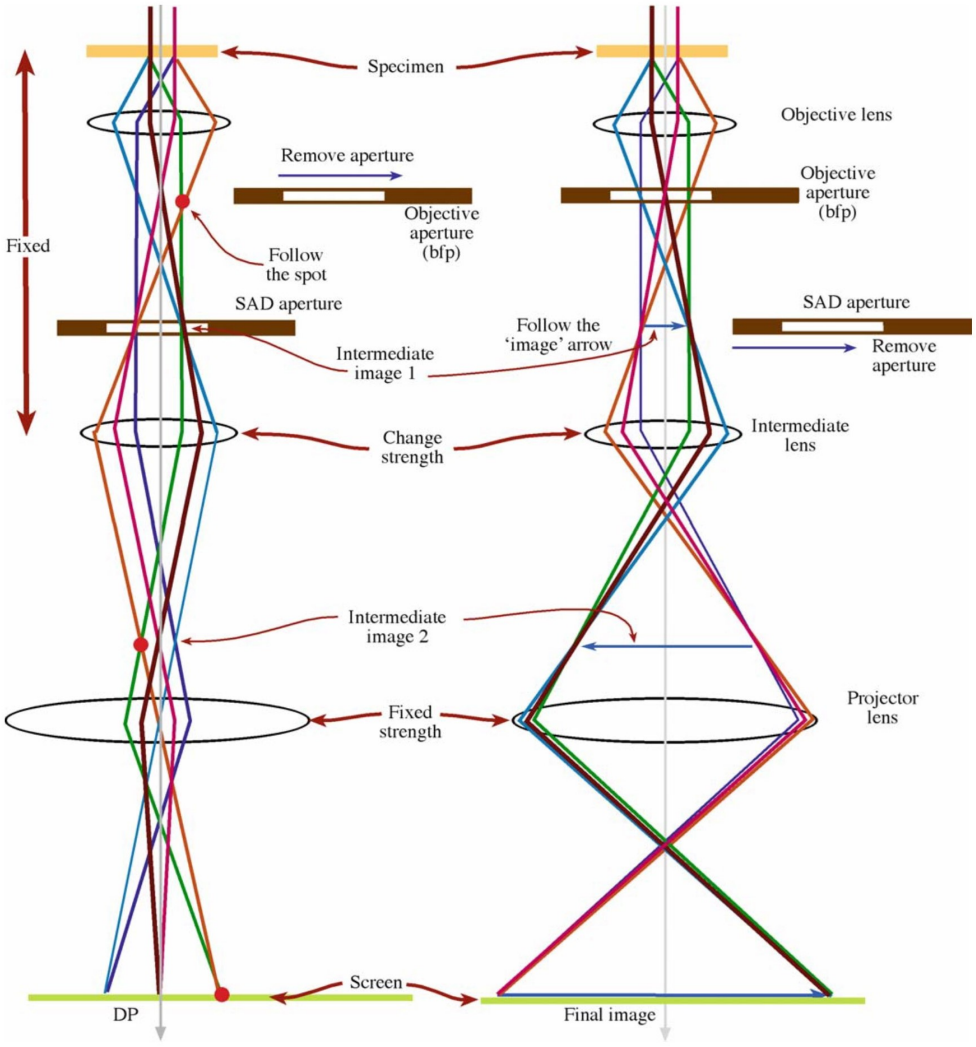


Figure 3.3: Schematic diagram of (a) diffraction mode and (b) imaging mode in a TEM operating at parallel beam mode. Reprinted with permission from Williams et al.[233]

When electrons interact with the thin specimens, they are either transmitted without changing direction shown as grey, pink and brown lines or scattered, shown as light blue, dark blue, orange and green lines. As shown in Figure 3.3a, in the diffraction mode, the direction of the scattered beams are projected to diffraction spots to form a diffraction pattern and direct parallel beams are converged to a spot on the screen. Following Bragg's Law,[224] each spot reflects a type of diffraction which

gives structured information.

As shown in Figure 3.3b, by adjusting the intermediate lens, the transmitted and forward scattered electrons are focused by the objective lens in the imaging mode and its object plane becomes the image plane of the objective lens. A BF image with enhanced contrast can be obtained when the objective aperture is inserted so that the central direct beam can pass through it but not the high-angle diffracted beams. When obtaining a DF image, the objective aperture allows only one or a few diffraction beams to pass with the direct beam being blocked. Thus most of the DF image is dark with only features that diffracting electrons towards the selected directions appear bright.

3.5.2 Twin-jet electropolishing

Specimens for initial microstructure TEM characterisation were prepared by electropolishing. Small pieces of alloy were first thinned using 1200 grit SiC paper to $\sim$120 μm in order to punch into 3mm disks using a TEM-disk punch. The 3 mm disks were then ground using 2500 and 4000 grit SiC paper. Twin-jet electropolishing was then employed to remove a surface layer with residual stress due to mechanical polishing.

Electropolishing was conducted using an electrolyte of 10 vol.% of perchloric with methanol at < -40℃. A Struers TenuPol 5 electropolisher was used to eject electrolyte at the centre of a 3mm disk while maintaining a potential difference across the sample, which removed the material from both sides. Figure 3.4a shows a schematic setup of the twin-jet pro-

cess with electrolyte flowed onto the specimen; and Figure 3.4b shows a schematic specimen with concave surface from twin-jet electropolishing.

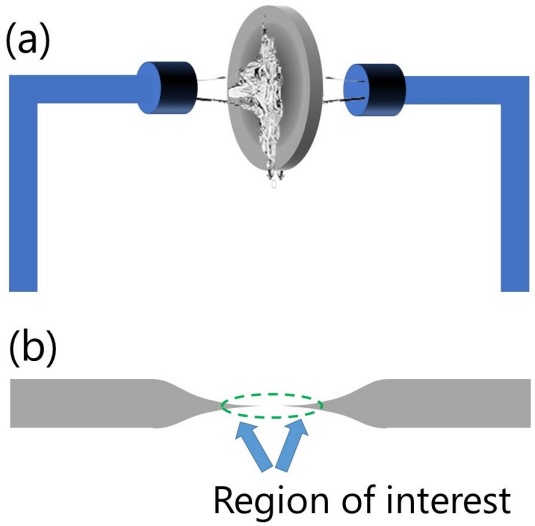


Figure 3.4: Schematic diagram of (a) the setup of the twin-jet process, and (b) a specimen with concave surface from twin-jet electropolishing. This figure was provided by courtesy of Matthew Riding.

Effective and immediate washing after electropolishing is essential in order to obtain a good specimen, which was divided into three steps. First, the specimen was dipped into cold ethanol with a few up and down motion for ∼5 seconds, which helped remove the majority of residual electrolyte. Second, the specimen was washed for 10 seconds in fresh, and cold ethanol. Finally, the specimen was washed for 10-20 seconds in a fresh, room temperature ethanol in order to avoid condensation of ethanol. Eventually, a small hole was formed in the centre and the edge around the hole was thin enough to be used in TEM (typically ∼100-200 nm). Figure 3.5a shows a SEM top view image of a TEM specimen made by twin-jet electropolishing and Figure 3.5b shows an enlarged SEM side view image, showing transparent regions around the edge of the hole.

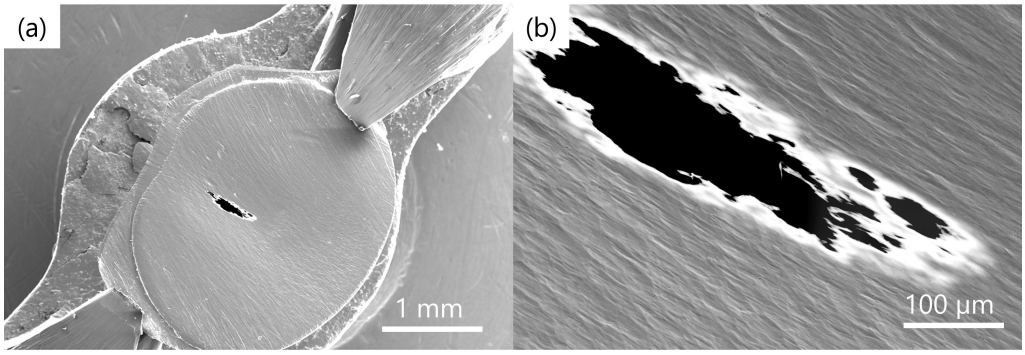


Figure 3.5: (a) SEM top view image and (b) side view image of a TEM specimen made by twin-jet electropolishing.

3.5.3 Focused ion beam assisted in-situ lift-out for TEM

Specimens to examine the deformed microstructure and irradiation damage by TEM were prepared by focused ion beam (FIB) assisted in-situ lift-out. This method provides advantages that regions of interest from a foil can be carefully selected in order to obtain foils with features of interest, such as grain boundaries, precipitates and cracks. Compared with twin-jet electropolishing, foils made by FIB lift-out usually have larger flat and transparent region ($\sim$10-20 μm^2), allowing for a higher possibility to capture the characteristics of interest. In addition, the foils are usually cross-sectional, which is particularly useful for the characterisation of irradiation damage.

In this thesis, a ZEISS Nvision dual-beam FEG SEM-FIB workstation equipped with Kleindiek MM3A micromanipulator was used, allowing for simultaneous milling and imaging. In the FIB column, a beam of Ga ions was used to deposit certain protective layers on the surface of materials and to bombard and remove materials in certain shapes on a micro-scale.

Figure 3.6 shows the step-by-step operations of in-situ lift-out processes.

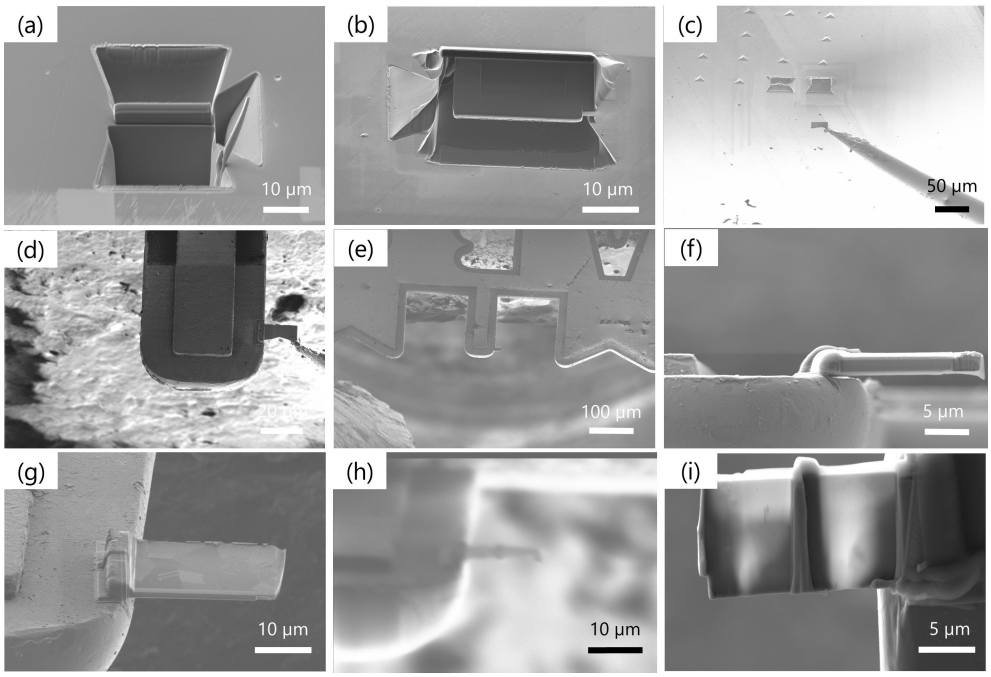


Figure 3.6: (a)-(i) The step-by-step in-situ lift-out processes used in this thesis.

Before milling, a protective layer of C of $\sim 20 \times 2 \times 2\ \mu m^3$ was first deposited over the region of interest in order to reduce possible damage induced by the 30 kV Ga^+ beam.[234] Trenches typically with depth of $\sim 15\ \mu m$ and width of $\sim 20\ \mu m$ were subsequently milled using milling current of 6500-750 pA in both sides of the C layer when the stage was tilted to 54-55°, as shown in Figure 3.6a. A trench in the side where micro-manipulator came in was also milled in order to avoid touching between the needle and the sample. The sample was then tilted to 0° in order to achieve a "U-cut" of the lamella shown in Figure 3.6b. After inserting an in-situ micro-manipulator and welding it to the corner of the lamella using C, the lamella was fully cut free from the bulk sample and lifted out (Figure 3.6c). The lamella was positioned to touch the side of

a 3 mm TEM Cu grid and welded onto it, shown in Figure 3.6d. Figures 3.7e and f show a lamella welded on the pillar in the center (shown in Figure 3.7e) of the TEM grid. Progressive thinning with milling current of 1500-300 pA at 30 kV was performed on both sides to achieve electron transparency at 12 kV, shown in Figure 3.6g. As shown in Figure 3.6h, the lamella went through final polishing using 5 kV and 200 pA when the stage was titled to 40°. Finally, a lamella, still with some of the protective layer, having a relatively uniform and transparent region at 5 kV was produced, shown in Figure 3.6i.

TEM specimens produced by the FIB lift-out method are large enough to encompass both the irradiated layer and the unirradiated inner layer of the specimen. It is worth noting that the 30 keV Ga ions used in the FIB typically create a damaged layer of 30-50nm, which reduces visibility level of defects induced by V^+ and Ni^+ ions. A typical weak-beam DF TEM image with inverted contrast for YCSW irradiated using V^+ at 2.33 dpa is presented in Figure 3.7, showing a typical protective layer, the FIB-damaged layer (34 nm), irradiated layer (820 nm) and the unirradiated region underneath.

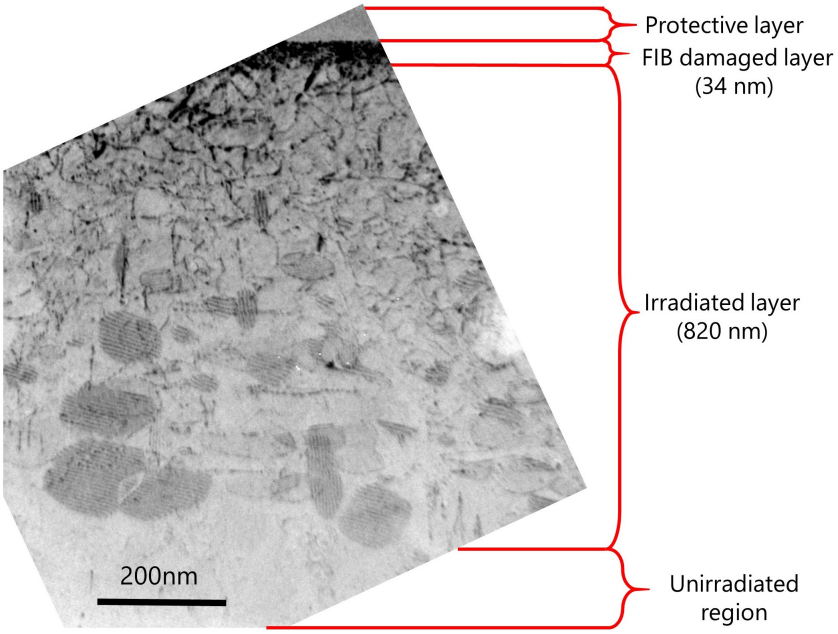


Figure 3.7: A typical weak-beam DF image with inverted contrast for YCSW irradiated using V^+ at 2.33 dpa.

3.5.4 Dislocation loops imaging

Kinematical bright-field (KMBF) and weak-beam dark-field (WBDF) are commonly used to image dislocation loops. Figure 3.8 shows three different types of diffraction conditions used to image diffraction contrast. s_g is the deviation parameter which describes the distance of the reciprocal lattice point g from the Ewald sphere. Ewald sphere is a sphere of radius defined as the reciprocal of the wavelength of the incident wave $(1/\lambda)$ passing through the origin of the reciprocal lattice. As shown in Figure 3.8, under the two-beam dynamical condition, the beam g diffracts similarly to the incident beam and $s_g = 0$ or very small. In order to avoid the dynamic contrast effect in the two-beam condition, KMBF is used with a small positive deviation parameter, i.e. $s_g > 0$.

However, for quantitative measurements, such as size measurement and measuring small loops (<5nm), WBDF is the best technique for sizing and counting dislocation loops as it produces a high defect peak intensity relative to the background.[235] As shown in Figure 3.8, in the (g,3g) WBDF condition, the Ewald sphere cuts the line 3g reflection, and thus the bright Kikuchi line corresponding to the reflection 3g passes through the 3g diffraction spot. In practice, s_g can either be positive or negative. The details of WBDF and the set-ups of WBDF are well described in references.[235]

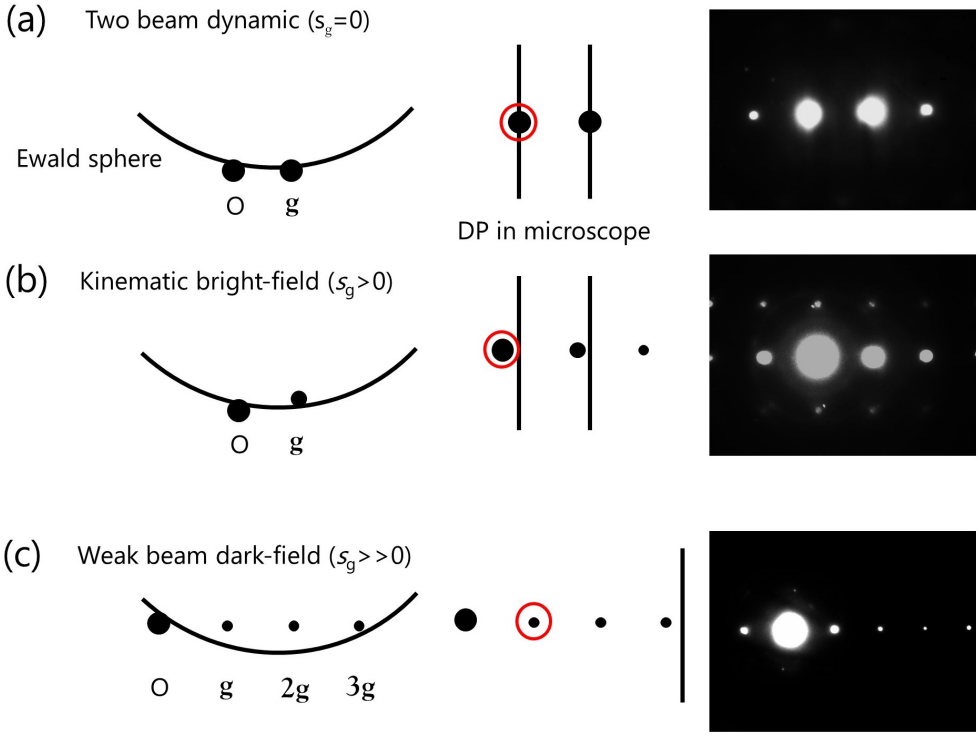


Figure 3.8: Three different types of diffraction conditions used to image diffraction contrast: (a) two-beam dynamical, (b) KMBF and (c) WBDF. The exaggerated Ewald sphere is shown on the left-hand side with a schematic diffraction pattern (DP) showing the position of Kikuchi lines in the center and an actual corresponding DP on the right-hand side.

Figure 3.9 shows TEM images of irradiation-induced dislocation loops

obtained using KMBF and WBDF conditions in the same region of CSW. The nature and size of loops are more distinguishable under the WBDF condition. In this thesis, WBDF was used for all quantitative analysis of dislocation loops whereas occasional KMBF was used to aid interpretation of WBDF micrographs when contrast was insufficient. Due to Ga^+ damage derived from FIB processing, irradiation-induced defects smaller than 3 nm were indistinguishable from FIB damage, thus a minimum size of loops was assigned as 3 nm. On most occasions, WBDF images with inverted contrast were used and thus defects appear dark on a light background.

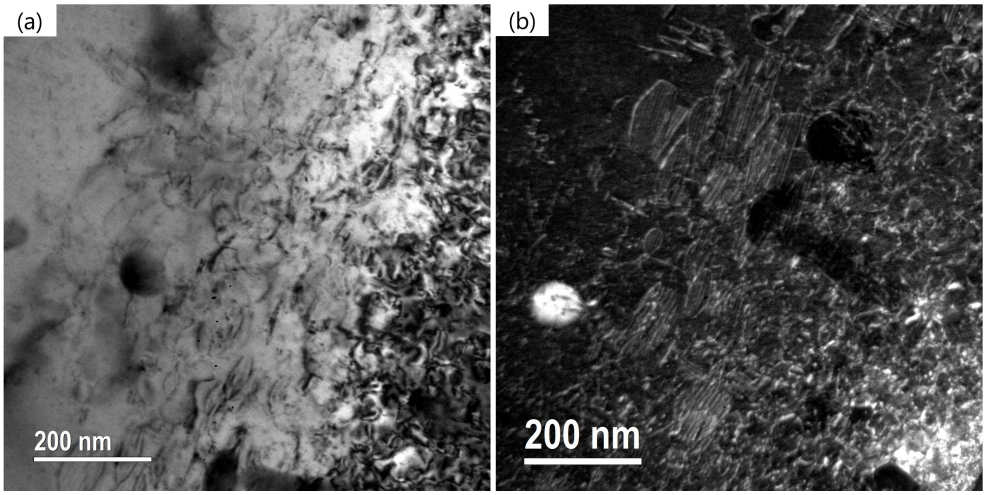


Figure 3.9: TEM images of irradiation-induced dislocation loops obtained using (a) KMBF and (b) WBDF conditions in the same region of CSW.

SingleCrystal software (http://crystalmaker.com/singlecrystal/) was used to label electron diffraction patterns. Figure 3.10a shows a typical diffraction pattern captured on a charge-coupled device (CCD) camera and Figure 3.10b shows the diffraction pattern with the same crystal parameters, i.e. crystal structure and lattice parameter, obtained from

Inorganic Crystal Structure Database (ICSD). The pole points upwards along [111] direction, thus the electron beam points along $[\bar{1}\bar{1}\bar{1}]$ direction.

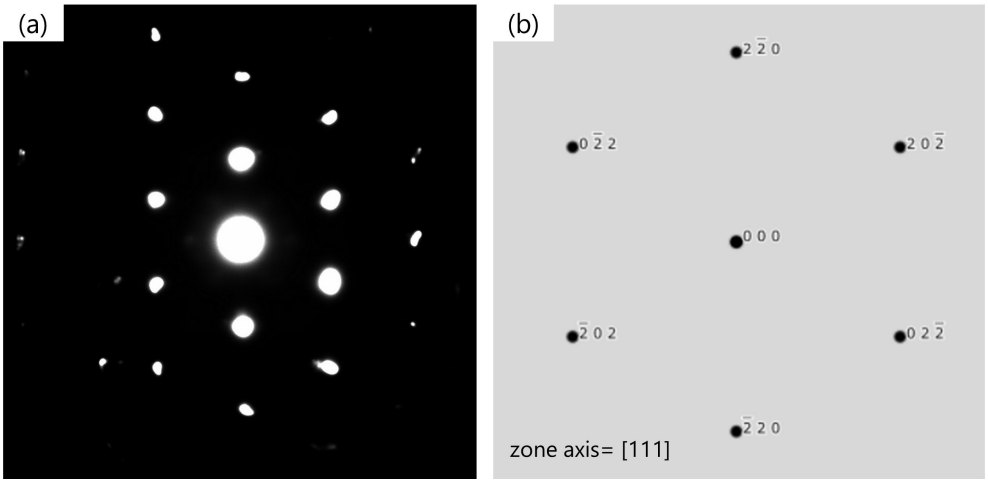


Figure 3.10: (a) Actual diffraction pattern and (b) archived diffraction pattern with the same crystal parameters in the database using Single-Crystal software showing the zone axis is [111].

To obtain the number density of dislocation loops per unit volume, the foil thickness was determined from convergent beam electron diffraction (CBED) patterns in a convergent, two-beam diffraction condition.[233] The foil thickness t can be obtained based on Equations 3.2 and 3.3:

$$\frac{s_i^2}{n_k^2} + \frac{1}{\xi_g^2 n_k^2} = \frac{1}{t^2} \tag{3.2}$$

$$s_i = \lambda \frac{\triangle \theta_i}{2\theta_B d^2} \tag{3.3}$$

where λ is the electron wavelength, d is the spacing of the operating reflection, n_k is an interger, s_i is the deviation of the i-th minimum from the perfect Bragg condition, θ_i and θ_B are the fringe spacing and measured directly from the CBED pattern. The values of $\frac{s_i^2}{n_k^2}$ can be plotted

as a function of $\frac{1}{n_k^2}$ with the intercept of $\frac{1}{t^2}$ and thus t is determined. The details of CBED method to measure foil thickness are well described in reference.[233]

3.5.5 The counting and sizing of loops

For every g-vector condition captured in WBDF, the negative g-vector condition was also captured. Dislocation loops were counted by comparing both sets of images, to minimise ambiguous defect contrast due to inside-outside contrast effects.[235] This effect relates to whether the planes around a dislocation loop diffract the electron beam on the inside-edge or the outside-edge of the dislocation core. Defects were counted for a particular g-reflection ±g pair if they showed obvious contrast. The final count reported refers to only dislocation loops sized larger than 3 nm as mentioned earlier.

Dislocation loops were sized by measuring the longest axis of loops after comparing the ±g-vector WBDF micrograph pairs. Figure 3.11 shows an example imaged with ±g-vector conditions where two $\frac{1}{3}\langle 111\rangle$ type loops in YCSW showed both outside and inside contrast. The size was relatively smaller when the loops showed inside contrast.

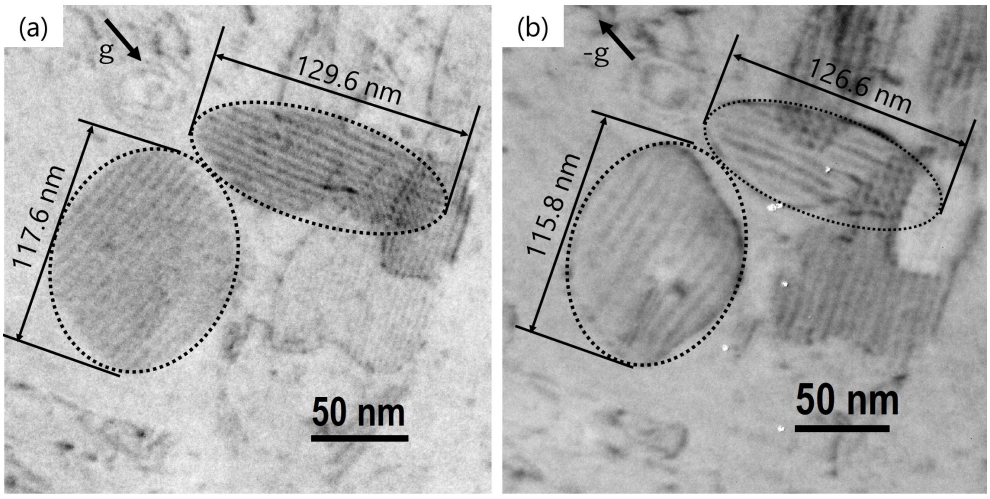


Figure 3.11: WBDF inverted contrast images of two $\frac{1}{3}\langle 111\rangle$ type dislocation loops in YCSW imaged with ±g-vector conditions. (a) Outside contrast and (b) inside contrast.

Loop counts were carried out using automated counting package available in ImageJ[236] and the method described by Haley,[237] which involved setting up a threshold to convert the image from grey scale to binary. Ellipses were then automatically attributed to the defects visible in the image. Quantitative information, including the size, numbers and distribution was then available.

3.5.6 Dislocation loops characterisation

The Burgers vector, b, of a dislocation loop can be measured by capturing a series of g-vector conditions over the same region, and observing the visibility and invisibility changes of defects with g. Considering a family of loops with $b = 1/3\langle 111\rangle$ $b = 1/2\langle 110\rangle$ observed in FCC metals and alloys, a $g \cdot b$ table with the visibility information is given in Table 3.4, which allows unambiguous determination of the nature of each pos-

sible dislocation loop. Note here commonly shared Kikuchi bands when using different poles were only listed once. Figure 3.12a shows a Kikuchi map from FCC metals and alloys containing commonly used poles and bands. Figure 3.12b, 3.12c and 3.12d show the Kikuchi lines along a certain pole when indexing dislocation loops in this thesis with simulated SAED pattern along the same zone axis in Figures 3.12e, 3.12f and 3.12g. In practice, this loop-by-loop correlation method was only possible for reasonably large dislocation loops (>10 nm) and when dislocation loop did not overlap significantly. The identification of nature of loops does not necessarily require imaging at all shown conditions.

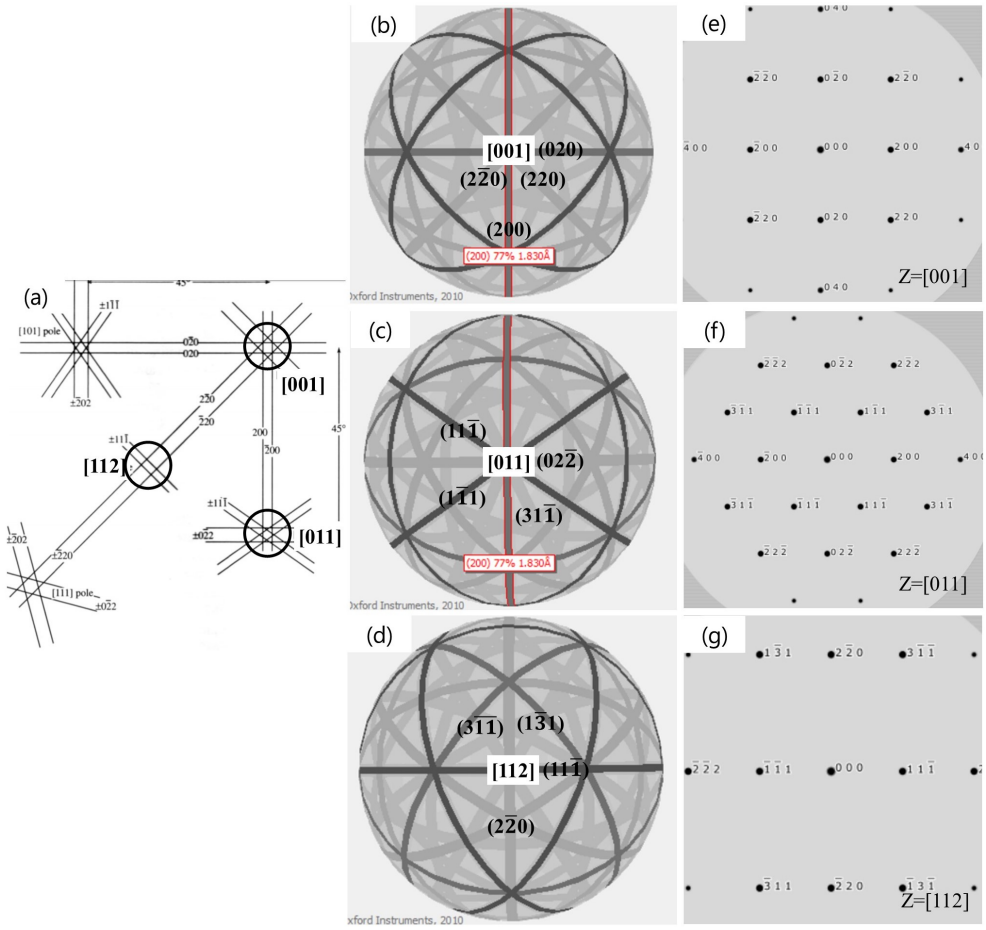


Figure 3.12: (a) Kikuchi map from FCC metals and alloys. (b), (c) and (d) Kikuchi lines corresponding to [001], [011] and [112] zone axis in (a) generated by Spherical Kikuchi Maps package provided by Oxford Instrument CHANNEL 5 software. (e), (f) and (g) Corresponding simulated SAED pattern in CSW along [001], [011] and [112] zone axis.

The inside-outside contrast method was used to measure the vacancy or interstitial nature of dislocation loops. Figure 3.13 shows a schematic diagram showing the basic principle for inside-outside technique for loop nature determination with Figures 3.13a and 3.13b as an interstitial loop, and Figures 3.13c and 3.13d as a vacancy loop. A full description can be found in reference[235]

Table 3.4: $g \cdot b$ table that is used to distinguish $b = \frac{1}{3}\langle 111 \rangle$ and $b = \frac{1}{2}\langle 110 \rangle$ dislocation loops.

ZA	gb	$\frac{1}{3}[111]$	$\frac{1}{3}[1\bar{1}1]$	$\frac{1}{3}[\bar{1}11]$	$\frac{1}{3}[\bar{1}\bar{1}1]$	$\frac{1}{2}[110]$	$\frac{1}{2}[101]$	$\frac{1}{2}[\bar{1}10]$	$\frac{1}{2}[\bar{1}01]$	$\frac{1}{2}[011]$	$\frac{1}{2}[0\bar{1}1]$
[001]	(200)	$\frac{2}{3}$	$\frac{2}{3}$	$-\frac{2}{3}$	$-\frac{2}{3}$	1	1	-1	-1	0	0
	(020)	$\frac{2}{3}$	$-\frac{2}{3}$	$\frac{2}{3}$	$-\frac{2}{3}$	1	0	1	0	1	-1
	(220)	$\frac{4}{3}$	0	0	$-\frac{4}{3}$	2	1	0	-1	-1	-1
	$(2\bar{2}0)$	0	$\frac{4}{3}$	$-\frac{4}{3}$	0	0	1	-2	-1	-1	1
[011]	$(11\bar{1})$	$\frac{1}{3}$	$-\frac{1}{3}$	$-\frac{1}{3}$	1	1	0	0	-1	0	-1
	$(1\bar{1}1)$	$\frac{1}{3}$	1	$-\frac{1}{3}$	$-\frac{1}{3}$	0	1	-1	0	0	1
	$(31\bar{1})$	1	$\frac{1}{3}$	-1	$\frac{5}{3}$	2	1	-1	-2	0	-1
[112]	$(1\bar{3}1)$	$-\frac{1}{3}$	$\frac{5}{3}$	-1	1	-1	1	-2	0	-1	2

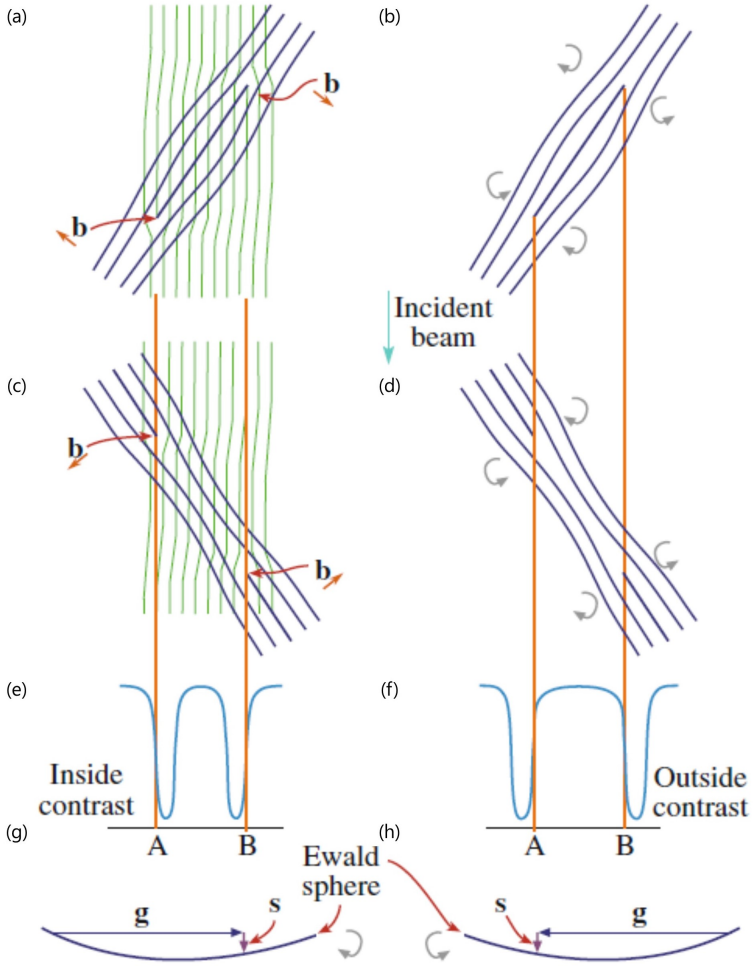


Figure 3.13: Schematic diagrams showing the basic principle for inside-outside technique for loop nature determination. (a) An interstitial loop with diffracting planes (green lines) and arrows showing the plane rotation in (b). (c) and (d) The case for a vacancy loop. (e) and (f) The position of the image contrast relative to the projection of loops for the diffraction conditions shown in (g) and (h). Figure adapted with permission from Williams et al.[233]

Whether inside or outside contrast is observed depends on the inclination of the dislocation loop with respect to the beam, the direction of the g-vector, the sign (plus or minus) of the deviation parameter, and the vacancy or interstitial nature of the loop. The inclination of the dislocation loop can be determined via Burgers vector analysis, and the g-vector and deviation parameter can be well controlled (all WBDF imaging in

this thesis were operated with a positive deviation parameter, i.e. s_g). As shown in Figures 3.13g and 3.13h, inside contrast results when clockwise rotation of the diffracting planes brings them into the Bragg condition whereas outside contrast results for anticlockwise case. In practice, outside contrast arises for interstitial loops when $(g \cdot b)s_g > 0$, and $b \cdot z < 0$ whereas inside contrast forms for vacancy loops when $(g \cdot b)s_g < 0$ and $b \cdot z > 0$.

3.6 Mechanical testing

3.6.1 Nanoindentation

Nanoindentation allows for mechanical properties such as hardness and elastic modulus to be extracted from a small volume of material as a function of indentation depth. The most commonly used methodology for nanoindentation is called the Continuous Stiffness Measuremen (CSM), whereby an oscillating load is applied on top of the static load, and the full description can be found in Oliver et al.[238] The hardness increases strongly with decreasing indentation depth, particularly at depths of less than a few micrometers, which is known as the indentation size effect.[239] In other words, the hardness measured by nanoindentation is in general higher than that measured by bulk testing.

In this study, samples used for nanoindentation had the same surface quality with those used for EBSD. The samples were mounted on an Al stub using a thin layer of Crystalbond resin. A pyramidal Berkovich tip

with centreline to face angle of 65.3° was used. The tip was calibrated by indenting a reference fused silica sample with a known elastic modulus of 72 GPa in order to find the area function. A MTS Nanoindenter XP was used to create arrays of 4×4 indents with a spacing of 50 μm and a depth of 2000 μm at a strain rate of 0.05 s^{-1}. Figure 3.14a shows a SEM image containing a array of 4×4 indents and Figure 3.14b shows typical hardness and modulus as a function of depth curves for one indent of CSW.

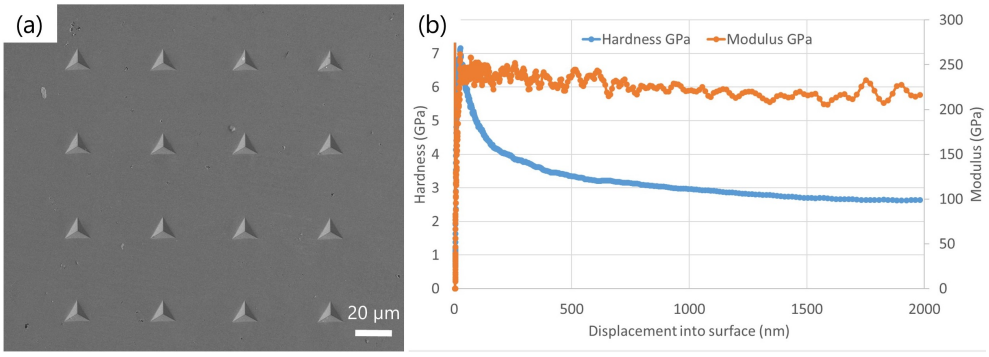


Figure 3.14: (a) SEM image containing an array of 4×4 indents and (b) hardness and modulus as a function of depth for one indent of CSW.

3.6.2 Tensile testing and finite element analysis

For tensile testing at room temperature, miniature specimens with a cross section of 1×1 mm^2, a gauge length of 14 mm and an overall length of 36 mm according to ASTM E8M standard[240] were obtained using wire-based electrical discharge machining for 1 mm slices, followed by water jet cutting to a dog-bone shape. As for tensile testing at -196℃, round specimens with a gauge length of 12.7 mm and M5 threaded end were machined according to ASTM E8M standard. The specimens were

then polished with 1200 grit SiC paper in order to remove any residual stress from machining processes. A constant strain rate of 10^{-3} s^{-1} was used for all tests. Testing was carried out by Westmoreland Mechanical Testing & Research Ltd.

In order to investigate the deformation behaviour, a finite element model (FEM) was established by Abaqus to provide an estimate of the stress and strain distribution in the specimen at the final stage of failure. The model geometry was built on the failed specimen geometry by extending the cross-section into 3D. Fix and displacement boundary conditions were applied to the fracture surface and one end of a specimen, respectively, to simulate the loading conditions. The FEM conditions and solution were essentially standard and no new methodology was needed. All the FE modelings were conducted by Dr. Jicheng Gong.

3.7 Irradiation facilities and conditions

3.7.1 Heavy ion irradiation

Heavy ion irradiation was used as an analogue for neutron irradiation due to the difficulties of accessing using neutron irradiation and arising radioactivity. Compared with neutron irradiation, ion irradiation consumes less time, money, and materials after irradiation exhibit no residual radioactivity[241] that they can be investigated safely in the research lab. The conditions of ion irradiation, such as temperature, atmosphere, ion flux and time, can be easily controlled and tailored.[167]

However, several drawbacks arise in heavy ion irradiation.[242] One is the effect of accelerated damage rate of ion irradiation on the irradiation microstructure, such as radiation-induced segregation and void swelling.[243] In order to achieve the same damage dose, although ion irradiation is 100 to 10000 times quicker than test reactor irradiation, the dose rate of ion irradiation is 100 to 10000 times that of reactor irradiation.[241,244] The temperature-dose rate interdependence for stainless steel over a wide range of temperatures and dose rates has been reported,[167,245] which indicated that the higher dose rate in ion irradiation relative to a reactor requires a corresponding increase in temperature to achieve the same result. This effect is addressed using invariance theory by Mansur.[243] Discussion in detail can be found in Mansur's work[243] and is beyond the scope of the thesis.

Another disadvantage of ion irradiation is varied dose over the penetration depth, which is shown later in Figure 3.16. In this case, in order to avoid dose or dose rate variation effects on irradiation damage among different samples, careful and consistent selection of the region of interest is needed.

All ion irradiation experiments in this thesis were carried out at the Surrey Ion Beam Centre (a University of Surrey facility) with the help of Dr Nianhua Peng. Samples with EBSD quality surface polish finish were mounted on rails that were then mounted onto a temperature-controlled stage. Figure 3.15 shows a photograph of the rail with samples

mounted and a region that was exposed to irradiation and a region that was covered by a Cu grid and was thus shielded from irradiation. The covered region was used as reference to identify any irradiation-induced microstructural change.

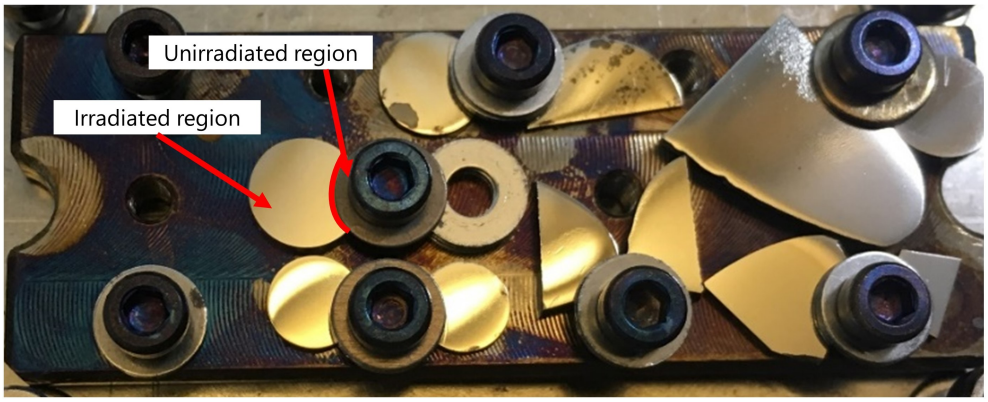


Figure 3.15: A photograph of the transport rail with samples mounted, showing an irradiation region exposed to ions and an unirradiated region covered by a Cu grid.

Ni^+ ions were chosen because self-ions irradiations do not change the chemistry of the material and are regarded to effectively mimic the PKA from a neutron collision.[246] V^+ ions irradiations were conducted in the purpose to compare with self-ions irradiations. All experiments are summarised in Table 3.5.

Table 3.5: The summary of irradiation conditions.

Ions	Energy (MeV)	Fluence (ions·cm^{-2})	Dose rate (10^{-5} dpa/s)	Temperature (℃)
V^+	2	5×10^{14}	4.3	500 ± 20
V^+	2	2.26×10^{15}	3.5	500 ± 20
Ni^+	2	5×10^{14}	6.7	500 ± 20
Ni^+	2	2.26×10^{15}	4.9	500 ± 20

3.7.2 SRIM simulation

The SRIM-2008 (Stopping Ranges of Ions in Matter) simulation program[247] was used to calculate the displacements per atom (dpa) - a prediction of the average number of times each atom in a material has been displaced during irradiation, and damage profile of the charged-particle irradiation used in this thesis. SRIM uses a binary-collision-approximation (BCA) algorithm to compute the energy losses of ions as they propagate through materials. The quick (Kinchin-Pease) cascade option recommended by Stoller[248] was selected and a displacement energy of 40 eV was used. A density of 7.8 g/cm^3 for CSW measured by Archimedes density method was used in simulations. The dpa (N_{dpa}) was calculated by the number of vacancies ($N_{vacancy}$) produced per Å and per incoming projectile, provided by the SRIM output VACANCY.txt. To convert this value to dpa, the SRIM value, the following equation was used,

$$N_{dpa} = \frac{N_{vacancy} \times F \times 10^8}{\rho_N} \tag{3.4}$$

where F represents the fluence (ions·cm^{-2}) and $\rho_N = 8.48{\times}10^{22}$ atoms·cm^{-2} is the atomic density of targeted material (CSW).

Although the use of SRIM to predict the damage production is convenient, there are some limitations. One is that there is no build-up of ions or damage in the target which means that every ion interacting with the target is not affected by previous ions.[249] Temperature is known to have a modest impact on point defect production in MD simulations but this

is not accounted for in SRIM which only considers the temperature of 0 K.[248] Moreover, SRIM does not consider any crystal effects.[248,249] Nevertheless, SRIM remains a convenient tool and the most widely adopted program to simulate radiation damage production.

The damage profiles for all four irradiation conditions are given in Figure 3.16. The peak damage achieved in four irradiation conditions as numbered in Table 3.5 were 0.51, 2.33, 0.63 and 2.84 dpa. The depth where peak damage was obtained was 620 nm and 600 nm for V^+ and Ni^+ ion irradiation respectively.

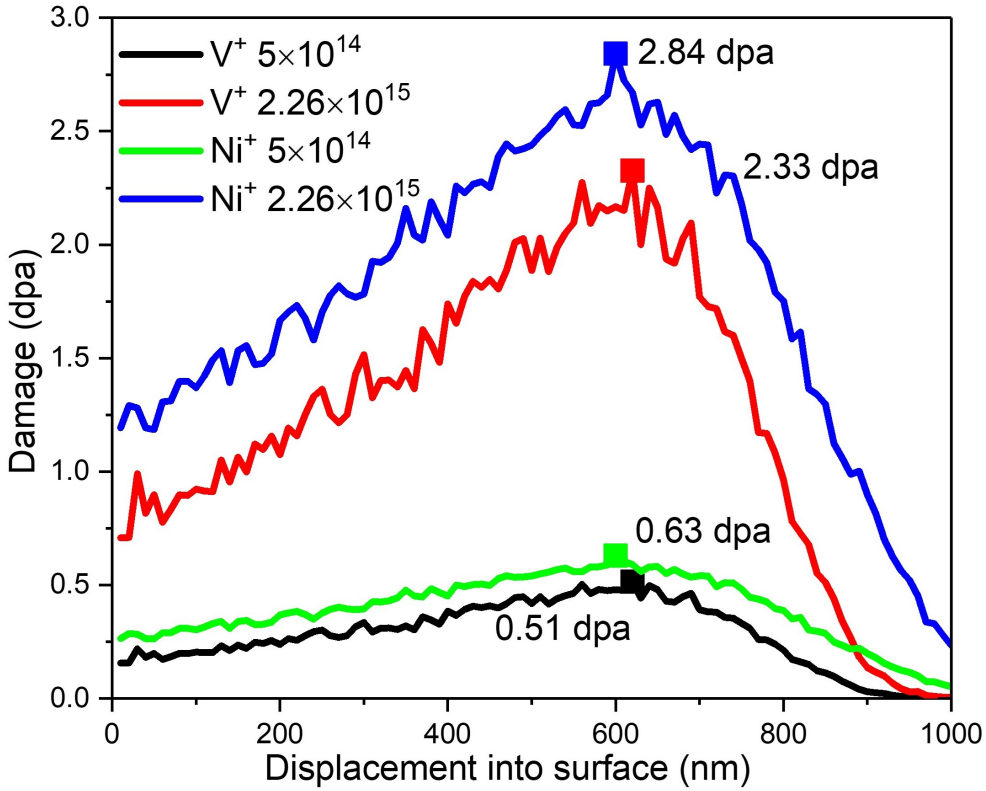


Figure 3.16: Damage profiles calculated by SRIM for all four irradiation conditions with peak damage in dpa marked on the curves.

3.8 Irradiation-induced hardening by nanoindentation

Nanoindentation is particularly useful for detecting irradiation-induced hardening as it can efficiently provide mechanical information, such as hardness and elastic modulus, as a function of depth within the thin irradiated layer. In order to obtain hardness data from the thin irradiated layer (approximately 1 μm), samples used for heavy ion irradiation were first polished. Several arrays of 4×4 indents were placed both in the irradiated region and in the unirradiated region shown in Figure 3.15. Figure 3.17 shows typical hardness curves as a function of depth for unirradiated (shown as black) and irradiated (shown as red) region of CSW irradiated with 2 MeV V^+ at 2.33 dpa. An average value for hardness was calculated based on at least three sets of hardness data.

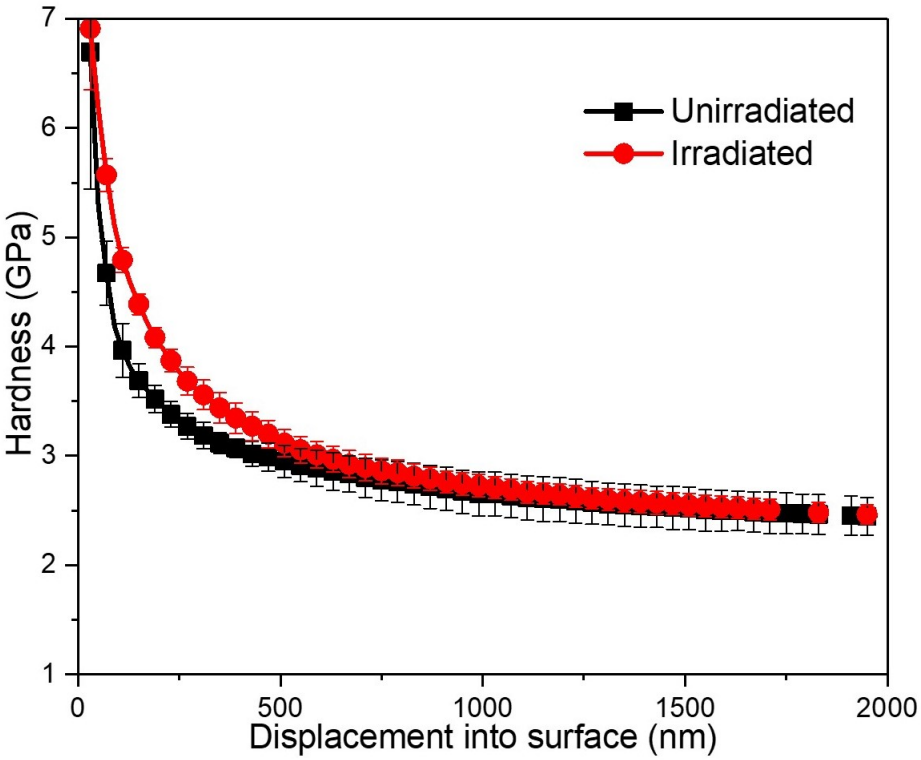


Figure 3.17: Hardness curves as a function of depth for unirradiated (shown as black) and irradiated (shown as red) region of CSW irradiated with 2 MeV V^+ at 2.33 dpa.

4 Microstructure of CrMnFeCoNi-(Y)

This chapter first reports the chemical composition and crystal structure of CrMnFeCoNi-(Y) and then discusses the initial microstructure of CrMnFeCoNi-(Y), particularly the characteristics of oxide particles in YCSW.

4.1 Chemical composition

The composition of CSP and YCSP measured using ICP-OES is shown in Table 4.1 together with the nominal CSP composition, showing good agreement. The non-metallic element concentrations were approximately 200 ppm C, 50 ppm S, 440 ppm O and $<$ 500 ppm Si), which arose from impurities carried over from the feed stock, and/or contamination during vacuum induction casting that is to some extent an inevitable consequence of bulk, high temperature melt processing of commercial purity materials using refractory ceramics. The concentration of Y in YCSP was 0.261 wt.%, slightly higher than the nominal concentration of 0.19 wt.%.

Table 4.1: The nominal composition (wt.%) of CSP and actual composition (wt%) of CSP and YCSP measured using ICP-OES.

	Cr	Mn	Fe	Co	Ni	C	S	O	Si	Y
Nominal	18.54	19.59	19.92	21.02	20.93	-	-	-	-	-
CSP	18.50	20.24	20.07	20.79	20.07	0.020	0.005	0.044	< 0.05	-
YCSP	18.72	19.42	19.82	21.07	20.44	0.072	0.002	0.116	< 0.05	0.261

4.2 Crystal structure

The XRD patterns of CSP, CSW, YCSP and YCSW are shown in Figure 4.1. There was one principal FCC phase with lattice parameter a = 0.360 nm calculated by Rietveld refinement method, for all four alloys. The lattice parameter was close to 0.3597 nm for a sintered Cantor alloy measured using neutron diffraction.[250] The single phase agreed well with the reported thermal stability of the Cantor alloy at annealing temperatures higher than 800℃.[33] Any secondary precipitates (e.g. carbides and oxides) were not resolved by XRD.[251]

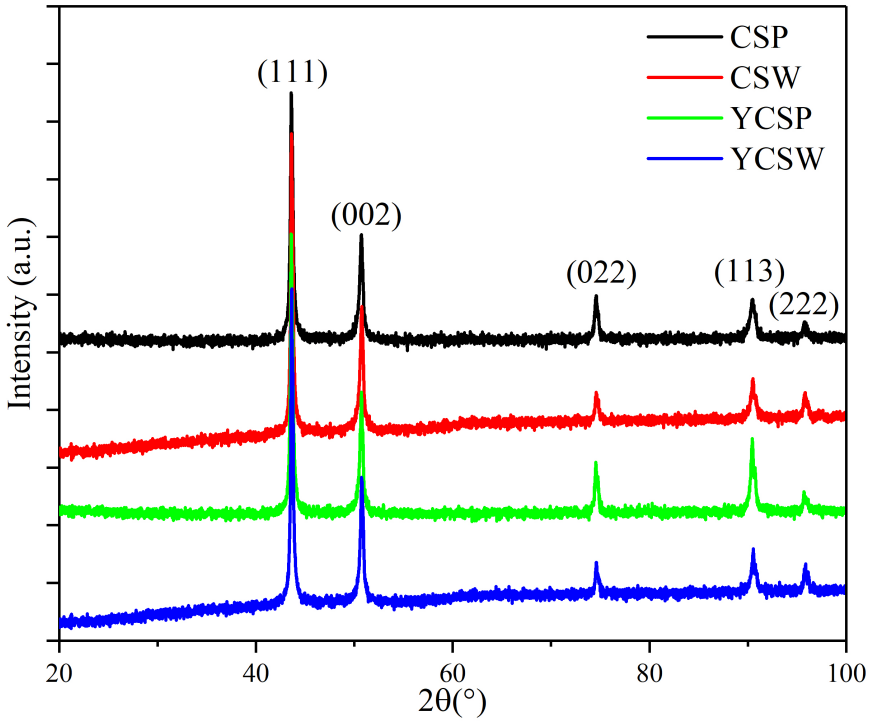


Figure 4.1: X-ray diffraction patterns of CSP, CSW, YCSP and YCSW. There was one FCC phase with lattice parameter a = 0.360 nm.

4.3 Initial microstructure of CrMnFeCoNi-(Y)

As shown in the optical microscopy (OM) images of CSP (Figure 4.2a), YCSP (Figure 4.2b), CSW (Figure 4.2c) and YCSW (Figure 4.2d), CSP and YCSP exhibited an equiaxed polygonal grain structure typical of spray forming under optimal conditions. There were no obvious large pores (>1 μm) based on OM images. There were a small fraction of scattered "white" precipitates diffracting strongly in CSP (Figure 4.2a), potentially non-metallic inclusions as suggested by Table 4.1. There were also dispersed white precipitates in YCSP (Figure 4.2b) and analysis of secondary precipitates is presented later. CSW (Figure 4.2c) and YCSW (Figure 4.2d) showed much finer grains and there were many annealing twins as shown in the inset of Figures 4.2c and 4.2d, which are again discussed in more detail subsequently.

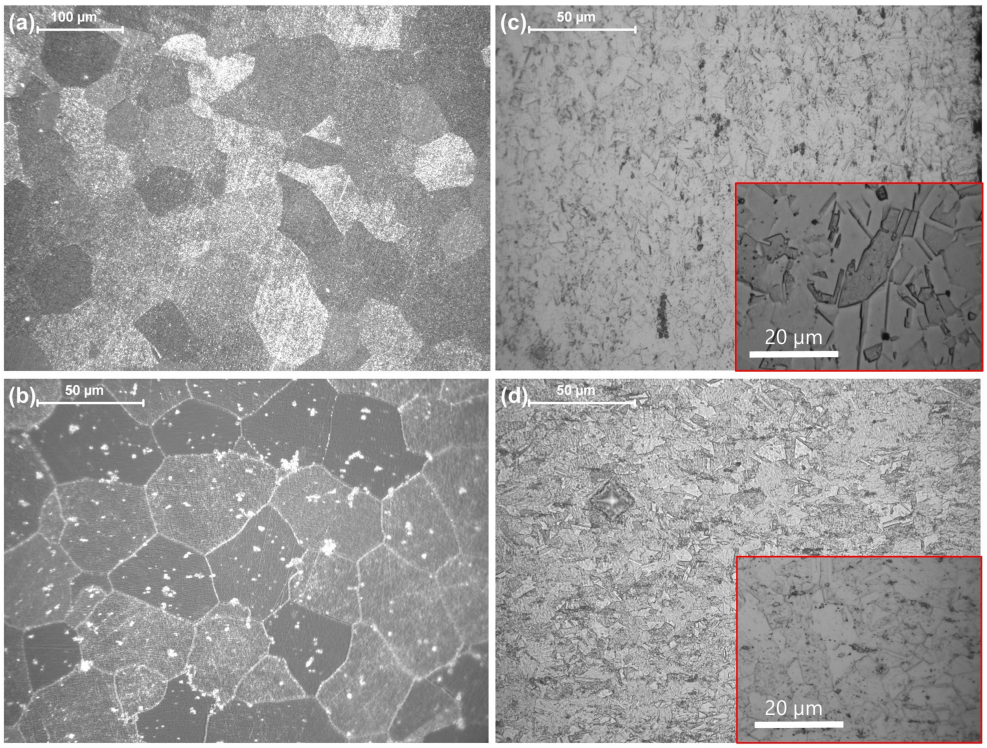


Figure 4.2: Optical microscopy (OM) images of (a) CSP, (b) YCSP, (c) CSW and (d) YCSW showing an equiaxed, polygonal grain structure. There was a low volume fraction of "white" spots in CSP which are suggested to be non-metallic inclusions. Dispersed white spots in YCSP were possibly Y-based oxides.

Figs. 4.3 displays the colour-coded grain orientation maps of CSP (Figure 4.3a), YCSP (Figure 4.3b), CSW (Figure 4.3c) and YCSW (Figure 4.3d), with the crystal orientation parallel to the swaging direction indicated in the right upper corner of Figure 4.3a. The as-sprayed equiaxed, polygonal grain structures were emphasised even at as-sprayed state. The average grain size for CSP, YCSP, CSW and YCSW determined by the linear intercept method was 48.5, 22.3, 8.2 and 5.4 μm respectively without counting annealing twin boundaries, as summarised in Table 4.2. The average grain size of CSP was significantly smaller than the average grain size (1000 μm) of as-cast Cantor alloy made by vacuum induction melt-

ing[36] due to the self-graining refining advantages of spray forming.[63,79] This arises from the reheating and remelting that occurred for a large number of depositing solid and droplets at the forming billets surfaces, which destabilises their dendritic/cellular microstructure, causing incipient grains to fragment to provide a potent grain multiplication effect. The addition of Y produced a 54% reduction in grain size, either by promoting grain formation further, and/or by exerting a pinning pressure on migrating boundaries due to solute drag (unlikely at low Y concentrations) or due to the presence of fine particles.[252]

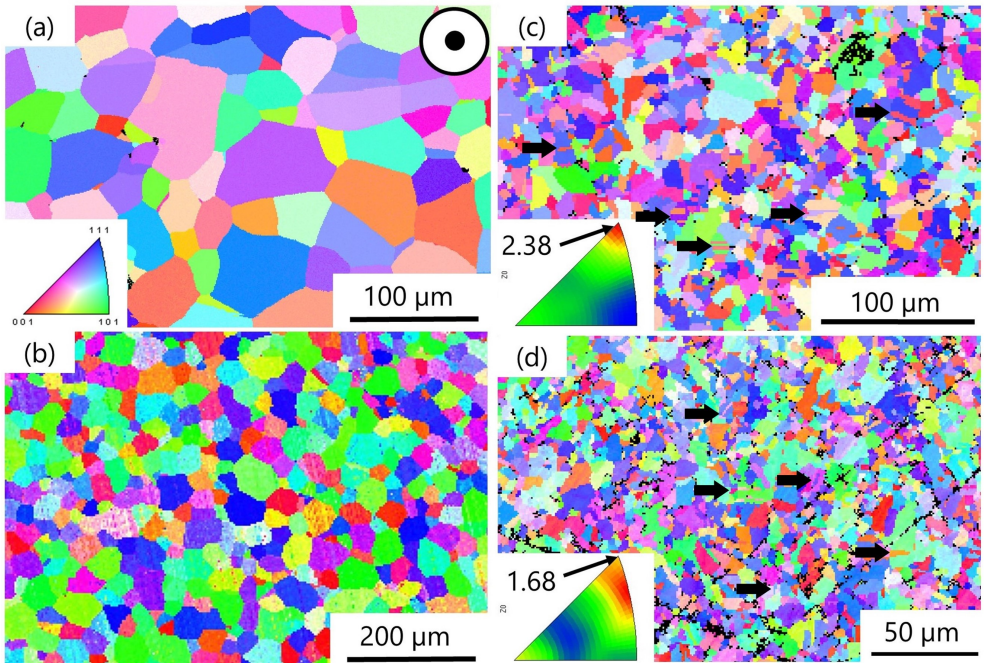


Figure 4.3: False coloured EBSD orientation maps and inverse pole figure texture plots for (a) CSP, (b) YCSP, (c) CSW and (d) YCSW. The swaging direction for (c) and (d) is shown in (a). Orientation maps show polygonal grain structure in all four alloys while annealing twins were observed in CSW and YCSW. There was an effective grain size reduction after yttrium addition. The IPF texture on the left side showed a minor $\langle 111 \rangle$ texture in CSW and YCSW.

Table 4.2: The average grain size of CSP, YCSP, CSW and YCSW determined by the linear intercept method.

Materials	CSP	YCSP	CSW	YCSW
Grain size (μm)	48.5	22.3	8.2	5.4

As shown in Figure 4.3c and 4.3d, the grain sizes reduced by 83% and 76% for CSW and YCSW compared with CSP and YCSP after swaging and subsequent annealing. There were many annealing twins in CSW and YCSW, some of which were marked by black arrows. On the left side of Figure 4.3c and 4.3d, the IPF texture along the rod axis indicated that both CSW and YCSW showed a relatively weak, residual $\langle 111 \rangle$ texture, which is common in Cantor alloys made by swaging and then heat treatment under similar conditions.[35]

Figure 4.4 shows a representative SEM-EDS chemical composition true map from a CSP billet for Cr, Mn, Fe, Co, Ni, C, S, O and Si. The metallic elements showed no resolvable micro-segregation on the scale of the technique. There was evidence of non-metallic inclusions, suggested to be carbon, oxides, Cr and Mn-rich sulfides and SiO_2, and consistent with the composition in Table 4.1.

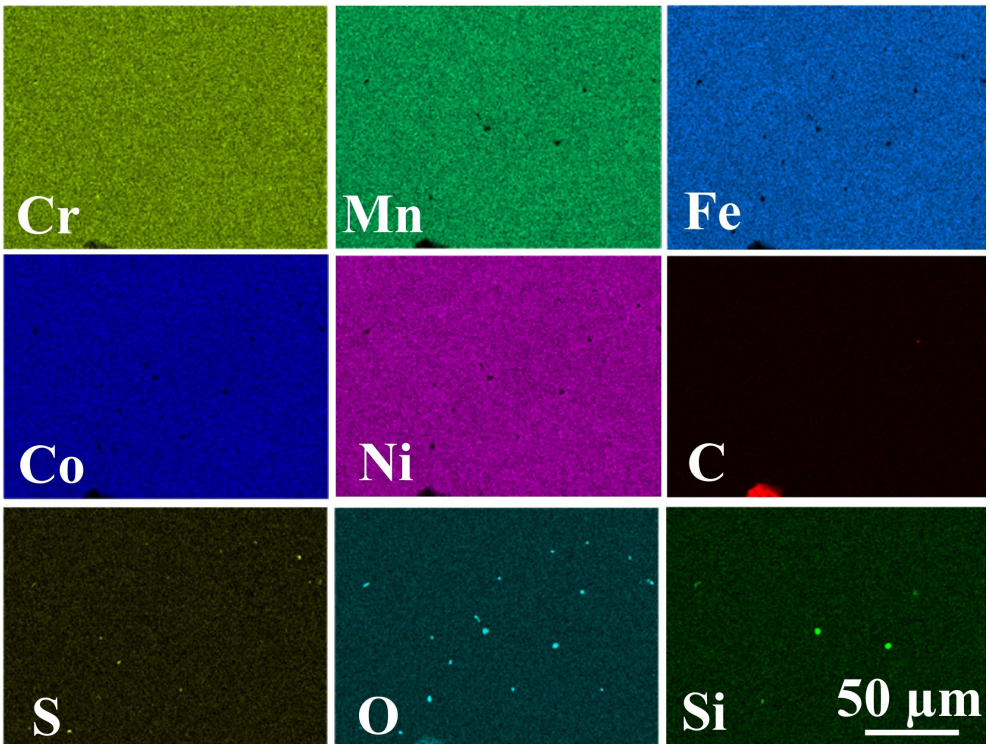


Figure 4.4: Composition true maps (by SEM-EDS) from CSP. The alloy was single FCC phase with five principal elements uniformly distributed. A low fraction of fine-scale carbon, oxide, sulfide and silicide inclusions were suggested to derive from the raw materials.

With regards to YCSP, as shown in Figure 4.5, again, the metallic elements showed no resolvable micro-segregation on the scale of the technique. There were SiO_2 and Y-oxides both with and without Si. Si likely induces clustering of Y-oxides,[253] as shown in the left bottom corner of Figure 4.5. As intended, Figure 4.5 suggests that Y reacted with internal oxygen (i.e. oxygen in the feedstock material, or introduced in melting and atomisation despite the use of Ar atmosphere) and to form scattered Y-oxides, with an average size of 3.94 μm. Figure 4.6 shows the representative EDS spectrum with an enlarged spectrum at the range of 0-3 KeV in the inset based on SEM-EDS maps of YCSP. The magenta curve

is the fitted spectrum by subtracting the background and deconvoluting overlapping peaks based on Aztec self-contained algorithms. It can be seen that all peaks were explicitly identified.

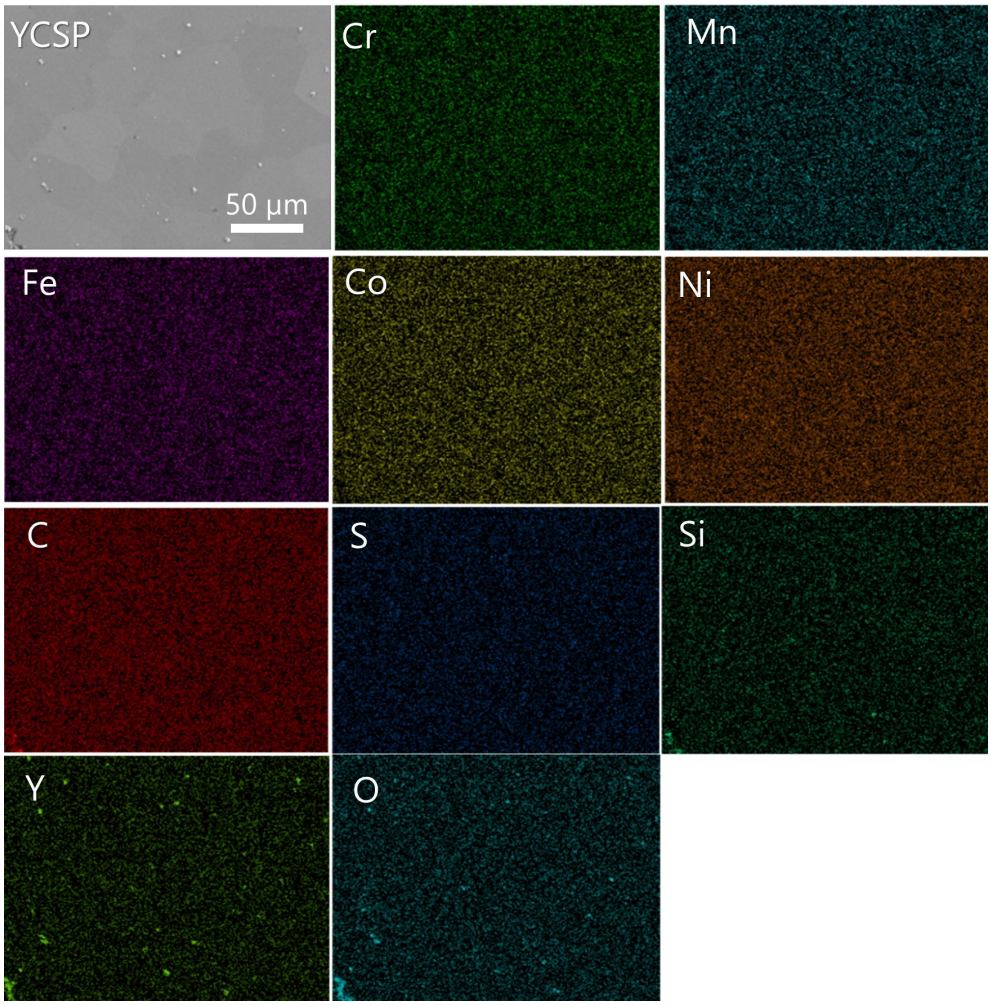


Figure 4.5: SEM image and the composition true maps (by SEM-EDS) from YCSP with five principal elements uniformly distributed. Scattered Y-oxides had an average size of 3.94 μm.

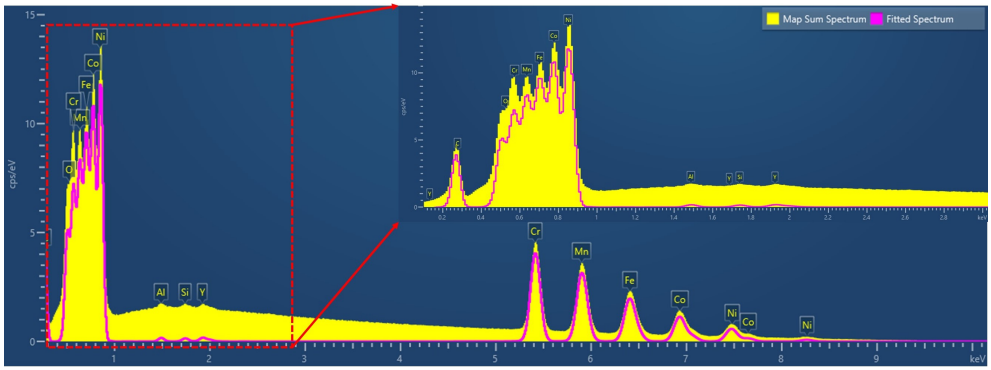


Figure 4.6: EDS spectrum with an enlarged spectrum in the inset based on SEM-EDS maps of YCSP. The magenta curve is the fitted spectrum.

Figure 4.7 shows a SEM image and SEM-EDS chemical composition true maps from CSW for Cr, Mn, Fe, Co, Ni, C, Si, O and S. Again, the metallic elements showed no resolvable micro-segregation; a few Si-based oxide inclusions were suggested.

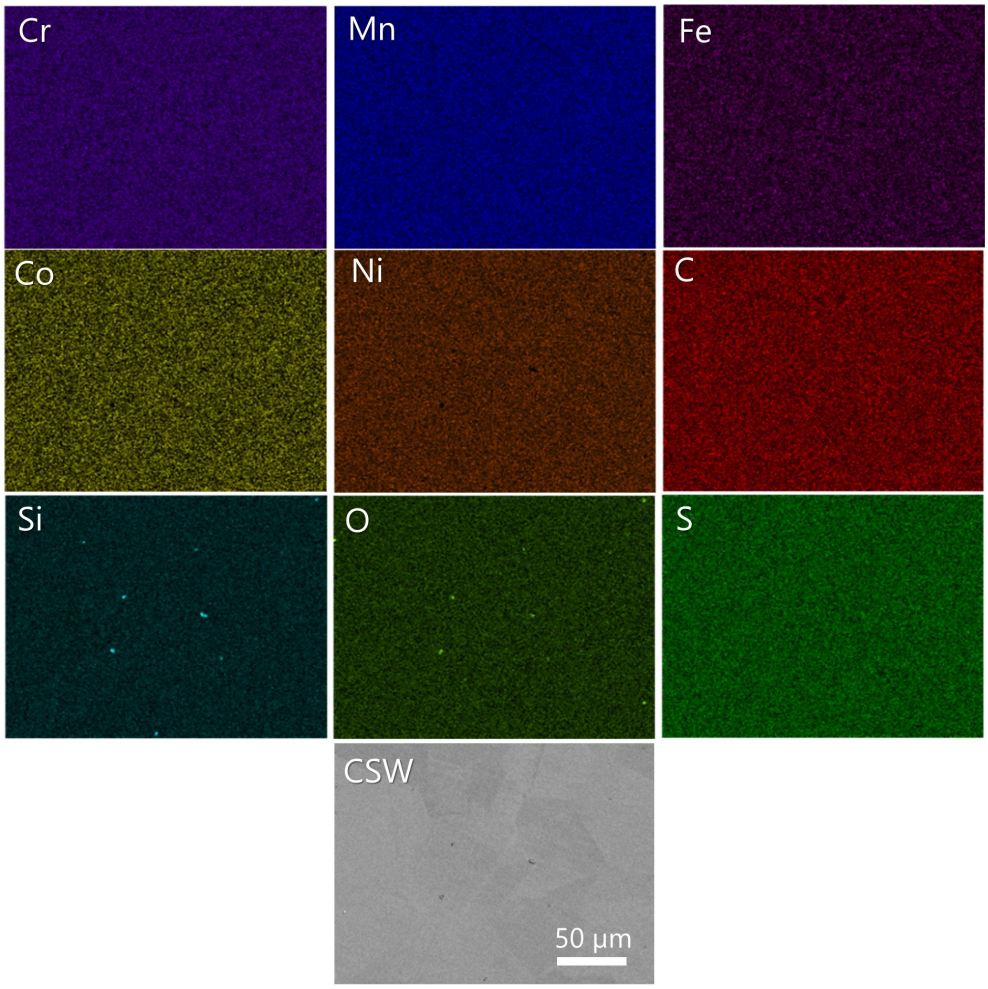


Figure 4.7: Composition true maps (by SEM-EDS) and SEM image of CSW with five principal elements uniformly distributed with a few Si-based oxide inclusions.

Figure 4.8 shows a SEM image and representative SEM-EDS chemical composition true maps from YCSW for Cr, Mn, Fe, Co, Ni, Y and O. No non-metallic inclusions and Y-oxides with average size of 425 ± 17 nm measured by SEM using ImageJ were observed. Y-based oxides formed during spray forming were apparently broken into smaller precipitates during the severe plastic deformation of swaging,[254] and some finer Y-based oxides may have formed during heat treatment, which likely inhibited grain growth during recrystallisation. As discussed in Chapter 3.3,

the measurement of the average size of Y-based oxide particles can be affected by the spatial resolution of SEM-EDS. It has been shown in a stainless steel (similar density and elements to the Cantor alloy) that detection limits (in diameter) for Al (Kα1=1.488 keV) and C (Kα1=0.28 keV) were <100 nm and <500 nm at 10 kV respectively.[229] With respect to Y (Lα1=1.923 keV) and O (Kα1=0.524 keV) in YCSW, it is likely that a spatial resolution of ∼100 nm might be achieved, suggesting credible identification of Y-based oxide particles >100 nm.

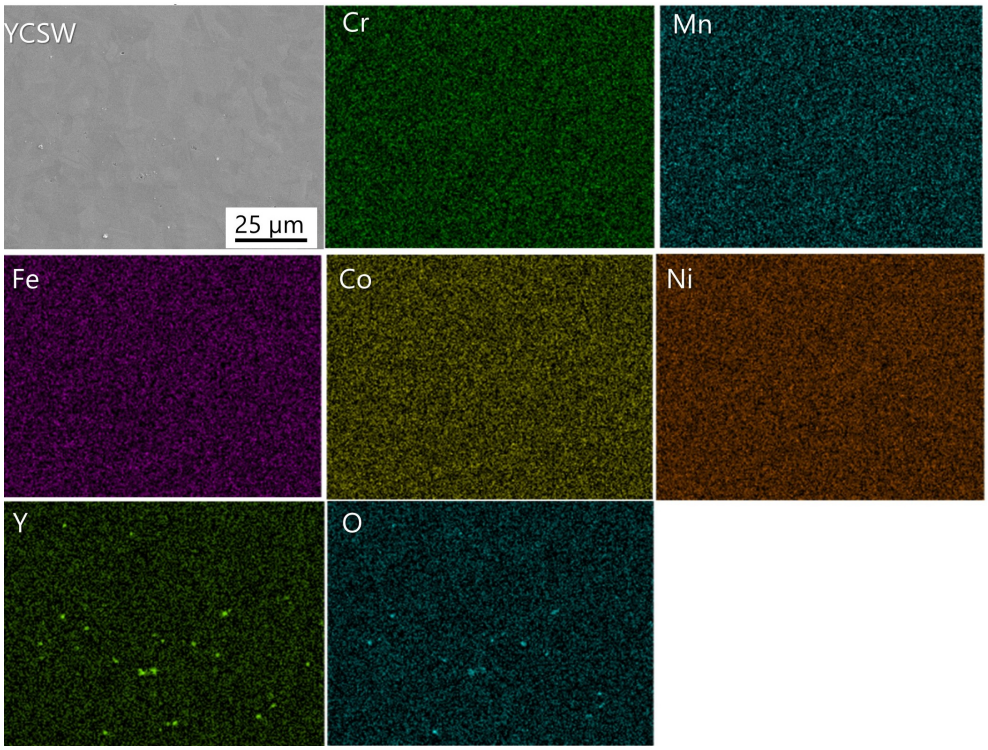


Figure 4.8: SEM image and the composition true maps (by SEM-EDS) from YCSW with five principal elements uniformly distributed. Y-oxides had an average size of 425 ± 17 nm.

Figure 4.9a and 4.9b are representative TEM bright-field (BF) images of CSP and as-swaged CSP, with SAED pattern from as-swaged CSP in the inset of Figure 4.9b. CSP was largely free of dislocations in the

as-sprayed condition and there were contours due to bending or uneven thickness of the TEM foil. In Figure 4.9b, a large number of dislocations marked by white circle were introduced into as-swaged CSP prior to heat treatment and the as-sprayed polygonal grains were elongated into thin lamella and then sheared to form ultrafine grains (a few hundred nanometers). The SAED shows an approximate ring pattern indexed as FCC with a lattice parameter of 0.356 nm. Figures 4.8c and 4.8d are BF and dark-field (DF) images of as-swaged YCSP, which better shows the elongated and then ultrafine grains and some of the grains showed strong contrast in BF mode due to severe strain retained in the as-swaged condition.

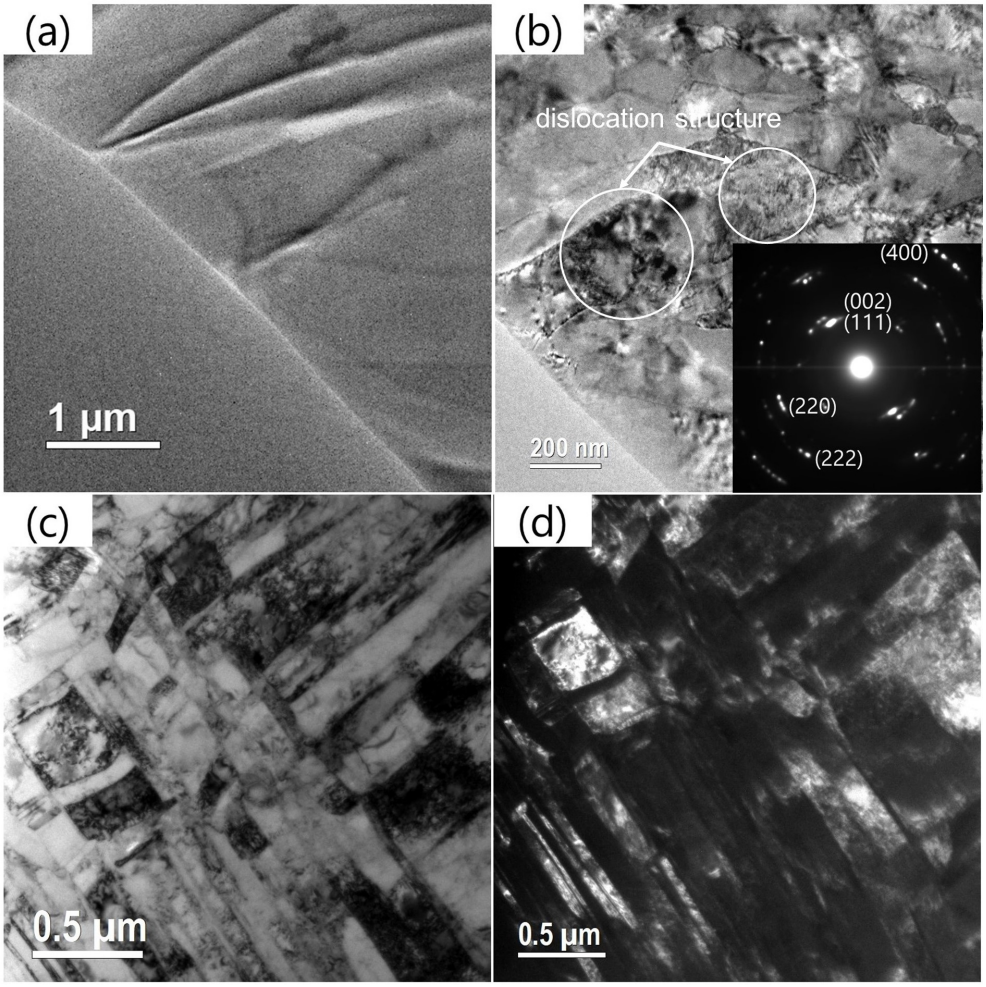


Figure 4.9: TEM BF images (a) CSP and (b) as-swaged CSP. (c,d) BF and dark-field (DF) images of as-swaged YCSP. (a) shows CSP was largely free of dislocations while (b) shows there were a large number of dislocations in as-swaged CSP and initial grains were sheared into ultrafine grains (a few hundred nanometers).

Figure 4.10 shows representative TEM BF images of CSW (Figure 4.10a and 4.10b) and YCSW (Figure 4.10c and 4.10d). Even after annealing for 1 h at 800℃, some dislocations marked by white arrows remained in CSW (Figure 4.10a). Occasionally, as shown in Figure 4.10b, there were secondary precipitate particles (identified as Cr-rich carbides) both along grain boundaries and within the grains. Details will be presented in Figure 4.11. Figure 4.10c shows dislocation entanglement around pre-

cipitates in YCSW and dislocation pinning by a particle is presented in Figure 4.10d. SAED analysis in the inset of Figure 4.10c shows FCC main phase and a secondary phase identified as Y_2O_3. Details of these Y_2O_3 or other oxides in YCSW are discussed in detail in Chapter 4.4.

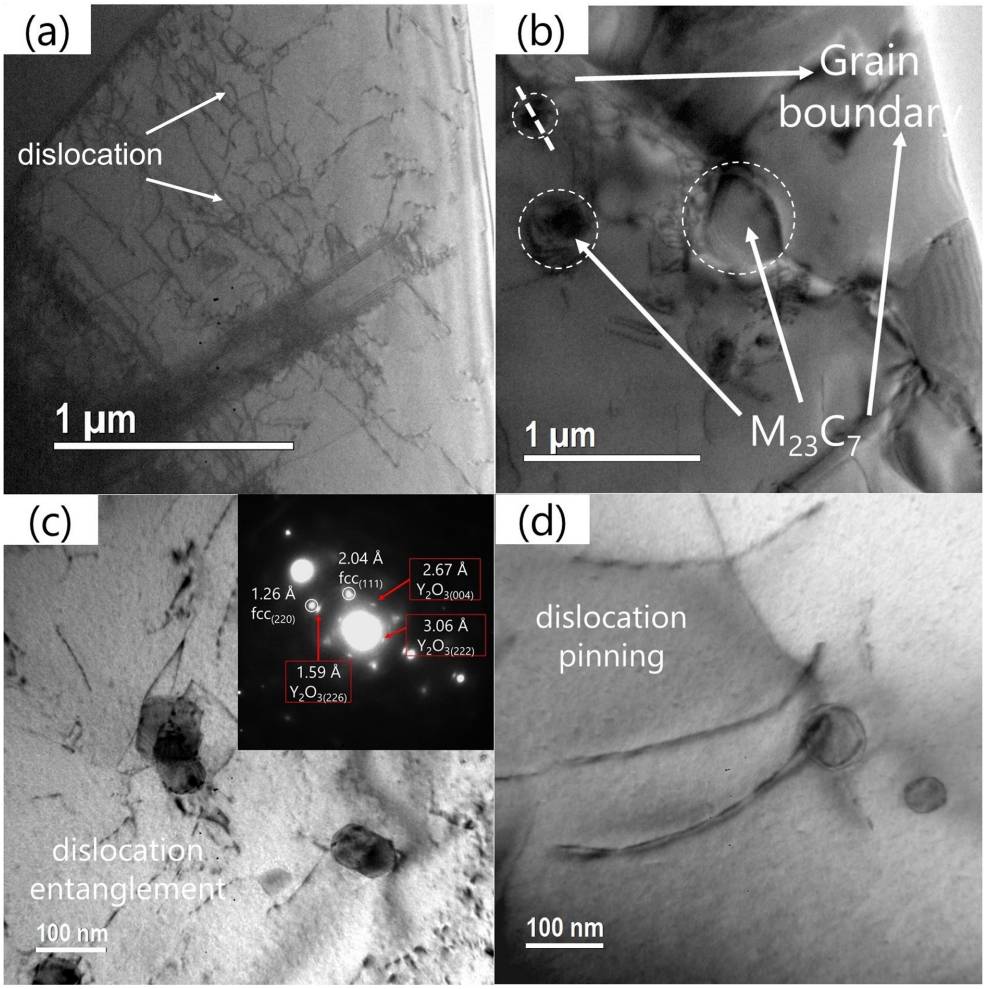


Figure 4.10: TEM BF images of the microstructure of (a,b) CSW and (c,d) YCSW. (a) Some dislocations marked by white arrows remained in CSW. (b) Precipitates in CSW both along grain boundaries and in grains. (c) and (d) Dislocation entanglement and dislocation pinning by particles in YCSW.

Figure 4.11a shows the SAED pattern of the region in Figure 4.10b, suggesting precipitates had FCC structure with a lattice parameter of ~1.06 nm, which is consistent with $M_{23}C_6$. The simulated SAED of

$M_{23}C_6$ in the inset of Figure 4.11a agreed well with the experimental results. Figure 4.11b shows STEM-EDS linescan profiles traversing a $M_{23}C_6$ particle marked by the dotted white line in Figure 4.10b, which confirmed Cr enrichment. The concentration of Cr and C approximately agrees with $Cr_{23}C_6$. Similar Cr-rich carbides were also observed by Pickering et al.[33] after heat treatment of Cantor alloy for 1000 h at 700°C, and again likely due to trace C in the starting alloy as well as pick-up during melting and dispensing. The formation of $M_{23}C_6$ carbides is also a common phenomenon occurring in austenitic steels during heat treatment,[255] which might cause hardening and embrittlement.

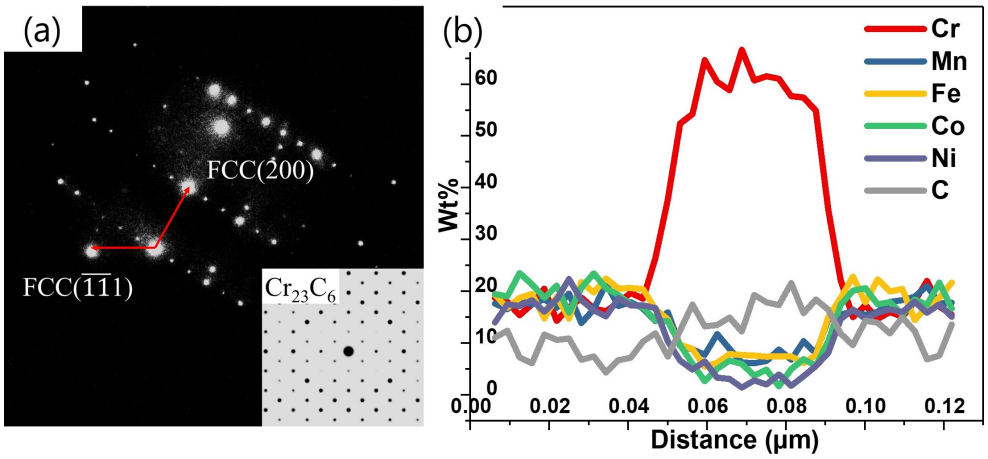


Figure 4.11: (a) SAED pattern of the region in Figure 4.10b with a simulated $Cr_{23}C_6$ SAED pattern in the inset. The experiment result was in agreement with $M_{23}C_6$ structure. (b) The line-scan profiles of a $M_{23}C_6$ particle, showing enrichment in Cr. The concentration of Cr and C approximately agreed with $Cr_{23}C_6$.

4.4 Oxide particles

Y has been suggested to react with internal O to form Y-based oxides.[123,256] The crystal structure and chemical composition of Y-based

oxides is now considered further. Figure 4.12 shows a STEM annular dark-field (ADF) image and STEM-EDS maps for Cr, Mn, Fe, Co, Ni, Y, C and O from YCSW. There were Y-based oxides, Cr-rich carbides and Cr-rich precipitates. Other than the precipitates, the five principal elements were uniformly distributed.

Figure 4.13 shows a STEM-ADF image containing some particles marked by white arrows with corresponding linescan profiles (Figure 4.13b-e) across the particles. The Y-based oxides contained metallic elements, which was artefacts due to the signal derived from the "matrix" underneath the particle when the TEM foil thickness (∼180 nm) was larger than the diameter of the particle of interest (∼100-150 nm). In addition, Y-based oxides may be non-stoichiometric and the ratio between Y and O was from 1:1.5 to 2:1 after subtracting the concentration of O due to possible oxidation of the foil. Note that at least five linescan profiles were measured in order to confirm the repeatability. Similarly, Cr-rich precipitates also exhibited varying concentrations of Cr which was either due to intrinsic compositional differences or artifacts derived from EDS signals in the matrix underneath.

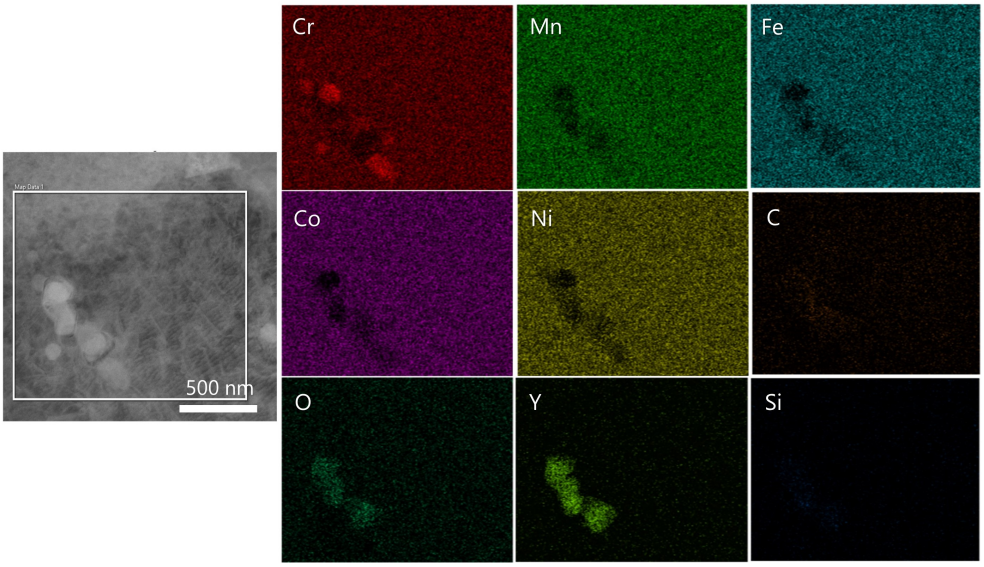


Figure 4.12: STEM-ADF image and compositional maps for Cr, Mn, Fe, Co, Ni, Y, C and O in YCSW, indicating Y-based oxides, Cr-rich carbides and Cr-rich precipitates.

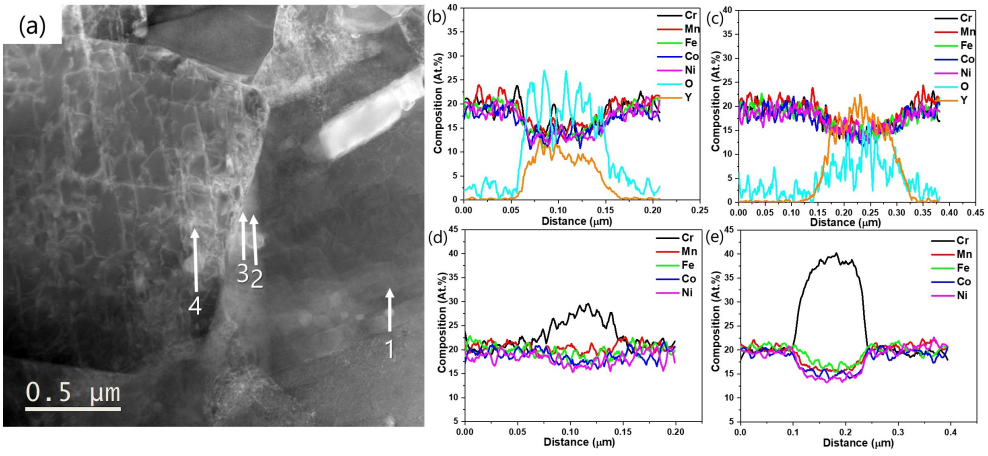


Figure 4.13: (a) STEM-ADF image containing some particles marked by white arrows and (b-e) corresponding STEM-EDS linescan profiles across four particles showing the detailed compositions of Y-based oxides and Cr-rich precipitates. In this figure, linescan 1 to 4 corresponds to (b) to (e) respectively.

Figure 4.14a shows a STEM-ADF image of YCSW containing several Y-based oxide particles with composition maps for Y and O below. Figure 4.14b shows a HRTEM image of the region marked by the white dotted square in one Y-based oxide particle with Fast Fourier Transform

(FFT) pattern in the inset. Ring patterns shown in the FFT indicated that the particle was nanocrystalline Y_2O_3. There were numerous sub-grains with size of a few nanometers shown in Figure 4.14b, some of which were marked by two parallel lines indicating the typical 3.06 Å spacing in Y_2O_3. Note that the secondary phases in YCSW could be compositionally complex, and exhaustive analyst is challenging using such fine-scale characterisation techniques like STEM and TEM. It can only be robustly concluded that Y reacted with internal oxygen and formed some Y_2O_3 particles, possibly as well as other Y-based oxides of differing composition.

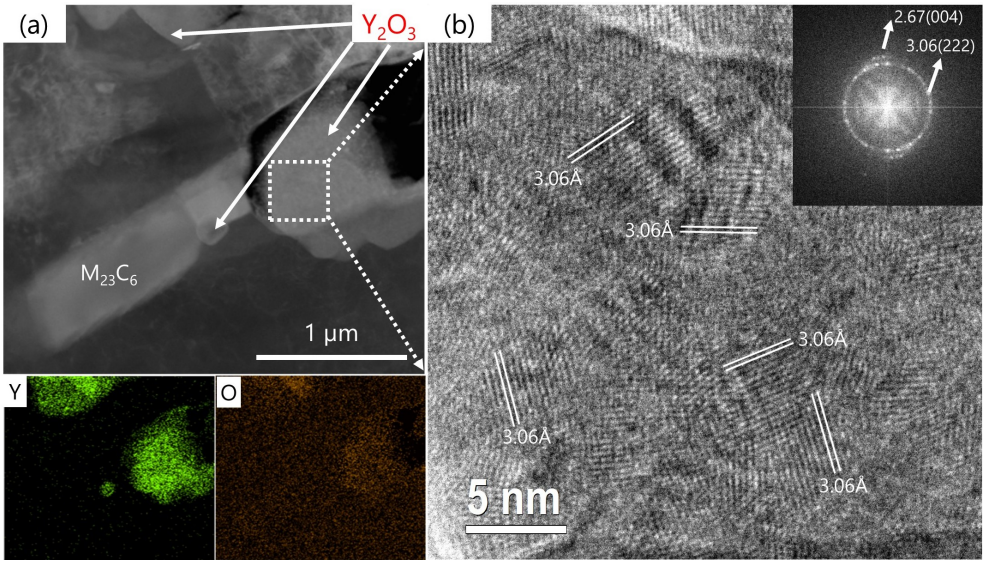


Figure 4.14: (a) STEM-ADF image of YCSW containing several Y-based oxide particles with composition maps for Y and O below. (b) HRTEM image of the region marked by white dotted square in one Y_2O_3 particle with the FFT pattern in the inset showing ring patterns identified as Y_2O_3.

Figure 4.15a and 4.15b show a TEM image of YCSW and SAED pattern in the region marked by white dotted circle. Figure 4.15c shows

a HRTEM image of the region close to the edge of the specimen with FFT pattern in the inset and Figure 4.15d shows the FFT pattern of the matrix marked by green dotted square whereas Figure 4.14e shows the FFT pattern of Y_2O_3 marked by red dotted square. For clearer illustration, the colour of frame for Figure 4.15d and 4.15e was set the same with the colour of mark in Figure 4.15c. Although the average size of Y_2O_3 particles were approximately 425 ± 17 nm according to previous characterisation results, these images and patterns suggested that there was also a population of finer Y-based oxide dispersoids of just a few nanometers.

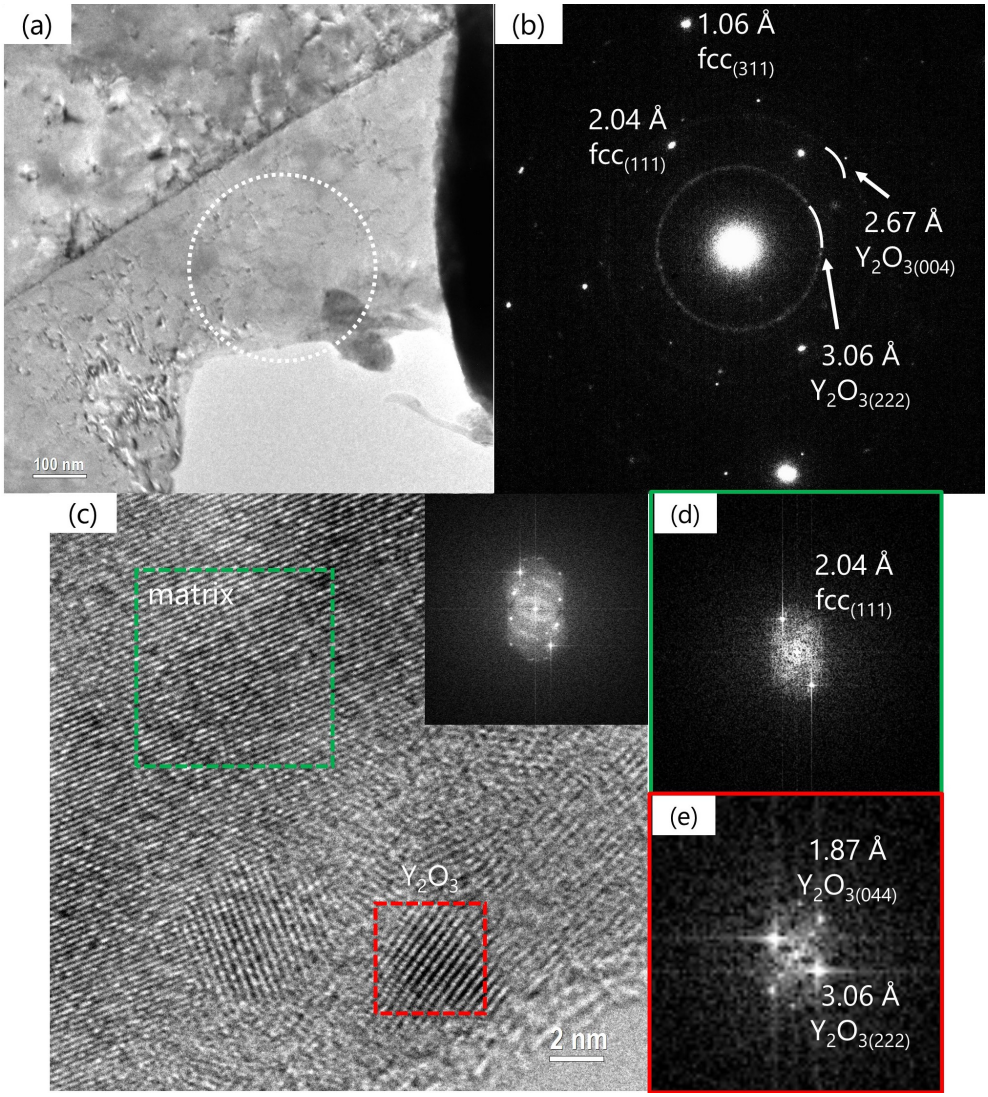


Figure 4.15: (a) TEM image of YCSW, (b) SAED pattern in the region marked by white dotted circle, (c) HRTEM image of the region close to the edge of the specimen with FFT pattern in the inset, showing the existence of nanosized feature, (d) FFT pattern of the region marked by green dotted square and labeled as matrix and (e) FFT pattern of the nanosized feature marked by red dotted square and labeled as Y_2O_3. For clearer illustration, the colour of frame for (d) and (e) was set the same with the colour of marks in (c).

As discussed earlier in Chapter 2.3, other ODS-HEAs were produced by the MA/SPS route. In general, Y_2O_3 was directly added during MA[139–141] whereas in one study[142] a small concentration of Y (1.2 wt%) was pre-alloyed with Cantor alloy powder before MA with the intention

that Y-based oxides would be formed through in-situ reactions during MA and SPS. The average size of Y-based oxides in the present work is larger than that reported in other studies (< 50 nm). Immediate pick-up of O by Y during melting before spray forming likely causes the formation of the relatively coarse Y-based oxides in this thesis. Y-based oxides in ODS-HEAs usually exhibited complex chemical compositions, including Y_2O_3, $YCrO_4$ and YMnNi-based oxides, which agrees with the varying compositions of Y-based oxides observed in the present study.

4.5 Conclusions

CSP, YCSP, CSW and YCSW exhibited a single phase grain structure with the five principal elements uniformly distributed, even at high resolution analysis. There was a very low volume fraction of non-metallic inclusions in CSP, possibly due to impurities in the feedstock materials and/or contamination during vacuum induction casting, which is somewhat inevitable for bulk melt processing of commercial purity materials using refractory ceramics. The average grain size for CSP, YCSP, CSW and YCSW was 48.5, 22.3, 8.2 and 5.4 μm. The advantages of solidification by spray forming led to a refined equiaxed, polygonal (i.e. dendrite-free) grain structure, even in billets up to 15 kg, and distinct from columnar/dendritic morphologies and associated micro-segregation obtained in as-cast billets by arc melting and vacuum induction melting.

The addition of Y significantly refined grains, principally by reacting

with internal oxygen and forming pinning oxide particles. A low incidence of Cr-rich carbides with structure of $M_{23}C_6$ formed and were likely due to trace C in the starting alloy as well as pick-up during melting and dispensing. The average size of Y-based oxides was 425 ± 17 nm and some of the Y-based oxide particles were identified as nanocrystalline Y_2O_3 although there were many Y-based oxides of different composition. Along side the large Y-based oxides, there were also likely Y_2O_3 dispersoids of a few nanometers in YCSW.

5 Mechanical behaviour of CrMnFeCoNi-(Y)

In this chapter, the hardness of CSP, YCSP, CSW and YCSW by nanoindentation is first presented, followed by the discussion on tensile properties and strengthening mechanisms of CSW and YCSW at -196℃ and 23℃. Tensile properties of the alloys in the present study are compared with Cantor alloys made by other techniques and other ODS-Cantor alloys. Lastly, deformation behaviour at -196℃, particularly twinning deformation of CSW and YCSW is discussed using post-mortem characterisation.

5.1 Nano-hardness

Figure 5.1 shows hardness as a function of displacement for CSP, YCSP, CSW and YCSW where the error bar represents the standard deviation. The average hardness was calculated from data at a depth of 400-2000 nm, giving 2.47, 2.88, 3.12 and 3.44 GPa for CSP, YCSP, CSW and YCSW respectively. The increasing trend was expected due to decreasing grain size (48.5, 22.3, 8.2 and 5.4 μm for CSP, YCSP, CSW and YCSW respectively), consistent with a Hall-Petch relationship $\sigma_y = \sigma_0 + k_y d^{-1/2}$, where k_y is the strengthening coefficient, d is the grain size and σ_0 is a materials constant for the resistance of the lattice to dislocation motion. Figure 5.2 shows hardness as a function of $d^{-1/2}$ for

the four alloys. According to a best fit line, k_y=3.082 GPa $\cdot$ μm$^{-1/2}$ and σ_0=2.104 GPa. The hardness of CSP was similar to the nano-hardness ($\sim$2.3 GPa) of coarse-grained Cantor alloys reported by Maier et al.[257] The values of k_y and σ_0 were higher than the values obtained by Liu et al.[258] using Vickers micro-hardness measurements (k_y=676 MPa$\cdot\mu$m$^{-1/2}$ and σ_0=1227 MPa), possibly due to the well-known indentation size effect.[259]

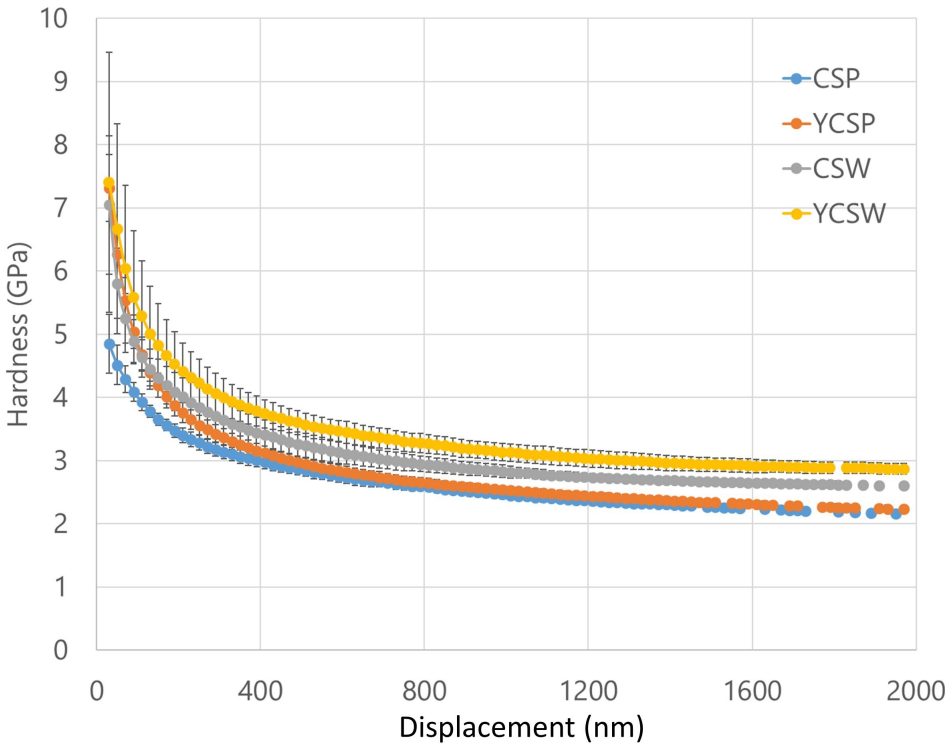


Figure 5.1: Hardness (GPa) as a function of displacement (nm) for CSP, YCSP, CSW and YCSW with standard error bar.

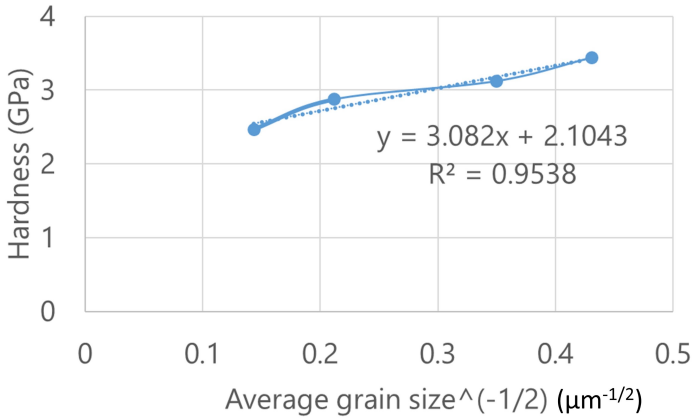


Figure 5.2: Hardness as a function of $d^{-1/2}$ (d = the average grain size) for CSP, YCSP, CSW and YCSW with linear best-fit line.

Figure 5.3 shows the elastic modulus as a function of displacement for CSP, YCSP, CSW and YCSW with standard error. Similarly, the average modulus was calculated from data at a depth range of 400-2000 nm, which was 201.0, 195.2, 206.8 and 223.4 GPa for CSP, YCSP, CSW and YCSW respectively. Laplanche et al. reported an elastic modulus measured by the resonant frequency technique in bending mode of 203 GPa for a Cantor alloy with average grain size of 15±5 μm,[58] similar to CSW with an average grain size of 8.2 μm.

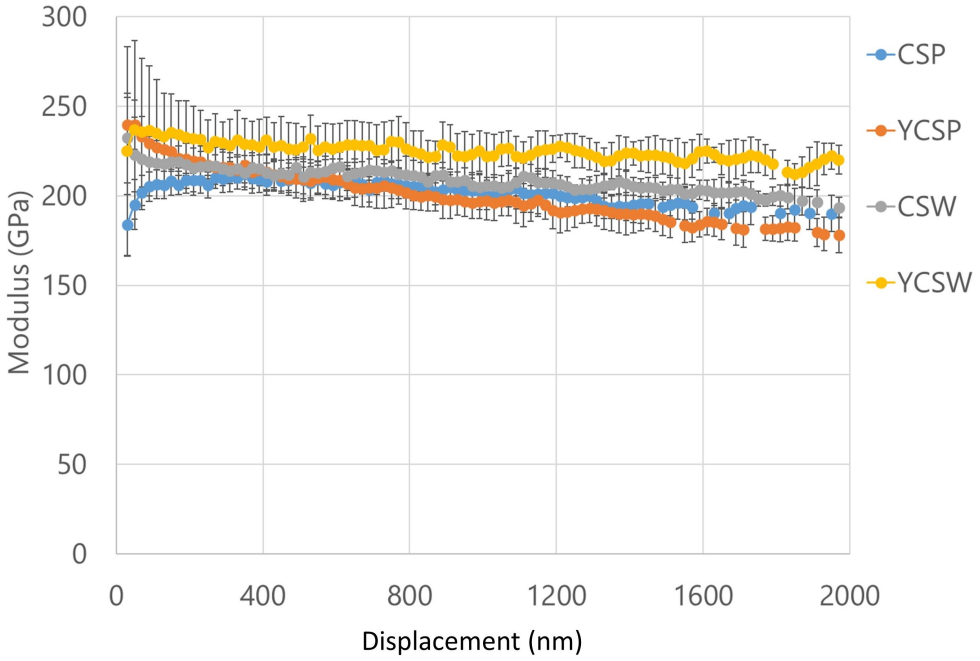


Figure 5.3: Modulus (GPa) as a function of displacement (nm) for CSP, YCSP, CSW and YCSW with standard error.

5.2 Tensile properties at -196℃ and 23℃

5.2.1 Grain boundary strengthening

CSP, CSW and YCSW were tensile tested at -196℃ and 23℃ at a strain rate of $1 \times 10^{-3}\text{s}^{-1}$. Table 5.1 shows the average yield strength σ_y, ultimate tensile strength σ_{uts} and fracture elongation ε of CSP, CSW and YCSW at -196℃ and 23℃.

Table 5.1: The average yield strength σ_y, ultimate tensile strength σ_{uts} and fracture elongation ε and standard deviation for CSP, CSW and YCSW at -196℃ and 23℃.

		σ_y (MPa)	σ_{uts} (MPa)	ε (%)
-196℃	CSP	489±1	1027±6	71±1.4
	CSW	623±1	1204±5	53±4.2
	CYSW	723±2	1261±4	56±2.3
23℃	CSP	209±4	584±1	61.3±1.8
	CSW	387±2	712±1	42.8±1.1
	CYSW	430±2	757±2	38±1.3

Yield strength showed a dependence on $d^{-1/2}$ and Figure 5.4 plots σ_y as a function of $d^{-1/2}$ at -196℃ and 23℃ for CSP, CSW and YCSW with the best-fit line shown in red dashed line for the present study (red marks), together with the data and best-fit lines of Cantor alloys with grain sizes ranging from 4.4 μm to 155 μm (black marks) from Otto et al.,[16] and alloys with average grain sizes from 500 nm to 90 μm (blue line) from Sun et al.[66]

Best-fit values gave k_y= 789.3 ± 74.0 MPa · μm$^{-1/2}$ and σ_0= 99.1 ± 24.4 MPa. The strengthening coefficient was higher than the available data reported by Otto et al.,[16] Sun et al.[66] and that for 304 stainless steel[260] considering the scattering error. Moreover, other strengthening mechanisms apart from grain boundary strengthening may contribute to the overall yield strength. For instance, carbides in CSW and Y-based oxides in YCSW may provide precipitate hardening. Thus, the Hall-Petch relationship obtained in Figure 5.4 may be problematic as the microstructure was different excluding different grain size.

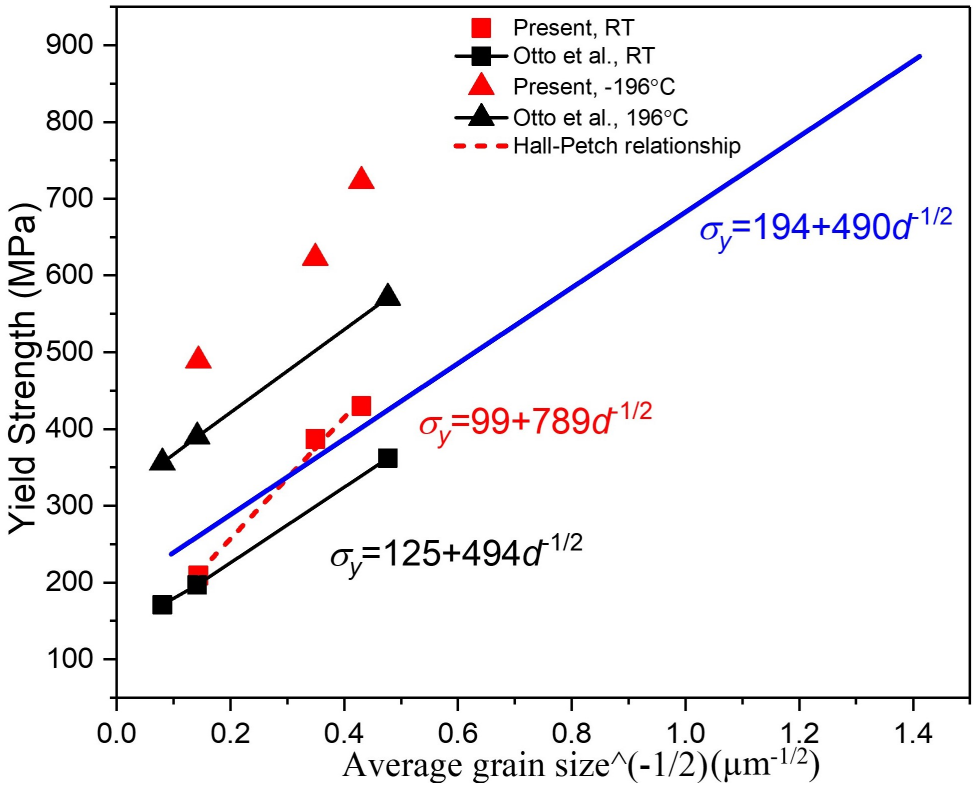


Figure 5.4: Tensile yield strengh as a function of $d^{-1/2}$ (d = the average grain size) for CSP, CSW and YCSW with best-fit line (red marks) as well as data and best-fit lines for Cantor alloys taken from Otto et al. and Sun et al.[16,66]

5.2.2 Comparison of Cantor alloy tensile properties

Figure 5.5 shows σ_y and ε as a function of $d^{-1/2}$ (d = the average grain size) at room temperature from this study and various literature resources. There is significant scatter in the data, particularly for elongation to failure which is sensitive to microstructural flaws, but approximately, σ_y increases with $d^{-1/2}$.

Both CSW and YCSW alloys marked by red squares locate in the region of comparatively well-balanced strength and ductility for their average grain size (red dotted box). CSP had similar properties to Can-

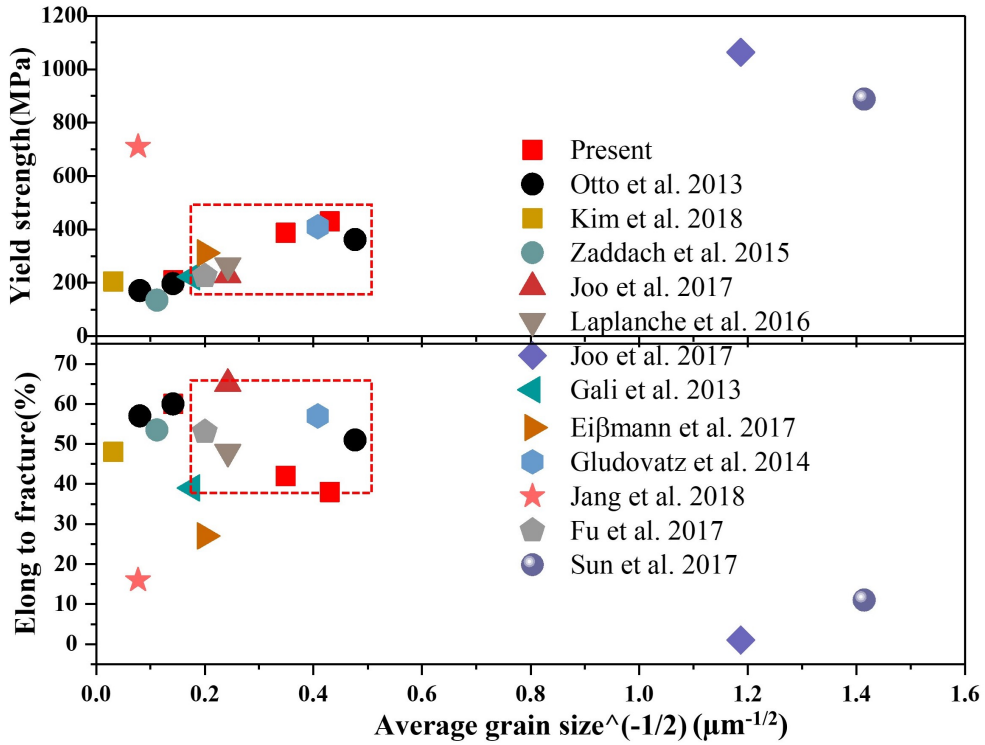


Figure 5.5: Yield strength σ_y (upper axis) and elongation to fracture ε (lower axis) as a function of $d^{-1/2}$ (d = the average grain size) at room temperature for Cantor alloys fabricated using different techniques. The data is taken from the work of Otto et al. (2013),[16] Kim et al. (2018),[36] Zaddach et al. (2015),[56] Joo et al. (2017),[81] Laplanche et al. (2016),[34] Joo et al. (2017),[69] Gali et al. (2013),[89] Eißmann et al. (2017),[70] Gludovatz et al. (2014),[9] Jang et al. (2018),[76] Fu et al. (2017)[82] and Sun et al. (2017).[66]

tor alloys with similar grain sizes which were made by arc-melting, cold rolling and then heat treatment (black circles). However, the spray-formed Cantor alloy was available in considerably large billets, and gave competitive properties even in the as-sprayed condition due to its refined microstructure and exceptional microstructural homogeneity. As expected, CSW and YCSW showed higher strength but with a reduction in ductility, likely due to the hindrance of dislocation movement from second phase precipitates, especially carbides in CSW and Y-based oxides in YCSW.

As shown earlier in Figure 2.5, yield strength and elongation to fracture of the Cantor alloy have a strong dependence on temperature, increasing with decreasing temperature. Figure 5.6 compares tensile properties at -196℃ of Cantor alloys in the present study and from the literature, again as a function of $d^{-1/2}$. The σ_y, σ_{uts} and ε are marked by solid squares, solid circles and half hollow triangles with arrows pointing towards the right y-axis. Although carbides and Y-based oxides might hinder dislocation motion, CSW and YCSW still exhibited elongation to fracture of 53% and 56% respectively as shown in Figure 5.6.

Linear best-fit lines to the yield strength for CSP, CSW and YCSW at -196℃ are shown in black with k_y=783 $\pm$ 128 MPa $\cdot$ μm$^{-1/2}$ and σ_0=370 $\pm$ 42 MPa. The value of k_y is slightly higher than Otto et al.[16] (538 MPa $\cdot$ μm$^{-1/2}$) while the intercept was similar considering error, which suggested a higher strengthening in spray-formed alloys, possibly due to refined equiaxed,

polygonal grain structure and microstructural homogeneity. As mentioned earlier, unlike Otto's work in which grain size was the only variable, other strengthening mechanism apart from grain boundary strengthening may contribute to the overall yield strength in the present study.

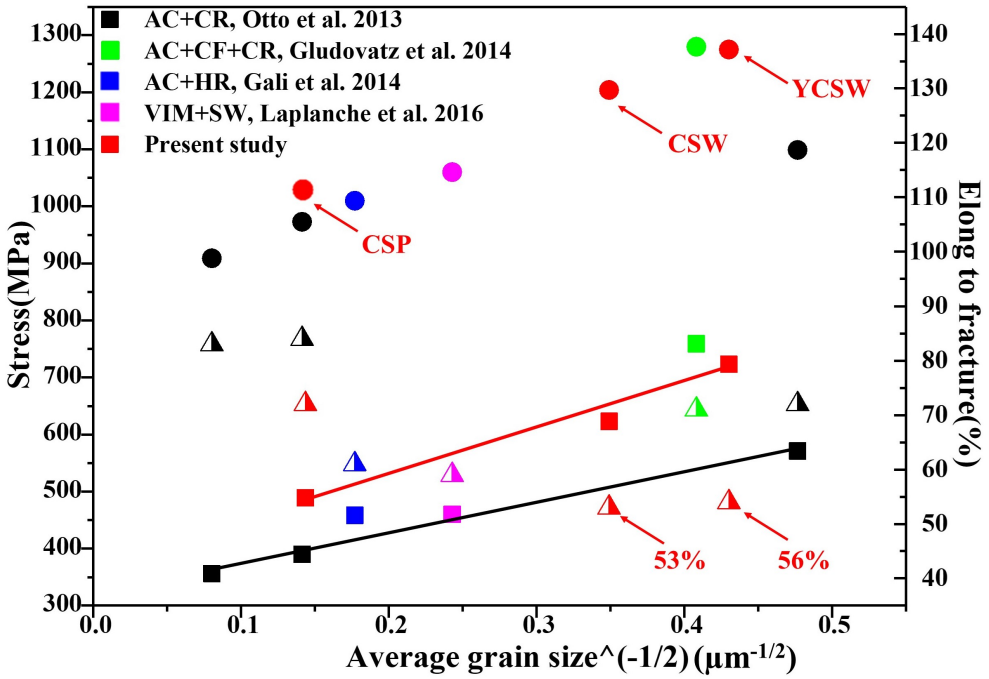


Figure 5.6: Average yield strength σ_y, ultimate tensile strength σ_{uts} (left y axis) and elongation to fracture ε (right y axis) as a function of $d^{-1/2}$ (d = the average grain size) of Cantor alloys from the literature and the present study at -196°C. σ_y, σ_{uts} and ε are marked by solid squares, solid circles and half hollow triangles with arrow. Linear best-fit lines to yield strength and ultimate tensile strength as a function of $d^{-1/2}$ are shown in black. AC (as-cast); CR (cold-rolled); HR (hot-rolled); CF (cold-forged); SW (swaging) and VIM (vacuum induction melting). The data is taken from the work of Otto et al. (2013),[16] Gludovatz et al. (2014),[9] Gali et al. (2013)[89] and Laplanche et al. (2016).[34]

5.2.3 Other strengthening mechanisms

It is well-known that there are several approaches for increasing the yield strength of metals and alloys and the most commonly used are work hardening (σ_{di}) determined by the dislocation density, solid solution

strengthening (σ_{ss}), grain boundary strengthening (σ_{gb}) and precipitation hardening (σ_{ppt}).[261]

It has been shown that CSP, CSW and YCSW all remained single FCC phase with the five principal elements homogeneously distributed even when analysed using STEM-EDS characterisation. For simplicity, it is assumed that solid solution strengthening is the same for four alloys given there is only a single solid solution microstructure here in all cases. Dislocation strengthening (σ_{di}) is quantified using the Bailey-Hirsch relationship:[262]

$$\sigma_{di} = M\alpha Gb\sqrt{\rho} \tag{5.1}$$

where $M = 3$ is the Taylor factor for polycrystalline materials, α is a material dependent constant, G=80 GPa is the shear modulus,[58] ρ is dislocation density and b is Burgers vector. $b = \frac{a}{2}\sqrt{h^2 + k^2 + l^2} = 0.255$ nm, where $a = 0.360$ nm is the lattice parameter, $h = k = 1$ and $l = 0$ in the FCC lattice.

Dislocation density is related to peak broadening in X-ray diffraction experiments and can be measured by FWHM according to the modified Williamson–Hall relationship[263] which has often been adopted to obtain relative crystallite sizes and strains. Figure 5.7 shows enlarged XRD patterns from Figure 4.1 for all four alloys. After Rietveld refinement analysis, there was no clear difference in the crystalline size and FWHM among the four alloys. Furthermore, the characterisation results shown earlier suggested a low dislocation density and a fully recrystallised grain

structure in the case of the swaged and annealed alloys.

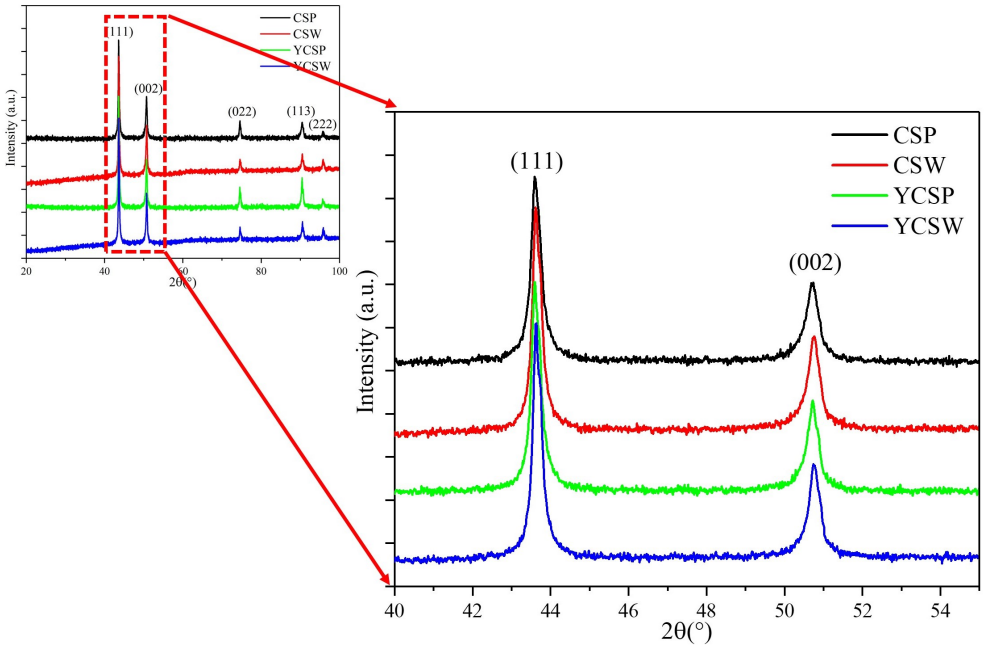


Figure 5.7: Enlarged X-ray diffraction patterns from 40 to 58° for CSP, CSW, YCSP and YCSW.

As for precipitation hardening, dislocations can either shear precipitates or bypass them depending on the average size of precipitates and interface relationship.[7] Orowan bowing occurs when the obstacle is impenetrable, whereas shearing occurs when dislocations interact with penetrable soft obstacles.[264] Assuming a dispersed barrier model which can be described by the following equation:

$$\sigma_{ppt} = 0.8M\alpha(r)Gb/\lambda \tag{5.2}$$

where $\alpha(r)$ denotes the shear strength of the obstacle and λ is the center-

to-center spacing between particles. $\alpha(r)$ is given by

$$\alpha(r) = -0.017 + 0.374log\frac{d}{4b} \tag{5.3}$$

where d is the average diameter of particles. λ can be expressed as:

$$\lambda = \sqrt{\frac{2}{3}}(\sqrt{\frac{\pi}{4f}} - 1)d \tag{5.4}$$

where f is the particle volume fraction. For YCSW, the average size of Y-based oxides (d) was 425$\pm$17 nm (assuming spherical shape), obtained from SEM images. The volume fraction (f) was estimated from the area fraction of Y-based oxides using Delesse's principle[265,266] as 0.307$\pm$0.02%. The Delesse's principle is commonly used in stereology and is based on a cube containing only one component of irregular objects embedded in a matrix, which provides an unbiased estimate of VV based on the estimate of AA on unbiased sections.[267] Consequently, $\alpha(r)$, λ and corresponding σ_{ppt} were estimated as 0.96, 5.2 μm and 9.06 MPa, respectively. Note this assumes the possible contribution of ultra-fine oxides $<$ 10 nm is ignored, because it was not possible to quantify them robustly.

Assuming Y-based oxides as hard precipitates ($\alpha(r)$=1), the increase in strength due to the Orowan bypass mechanism (σ_{Orowan}) can be estimated from:

$$\sigma_{Orowan} = \frac{0.4MGb}{\pi\sqrt{1-v}} \cdot \frac{ln\frac{d}{b}}{\lambda} \tag{5.5}$$

where v is the Poisson's ratio = 0.263.[93] σ_{Orowan} was estimated as 12.9

MPa. From Equation 5.3, $\alpha(r) = 0.96$, which is typical for hard precipitates,[264] indicating the Y-based oxides can be considered as "hard" precipitates. This is in agreement with TEM observation that Y-based oxides caused dislocation pinning and entanglement, for example as shown earlier in Figure 4.10.

Precipitate hardening by Y-based oxides was relatively small at 9.06 MPa and it can be implied that the main strengthening mechanism in CrMnFeCoNi-(Y) was grain boundary strengthening. This arises because Y-based oxides was 425 ± 17 nm, relatively coarse compared with conventional ODS alloys where oxides are generally in the range of 10–40 nm.[131,132]

5.2.4 Comparison with other ODS HEAs

As mentioned in Chapter 2.3, several studies have reported tensile properties of ODS-Cantor alloys.[140–143] Figure 5.8 summarises elongation to fracture (%) as a function of yield strength (MPa) for CSW, YCSW and other ODS Cantor alloys[140–143] and commercial ODS steels.[147–154]

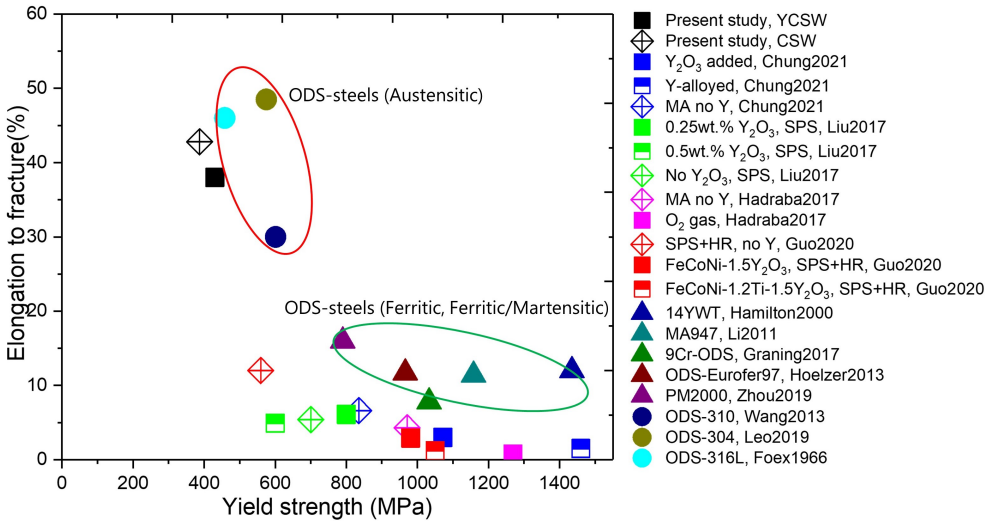


Figure 5.8: Elongation to fracture (%) as a function of yield strength (MPa) for CSW, YCSW and other ODS Cantor alloys[140–143] and commercial ODS steels.[147–154] ODS steels with austensitic structure are marked by solid circles whereas ODS steels either with ferritic or ferritic/martensitic structure are marked by solid triangles. ODS Cantor alloys are marked using solid squares and half solid squares whereas the corresponding Cantor alloys without yttrium's addition are marked by diamonds.

CSW and YCSW performed similarly to austenitic ODS steels with a yield strength $>$ 400 MPa and ductility $>$ 30%. Other ODS Cantor alloys, largely produced by MA+SPS had high strength ($>$ 800 MPa) but with limited elongation ($<$ 5%). ODS steels with ferritic (F) or ferritic/martensitic (F/M) structure, shown in the green oval-shaped circle, usually had high strength ($>$ 800 MPa) and intermediate elongation ($<$ 20%). Other ODS Cantor alloys had high strength ($>$ 800 MPa) but their relative brittleness compared with ODS steels undermines their practical usability.

Overall, tensile properties of YCSW lie in the region of balanced intermediate strength and ductility. Using dissolved Y, its subsequent reac-

tion/precipitation with oxygen was successfully realised in spray forming for the first time and ∼15 kg billets was fabricated by a casting and scalable route. However, in terms of properties, the Y-based oxides contribution to tensile properties was small because of coarse size and low volume fraction. Nonetheless, there was some suggestion of a population of smaller Y-based precipitates (<10 nm), and future work might explore how to develop this fraction further. In that case, it would represent a significant development in scalability in ODS alloy processing.

5.3 Deformation behaviour of CrMnFeCoNi-(Y)

To gain a greater mechanistic understanding of the deformation behaviour of CrMnFeCoNi-(Y), post-mortem characterisation on fractured tensile specimens was performed. Figure 5.9a displays a SEM image in the longitude direction of CSW fractured sample at -196℃ parallel to TA indicated by the black arrow. EBSD analysis was performed at the necking region (N) and the middle region (M), 3 mm from region N. Figures 5.9b and 5.9c show the corresponding IPF and image quality (IQ) maps overlay from M and N respectively, with texture information given in the inset. The starting equiaxed grains were severely elongated parallel to TA. Null points in the map were due to the roughened surface or very high dislocation densities. As Figures 5.9b and 5.9c show, there was a strong ⟨111⟩ and moderate ⟨001⟩ texture, which is typical of FCC materials after tensile deformation.[117]

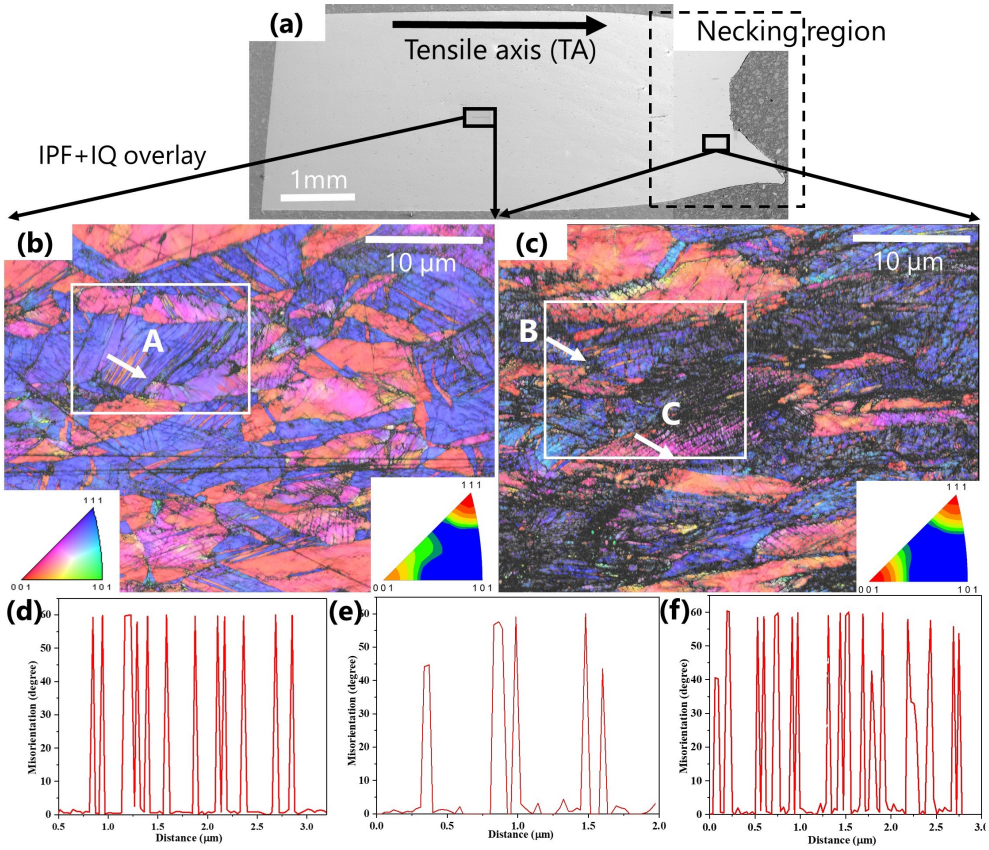


Figure 5.9: (a) SEM image of the longitude section parallel to TA indicated by black arrow of CSW tensile fractured specimen at -196°C and the necking region was selected by black dotted box. Two regions, marked by black squares, one from the necking region (region N) and one from the region 3 mm away from region N (region M) were further investigated. (b) and (c) EBSD maps of region M and region N shown in (a) with coloured scale bar and stereographic triangle showing a strong ⟨111⟩ and a moderate ⟨001⟩ deformation texture inserted below. (d), (e) and (f) Misorientation profiles (point-to-point) of three white arrows crossing several twin boundaries marked by A, B and C in (b) and (c), which clearly shows deformation nano-twinning within each grain.

In order to obtain an approximate strain level in M and N, a finite element model (FEM) was established with details shown in Chapter 3.6.2. The geometry of the failed specimen was shown in Figure 5.9a and the model geometry shown in Figure 5.10. Stress concentrated in the necking zone (region N). The primary component σ_{axis} in this region was several times higher than the non-necking area (region M). It is assumed

that the strain component ϵ_{axis} was proportional to $(\frac{1}{r})^2$ where r is the radius as $\epsilon_{11} + \epsilon_{22} + \epsilon_{33} = 0$ in metallic materials.[268] The calculated axial strain ϵ_{axis} in region N was twice that of region M, consistent with stress concentration shown in Figure 5.10.

Figures 5.9d, 5.9e and 5.9f show misorientation profiles (point to point) as a function of distance for three lines crossing several grain boundaries marked by white arrows A, B and C respectively. There were many nano-deformation twins with relative misorientation of 60° in grains oriented close to ⟨111⟩ ∥ TA, both in region M and N. Grains oriented close to ⟨001⟩ ∥ TA, shown red in Figures 5.9b and 5.9c, were generally twin-free at the available spatial resolution. Nonetheless, there were some exceptions, with very narrow twins of width of a few tens of nanometres. A typical example was shown in Figure 5.9f.

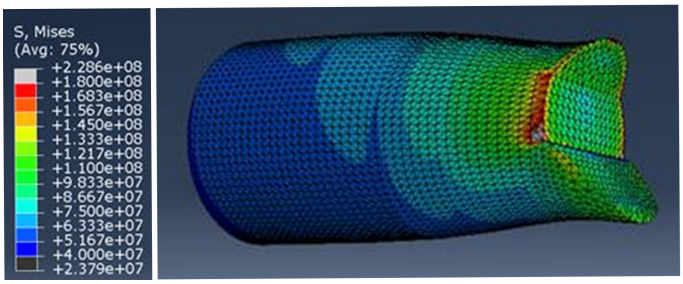


Figure 5.10: Finite element analysis of the von Mises stress stress distribution in the fractured CSW specimen shown in Figure 5.9.

In single FCC crystals, twinning can occur during tension in grains rotated towards ⟨111⟩ ∥ TA due to their comparatively high Schmid factor ($m = \cos\phi\cos\lambda$, where λ and ϕ are the angles between the load axis and the twinning plane normal and shear direction, respectively.)[269] For polycrystalline TWIP steels, grains orientated close to ⟨111⟩ ∥ TA

generally favoured twinning whereas grains with orientation close to ⟨001⟩ ∥ TA normally remained twin-free until failure.[117] This tendency was also readily observed in the Cantor alloy[81,118] as discussed in Chapter 2.2.5.

Apart from the twinning dependence on crystal orientation and texture, the activation of different twin systems in grains with different orientations and strains was investigated. Figures 5.11a and 5.11b show the overlay of enlarged IPF and IQ maps for two regions marked by rectangular white boxes in Figure 5.9b and 5.9c. Several grains, each with different orientation, were selected to compare the twinning behaviour in region M and N in detail. Figure 5.11c shows the {111} pole figures and inverse pole figures corresponding to the grains in Figures 5.11a and 5.11b marked by capital letters A to H. M and T represent the matrix and twinned grain and in some cases, such as Grain F and G, there were two twin variants marked as T1 and T2. The colour of traces are the same as the colour of letters and X0 is parallel to TA.

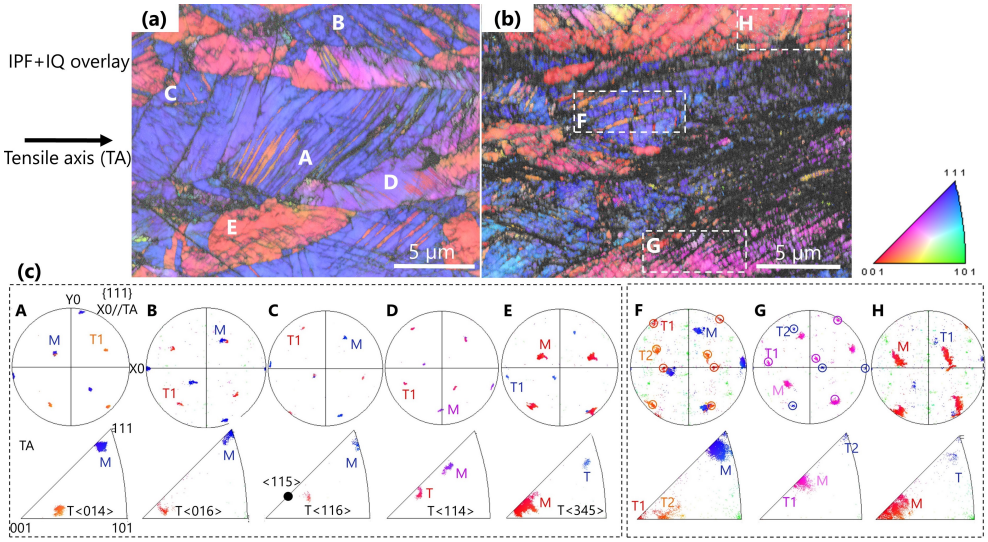


Figure 5.11: (a) and (b) Orientation maps and band contrast overlay of regions marked by the white squares in Figures 5.9b and 5.9c with TA on the left and colour scale on the right. Grain subdivision by twin-twin intersection was clearly observed in (b). (c) Pole figures and inverse pole figures of several grains, marked by white capital letters A to H in (a) and (b) showing the orientation relation between the matrix (M) and twins (T). In some cases, such as Grain F and G, two twin variants were observed and marked as T1 and T2. The colour of traces are the same with the colour of letters and X0 is in parallel with TA.

In region M, only one twin variant was activated in all grains, even in grains close to ⟨111⟩ ∥ TA, which are prone to twinning. Grains in which twinning was favoured, such as Grain A, B and C, likely developed twins with ⟨014⟩ or ⟨116⟩ orientations. Grains oriented to ⟨112⟩ ∥ TA, such as Grain D, developed twins with ⟨114⟩ orientation. Grains oriented close to ⟨001⟩ ∥ TA direction, such as Grain E, developed twins close to ⟨111⟩ ∥ TA orientation. The average width and density of twins in grains oriented to ⟨111⟩ ∥ TA was one magnitude larger than grains oriented ⟨001⟩ ∥ TA.

At low temperature, the adjustment in the grains and at grain boundaries to accommodate plastic deformation is limited, and the activation

of dislocation motion would largely be affected by the local stress intensity.[115,117] In this case, the onset of deformation twinning in grains ⟨001⟩ ‖ TA was likely derived from local stress concentrations due to the accumulation of high density of dislocations from neighbouring grains.[115,117] As seen in Grain D and E, twins developed from the grain boundaries (usually neighboured with a grain oriented close to ⟨111⟩ ‖ TA) where strain was localised.

In region N, within the necking region and where the strain was approximately two times higher than in region M, two twin variants were activated in grains close to ⟨111⟩ ‖ TA orientation, shown as Grain F. Similar to region M, Grain F also developed twins with ⟨001⟩ and ⟨016⟩ orientations. Grains close to ⟨113⟩ ‖ TA, shown as Grain G, also developed two twin variants, one with ⟨111⟩ ‖ TA orientation and the other with ⟨115⟩ ‖ TA orientation. In grains close to ⟨001⟩ ‖ TA where twinning is restrained, shown as Grain H, only one twin variant with ⟨111⟩ ‖ TA orientation was activated.

Figures 5.12a and 5.12b show the band contrast image and IPF map figure from fractured CSW measured by TKD. The fractured CSW foil was lifted out from region N, with morphology in the cross-section indicated in the left corner of Figure 5.12a. Similar to the results shown in Figure 5.9, there was a strong ⟨111⟩ and a moderate ⟨001⟩ texture. Deformation twins with width between 10-50 nm were readily observed, which may not be picked up in conventional EBSD due to more lim-

ited spatial resolution. Similarly, multiple twin variants were activated mainly in grains close to ⟨111⟩ ∥ TA. As shown in the region marked by the white dotted box in Figure 5.12, twin-twin intersections caused severe grain subdivision, which introduced numerous nanoscale sub-grain boundaries in grains oriented close to ⟨111⟩ ∥ TA, significantly reducing the mean free path for dislocation motion and likely contributing to a steady work hardening.

It has been demonstrated in single crystalline Cantor alloy with ⟨111⟩ ∥ TA that twin-twin interactions has latent hardening moduli one order of magnitude higher than those for slip-slip and slip-twin/twin-slip interactions,[119] i.e. higher proportion of strength contribution from twin-twin interactions. This study by EBSD and TKD provides very strong evidence to support this dynamic Hall-Petch effect in Cantor alloys at low temperature.

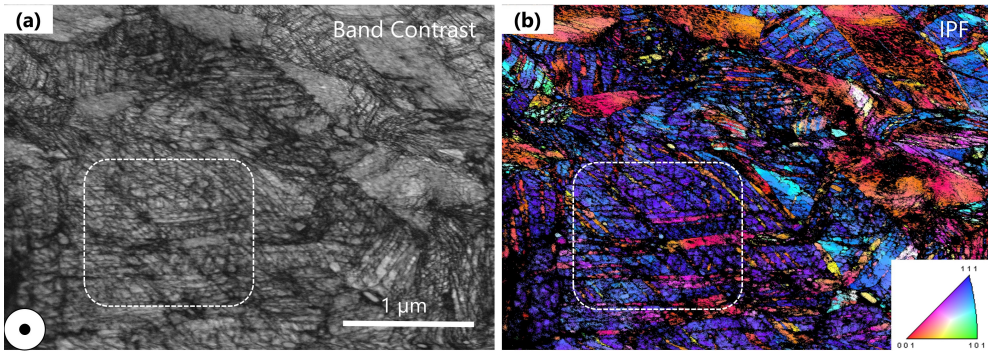


Figure 5.12: (a) Band contrast image perpendicular to TA, indicated on the left corner and (b) orientation map along TA with stereographic triangle in the inset measured by TKD for fractured CSW in the necking region. One grain oriented ⟨111⟩ ∥ TA is marked by the white dotted box in which multiple twin variants were activated. There were profuse twin-twin intersection in grains oriented close to ⟨111⟩ ∥ TA, causing severe grain subdivision and reducing the dislocation mean free path.

Figure 5.13 presents collages of BF and DF TEM images and SAED patterns from a foil taken from fracture CSW at -196℃ in the necking region, that was also used for the TKD characterisation. There were two active twin variants marked by the white arrows with a typical intersection angle of 70°, in agreement with the TKD observations. The SAED image in the inset shows the diffraction pattern in the [011] direction with two twin variants. When selecting each diffracted pattern, shown as red and green circles, two DF images from the same region circled by the white dotted circle are displayed in the left and framed correspondingly as red and green, in which the active twin variant showed as bright feature. The secondary twin system (Figure 5.13b) with an average twin width of 10 nm intersected the primary twin system (Figure 5.13c).

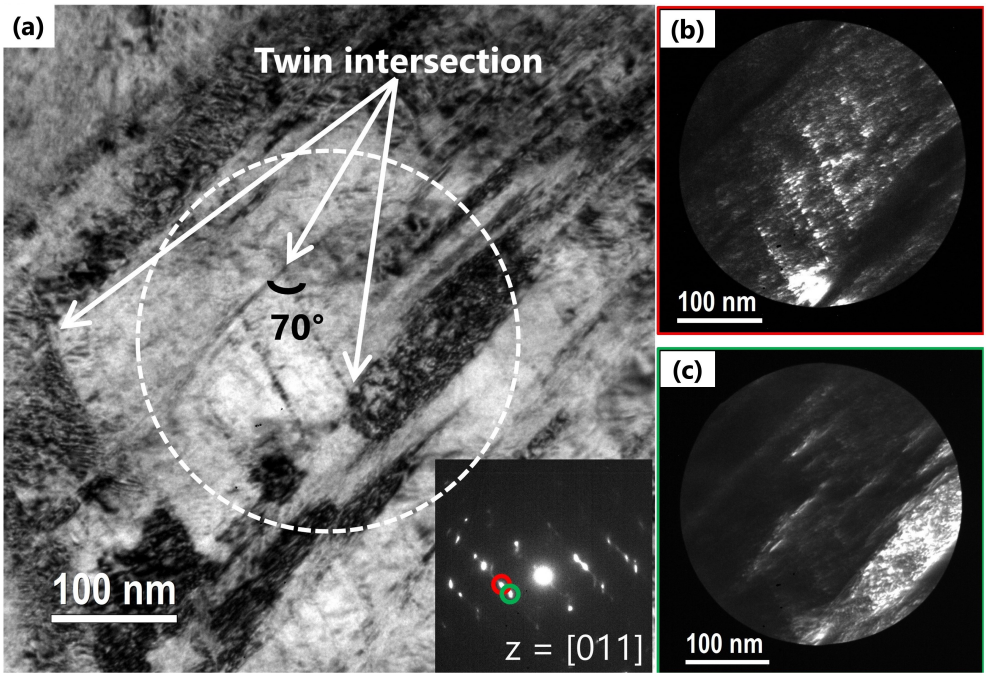


Figure 5.13: (a) Bright-field (BF) TEM images and SAED pattern from fractured CSW in the necking region. One primary twin system with width of 10-100 nm intersected the secondary twin system with width of a few nanometers, and the intersection angle is 70. The SAED pattern along the [011] direction shows two twin variants. By selecting pattern from each single twin variant, two DF TEM images framed by corresponding red and green boxes as red and green circles in the SAED pattern are shown in (b) and (c). The second twin variant and primary twin variant are respectively presented in (b) and (c) as bright features due to strong diffraction from twins.

Overall, based on the EBSD, TKD and TEM results, the twinning type was revealed to be dependent on the different strain levels in grains with different orientations. At a comparatively intermediate strain (one half of the necking strain), twinning was activated largely in grains that favoured twinning. At higher strains close to the crack tip, there was a significant increase in twinning, and the unusual onset of multiple twin variants even in unfavourably oriented grains was possibly due to stress concentration. The presence of multiple twin variants and twin-twin

interactions likely contributed to prolonged work-hardening under high strain and possibly in the post-necking phase.[119]

Figure 5.14 presents BF TEM images with deformation twins in addition to numerous stacking faults in the fractured CSW foil. The SAED pattern in the inset of Figure 5.14a again evidenced the existence of twinning. There were also streaks along the [111] direction, which is typical of nano-sized stacking faults. Figure 5.14b shows a close-up of nano-stacking faults embedded in the twin-matrix lamellae. The SAED pattern in the inset of Figure 5.14b also shows streaking associated with a high density of stacking faults.[270]

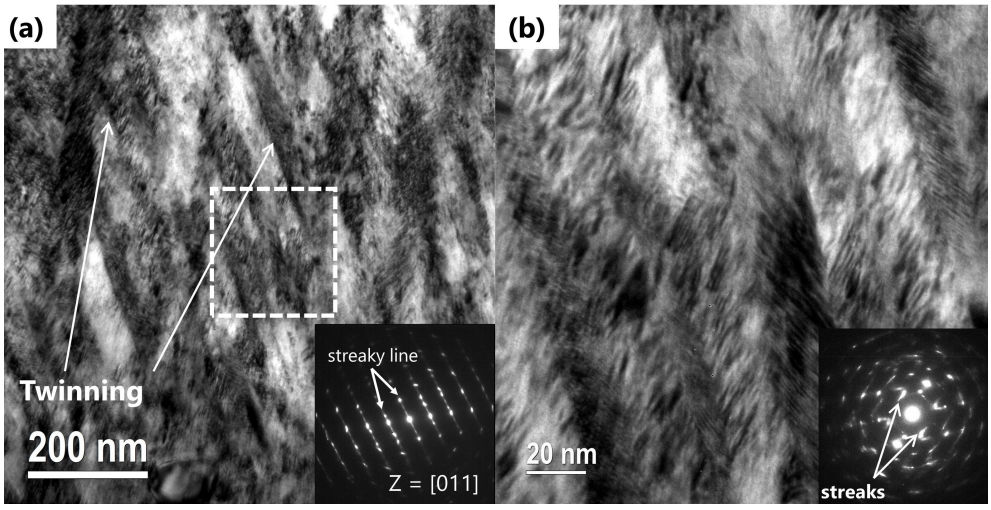


Figure 5.14: (a) BF TEM image and SAED pattern of fractured CSW at -196℃ in the necking region. There were deformations twins in addition to numerous stacking faults evidenced by streaky pattern along [111] direction in SAED pattern. (b) Enlarged BF TEM image of the region marked by white dotted circle in (a) showing profuse stacking faults embedded in the twin-matrix lamellae.

Figures 5.15a, 5.15b and 5.15c show representative BF, DF images and SAED pattern from twin-matrix lamellae containing stacking faults. Extra spots were formed in the SAED pattern, shown in the close-ups

in Figure 5.15c, and when selecting these weak spots only, the DF image shown in Figure 5.15b revealed different strain effects caused by stacking faults. Figures 5.15d and 5.15e present HRTEM images of this region where the Fast Fourier Transformation (FFT) pattern in Figure 5.15d again shows strong streaks extending in the [111] direction from nano-stacking faults. Figure 5.15e presents a close-up of the region marked by the red square in Figure 5.15d and according to the stacking sequence, the profuse stacking faults marked in red are identified as intrinsic stacking faults. There is a missing sequence plane in intrinsic stacking fault whereas there is an extra sequence plane in extrinsic stacking fault.[271] It was suggested that when the trailing partial (a Shockley partial dislocation splited from a perfect dislocation[272]) is not forced out due to insufficient local stress intensity and unfavoured crystal orientation, a stacking fault is left instead of the formation of deformation twin.[273] As already shown, although twins are present, twinning activity is largely within extremely fine sub-grain domains (dozens of nanometers) derived from severe grain subdivision.[67] Alongside these nano-twins, stacking faults formed to increase the dislocation storage (shown in Figure 5.14 and Figure 5.15) under plastic deformation, delaying the onset of strain instability and fracture.

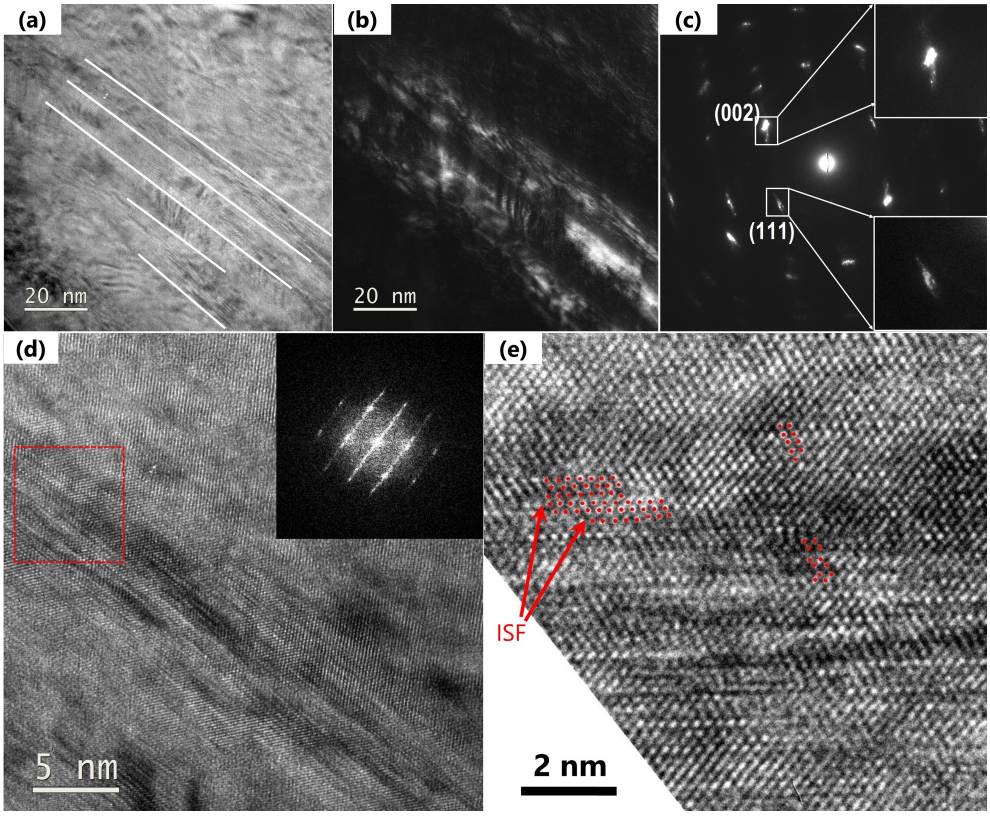


Figure 5.15: (a) BF and (b) DF images of a region of twin-matrix lamellae with embedded stacking faults. (c) SAED pattern from the region shown in (a) and (b). Extra spots were observed in addition to those from twins and matrix. By selecting the extra spots, stacking faults diffracted strongly in (b). (d) HRTEM image with Fast Fourier Transformation (FFT) pattern in the inset. FFT pattern contained streaky lines, evidencing numerous nano-stacking faults. (e) Magnified HRTEM image from the region marked by the red box in (d), showing the atomic structure and stacking sequence (a typical one is marked in red), which were identified as intrinsic stacking faults.

Figures 5.16a and 5.16b present a comparison of orientation maps from CSW and YCSW fractured at -196℃ , along the TA. YCSW resembled CSW at -196℃ in terms of twinning dependence on grain orientation, texture as well as the activation of different twin systems. However, as shown in Figure 5.16c, there were microcracks in fractured YCSW specimen, which might result from strain localisation effect of Y-based oxides.

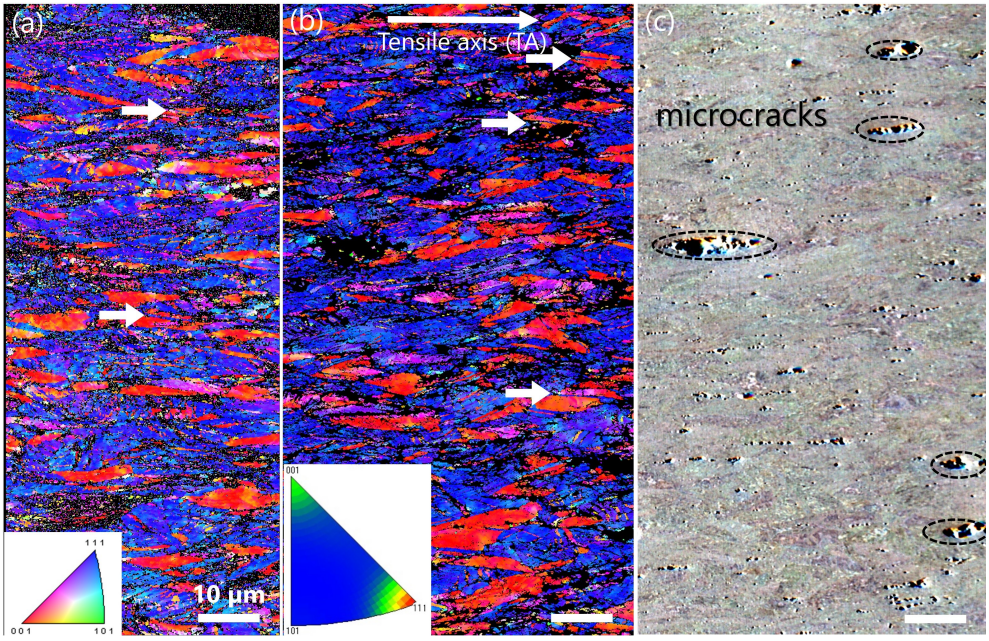


Figure 5.16: Orientation maps of (a) CSW and (b) YCSW fractured at -196℃, along TA indicated in (b) with IPF texture in the inset of (b) showing a strong ⟨111⟩ and a moderate ⟨001⟩ texture. Several twins in grains oriented close to ⟨001⟩ are marked by white arrows. (c) Band contrast image of YCSW showing several microcracks marked by the black dotted ovals.

5.4 Conclusions

The hardness of CSP, YCSP, CSW and YCSW measured by nanoindentation increased with reducing grain size, in agreement with a Hall-Petch relationship with k_y=3.082 GPa $\cdot$ nm$^{-1/2}$ and σ_0=2.104 GPa. The uniaxial tensile properties of CSP, CSW and YCSW at 23℃ and -196℃ were compared with Cantor alloys made by different techniques and with various average grain sizes. CSP showed strength and ductility comparable with the Cantor alloy of similar grain size but made by arc-melting, cold rolling and then heat treatment. CSW and YCSW exhibited comparatively well-balanced strength and ductility for their grain size. CSP, CSW

and YCSW made by spray forming showed at least as good properties as alloys made by processes that can only provide billets weighing a few 100g. All the spray-formed billets had refined, low elemental segregation microstructure.

Yield strength of alloys also followed Hall-Petch relationship with k_y=789.3 ± 74.0 MPa · μm$^{-1/2}$ and σ_0=99.1 ± 24.4 MPa at 23℃ and k_y= 783±128 MPa·μm$^{-1/2}$ and σ_0=370 ± 42 MPa at -196℃. A slightly higher strengthening coefficient than the literature was likely due to other strengthening mechanisms, such as limited precipitation hardening. Moreover, grain boundary strengthening was the most significant contributor for all alloys, with only a limited precipitation hardening effect, even in YCSW, possibly due to a relatively low fraction of coarse Y-based oxides (425 ± 17 nm), compared with conventional ODS alloys (10-40 nm). Nevertheless, unlike high strength (> 800 MPa) but low elongation to fracture (< 5%) in ODS HEAs made by MA+SPS, YCSW showed a more balanced strength and ductility, similar to conventional austensitic ODS steels. The novel approach of seeking to react dissolved Y with internal oxygen, a residual of which is always present even in VIM/Ar backfill processing, showed significant encouragement. Note, the alternative of adding fine-scale Y_2O_3 into the melt has been tried many times and never succeeded, with excessive agglomeration and flotation enduring problems. The very high affinity of Y for O not only facilitates the "internal oxidation" reaction during heat treatment in the solid-state, it

also leads to reactions of free Y in the melt with foundry ceramics used to line the VIM furnace and the launders and nozzles used in the spray forming process. Nevertheless, the large-scale melt processing and associated multi-kg billet fabrication is attractive, and further improvements beyond the essentially "proof-of-concept" results can be expected.

The deformation and fracture behaviour of CSW and YCSW at low temperature where microstructural features were most complex was investigated by EBSD, TKD, TEM and HRTEM. There was a strong ⟨111⟩ and a moderate ⟨001⟩ deformation texture, typical of FCC materials. The occurrence of deformation nano-twinning depended strongly on crystallographic orientation of the grain, in which grains oriented close to ⟨111⟩ ∥ TA favoured twining whereas grains oriented close to ⟨001⟩ ∥ TA were largely twins free. Multiple twin variants were activated even in grains where twinning was not preferred in the higher strain necking region. The onset of multiple twin variants caused twin-twin intersections, contributing to the dynamic Hall-Petch effect. Profuse nano-stacking faults also formed when twinning activity was restrained, which also likely increased the dislocation storage capacity and supported steady work-hardening in the later stages of deformation, and delayed the onset of fracture.

6 Irradiation response of CrMnFeCoNi-(Y)

Alongside the low temperature mechanical response of CrMnFeCoNi-(Y) that was identified in Chapter 2 as having some intriguing features,

which were explored in Chapter 4 and 5, the response to irradiation was also described. This chapter investigates the response of CrMnFeCoNi-(Y) to ion bombardment, with an emphasis on exploring if the multi-principal-element nature of the alloys offers any inherent differences in response to simpler formulations.

6.1 Radiation-induced segregation

As described in Chapter 2.4.2, RIS in alloys can result in the degradation of macroscopic properties.[179,180] Figure 6.1 shows BSE images of an indent by nanoindentation in YCSW before and after 2 MeV V^+ irradiation to 2.33 dpa. As described earlier in Chapter 4, there were some particle inclusions in YCSW which were likely complex Y-based oxides or non-metallic inclusions. Nonetheless, Figure 6.1b suggested that there was further segregation to grain boundaries (GBs) after irradiation, shown by the white arrows.

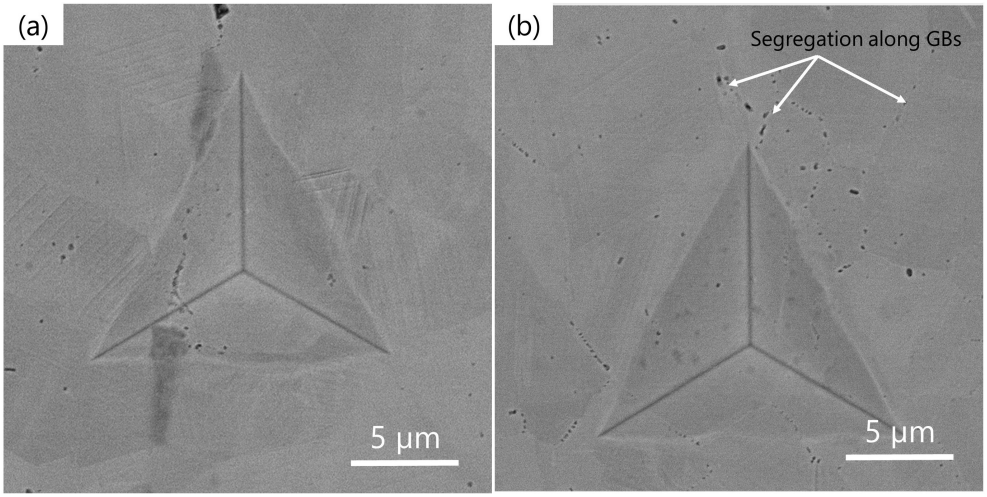


Figure 6.1: BSE images of YCSW containing an indent by nanoindentation (a) before and (b) after 2 MeV V^+ irradiation at 2.33 dpa. Some particle inclusions were likely complex Y-based oxides or non-metallic inclusions. There was further segregation to GBs in (b) irradiated YCSW sample.

Figures 6.2a, 6.2c and 6.2e show SEM-EDS linescan profiles for Cr, Mn, Fe, Co and Ni across high-angle GBs in both unirradiated and irradiated regions of CSW. Figures 6.2b, 6.2d and 6.2f show similar RIS information of YCSW.

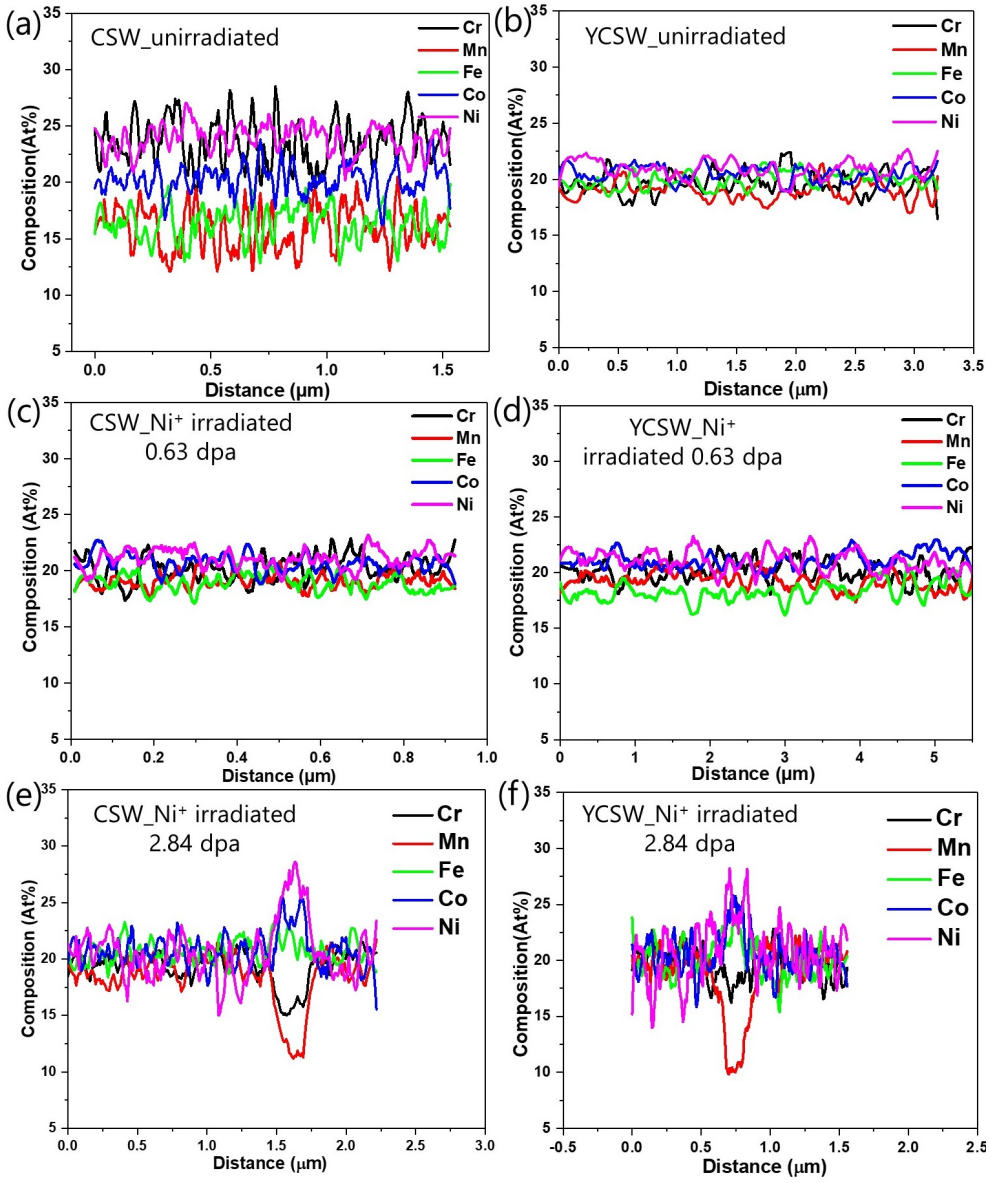


Figure 6.2: SEM-EDS linescan profiles of Cr, Mn, Fe, Co and Ni across high-angle GBs in unirradiated and irradiated regions in CSW and YCSW. (a) Unirradiated CSW, (b) unirradiated YCSW, (c) irradiated CSW and (d) YCSW using 2 MeV Ni^+ ions at 0.63 dpa, (e) irradiated CSW and (f) YCSW using 2 MeV Ni^+ ions at 2.84 dpa.

There was no clear difference in concentration for each element between the GBs and the region away from GBs in unirradiated CSW and YCSW. In each case, the GB is approximately at the mid-point of the linescan. However, the concentration of Mn and Fe was 25% lower than

the bulk concentration, compared by an approximate 25% increase in Cr and Ni concentration. This probably arose from difficulties in distinguishing adjacent and overlapping peaks when analysing data using Aztec Quant mode. Figure 6.3 shows two EDS spectrums in the range from 0 to 20 keV with an enlarged spectrum in the energy range from 0 to 2.2 KeV in the inset. The magenta curve is the fitted spectrum by subtracting the background and deconvoluting overlapping peaks based on Aztec self-contained algorithms. Note that EDS analysis involve all peaks from 0 to 20 keV.

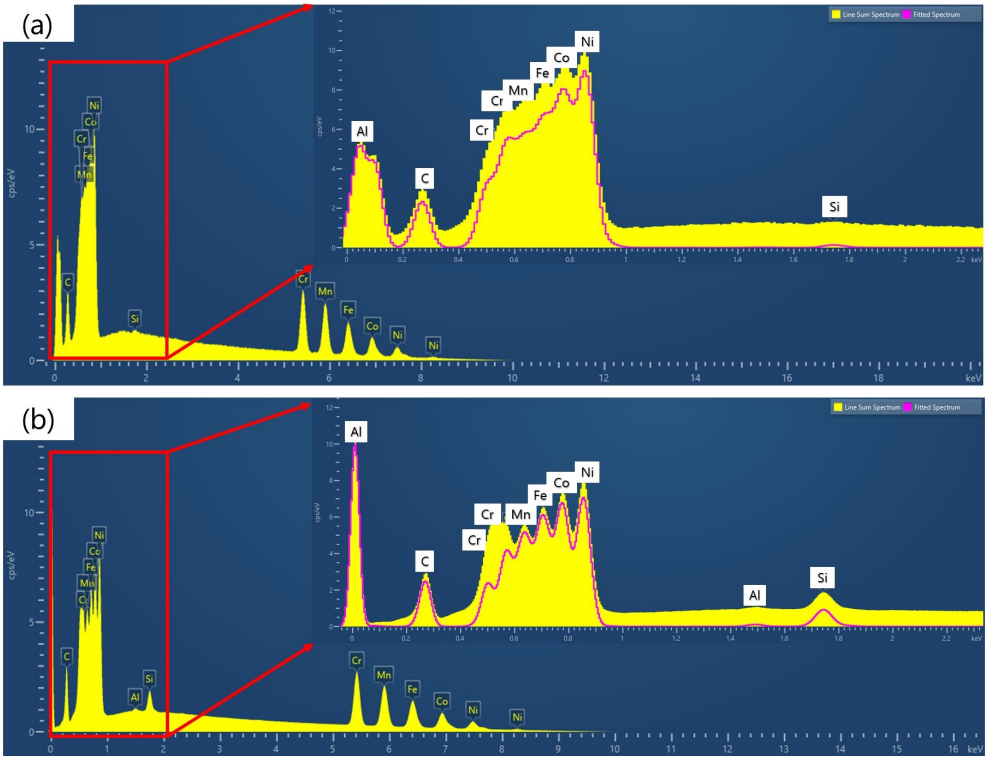


Figure 6.3: EDS spectrums of two linescan datasets at the range from 0 to 20 KeV where there is an enlarged spectrum at the energy range from 0 to 2.2 KeV in the inset. The magenta curve is the fitted spectrum by subtracting the background and deconvoluting overlapping peaks. (a) Characteristic X-ray peaks from different elements were overlapping at low energy (<3 keV). (b) Peaks from different elements were eaily distinguished. Note that EDS analysis involve all peaks from 0 to 20 keV.

The EDS signal mainly came from the K series (including $K\alpha 1$ and $K\beta 1$) while the bombarding electrons gave rise to a broad spectrum, which limited the separation of small peaks shown in the enlarged spectrum at low energy (<3 keV), owing to the presence of 'background'. The concentration of Mn and Fe was likely underestimated as the fitted curve failed to capture the correct intensity of signals for Mn and Fe whereas the concentration of Cr and Ni was overestimated in Figure 6.2a. In contrast, as shown in Figure 6.3b, peaks from Cr, Mn, Fe, Co and Ni were more easily separated and linescans were a better fit to alloy composition determined by bluk chemical analysis. Given this sensitivity of the EDS data, especially when identifying peaks that are closely spaced and overlapping, a relatively long process time (5 or 6) which is the length of time spent reducing noise from the X-ray signal coming from the EDS detector during processing, is used in Figure 6.3b and was subsequently adopted.

Figures 6.2c and 6.2d show the linescan profiles across GBs of CSW and YCSW irradiated using 2 MeV Ni^+ ions at 0.63 dpa with no compelling evidence of RIS. However in Figures 6.2e and 6.2f, when the peak dose increased to 2.84 dpa, there was depletion of Mn, slight depletion of Cr, enrichment of Ni and slight enrichment of Co and Fe.

Figure 6.4 shows SEM-EDS linescan profiles across GBs for unirradiated and irradiated CSW and YCSW using 2 MeV V^+ at 0.51 dpa and 2.33 dpa. Similarly, there was no RIS for unirradiated CSW and YCSW

or irradiated at 0.51 dpa, while at 2.84 dpa, there was a similar trend in the onset of RIS.

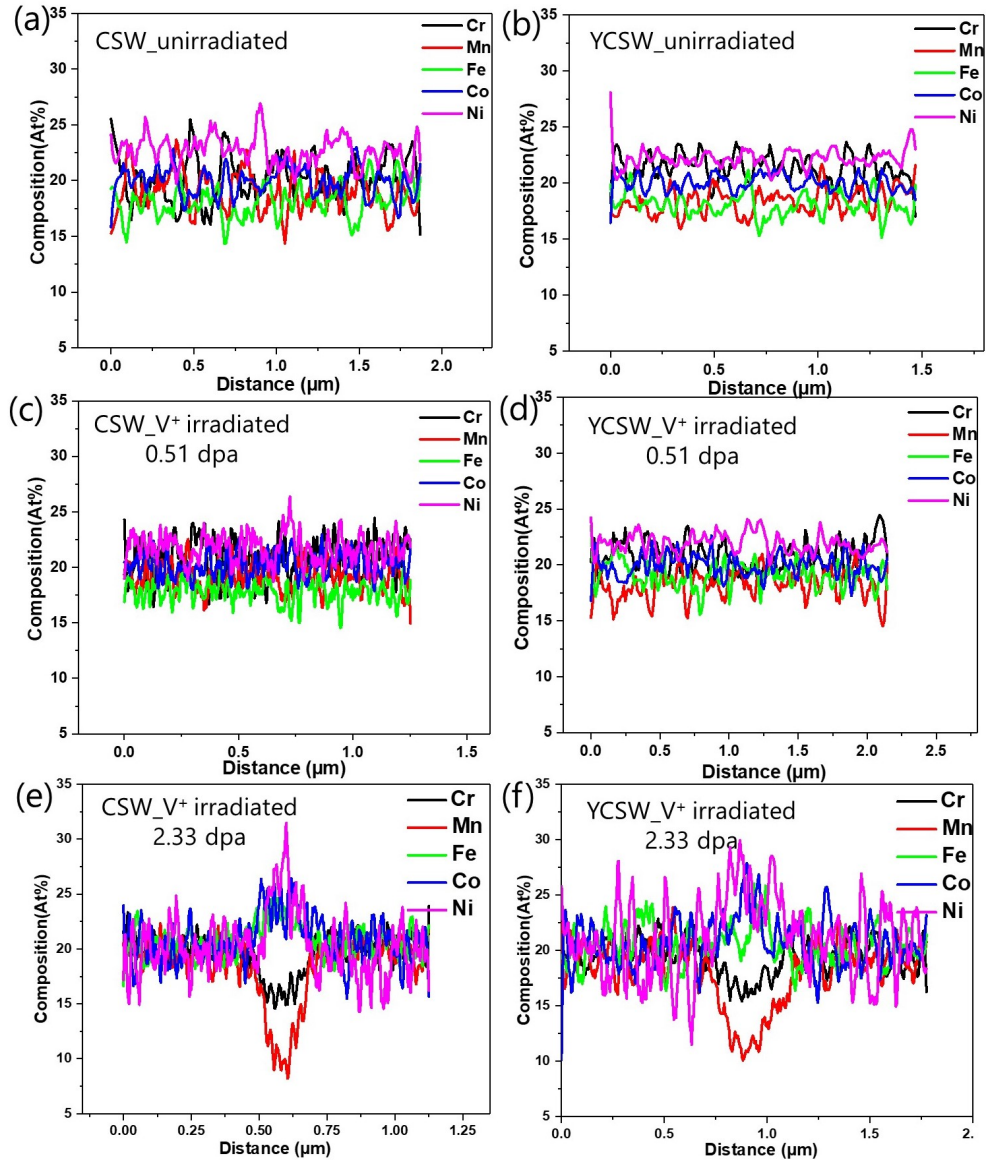


Figure 6.4: SEM-EDS linescan profiles of Cr, Mn, Fe, Co and Ni across high-angle GBs in unirradiated and irradiated regions in CSW and YCSW. (a) Unirradiated CSW, (b) unirradiated YCSW, (c) irradiated CSW and (d) YCSW using 2 MeV V^+ ions at 0.51 dpa, (e) irradiated CSW and (f) YCSW using 2 MeV V^+ ions at 2.33 dpa.

Figures 6.5a and 6.5b show the average concentration for the principal alloying elements at the point where the concentration of Mn was the lowest, taken from at least three linescan datasets. Figures 6.5c and 6.5d

show the change (at.%) in concentration with standard deviation at the same point as Figures 6.5a and 6.5b. Figures 6.5a and 6.5c show results for 2 MeV Ni^+ ion irradiation at 2.84 dpa while Figure 6.5b and 6.5d show results for 2 MeV V^+ ion irradiation at 2.33 dpa. Considering the scatter and inaccuracy, the magnitude of compositional change at GBs was approximately similar in CSW and YCSW for both Ni^+ and V^+ ion irradiation with concentration of Mn decreased from 20 to 10 at.%; Cr decreased slightly to 16 at.%; Ni increased significantly to ∼25-30 at.% and Co and Fe increased slightly to ∼22-25 at.%.

The trend agrees with the RIS behaviour along high-angle GBs in the Cantor alloy reported by Barr et al.[185] under 3 MeV Ni ion irradiation at 500℃ and 3 dpa. Compared with the compositional change across GBs for conventional FCC alloys shown earlier in Figure 2.15b, the magnitude of segregation was approximately similar.[185]

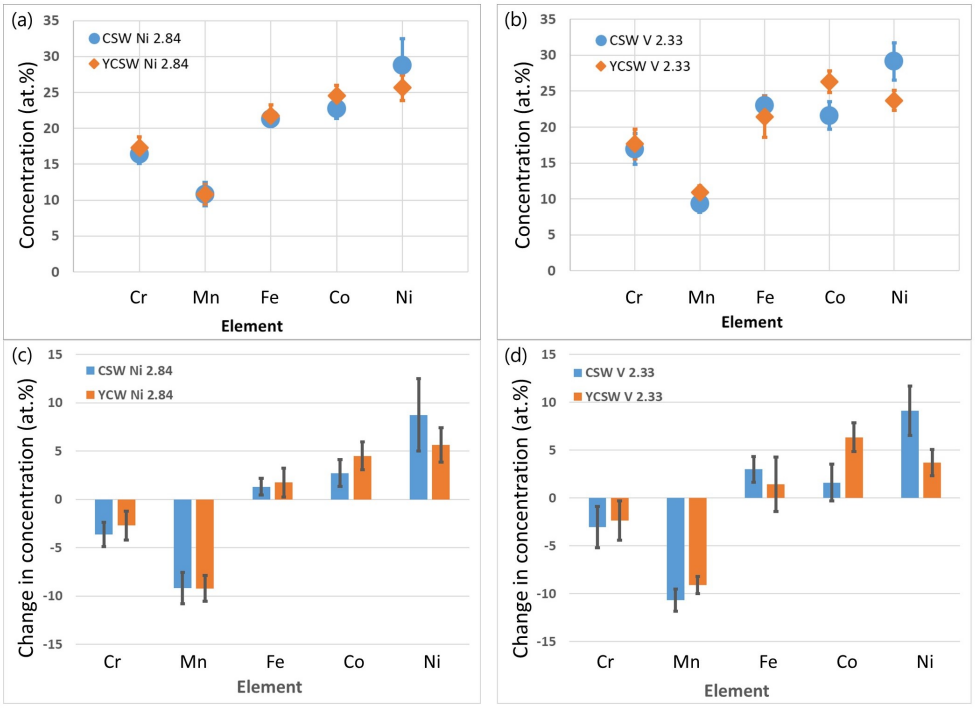


Figure 6.5: The average concentration for the principal elements at the point where the concentration of Mn was the lowest, taken from at least three linescan datasets for (a) 2 MeV Ni^+ ion irradiation at 2.84 dpa and (b) 2 MeV V^+ ion irradiation at 2.33 dpa. (c) and (d) Change in concentration (at.%) with standard deviation for the principal elements.

The mechanistic understanding of RIS in conventional FCC alloys such as 304 and 316 stainless steels is based on modified inverse Kirkendall (MIK) model,[157] itself based on the Perks model but incorporating the effects of pair interaction, ordering, and local atomic configuration for the calculation of vacancy migration energies. This approach has been used to describe substantial Ni enrichment and Cr depletion at GBs, as well as either small depletion or enrichment of Fe depending on the relative concentrations of Ni and Cr in commercial austenitic Fe-Ni-Cr alloys.[156]

In the Cantor alloy and other HEAs, ab-initio calculated and experi-

mental interstitial-atom binding energies and vacancy migration energies are generally unavailable, therefore, one can only explain this generalised trend based on MIK model in CSW and YCSW. The fastest vacancy diffuser - Mn, as reported by Vaidya et al.[187] based on self-diffusion radiotracer diffusion coefficient measurements, depletes significantly whereas the slowest and second slowest vacancy diffuser, Co and Ni, enriches significantly under irradiation conditions. Cr, the second fastest vacancy diffuser, tends to deplete slightly while Fe, the third fast vacancy diffuser either enriches or depletes slightly across GBs. It is worth noting that detailed energetic and kinetic calculations are needed to validate the MIK model to understand the RIS behaviour.

Figures 6.6a and 6.6c show WBDF images with inverted contrast of CSW and YCSW irradiated using V^+ ions at 2.33 dpa with corresponding SAED patterns from the marked region shown in Figures 6.6b and 6.6d. There was one FCC phase identified in CSW and two phases in YCSW due to the presence of Y_2O_3. No additional irradiation-induced secondary phases were observed.

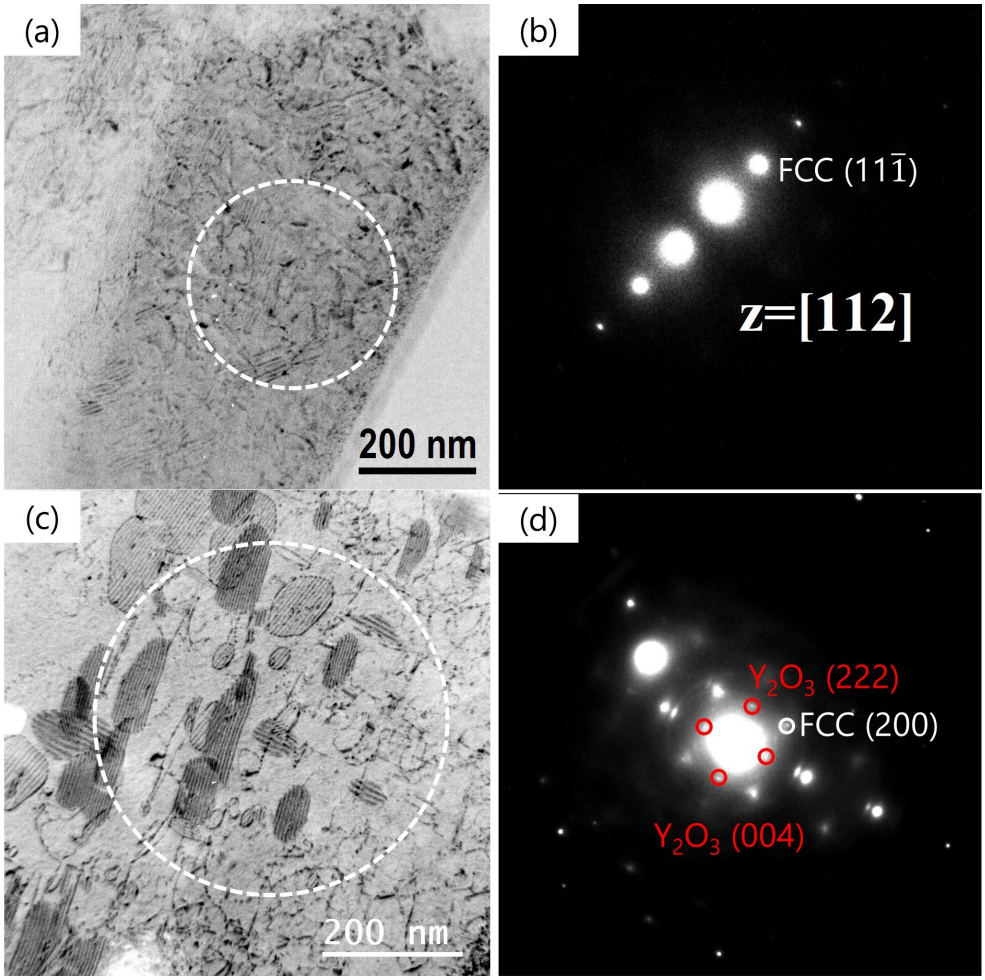


Figure 6.6: (a) WBDF inverted contrast image of CSW irradiated using V^+ ions at 2.33 dpa with corresponding (b) SAED pattern from the marked region. (c) WBDF inverted contrast image of YCSW irradiated under the same condition with corresponding (d) SAED pattern.

Due to their generally helpful effect on mechanical properties, dimensional stability and irradiation resistance, the stability of the Y-based oxides themselves in ODS alloys after irradiation has been a research focus. Figure 6.7 shows an STEM-ADF image of YCSW irradiated using V^+ ions at 2.33 dpa, along with STEM-EDS maps for Cr, Mn, Fe, Co, Ni, C, O, Y and Si from the irradiated region. As in the unirradiated state, there were again some Cr-rich precipitates and Y-based oxides that

were likely Y_2O_3, based on analysis of the SAED. The C-rich area at the upper left corner in Figure 6.7 is due to C protective layer at the surface.

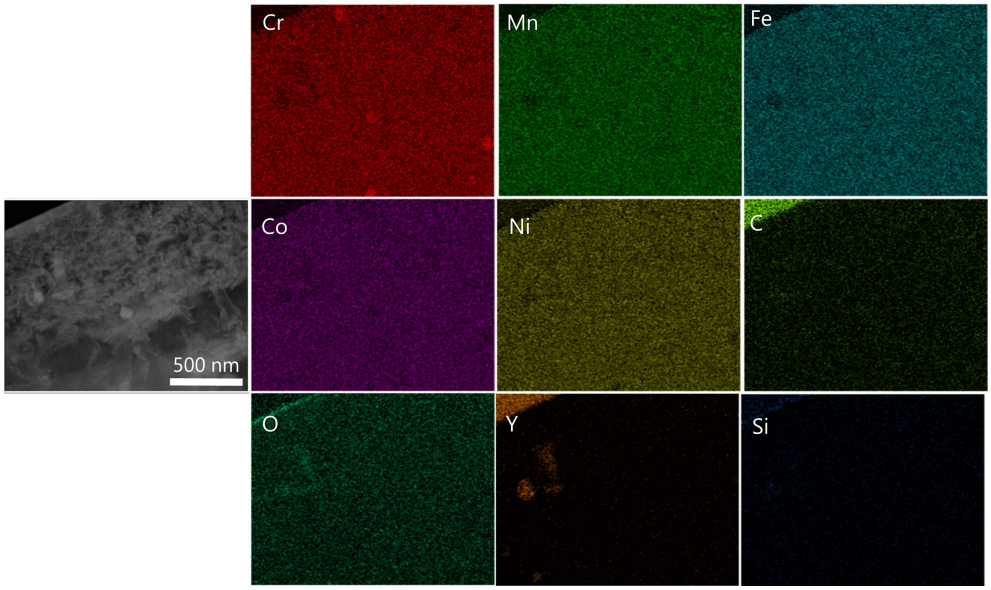


Figure 6.7: STEM-ADF image of YCSW irradiated using V^+ ions at 2.33 dpa and STEM-EDS maps for Cr, Mn, Fe, Co, Ni, C, O, Y and Si in the irradiated region.

Figure 6.8 shows the STEM-BF image of YCSW irradiated using V^+ ions at 2.33 dpa and STEM-EDS maps for Cr, Mn, Fe, Co, Ni, C, O, Y and Si from another irradiated region. There were again Cr-rich precipitates and Y-based oxides particles. Moreover, there were Cr-rich carbides and complex Y-based oxides enriched with Si. The clustering of Y-based oxides in this case was likely due to Si, and where Si has been implicated in promoting the nucleation of Y-based oxides,[253] similar to the observation shown in Figure 4.5. However, there was no strong evidence to suggest that irradiation damage itself was directly linked to localised precipitation of Y or Y-based oxide clusters.

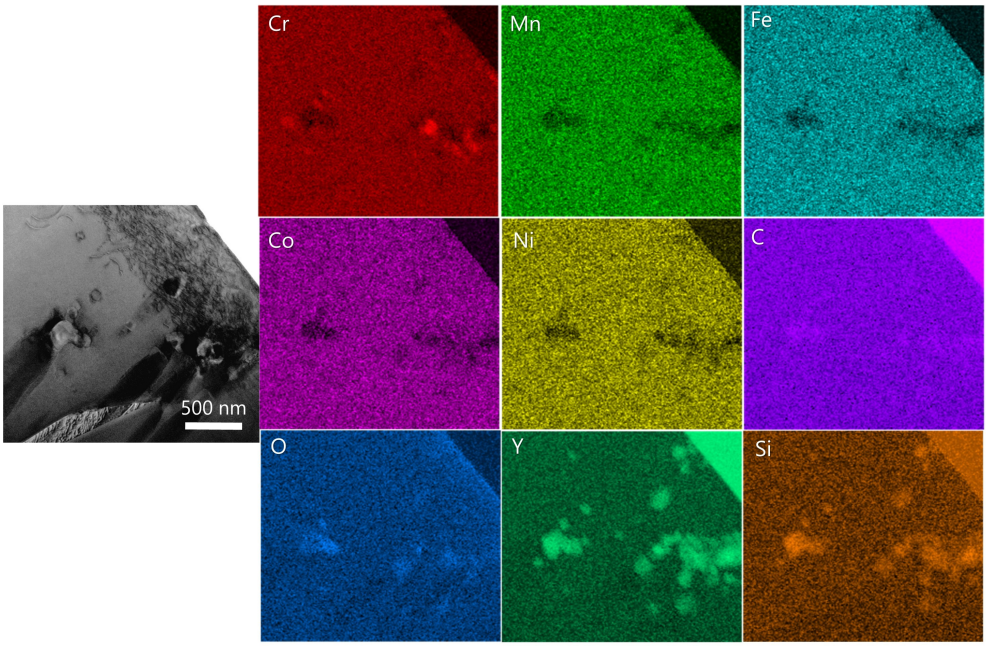


Figure 6.8: STEM-BF image of YCSW irradiated using 2 MeV V^+ ions at 2.33 dpa and STEM-EDS maps for Cr, Mn, Fe, Co, Ni, C, O, Y and Si from an irradiated region.

Figure 6.9 shows four STEM-EDS linescan profiles taken across Y_2O_3 particles in the irradiated region of YCSW. As shown in Figure 6.9a, the signal from the location of particles included the five principal alloying elements (overall ~62 at.%), because in this case the signal derived from an excitation volume that included material beyond the small particle itself, as discussed in Chapter 4.4. In contrast, as shown in Figures 6.9c and 6.9d, for some particles it is possible to contrive imaging/measurement conditions such that the measurement signal arose principally from the particle only showing high concentrations of Y and O. It is also worth noting that the TEM foils were to some extent oxidised, producing a background of O in the linescan profiles. The ratio between the concentration of Y and O was approximately from 1:1.5 to 1:2 after subtract-

ing the background signal from O, and was reasonable for Y_2O_3 but in general, the Y-based oxides were likely non-stoichiometric, although the accuracy of the measurement makes quanlified statements on the nature of the oxides difficult.

Overall, the impression was that the chemical and microstructural features of Y-based oxides were similar to those observed before irradiation. This impression is consistent with reports that nano-sized Y-based oxides particles in ODS alloys show irradiation resistance to over 150 dpa at elevated temperatures.[136] The present study is one of the first to investigate the effect of irradition on ODS-HEA, and it is not surprising, but reassuring, that the Y-based oxides here showed similar stability to those in conventional alloys. Nonetheless, additional detailed studies are required to confirm those preliminary findings.

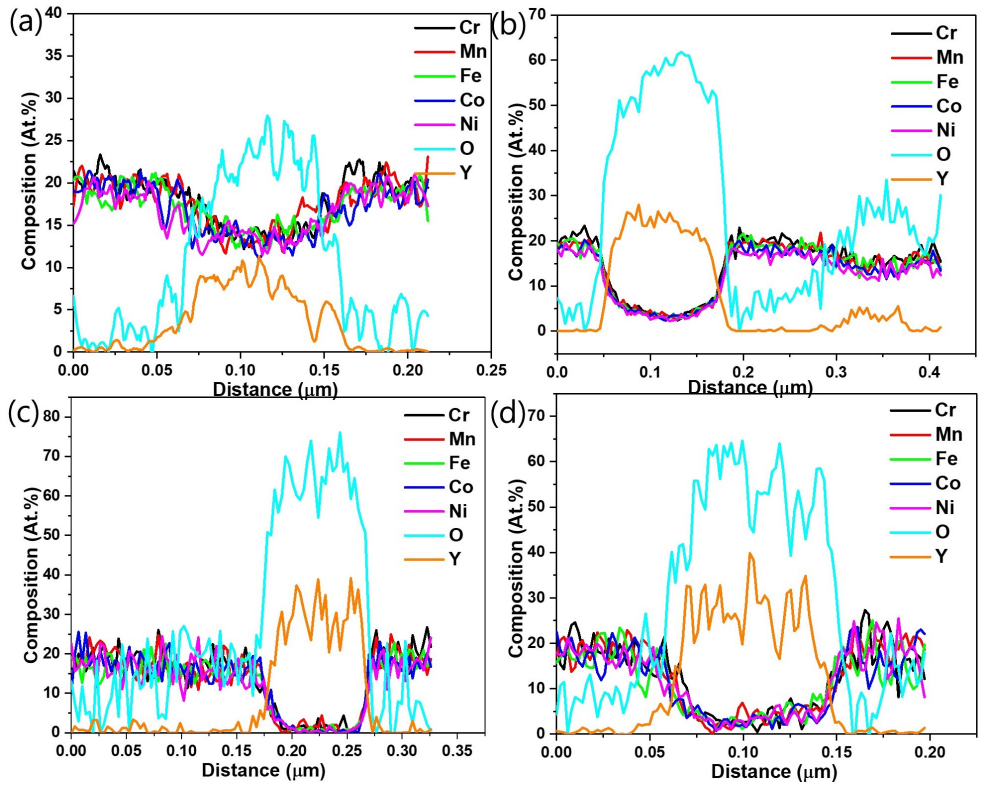


Figure 6.9: STEM-EDS linescan profiles across Y-based oxide particles in the irradiated region of YCSW under irradiation of 2 Mev V^+ ions at 2.33 dpa. In each case, the particle is approximately in the middle of the linescan.

As mentioned in Chapter 2.4.2, the Cantor alloy is not thermodynamically stable at 500-700℃ and decomposes through the precipitation of several minority secondary phases, i.e. $L1_0$-type NiMn, BCC Cr-rich solid solution and B2-type FeCo[21] at intermediate annealing temperatures after 500 days,[21,33] or as quickly as 5 mins for a nanocrystalline Cantor alloy.[22] CSW and YCSW in the high dose (2.33 dpa or 2.84 dpa) ion irradiation experiments were exposed to 500℃ for 20 hours. Therefore it was important to understand what effect the temperature, distinct from the irradiation, may have on microstructural change.

Figure 6.10a shows a STEM-ADF image of YCSW irradiated using 2

MeV V^+ ions at 2.33 dpa. Below the irradiated layer in the top of image, there was a GB triple junction and a GB decorated by precipitates in the unirradiated region. Figures 6.10b-e show STEM-EDS linescan profiles across the grain boundary marked by white arrows in Figure 6.10a. There were no changes across GB at the point marked by arrow 1. However, Figure 6.10c shows an enrichment of Mn and Ni ($\sim$ 25-30 at.%) and a depletion of Fe, Co and Cr ($\sim$ 12.5-15 at.%) across GB at the point marked by arrow 2. Across GB at the point marked by arrow 3, there was a significant enrichment of Cr ($\sim$ 40 at.%). As shown in Figure 6.10e, there were two different kinds of segregation: Mn and Ni enrichment segregation; and Fe and Co enrichment.

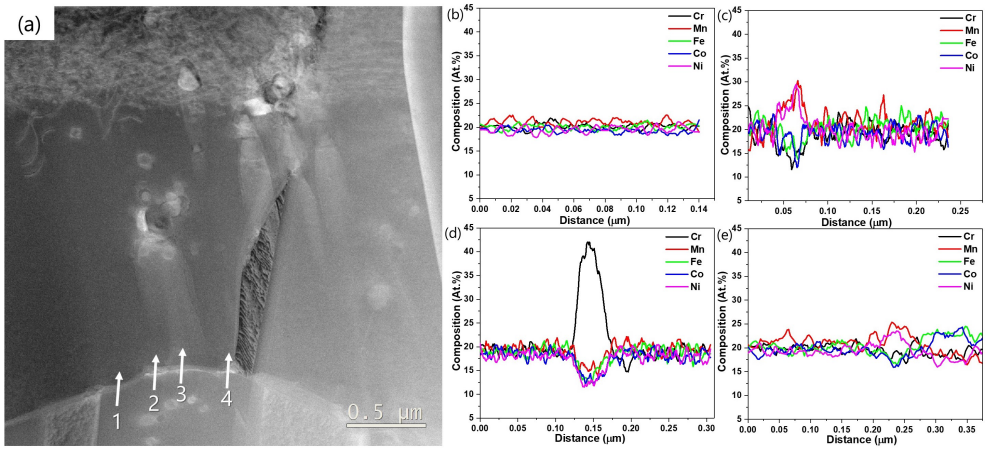


Figure 6.10: (a) STEM-ADF image of YCSW irradiated using 2 MeV V^+ ions at 2.33 dpa. (b-e) STEM-EDS linescan profiles across the GB marked by white arrows in (a). Linescan 1 to 4 corresponds to (b) to (e) respectively.

Figure 6.11 shows a STEM-ADF image of a GB triple junction from the unirradiated region of YCSW irradiated using 2 MeV V^+ ions at 2.33 dpa, and STEM-EDS maps showing segregation to GBs. There were Cr-

rich and MnNi-rich precipitates and a Y-based oxide particle suggested by the maps and marked by white boxes. Compared with Cr-rich precipitates observed in Figure 4.11 before irradiation, the Cr-rich precipitates in Figure 6.10 and 6.11 were present exclusively at GBs and the chemical concentration was approximately 45Cr-17Mn-13Fe-16Co-9Ni (at.%) based on Point&ID results. Similar Cr-rich σ phase precipitates (46.5Cr-16.6Fe-17.6Co-12.7Mn-6.6Ni, in at.%) were also reported after prolonged annealing at 700℃ .[21] A more thorough comparison between Cr-rich precipitates before and after irradiation and before and after annealing at 500℃ is needed to separate unambiguously distinct effects of temperature and irradiation. The preliminary results have suggested that irradiation in the range available in this study does not appear to make a dramatic change in the tendency for minority phase to appear at 500℃. However, it is of concern that decomposition occurs at 500℃ because it falls in the range of service temperature for structural materials in advanced nuclear reactors[43,47] as discussed in Chapter 2.4.2. These precipitates usually have relatively complex crystal structures, such as Cr-rich σ phase, MnNi-rich tetragonal phase,[21] which tend to form in angular, anisotropic morphologies that cause strain inhomogeneity, and early onset of localised cracking. Note that there were three different kinds of precipitates (i.e. Cr-rich, MnNi-rich and FeCo-rich) in the unirradiated region at GBs both in CSW and YCSW using two different ion species at 2.33 or 2.84 dpa. Figure 6.10 and 6.11 were displayed as an representative

example.

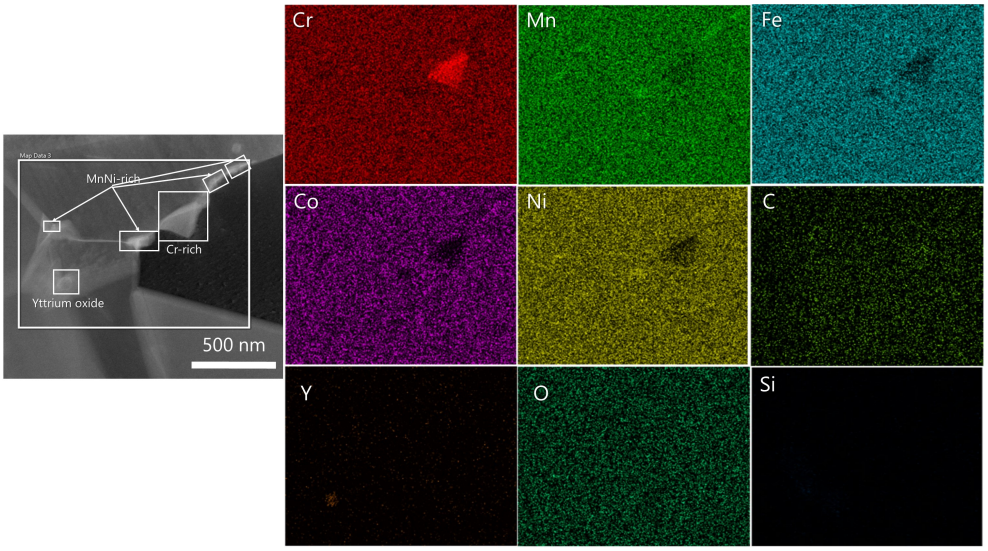


Figure 6.11: STEM-ADF image of YCSW irradiated using 2 MeV V^+ ions at 2.33 dpa and STEM-EDS maps for Cr, Mn, Fe, Co, Ni, C, O, Y and Si in the region marked by the white box.

6.2 Radiation-induced dislocation lines and loops

The accumulation of a high volume fraction and numbers of dislocation lines and loops can impact the macroscopic properties of alloys, for example causing hardening, embrittlement and reduction of fracture toughness.[192,193,274] Consequently, studying dislocations induced by irradiation was performed using a variety of microscopes.

Figure 6.12 shows representative WBDF images with inverted contrast of CSW and YCSW irradiated using 2 MeV Ni^+ ions at 0.63 dpa and 2.84 dpa. There were dislocation loops and lines under all conditions. Note that there was some FIB damage in the TEM foils, such as shown in Figure 6.12b, but was generally in a consistent direction and could usually be distinguished from irradiation-induced defect clusters. One of

the most distinctive features of loops was the Frank partial dislocation loops with stacking faults marked by the red boxes, which was likely due to a relatively low intrinsic stacking fault energy.[40,116] Figure 6.13 shows WBDF images with inverted contrast of CSW and YCSW but irradiated using 2 MeV V^+ ions at 0.51 dpa and 2.33 dpa. Similarly, there were again dislocation lines and loops. The average size of loops at higher dose was higher than those at a lower dose. A more detailed comparison is given later.

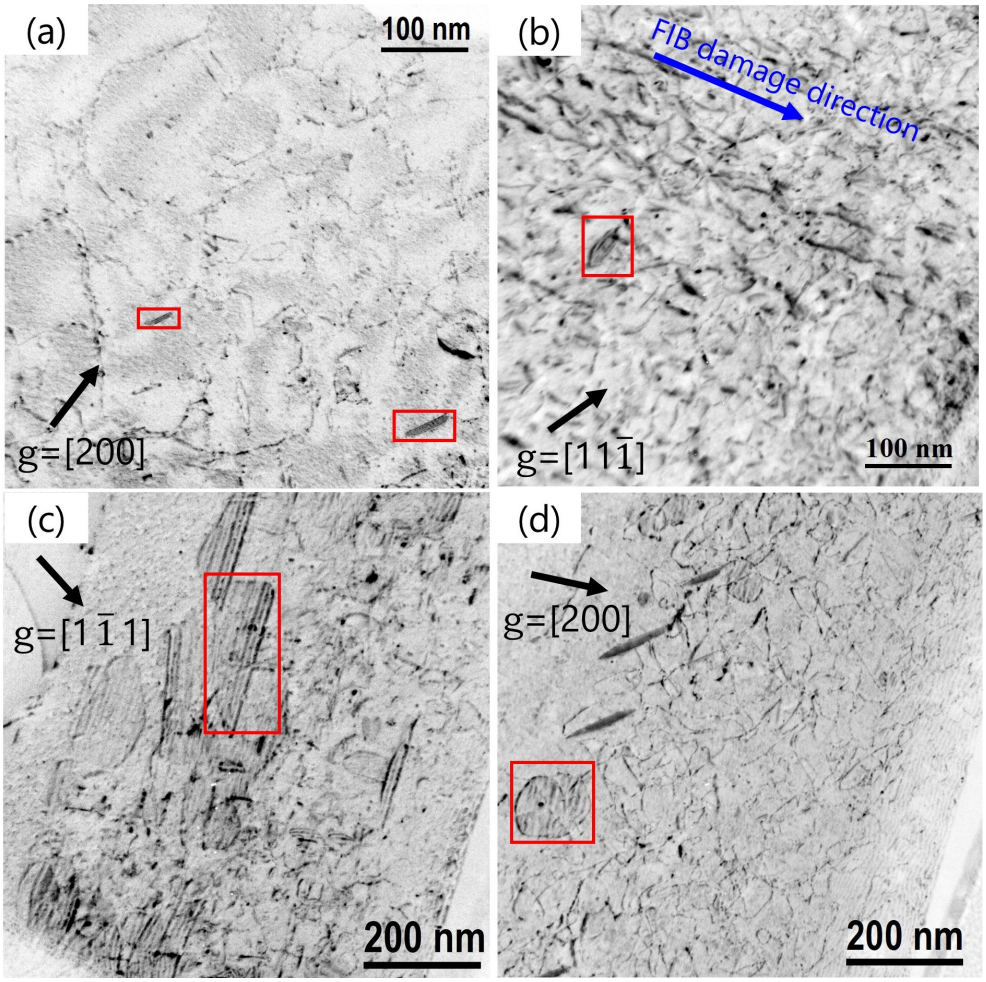


Figure 6.12: WBDF images with inverted contrast for CSW and YCSW irradiated using 2 MeV Ni^+ ions at 0.63 dpa and 2.84 dpa. (a) CSW at 0.63 dpa, (b) YCSW at 0.63 dpa, (c) CSW at 2.84 dpa and (d) YCSW at 2.84 dpa.

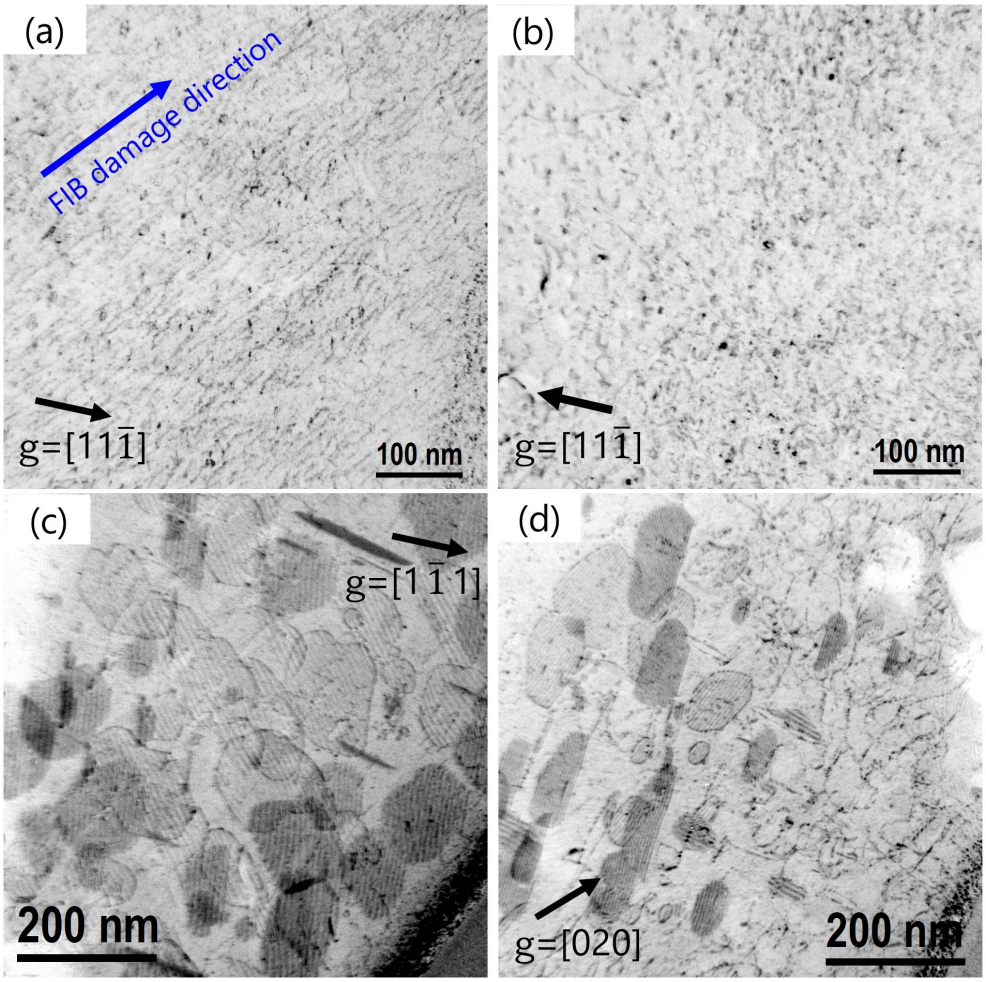


Figure 6.13: WBDF images with inverted contrast for CSW and YCSW irradiated using 2 MeV V^+ ions at 0.51 dpa and 2.33 dpa. (a) CSW at 0.51 dpa, (b) YCSW at 0.51 dpa, (c) CSW at 2.33 dpa and (d) YCSW at 2.33 dpa.

Figure 6.14 shows a series of WBDF images with inverted contrast for YCSW using 2 MeV V^+ ions at 2.33 dpa using g=[020], g=[0$\bar{2}$0], g=[200], g=[$\bar{2}$00], g=[2$\bar{2}$0] and g=[31$\bar{1}$]. The Burgers vectors and loops can be analysed by standard contrast analysis and the arising $g \cdot b$ table is shown in Table 3.4. The interstitial or vacancy nature of the dislocation loops was measured by the inside-outside method as discussed in Chapter 3.5.6. Thus, for instance, the dislocation loop marked by the red box was out of

contrast in g=[200] and was shown to have Burgers vector b=$\pm\frac{1}{2}[0\bar{1}1]$. In addition, this perfect loop showed inside contrast in g=[020] and outside contrast in g=[$0\bar{2}0$], which makes $g \cdot b < 0$ in g=[020], and thus b=$\frac{1}{2}[0\bar{1}1]$. Due to $b \cdot z < 0$, this perfect loop was identified as an interstitial loop. With regards to partial dislocation loops, such as the loop marked by the white mark, this loop was identified as interstitial type loop with Burgers vector b=$\frac{1}{3}[\bar{1}\bar{1}1]$.

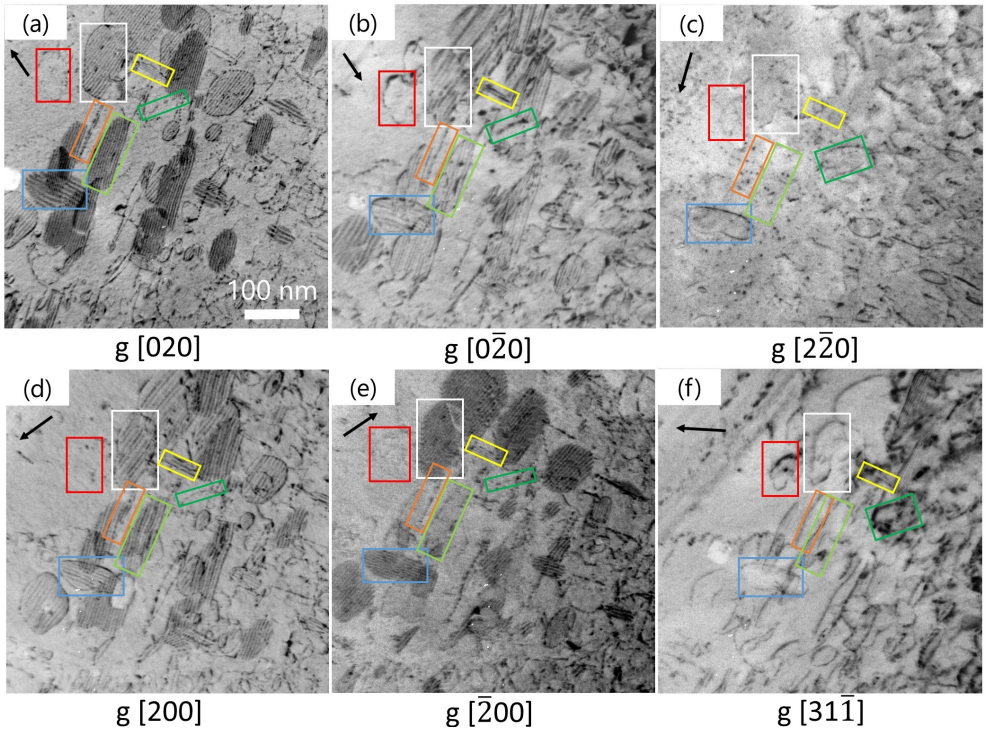


Figure 6.14: A series of WBDF images with inverted contrast for YCSW using 2 MeV V^+ ions at 2.33 dpa using (a) g=[020], (b) g=[$0\bar{2}0$], (c) g=[$2\bar{2}0$], (d) g=[200], (e) g=[$\bar{2}00$], and (f) g=[$31\bar{1}$].

The table of visibility and inside-outside contrast showing the nature of each type of dislocation loop is summarised in Table 6.1 for YCSW irradiated using 2 MeV V^+ ions at 2.33 dpa. It is worth pointing out that due to artifacts derived from FIB damage and defect cluster being in gen-

eral small (<10 nm) in CSW and YCSW irradiated at low dose (0.51 dpa and 0.63 dpa), identification of the nature of all loops was challenging. Thus this inside-outside operation was only conducted in irradiated specimens at high dose (2.33 dpa and 2.84 dpa). In addition, the TEM foil used for nature identification were fairly thick (120-170 nm), the visibility of some dislocation loops > 10 nm was reduced using certain g-vectors. Also due to strain contrast caused by dislocation lines and network, the nature of some loops were unable to be identified. Consistent with the literature,[185] all identified loops were interstitial type.

By analysing WBDF images in different conditions using ImageJ and measuring the foil thickness based on the CBED method (see Chapter 3.8.3), the average size and number density of dislocation loops was obtained. Table 6.2 summarises the foil thickness, the average size, the maximum size and the number density of CSW and YCSW specimens irradiated at different conditions. Figure 6.15 shows the number density ($10^{20}m^{-3}$) as a function of the average size of dislocation loops in CSW and YCSW irradiated at different conditions.

Table 6.1: Visibility and inside-outside contrast showing the nature of each type of dislocation loop in YCSW irradiated using 2 MeV V^+ ions at 2.33 dpa. V=visible and I=invisible.

	ZA=[001]					ZA=[113]	b
	g=[020]	g=[$0\bar{2}0$]	g=[200]	g=[$\bar{2}00$]	g=[$2\bar{2}0$]	g=[$31\bar{1}$]	
white	V,inside	V,outside	V,inside	V,outside	I	V	$\frac{1}{3}[\bar{1}\bar{1}1]$
light green	V,outside	V,inside	V,outside	V,inside	I	V	$\frac{1}{3}[111]$
blue	V,outside	V,inside	V,inside	V,outside	V	V	$\frac{1}{3}[\bar{1}11]$
yellow	V,inside	V,outside	V,outside	V,inside	V	V	$\frac{1}{3}[1\bar{1}1]$
orange	V,edge-on	V,edge-on	V,edge-on	V,edge-on	I	V	$\pm\frac{1}{2}[110]$
dark green	V,edge-on	V,edge-on	V,edge-on	V,edge-on	V	V	$\pm\frac{1}{2}[\bar{1}10]$
red	V,inside	V,outside	I	I	V	V	$\frac{1}{2}[0\bar{1}1]$

Table 6.2: The foil thickness, the average size with standard deviation, the maximum size and the number density of CSW and YCSW specimens irradiated at different conditions.

Ion species	Specimen	Foil thickness (nm)	Average size (nm)	Max size (nm)	Number density ($10^{20}m^{-3}$)
Ni	CSW 0.63	120	33±17	86	14.6
	YCSW 0.63	148	32±13	65	5.9
	CSW 2.84	151	98±65	289	6.9
	YCSW 2.84	158	65±32	135	4.8
V	CSW 0.51	135	13±7	35	35.6
	YCSW 0.51	142	13±3	27	25.2
	CSW 2.33	170	89±36	175	13.1
	YCSW 2.33	141	43±44	168	9.7

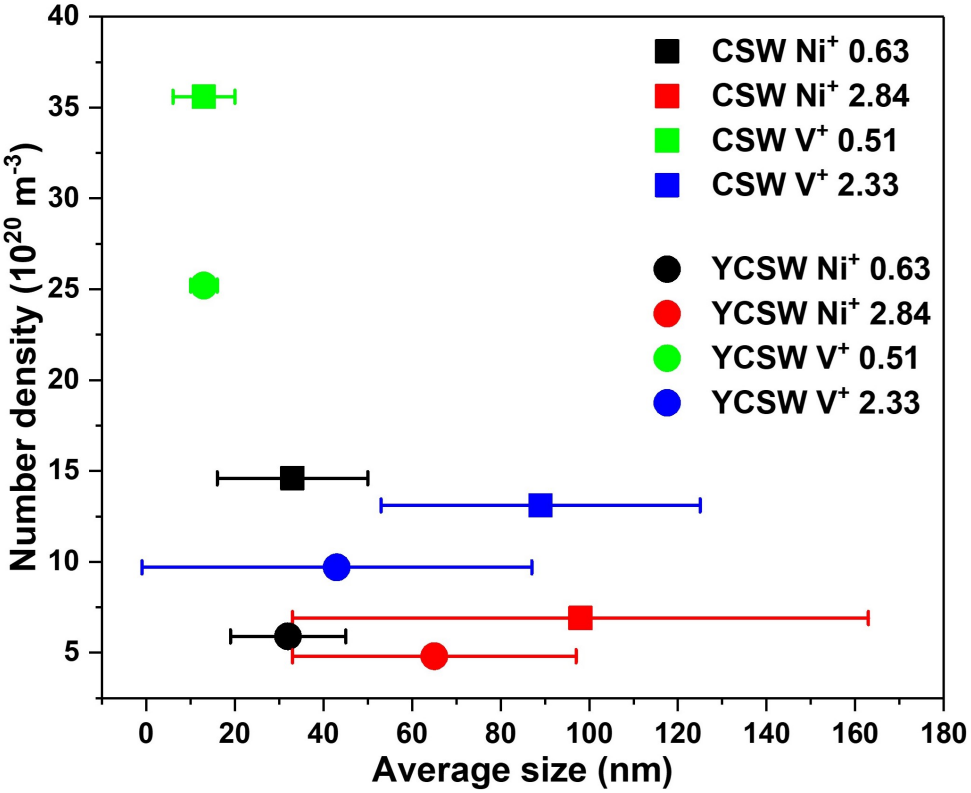


Figure 6.15: The number density (10^{20} m^{-3}) as a function of the average size of dislocation loops in CSW and YCSW irradiated at different conditions.

Figures 6.12, 6.13 and 6.14 show that there were overlapping of dislocation loops, particularly at high dose, which may overestimate the average size of loops when two overlapped loops cannot be well distinguished using ImageJ. In addition, artifacts from FIB damage and long dislocation lines at high dose also affected the quantification of loops, particularly small loops, which may have overestimated the average size and underestimated the number density.

As seen in Table 6.2 and Figure 6.15, with increasing dose, the average size of loops in CSW and YCSW increased whereas the number density decreased. Using in-situ electron irradiation, it was shown that

in CrFeCoNi irradiated with 1250 keV electrons at 400 ℃, the longer axis length of partial dislocation loops increased from ∼40 nm to 55 nm and then to 100 nm when increasing the dose from 0.5 dpa to 0.6 dpa and then 1 dpa.[194] Comparatively, the average size of loops in CSW increased from 13 nm to 33 nm, 89 nm and 98 nm when increasing the dose from 0.51 dpa to 0.63 dpa, 2.33 dpa and 2.84 dpa. Generally speaking, the growth rates of loops in CSW and CrFeCoNi in previous work were similar, and is much slower than that of Ni.[194]

Dislocation loops in YCSW had smaller average size, lower number density and exhibited a slower growth rate than CSW. Dislocation loops in ODS austenitic stainless steels nucleated at the interface between oxide particles and matrix[275] and this interface was an effective sink for irradiation-induced point defects. With oxide particles acting as effective sinks, there were likely less surviving defect clusters in the displacement cascade and thus a smaller number density of loops in YCSW.

Given the newness of the field, there are understandably limited studies on the characteristics of dislocation loops, i.e. the average size and number density, for the Cantor alloys after ion irradiation. Nonetheless, Lu et al. reported that the average dislocation loop diameter and number density in a Cantor alloy irradiated using 3 MeV Ni ions at 38±5 dpa and 500℃ was 24 nm and $1 \times 10^{22} m^{-3}$ respectively based on two-beam kinematical BF images.[184] However, as shown in Figure 3.9, the identification of the nature and size of dislocation loops using two-beam

kinematical BF condition has limitations. Alternatively, under WBDF condition, Shi et al.[276] irradiated electron transparent foils of Cantor alloy with 1 MeV Kr ions and the Cantor alloy exhibited a number density of 1.8×10^{15} m^{-2} and an average size of 7 nm at 0.4 dpa and 500℃. When increasing the dose to 2 dpa, the number density and average size increased to 2.4×10^{15} m^{-2} and 15 nm. Note that only a WBDF condition with a reflection vector g=(200) was used, which inevitably neglected some information. Thus a detailed comparison between the present study and those two prior studies is difficult, and the results here are probably the most detailed to date.

In contrast, there has been much more quantification of dislocation loops in conventional alloys, such as 316SS and Fe-15Cr-16Ni. Table 6.3 summarises the quantitative data of dislocation loops, i.e. average size and number density of conventional alloys irradiated under similar conditions.

In general, the loop average size in CSW and YCSW was larger than that in 316SS whereas the number density was either similar or slightly lower in CSW and YCSW when irradiated under similar conditions. In terms of dislocation loops, CSW and YCSW showed no obvious improvement in irradiation resistance than conventional alloys.

Table 6.3: Quantitative data of dislocation loops, i.e. average size and number density of the Cantor alloys including the present study and conventional alloys (316SS and Fe-15Cr-16Ni) irradiated under similar conditions.

Materials	Temperature (°C)	Ions	dose (dpa)	Average size (nm)	Number density ($10^{21}m^{-3}$)
CSW	500	2 MeV Ni^{+}	0.63	32.9	1.5
CSW	500	2 MeV Ni^{+}	2.84	98.1	0.7
CSW	500	2 MeV V^{+}	0.51	12.9	3.6
CSW	500	2 MeV V^{+}	2.33	88.8	1.3
YCSW	500	2 MeV Ni^{+}	0.63	32	0.6
YCSW	500	2 MeV Ni^{+}	2.84	65	0.5
YCSW	500	2 MeV V^{+}	0.51	13	2.5
YCSW	500	2 MeV V^{+}	2.33	43	1.0
Cantor alloy[184]	500	3 MeV Ni	38±5	24	10
Cantor alloy[276]	500	1 MeV Kr	0.4	7	/
Cantor alloy[276]	500	1 MeV Kr	2	15	/
316SS-AST[208]	500	46.5 MeV Ni^{6+}	1	10.7	6.8
316SS-BST[208]	500	46.5 MeV Ni^{6+}	1	8.5	11
316SS-AA[208]	500	46.5 MeV Ni^{6+}	1	15.2	5.74
316SS-BA[208]	500	46.5 MeV Ni^{6+}	1	16.8	6.4
316SS[198]	500	5 MeV Ni^{2+}	0.5	22	0.43
316SS[199]	500	5 MeV Ni^{2+}	2	24	0.94
Fe-15Cr-16Ni[199]	500	4 MeV Ni^{3+}	0.17	/	2.94
Fe-15Cr-16Ni[199]	500	4 MeV Ni^{3+}	1.7	/	20.9

6.3 Radiation-induced hardening

Irradiation-induced defect clusters and precipitates act as obstacles to dislocation motion, thus causing hardening. In addition, irradiation-induced dislocation lines likely cause dislocation-dislocation interaction by local stress fields, which further leads to hardening.

Figure 6.16 shows the hardness change (%) as a function of displacement into surface (nm) in CSW and YCSW before and after irradiation using 2 MeV Ni^+ and V^+ ions respectively. The black curves show the hardness change at low dose whereas the red curves show high dose. YCSW showed less hardening than CSW at all conditions, which agreed with the quantitative results shown in Table 6.2 that YCSW showed resistance to induced dislocation loop formation. At a depth of 600 nm (where the highest dose was predicted by SRIM), CSW and YCSW showed 5.5% and 2.8% hardening at 0.63 dpa and 8% and 7.3% at 2.84 dpa. When irradiated with 2 MeV V^+ ions, CSW and YCSW showed 6.7% and 5.3% hardening at 0.51 dpa and 10.9% and 9% hardening at 2.33 dpa. The hardening (%) at the depth of 600 nm in irradiated CSW and YCSW was summarised in Table 6.4.

The increase in hardness was also likely dependent on the dose rate. Although irradiated at a relatively lower damage dose by V^+ ions (0.51 dpa) than Ni^+ ions (0.63 dpa), hardening in CSW and YCSW is higher at 0.51 dpa than that at 0.63 dpa, which is likely related to lower dose rate (4.3×10^{-5} dpa/s) at 0.51 dpa when using V^+ ions than the dose rate

(6.7×10^{-5} dpa/s) at 0.63 dpa when using Ni^+ ions. It is suggested by Abromeit[277] that defects tend to sink at dislocations and grain boundaries at low dose rates whereas annihilation by the recombination of a vacancy and interstitial dominates at a high dose rate. Hardie et al.[278] reported that greater hardening was found in the FeCr alloys irradiated at the lower dose rate possibly due to radiation-driven clustering of chromium atoms into Cr-rich precipitates. The swelling of 316 stainless steel under irradiation has been shown by Seran et al.[279] to decrease with increasing dose rate.

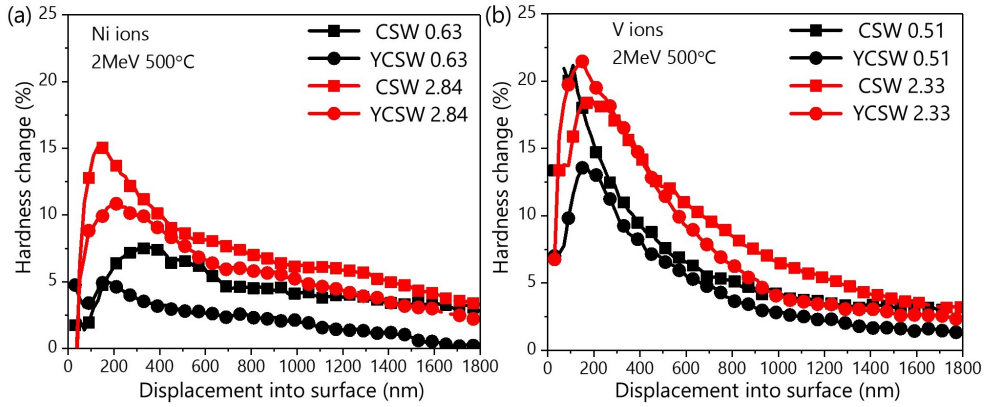


Figure 6.16: Hardness change (%) as a function of displacement into the surface (nm) in CSW and YCSW before and after irradiation using (a) 2 MeV Ni^+ and (b) 2 MeV V^+ ions at low and high dose.

Table 6.4: Hardening (%) at the depth of 600 nm in irradiated CSW and YCSW using 2 MeV Ni^+ and V^+ ions at different doses.

	Ni^+	Ni^+	V^+	V^+
	0.63 dpa	2.84 dpa	0.51 dpa	2.33 dpa
CSW	5.5	8	6.7	10.9
YCSW	2.8	7.3	5.3	9

There are several factors that may contribute to irradiation-induced hardening, including radiation-induced dislocation loops, dose rate, RIS

along GBs and complex dislocation lines and networks, mostly observed at high dose. In addition to hardening, irradiated austenitic steels have been shown to experience a loss of ductility due to interaction between dislocations and the irradiated microstructure.[280] Irradiation-induced microstructural change may lead to changes in deformation mechanisms. Deformation twinning due to localised increase of deformation was reported to occur in irradiated alloys.[281,282]

In order to investigate the deformation mechanism in a thin irradiated layer ($\sim 1\ \mu$m), nanoindentation at room temperature was combined with post-mortem characterisation, including TKD and TEM. The TEM foils were lifted out directly from underneath the indent. Figure 6.17 shows cross-sectional TKD band contrast images and orientation maps of CSW and YCSW before irradiation. As shown in Figures 6.16a and 6.16b, in CSW, there were only dislocation cells and subgrains in the most highly deformed region, near the surface. In contrast, there were thin (10-20 nm) deformation nano-twins (confirmed by 60° misorientation) in deformed YCSW.

Note that the average grain size for CSW and YCSW was 8.2 μm and 5.4 μm so that a single indent (shown in Figure 6.1) usually interacted with several grains, making the dependence of twinning on crystal orientation less significant. By examining at least three specimens, no deformation twinning was observed in CSW using on-axis TKD, within the spatial resolution of the technique. With regards to YCSW, deformation

twins were observed in all specimens, even though the crystal orientation of each of the multiple grains in the deformed region was different.

It has been shown that deformation twinning rarely occurred in the Cantor alloys at room temperature under uniaxial tensile deformation because the critical resolved shear stress (CRSS) for twinning was not achieved.[34] Although deformation mechanisms under nanoindentation are likely different from bulk uniaxial tensile deformation, it is safe to conclude that YCSW experienced more twinning activities than CSW, possibly due to local stress concentration by oxide particles.

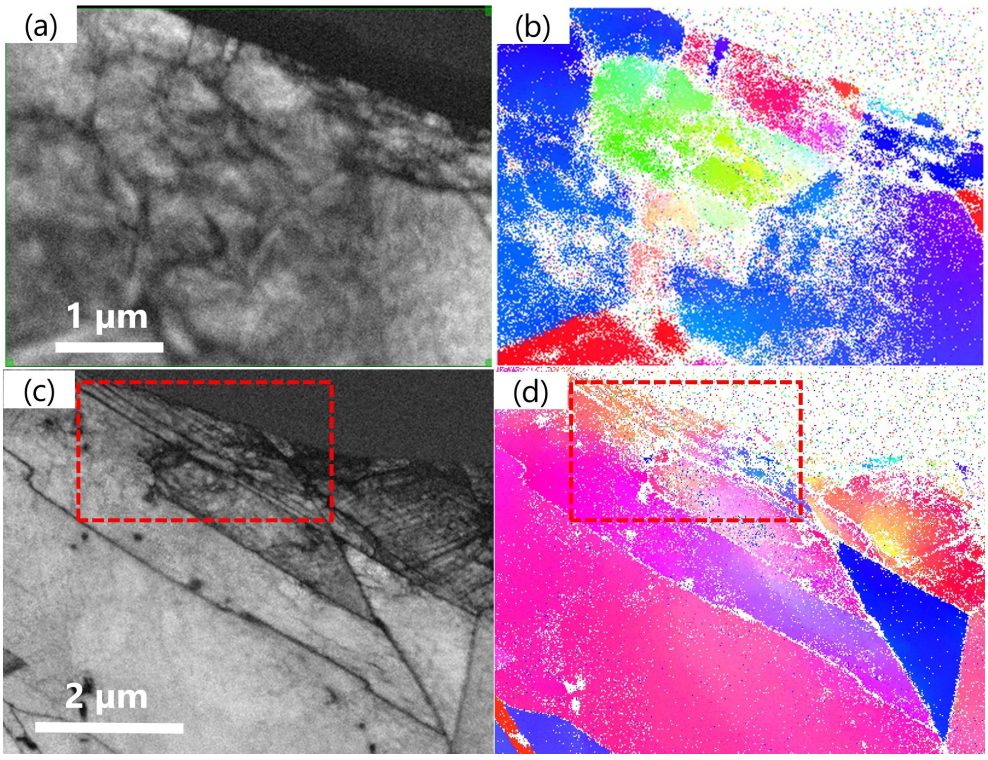


Figure 6.17: TKD band contrast images and orientation maps of indented, unirradiated (a,b) CSW and (c,d) YCSW from the cross-section obtained by FIB from the region of plastic deformation around the indent.

Figure 6.18 shows the TKD band contrast images and orientation

maps of indented CSW irradiated using 2 MeV Ni^+ ions at 0.63 dpa and 2.84 dpa. Different from the subgrains with misorientation shown in Figures 6.16a and 6.16b, there were deformation nanotwins in the highly deformed region (marked by white dotted box) in irradiated CSW. Figure 6.19 shows similar TKD band contrast images and orientation maps, but for the case of YCSW irradiated using 2 MeV Ni^+ ions at 2.84 dpa. As for unirradiated YCSW, deformation nano-twins were readily observed. Note that at least three specimens were examined to corroborate the findings.

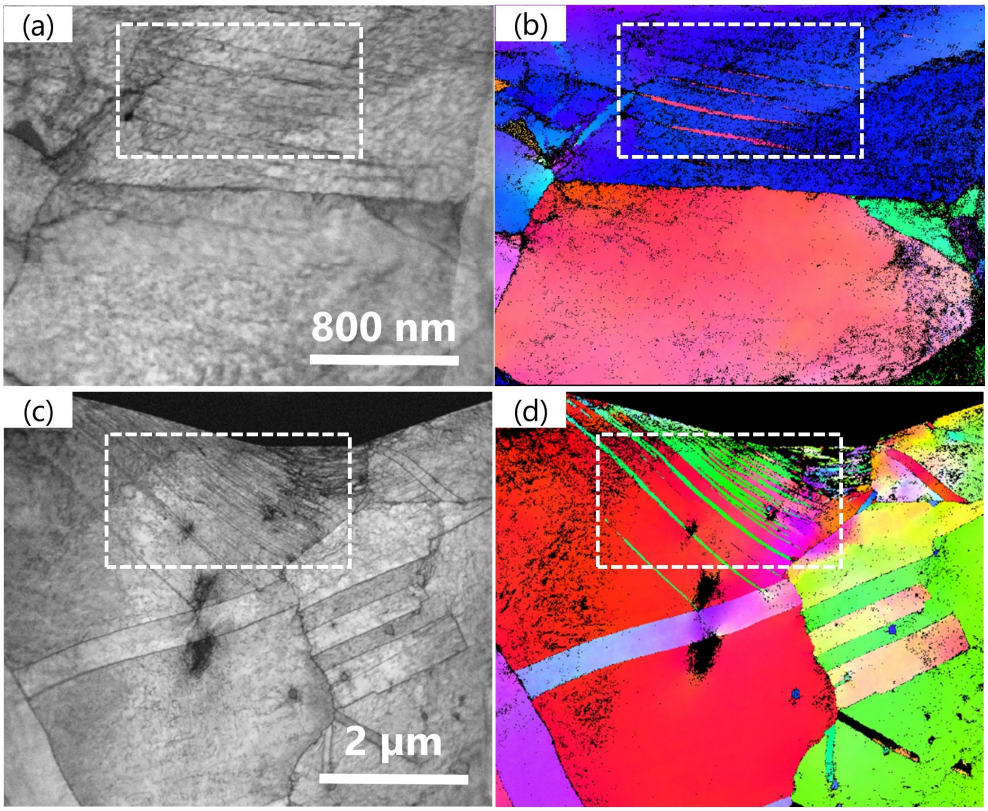


Figure 6.18: TKD band contrast images and orientation maps of indented CSW irradiated using 2 MeV Ni^+ ions at (a,b) 0.63 dpa and (c,d) 2.84 dpa. Note that the irradiated layer is 800-900 nm.

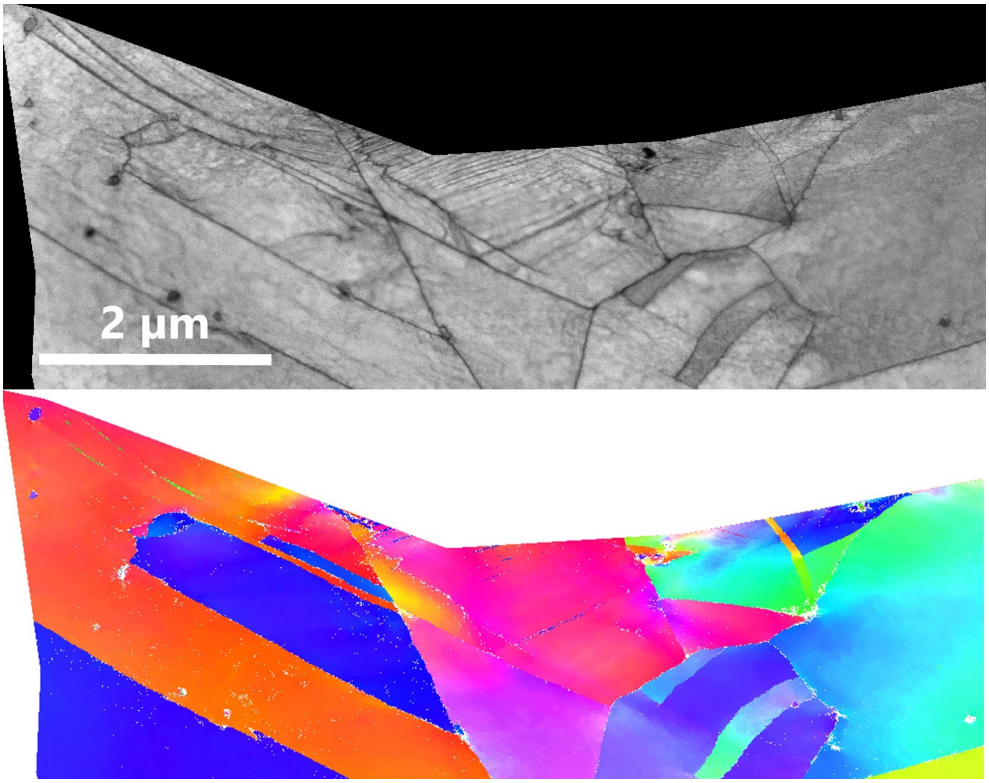


Figure 6.19: TKD band contrast images and orientation maps of indented YCSW irradiated using 2 MeV Ni^+ ions at 2.84 dpa. Note here that the irradiated layer is 800-900 nm.

Figure 6.20 shows STEM-ADF images of indented CSW and YCSW irradiated using 2 MeV Ni^+ ions at 2.84 dpa with corresponding SAED patterns in the region close to the top surface in the inset. There were extensive thin deformation nanotwins (10-20 nm), which were confirmed by the analysis of SAED pattern.

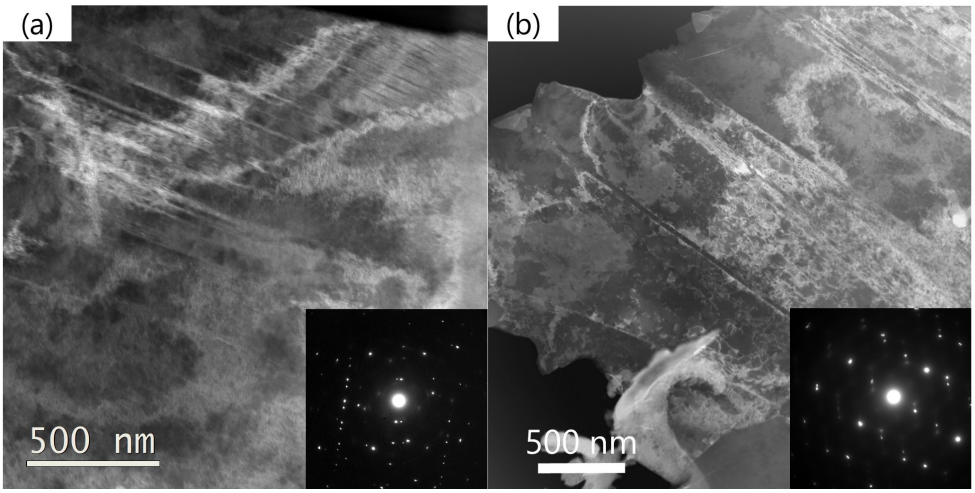


Figure 6.20: STEM-ADF images of indented CSW and YCSW irradiated using 2 MeV Ni^{+} ions at 2.84 dpa with corresponding SAED patterns in the region close to the top surface in the inset.

For CSW and YCSW after irradiation, induced dislocation loops, lines and networks are suggested to hinder dislocation motion which leads to local stress concentration, and the local stress exceeded the CRSS for twin formation. Similar phenomenon was observed in He-implanted F/M steels where the CRSS for twinning was exceeded due to the high stress level caused by the irradiation hardening effect.[281] In ion-irradiated 304L SS which also has a relatively low stacking fault energy as the Cantor alloy, large, stable interstitial loops were suggested to be effective in blocking dislocation motion and promoting twin nucleation at room temperature.[282] In the case of unirradiated YCSW, nano-twinning also occurred, suggesting that the presence of the dispersion of Y-based oxides, even a low volume fraction, was sufficient to pin dislocation activity, and promote twin nucleation.

As already investigated in this thesis, deformation twinning in the

Cantor alloy plays a significant role in providing a steady work hardening rate and delaying the onset of failure at cryogenic temperatures. The onset of deformation nano-twinning in irradiated Cantor alloys at room temperature helps accommodate plastic deformation, thus likely providing work-hardening when planar slip deformation is unavailable. This finding might suggest a pathway to alleviate the loss of bulk ductility in irradiated alloys. However, the present study shows only preliminary results, and further investigation is needed to examine the effect of irradiation on bulk mechanical properties.

6.4 Conclusions

The effect of irradiation on CSW and YCSW has been investigated in terms of radiation-induced segregation, dislocation lines and loops, and nanoindentation response. CSW and YCSW showed significant depletion of Mn (10 at.%), slight depletion of Cr (16 at.%), significant enrichment of Ni (∼25-30 at.%) and slight enrichment of Co and Fe (∼22-25 at.%) at GBs when irradiated at high dose (2.33 dpa and 2.84 dpa), which was consistent with the MIK model. The magnitude of RIS was similar for CSW and YCSW. There was no obvious evidence for any irradiation-induced change in Y-based oxides formed in YCSW. Secondary phases, including Cr-rich, MnNi-rich and FeCo-rich precipitates formed at GBs, possibly due to exposure at 500℃. This temperature is likely typical of the service temperature of core structural materials in GenIV reactors.

Irradiated CSW and YCSW contained partial and perfect dislocation loops. Long dislocation lines and dislocation networks were mostly observed at high dose. No voids or stacking fault tetrahedra (SFT) were observed. Quantitative examination of loops suggested that YCSW showed better irradiation resistance than CSW in terms of smaller average size, lower number density and slower growth rate of loops, which was likely due to the oxide particles acting as sink for point defects. In general, CSW and YCSW showed no obvious improvement in irradiation resistance over comparable conventional alloys such as 316SS.

At the depth with highest damage predicted by SRIM, CSW and YCSW showed 5.5% and 2.8% hardening at 0.63 dpa and 8% and 7.3% at 2.84 dpa when irradiated with 2 MeV Ni^+ ions. When irradiated with 2 MeV V^+ ions, CSW and YCSW showed 6.7% and 5.3% hardening at 0.51 dpa and 10.9% and 9% hardening at 2.33 dpa. YCSW showed less hardening than CSW, agreeing with higher resistance to loop formation. In addition, hardening is likely related to dose rate and lower dose rate causes higher hardening in CSW and YCSW. A FIB-based technique was used to selectively obtain foils from regions of severe plastic deformation under nano-indents. Comparing the microstructure after nanoindentation, irradiation-induced hardening was suggested to be a synergistic effect from dislocation loops, dose rate, RIS along GBs, secondary phase precipitates at GBs as well as complex dislocation lines and network. Irradiation-induced defect clusters were suggested to cause stress con-

centration, which promoted the onset of fine-scale twinning in CSW that were otherwise rarely present.

7 Conclusions

The thesis has investigated the microstructure, mechanical properties and irradiation response of bulk spray-formed CrMnFeCoNi-(Y) using advanced characterisation techniques, such as FIB, EBSD, TEM and TKD, along with both bulk and micromechanical testing, and heavy ion irradiation. The key findings are summarised below:

CSP, YCSP, CSW and YCSW (∼15 kg billets) showed single phase structures as spray-formed, with equiaxed, polygonal (non-dendritic) grains with a high-level of principal elemental homogeneity and absence of micro-segregation, characteristic of spray forming under optimum conditions. Immediately prior to dispensing the melt, Y was added in an attempt to subsequently precipitate a fine dispersion of Y-based oxides.

There was a low fraction of non-metallic inclusions in CSP, possibly due to impurities in feedstock materials and/or contamination during vacuum induction casting, which is somewhat inevitable for bulk, high temperature melt processing of commercial purity materials and very reactive Y, using refractory ceramics. The average grain size of CSP, YCSP, CSW and YCSW was 48.5, 22.3, 8.2 and 5.4 μm. The addition of Y significantly inhibited grain growth by reacting with "internal" oxygen to form Y-based oxides with average size of 425 ± 17 nm and volume fraction of $0.307 \pm 0.02\%$. These "in situ" oxides were significantly larger than those in conventional ODS alloys (10-40 nm) made in small batches by powder processing. There was also a population of Y_2O_3 dispersoids

of a few nanometers identified using TEM and HRTEM. Some Y-based oxides were nanocrystalline Y_2O_3 while other were Y-based oxides of varying composition. Cr-rich $M_{23}C_6$ in CSW was likely due to trace C in the feedstock materials as well as pick-up during melting and dispensing.

Uniaxial tensile properties of CSP, CSW and YCSW were obtained at 23℃ and -196℃. Compared with Cantor alloys made by other techniques (usually at a small scale), and thus with various average grain sizes, the alloys showed comparable tensile properties, which confirmed the potential for spray forming of large ingots. Rather than the limited ductility ($< 5\%$) of other ODS-HEAs, especially those produced from powders, YCSW showed well-balanced strength and ductility, similar to conventional austensitic ODS steels. The approach of forming a dispersion of Y-based oxides in-situ during spray forming showed encouragement, but further optimisation is needed.

Grain boundary strengthening was shown as the main strengthening mechanism in all alloys with only limited precipitation strengthening in YCSW due to low volume fraction and relatively coarse Y-based oxides. Yield strength in general followed a Hall-Petch relationship with k_y=789.3 $\pm$ 74.0 MPa $\cdot$ μm$^{-1/2}$ and σ_0=99.1 $\pm$ 24.4 MPa at 23℃ and k_y=783 $\pm$ 128 MPa $\cdot$ μm$^{-1/2}$ and σ_0=370 $\pm$ 42 MPa at -196℃.

The deformation behavior of CSW and YCSW deformed and fractured at -196℃ was investigated post-mortem by EBSD, TEM, HRTEM and TKD. There was a strong $\langle 111 \rangle$ and a moderate $\langle 001 \rangle$ deformation

texture, typical in FCC metals and alloys after tensile deformation. Deformation nano-twinning depended strongly on crystallographic orientation relative to TA, in which grains oriented close to ⟨111⟩ ∥ TA favoured twining whereas grains oriented close to ⟨001⟩ ∥ TA were largely twin free. There were many multiple twin variants, in regions of higher strain, even in grains where twinning was not preferred. Widespread twinning caused twin-twin intersections that helped to accommodate plastic deformation. Profuse nano-stacking faults evidenced by HRTEM were also suggested to increase dislocation storage capacity and sustain a steady work-hardening rate at the later stage of work hardening.

CSW and YCSW were irradiated using 2 MeV V^+ ions of 0.51 and 2.33 dpa at 500℃ and 2 MeV Ni^+ ions of 0.63 and 2.84 dpa at 500℃, and the effect on RIS, radiation-induced dislocation lines and loops as well hardening was studied. CSW and YCSW showed significant depletion of Mn (10 at.%), slight depletion of Cr (16 at.%), significant enrichment of Ni (∼25-30 at.%) and slight enrichment of Co and Fe (∼22-25 at.%) at grain boundaries (GBs) when irradiated at high dose. There was no obvious irradiation-induced change in Y-based oxides. Secondary phases, including Cr-rich, MnNi-rich and FeCo-rich precipitates formed at GBs, likely due to thermal exposure at 500℃ during irradiation. There were $1/3\langle 111\rangle$ partial dislocation loops and $1/2\langle 110\rangle$ perfect loops in CSW and YCSW irradiated at all conditions. Loops showing good contrast were interstitial type, but with the nature of some loops unidentified.

Long dislocation lines and dislocation networks were mostly observed at high dose. YCSW showed better irradiation resistance than CSW with smaller average size, lower number density and slower growth rate of loops, which was likely due to oxide particles acting as sinks for point defects. In terms of RIS and dislocation loops, CSW and YCSW showed no obvious improvement in irradiation resistance than conventional alloys such as 316SS.

At the depth at the highest damage occurred as predicted by SRIM, CSW and YCSW irradiated with 2 MeV Ni^+ ions showed 5.5% and 2.8% hardening at 0.63 dpa and 8% and 7.3% at 2.84 dpa. When irradiated with 2 MeV V^+ ions, CSW and YCSW showed 6.7% and 5.3% hardening at 0.51 dpa and 10.9% and 9% hardening at 2.33 dpa. Irradiation-induced hardening was likely caused by a synergistic effect from the interaction of induced dislocation loops, dose rate, RIS along GBs, secondary phase precipitates at GBs, and complex dislocation network. Using TKD, deformation twinning, rarely observed in unirradiated CSW, occurred in irradiated CSW, likely because of stress concentration effects due to irradiation-induced defect clusters.

8 Future work

There are still many unanswered questions and areas which merit further study. Some suggestions for future work are shown below:

In the spray-formed Cantor alloy+Y billet, the Y-based oxides were not as finely dispersed as achieved in mechanical alloying followed by consolidation, leading to limited precipitation hardening. It is not known if greater control in oxide fraction and size might be achieved in the spray forming route, but the potential scale-up benefits warrant further investigation, including the effect of swaging and annealing procedures on the distribution of Y-based oxides.

The formation of Y-based oxides and especially Cr-rich precipitates during long-term thermal exposure needs greater understanding, independent of any irradiation effects. A comparative examination between secondary phase precipitates (including Y-based oxides, Cr-rich, MnNi-rich and FeCo-rich precipitates) before and after irradiation might be needed in order to better understand the differential effect of irradiation on this alloy class.

In order to understand the underlying mechanism of improved radiation resistance in YCSW, it would be interesting to use in-situ TEM to look at the effect of Y-based oxides and fine dispersoids on the formation and growth of irradiation-induced defect cluster.

Because the TEM foils used for radiation damage characterisation were fairly thick, the visibility of some dislocation loops was affected in

certain g-vectors, leading to incomplete identification of all dislocation loops. It would be desirable - although painstaking - to confirm the nature of dislocation loops, although this may not be critical to understand the overall macroscopic response of the alloy to irradiation.

The range of irradiation doses in the thesis was quite narrow and obvious next step would be to study the irradiation response of CSW and YCSW at different damage doses, dose rates and irradiation temperatures. It would also be interesting to conduct ion irradiation experiments on both the Cantor alloy and conventional alloys simultaneously in order to directly compare their irradiation responses, and confirm if the alloying complexity but microstructural simplicity of the Cantor alloy offers intrinsic irradiation resistance benefits.

The question whether and how well investigations of heavy ions can represent fast neutron irradiation remains essentially unknown in HEAs, and should be addressed in future research.

References

[1] H Zhang, Y Huang, H Ning, CA Williams, AJ London, K Dawson, Z Hong, MJ Gorley, CRM Grovenor, GJ Tatlock, et al. Processing and microstructure characterisation of oxide dispersion strengthened fe–14cr–0.4 ti–0.25 y2o3 ferritic steels fabricated by spark plasma sintering. *Journal of Nuclear Materials*, 464:61–68, 2015.

[2] A Verma, S Kumar, PS Grant, and KAQ O'Reilly. Influence of cooling rate on the fe intermetallic formation in an aa6063 al alloy. *Journal of Alloys and Compounds*, 555:274–282, 2013.

[3] B Cantor, P Grant, and C Johnston. *Automotive Engineering: Lightweight, Functional, and Novel Materials*. CRC Press, 2008.

[4] C Leyens and M Peters. *Titanium and titanium alloys: fundamentals and applications*. John Wiley & Sons, 2003.

[5] J Mi and PS Grant. Modelling the shape and thermal dynamics of ni superalloy rings during spray forming part 1: Shape modelling–droplet deposition, splashing and redeposition. *Acta Materialia*, 56(7):1588–1596, 2008.

[6] RC Reed. *The superalloys: fundamentals and applications*. Cambridge university press, 2008.

[7] JY He, H Wang, HL Huang, XD Xu, MW Chen, Y Wu, XJ Liu, TG Nieh, K An, and ZP Lu. A precipitation-hardened high-entropy alloy with outstanding tensile properties. *Acta Materialia*, 102:187–196, 2016.

[8] YH Zhao, YT Zhu, XZ Liao, Z Horita, and TG Langdon. Tailoring stacking fault energy for high ductility and high strength in ultrafine grained cu and its alloy. *Applied physics letters*, 89(12):121906, 2006.

[9] B Gludovatz, A Hohenwarter, D Catoor, EH Chang, EP George, and RO Ritchie. A fracture-resistant high-entropy alloy for cryogenic applications. *Science*, 345(6201):1153, 2014.

[10] BL Mordike. Development of highly creep resistant magnesium alloys. *Journal of Materials Processing Technology*, 117(3):391–394, 2001.

[11] PK Huang, JW Yeh, TT Shun, and SK Chen. Multi-principal-element alloys with improved oxidation and wear resistance for thermal spray coating. *Advanced Engineering Materials*, 6(1-2):74–78, 2004.

[12] W Xu, N Birbilis, G Sha, Y Wang, JE Daniels, Y Xiao, and M Ferry. A high-specific-strength and corrosion-resistant magnesium alloy. *Nature materials*, 14(12):1229–1235, 2015.

[13] T Smith, K O'Reilly, S Kumar, and I Stone. Influence of grain-refiner addition on the morphology of fe-bearing intermetallics in a semi-solid processed al-mg-si alloy. *Metallurgical and Materials Transactions A*, 44(11):4866–4871, 2013.

[14] A Devaraj, VV Joshi, A Srivastava, S Manandhar, V Moxson, VA Duz, and C Lavender. A low-cost hierarchical nanostructured beta-titanium alloy with high strength. *Nature communications*, 7(1):1–8, 2016.

[15] J Williams. Thermo-mechanical processing of high-performance ti alloys: recent progress and future needs. *Journal of materials processing technology*, 117(3):370–373, 2001.

[16] F Otto, A Dlouhý, C Somsen, H Bei, G Eggeler, and EP George. The influences of temperature and microstructure on the tensile properties of a cocrfemnni high-entropy alloy. *Acta Materialia*, 61(15):5743–5755, 2013.

[17] YJ Zhou, Y Zhang, YL Wang, and GL Chen. Solid solution alloys of al co cr fe ni ti x with excellent room-temperature mechanical properties. *Applied physics letters*, 90(18):181904, 2007.

[18] Z Zhang, H Zhang, Y Tang, Y Ye, S Li, S Bai, et al. Microstructure, mechanical properties and energetic characteristics of a novel high-entropy alloy hfzrtita0. 53. *Materials & Design*, 133:435–443, 2017.

[19] B Cantor, ITH Chang, P Knight, and AJB Vincent. Microstructural development in equiatomic multicomponent alloys. *Materials Science and Engineering A*, 375-377:213–218, 2004.

[20] JW Yeh, SK Chen, SJ Lin, JY Gan, TS Chin, TT Shun, CH Tsau, and SY Chang. Nanostructured High-Entropy Alloys with Multiple

Principal Elements: Novel Alloy Design Concepts and Outcomes. *Advanced Engineering Materials*, 6(5):299–303, 2004.

[21] F Otto, A Dlouhỳ, KG Pradeep, M Kuběnová, D Raabe, G Eggeler, and EP George. Decomposition of the single-phase high-entropy alloy crmnfeconi after prolonged anneals at intermediate temperatures. *Acta Materialia*, 112:40–52, 2016.

[22] B Schuh, F Mendez-Martin, B Völker, EP George, H Clemens, R Pippan, and A Hohenwarter. Mechanical properties, microstructure and thermal stability of a nanocrystalline cocrfemnni high-entropy alloy after severe plastic deformation. *Acta Materialia*, 96:258–268, 2015.

[23] S Singh, N Wanderka, BS Murty, U Glatzel, and J Banhart. Decomposition in multi-component alcocrcufeni high-entropy alloy. *Acta Materialia*, 59(1):182–190, 2011.

[24] CJ Tong, YL Chen, JW Yeh, SJ Lin, SK Chen, TT Shun, CH Tsau, and SY Chang. Microstructure characterization of al x cocrcufeni high-entropy alloy system with multiprincipal elements. *Metallurgical and Materials Transactions A*, 36(4):881–893, 2005.

[25] A Manzoni, H Daoud, R Völkl, U Glatzel, and N Wanderka. Phase separation in equiatomic alcocrfeni high-entropy alloy. *Ultramicroscopy*, 132:212–215, 2013.

[26] PK Huang, JW Yeh, TT Shun, and SK Chen. Multi-principal-element alloys with improved oxidation and wear resistance for thermal spray coating. *Advanced Engineering Materials*, 6(1-2):74–78, 2004.

[27] Y Zhang, G Stocks, K Jin, C Lu, H Bei, B Sales, L Wang, L Béland, R Stoller, G Samolyuk, et al. Influence of chemical disorder on energy dissipation and defect evolution in concentrated solid solution alloys. *Nature communications*, 6:8736, 2015.

[28] EJ Pickering and NG Jones. High-entropy alloys: a critical assessment of their founding principles and future prospects. *International Materials Reviews*, 61(3):183–202, 2016.

[29] Z Li, S Zhao, RO Ritchie, and MA Meyers. Mechanical properties of high-entropy alloys with emphasis on face-centered cubic alloys. *Progress in Materials Science*, 102:296 – 345, 2019.

[30] C Lu, L Niu, N Chen, K Jin, T Yang, P Xiu, Y Zhang, F Gao, H Bei, S Shi, et al. Enhancing radiation tolerance by controlling defect mobility and migration pathways in multicomponent single-phase alloys. *Nature communications*, 7:13564, 2016.

[31] ON Senkov, GB Wilks, JM Scott, and DB Miracle. Mechanical properties of Nb25Mo25Ta25W25 and V20Nb20Mo20Ta20W20 refractory high entropy alloys. *Intermetallics*, 19(5):698–706, 2011.

[32] B Gludovatz, A Hohenwarter, KVS Thurston, H Bei, Z Wu, EP George, and RO Ritchie. Exceptional damage-tolerance of a medium-entropy alloy crconi at cryogenic temperatures. *Nature communications*, 7(1):1–8, 2016.

[33] EJ Pickering, R Muñoz-Moreno, HJ Stone, and NG Jones. Precipitation in the equiatomic high-entropy alloy crmnfeconi. *Scripta Materialia*, 113:106–109, 2016.

[34] G Laplanche, A Kostka, OM Horst, G Eggeler, and EP George. Microstructure evolution and critical stress for twinning in the crmnfeconi high-entropy alloy. *Acta Materialia*, 118:152–163, 2016.

[35] G Laplanche, O Horst, F Otto, G Eggeler, and EP George. Microstructural evolution of a cocrfemnni high-entropy alloy after swaging and annealing. *Journal of Alloys and Compounds*, 647:548–557, 2015.

[36] J Kim, K Lim, J Won, Y Na, and H Kim. Mechanical properties and deformation twinning behavior of as-cast cocrfemnni high-entropy alloy at low and high temperatures. *Materials Science and Engineering: A*, 712:108–113, 2018.

[37] DB Miracle and ON Senkov. A critical review of high entropy alloys and related concepts. *Acta Materialia*, 122:448–511, 2017.

[38] Z Zhang, MM Mao, J Wang, B Gludovatz, Z Zhang, SX Mao, EP George, Q Yu, and RO Ritchie. Nanoscale origins of the damage tolerance of the high-entropy alloy crmnfeconi. *Nature communications*, 6(1):1–6, 2015.

[39] AJ Zaddach, C Niu, CC Koch, and DL Irving. Mechanical properties and stacking fault energies of nifecrcomn high-entropy alloy. *Jom*, 65(12):1780–1789, 2013.

[40] S Huang, W Li, S Lu, F Tian, J Shen, E Holmström, and L Vitos. Temperature dependent stacking fault energy of fecrconimn high entropy alloy. *Scripta Materialia*, 108:44–47, 2015.

[41] T Egami, W Guo, PD Rack, and T Nagase. Irradiation resistance of multicomponent alloys. *Metallurgical and Materials Transactions A*, 45(1):180–183, 2014.

[42] DJ Hill. Nuclear energy for the future. *Nature Materials*, 7(9):680–682, 2008.

[43] SJ Zinkle and GS Was. Materials challenges in nuclear energy. *Acta Materialia*, 61(3):735–758, 2013.

[44] TT Claudson, RW Barker, and RL Fish. The effects of fast flux irradiation on the mechanical properties and dimensional stability of stainless steel. *Nuclear applications and technology*, 9(1):10–23, 1970.

[45] P Yvon and F Carre. Structural materials challenges for advanced reactor systems. *Journal OF Nuclear Materials*, 385(2):217–222, MAR 31 2009. 3rd Symposium on Nuclear Materials held at the EMRS 2008 Spring Meeting, Strasbourg, FRANCE, MAY 26-30, 2008.

[46] M Matijasevic and A Almazouzi. Effect of cr on the mechanical properties and microstructure of fe–cr model alloys after n-irradiation. *Journal of Nuclear Materials*, 377(1):147–154, 2008.

[47] KL Murty and I Charit. Structural materials for gen-iv nuclear reactors: Challenges and opportunities. *Journal of Nuclear Materials*, 383(1-2):189–195, 2008.

[48] SJ Zinkle and LL Snead. Designing radiation resistance in materials for fusion energy. *Annual Review of Materials Research*, 44:241–267, 2014.

[49] M Rieth, Sergei L Dudarev, SM Gonzalez De Vicente, J Aktaa, T Ahlgren, S Antusch, DEJ Armstrong, M Balden, Nadine Baluc,

MF Barthe, et al. Recent progress in research on tungsten materials for nuclear fusion applications in europe. *Journal of Nuclear Materials*, 432(1-3):482–500, 2013.

[50] GS Was, P Ampornrat, G Gupta, S Teysseyre, EA West, TR Allen, K Sridharan, L Tan, Y Chen, X Ren, et al. Corrosion and stress corrosion cracking in supercritical water. *Journal of Nuclear Materials*, 371(1-3):176–201, 2007.

[51] A Kareer, JC Waite, B Li, A Couet, DEJ Armstrong, and AJ Wilkinson. 'low activation, refractory, high entropy alloys for nuclear applications'. *Journal of Nuclear Materials*, 526:151744, 2019.

[52] O El-Atwani, N Li, M Li, A Devaraj, JKS Baldwin, MM Schneider, D Sobieraj, JS Wróbel, D Nguyen-Manh, SA Maloy, et al. Outstanding radiation resistance of tungsten-based high-entropy alloys. *Science advances*, 5(3):eaav2002, 2019.

[53] Y Zhang, X Wang, Y Osetsky, Y Tong, R Harrison, S Donnelly, D Chen, Y Wang, H Bei, B Sales, et al. Effects of 3d electron configurations on helium bubble formation and void swelling in concentrated solid-solution alloys. *Acta Materialia*, 181:519–529, 2019.

[54] S Zhao, G Velisa, H Xue, H Bei, WJ Weber, and Y Zhang. Suppression of vacancy cluster growth in concentrated solid solution alloys. *Acta Materialia*, 125:231–237, 2017.

[55] YH Jo, S Jung, WM Choi, SS Sohn, HS Kim, BJ Lee, NJ Kim, and S Lee. Cryogenic strength improvement by utilizing room-temperature deformation twinning in a partially recrystallized vcrmnfeconi high-entropy alloy. *Nat Commun*, 8:15719, 2017.

[56] AJ Zaddach, RO Scattergood, and CC Koch. Tensile properties of low-stacking fault energy high-entropy alloys. *Materials Science and Engineering: A*, 636:373–378, 2015.

[57] Z Li, K G Pradeep, Y Deng, D Raabe, and CC Tasan. Metastable high-entropy dual-phase alloys overcome the strength-ductility trade-off. *Nature*, 534(7606):227–230, 2016.

[58] G Laplanche, P Gadaud, O Horst, F Otto, G Eggeler, and EP George. Temperature dependencies of the elastic moduli and thermal expansion coefficient of an equiatomic, single-phase cocrfemnni high-entropy alloy. *Journal of Alloys and Compounds*, 623:348–353, 2015.

[59] G Laplanche, O Horst, F Otto, G Eggeler, and EP George. Microstructural evolution of a cocrfemnni high-entropy alloy after swaging and annealing. *Journal of Alloys and Compounds*, 647:548–557, 2015.

[60] CC Tasan, Y Deng, KG Pradeep, MJ Yao, H Springer, and D Raabe. Composition dependence of phase stability, deformation mechanisms, and mechanical properties of the cocrfemnni high-entropy alloy system. *Jom*, 66(10):1993–2001, 2014.

[61] J Moon, SI Hong, JW Bae, MJ Jang, D Yim, and HS Kim. On the strain rate-dependent deformation mechanism of cocrfemnni high-entropy alloy at liquid nitrogen temperature. *Materials Research Letters*, 5(7):472–477, 2017.

[62] SI Hong, J Moon, SK Hong, and HS Kim. Thermally activated deformation and the rate controlling mechanism in cocrfemnni high entropy alloy. *Materials Science and Engineering: A*, 682:569–576, 2017.

[63] PS Grant. Solidification in spray forming. *Metallurgical and Materials Transactions A*, 38(7):1520–1529, Jul 2007.

[64] National Research Council. *Materials Science and Engineering for the 1990s: Maintaining Competitiveness in the Age of Materials*. The National Academies Press, Washington, DC, 1989.

[65] MC Flemings. What next for departments of materials science and engineering? *Annual Review of Materials Science*, 29(1):1–23, 1999.

[66] SJ Sun, YZ Tian, HR Lin, XG Dong, YH Wang, ZJ Zhang, and ZF Zhang. Enhanced strength and ductility of bulk cocrfemnni high entropy alloy having fully recrystallized ultrafine-grained structure. *Materials & Design*, 133:122–127, 2017.

[67] SJ Sun, YZ Tian, HR Lin, HJ Yang, XG Dong, YH Wang, and ZF Zhang. Transition of twinning behavior in cocrfemnni high entropy alloy with grain refinement. *Materials Science and Engineering: A*, 712:603–607, 2018.

[68] W Ji, W Wang, H Wang, J Zhang, Y Wang, F Zhang, and Z Fu. Alloying behavior and novel properties of cocrfenimn high-entropy alloy fabricated by mechanical alloying and spark plasma sintering. *Intermetallics*, 56:24–27, 2015.

[69] SH Joo, H Kato, MJ Jang, J Moon, EB Kim, SJ Hong, and HS Kim. Structure and properties of ultrafine-grained cocrfemnni high-entropy alloys produced by mechanical alloying and spark plasma sintering. *Journal of Alloys and Compounds*, 698:591–604, 2017.

[70] N Eißmann, B Klöden, T Weißgärber, and B Kieback. High-entropy alloy cocrfemnni produced by powder metallurgy. *Powder Metallurgy*, 60(3):184–197, 2017.

[71] D Yim, W Kim, S Praveen, MJ Jang, JW Bae, J Moon, E Kim, SJ Hong, and HS Kim. Shock wave compaction and sintering of mechanically alloyed cocrfemnni high-entropy alloy powders. *Materials Science and Engineering: A*, 708:291–300, 2017.

[72] Y Liu, J Wang, Q Fang, B Liu, Y Wu, and S Chen. Preparation of superfine-grained high entropy alloy by spark plasma sintering gas atomized powder. *Intermetallics*, 68:16–22, 2016.

[73] H Shahmir, J He, Z Lu, M Kawasaki, and TG Langdon. Effect of annealing on mechanical properties of a nanocrystalline cocrfenimn high-entropy alloy processed by high-pressure torsion. *Materials Science and Engineering: A*, 676:294–303, 2016.

[74] H Shahmir, T Mousavi, J He, Z Lu, M Kawasaki, and TG Langdon. Microstructure and properties of a cocrfenimn high-entropy alloy processed by equal-channel angular pressing. *Materials Science and Engineering: A*, 705:411–419, 2017.

[75] Z Tong, X Ren, J Jiao, W Zhou, Y Ren, Y Ye, EA Larson, and J Gu. Laser additive manufacturing of fecrcomnni high-entropy alloy: Effect of heat treatment on microstructure, residual stress and

mechanical property. *Journal of Alloys and Compounds*, 785:1144–1159, 2019.

[76] MJ Jang, S Praveen, HJ Sung, JW Bae, J Moon, and HS Kim. High-temperature tensile deformation behavior of hot rolled crmnfeconi high-entropy alloy. *Journal of Alloys and Compounds*, 730:242–248, 2018.

[77] J Chen, Z Yao, X Wang, Y Lu, X Wang, Y Liu, and X Fan. Effect of c content on microstructure and tensile properties of as-cast cocrfemnni high entropy alloy. *Materials Chemistry and Physics*, 2017.

[78] GH Sousa, G Zepon, and EM Mazzer. Microstructure evolution and strengthening by cold rolling of crmnfeconi high-entropy alloy processed by spray forming. *Materials Science and Engineering: A*, 793:139814, 2020.

[79] PS Grant. Spray forming. *Progress in Materials Science*, 39(4):497 – 545, 1995.

[80] M Naeem, H He, F Zhang, H Huang, S Harjo, T Kawasaki, B Wang, S Lan, Z Wu, F Wang, et al. Cooperative deformation in high-entropy alloys at ultralow temperatures. *Science advances*, 6(13):eaax4002, 2020.

[81] SH Joo, H Kato, MJ Jang, J Moon, CW Tsai, JW Yeh, and HS Kim. Tensile deformation behavior and deformation twinning of an equimolar cocrfemnni high-entropy alloy. *Materials Science and Engineering: A*, 689:122–133, 2017.

[82] JX Fu, CM Cao, W Tong, YX Hao, and LM Peng. The tensile properties and serrated flow behavior of a thermomechanically treated cocrfenimn high-entropy alloy. *Materials Science and Engineering: A*, 690:418–426, 2017.

[83] H Shahmir, J He, Z Lu, M Kawasaki, and TG Langdon. Evidence for superplasticity in a cocrfenimn high-entropy alloy processed by high-pressure torsion. *Materials Science and Engineering: A*, 685:342–348, 2017.

[84] S Zhao, Z Li, C Zhu, W Yang, Z Zhang, DEJ Armstrong, PS Grant, RO Ritchie, and MA Meyers. Amorphization in extreme deformation of the crmnfeconi high-entropy alloy. *Science advances*, 7(5):eabb3108, 2021.

[85] Z Yang, M Yang, Y Ma, L Zhou, W Cheng, F Yuan, and X Wu. Strain rate dependent shear localization and deformation mechanisms in the crmnfeconi high-entropy alloy with various microstructures. *Materials Science and Engineering: A*, 793:139854, 2020.

[86] J Moon, SI Hong, J Seol, J Bae, J Park, and H Kim. Strain-rate sensitivity of high-entropy alloys and its significance in deformation. *Materials Research Letters*, 7(12):503–509, 2019.

[87] Z Li, S Zhao, SM Alotaibi, Y Liu, B Wang, and MA Meyers. Adiabatic shear localization in the crmnfeconi high-entropy alloy. *Acta Materialia*, 151:424–431, 2018.

[88] American Society for Testing and Materials. Annual book of astm standards: Iron and steel products. steel-structural, reinforcing, pressure, vessel, railway. Astm, 1983.

[89] A Gali and EP George. Tensile properties of high-and medium-entropy alloys. *Intermetallics*, 39:74–78, 2013.

[90] TS Byun, N Hashimoto, and K Farrell. Temperature dependence of strain hardening and plastic instability behaviors in austenitic stainless steels. *Acta Materialia*, 52(13):3889–3899, 2004.

[91] Z Wu, H Bei, GM Pharr, and EP George. Temperature dependence of the mechanical properties of equiatomic solid solution alloys with face-centered cubic crystal structures. *Acta Materialia*, 81:428–441, 2014.

[92] DT Read and RP Reed. Fracture and strength properties of selected austenitic stainless steels at cryogenic temperatures. *Cryogenics*, 21(7):415–417, 1981.

[93] G Laplanche, P Gadaud, C Bärsch, K Demtröder, C Reinhart, J Schreuer, and EP George. Elastic moduli and thermal expansion coefficients of medium-entropy subsystems of the crmnfeconi high-entropy alloy. *Journal of Alloys and Compounds*, 746:244–255, 2018.

[94] J Hirth, J Lothe, and T Mura. Theory of dislocations. *Journal of Applied Mechanics*, 50(2):476, 1983.

[95] G Laplanche, J Bonneville, C Varvenne, WA Curtin, and EP George. Thermal activation parameters of plastic flow reveal deformation mechanisms in the crmnfeconi high-entropy alloy. *Acta Materialia*, 143:257–264, 2018.

[96] C Varvenne, A Luque, and WA Curtin. Theory of strengthening in fcc high entropy alloys. *Acta Materialia*, 118:164–176, 2016.

[97] MZ Butt, Z Rafi, and MA Khan. Low-temperature anomaly in the strength of copper-manganese alloy single crystals. *physica status solidi (a)*, 120(2):K149–K154, 1990.

[98] RJ Arsenault and S Li. Thermally activated dislocation motion in fcc solid solutions. In *Strength of Metals and Alloys (ICSMA 8)*, pages 187–192. Elsevier, 1989.

[99] MZ Butt. Correlation between temperature dependence of critical resolved shear stress and nature of solute distribution in aluminium-magnesium alloys. *Journal of Materials Science Letters*, 7(8):879–880, 1988.

[100] EH Lee, TS Byun, JD Hunn, MH Yoo, K Farrell, and LK Mansur. On the origin of deformation microstructures in austenitic stainless steel: part i—microstructures. *Acta materialia*, 49(16):3269–3276, 2001.

[101] Z Yanushkevich, SV Dobatkin, A Belyakov, and R Kaibyshev. Hall-petch relationship for austenitic stainless steels processed by large strain warm rolling. *Acta Materialia*, 136:39–48, 2017.

[102] RA Varin and KJ Kurzydlowski. The effects of nitrogen content and twin boundaries on the yield strength of various commercial heats of type 316 austenitic stainless steel. *Materials Science and Engineering: A*, 101:221–226, 1988.

[103] A Raturi, K Biswas, and NP Gurao. A mechanistic perspective on the kinetics of plastic deformation in fcc high entropy alloys: Effect of strain, strain rate and temperature. *Scripta Materialia*, 197:113809, 2021.

[104] X Chen, Q Wang, Z Cheng, M Zhu, H Zhou, P Jiang, L Zhou, Q Xue, F Yuan, J Zhu, et al. Direct observation of chemical short-range order in a medium-entropy alloy. *Nature*, 592(7856):712–716, 2021.

[105] R Zhang, S Zhao, J Ding, Y Chong, T Jia, C Ophus, M Asta, RO Ritchie, and AM Minor. Short-range order and its impact on the crconi medium-entropy alloy. *Nature*, 581(7808):283–287, 2020.

[106] C Lei, X Deng, X Li, Z Wang, G Wang, and RDK Misra. Mechanical properties and strain hardening behavior of phase reversion-induced nano/ultrafine fe-17cr-6ni austenitic structure steel. *Journal of Alloys and Compounds*, 689:718–725, 2016.

[107] BP Kashyap. Towards interrelationship of grain size, cell parameters and flow stress in type 316l stainless steel. *Acta materialia*, 50(9):2413–2427, 2002.

[108] SSS Kumar, M Vasanth, Vajinder Singh, P Ghosal, and T Raghu. An investigation of microstructural evolution in 304l austenitic stainless steel warm deformed by cyclic channel die compression. *Journal of Alloys and Compounds*, 699:1036–1048, 2017.

[109] K Kako, E Kawakami, J Ohta, and M Mayuzumi. Effects of various alloying elements on tensile properties of high-purity fe-18cr-(14-16) ni alloys at room temperature. *Materials transactions*, 43(2):155–162, 2002.

[110] H Traub, H Neuhäuser, and Ch Schwink. Investigations of the yield region of concentrated cuge and cuzn single crystals—i. critical resolved shear stress, slip line formation and the true strain rate. *Acta Metallurgica*, 25(4):437–446, 1977.

[111] NL Okamoto, S Fujimoto, Y Kambara, M Kawamura, ZMT Chen, H Matsunoshita, K Tanaka, H Inui, and EP George. Size effect, critical resolved shear stress, stacking fault energy, and solid solution strengthening in the crmnfeconi high-entropy alloy. *Scientific reports*, 6:35863, 2016.

[112] DR Steinmetz, T Jäpel, B Wietbrock, P Eisenlohr, I Gutierrez-Urrutia, A Saeed-Akbari, T Hickel, F Roters, and D Raabe. Revealing the strain-hardening behavior of twinning-induced plas-

ticity steels: Theory, simulations, experiments. *Acta Materialia*, 61(2):494–510, 2013.

[113] MC Gao, J Yeh, PK Liaw, Y Zhang, et al. High-entropy alloys. *Cham: Springer International Publishing*, 2016.

[114] FK Yan, NR Tao, and K Lu. Tensile ductility of nanotwinned austenitic grains in an austenitic steel. *Scripta Materialia*, 84:31–34, 2014.

[115] I Gutierrez-Urrutia, S Zaefferer, and D Raabe. The effect of grain size and grain orientation on deformation twinning in a fe–22 wt.% mn–0.6 wt.% c twip steel. *Materials Science and Engineering: A*, 527(15):3552–3560, 2010.

[116] S Zhao, GM Stocks, and Y Zhang. Stacking fault energies of face-centered cubic concentrated solid solution alloys. *Acta Materialia*, 134:334–345, 2017.

[117] H. Beladi, I.B. Timokhina, Y. Estrin, J. Kim, B.C. De Cooman, and S.K. Kim. Orientation dependence of twinning and strain hardening behaviour of a high manganese twinning induced plasticity steel with polycrystalline structure. *Acta Materialia*, 59(20):7787 – 7799, 2011.

[118] TK Liu, Z Wu, AD Stoica, Q Xie, W Wu, YF Gao, H Bei, and Ke An. Twinning-mediated work hardening and texture evolution in crcofemnni high entropy alloys at cryogenic temperature. *Materials & Design*, 131:419–427, 2017.

[119] Y Wu, M Bönisch, S Alkan, W Abuzaid, and H Sehitoglu. Experimental determination of latent hardening coefficients in femnnicocr. *International Journal of Plasticity*, 105:239–260, 2018.

[120] PD Edmondson, CM Parish, Y Zhang, Anders Hallén, and MK Miller. Helium bubble distributions in a nanostructured ferritic alloy. *Journal of Nuclear Materials*, 434(1-3):210–216, 2013.

[121] MB Toloczko, DS Gelles, FA Garner, RJ Kurtz, and K Abe. Irradiation creep and swelling from 400 to 600 c of the oxide dispersion strengthened ferritic alloy ma957. *Journal of nuclear materials*, 329:352–355, 2004.

[122] C Capdevila and HKDH Bhadeshia. Manufacturing and microstructural evolution of mechanuically alloyed oxide dispersion strengthened superalloys. *Advanced Engineering Materials*, 3(9):647–656, 2001.

[123] F Bergner, I Hilger, J Virta, J Lagerbom, G Gerbeth, S Connolly, Z Hong, PS Grant, and T Weissgärber. Alternative fabrication routes toward oxide-dispersion-strengthened steels and model alloys. *Metallurgical and Materials Transactions A*, 47(11):5313–5324, 2016.

[124] B Maier, M Lenling, H Yeom, G Johnson, S Maloy, and K Sridharan. A novel approach for manufacturing oxide dispersion strengthened (ods) steel cladding tubes using cold spray technology. *Nuclear Engineering and Technology*, 51(4):1069–1074, 2019.

[125] SC Connolly. *Manufacturing of oxide dispersion strengthened steels for nuclear applications*. PhD thesis, University of Oxford, 2018.

[126] Y De Carlan, JL Bechade, Ph Dubuisson, JL Seran, Ph Billot, A Bougault, T Cozzika, S Doriot, D Hamon, J Henry, et al. Cea developments of new ferritic ods alloys for nuclear applications. *Journal of Nuclear Materials*, 386:430–432, 2009.

[127] C Suryanarayana, E Ivanov, and VV Boldyrev. The science and technology of mechanical alloying. *Materials Science and Engineering: A*, 304:151–158, 2001.

[128] K Asano, Y Kohno, A Kohyama, T Suzuki, and H Kusanagi. Microstructural evolution of an oxide dispersion strengthened steel under charged particle irradiation. *Journal of Nuclear Materials*, 155:928–934, 1988.

[129] P Pareige, MK Miller, RE Stoller, DT Hoelzer, E Cadel, and B Radiguet. Stability of nanometer-sized oxide clusters in mechanically-alloyed steel under ion-induced displacement cascade damage conditions. *Journal of Nuclear Materials*, 360(2):136–142, 2007.

[130] N Akasaka, S Yamashita, T Yoshitake, S Ukai, and A Kimura. Microstructural changes of neutron irradiated ods ferritic and martensitic steels. *Journal of nuclear materials*, 329:1053–1056, 2004.

[131] DT Hoelzer, J Bentley, MA Sokolov, MK Miller, GR Odette, and MJ Alinger. Influence of particle dispersions on the high-temperature strength of ferritic alloys. *Journal of Nuclear Materials*, 367:166–172, 2007.

[132] MC Brandes, L Kovarik, MK Miller, and MJ Mills. Morphology, structure, and chemistry of nanoclusters in a mechanically alloyed nanostructured ferritic steel. *Journal of Materials Science*, 47(8):3913–3923, 2012.

[133] V De Castro, EA Marquis, S Lozano-Perez, R Pareja, and ML Jenkins. Stability of nanoscale secondary phases in an oxide dispersion strengthened fe–12cr alloy. *Acta Materialia*, 59(10):3927–3936, 2011.

[134] D Bhattacharyya, P Dickerson, GR Odette, SA Maloy, A Misra, and MA Nastasi. On the structure and chemistry of complex oxide nanofeatures in nanostructured ferritic alloy u14ywt. *Philosophical Magazine*, 92(16):2089–2107, 2012.

[135] IS Kim, JD Hunn, N Hashimoto, DL Larson, PJ Maziasz, K Miyahara, and EH Lee. Defect and void evolution in oxide dispersion strengthened ferritic steels under 3.2 mev fe+ ion irradiation with simultaneous helium injection. *Journal of Nuclear Materials*, 280(3):264–274, 2000.

[136] AJ London. *Irradiation damage of oxide dispersion strengthened steels*. PhD thesis, University of Oxford, 2016.

[137] CS Zener. quoted by cs smith. *Trans. AIME*, 175:15, 1948.

[138] Manohar PA, M Ferry, and T Chandra. Five decades of the zener equation. *ISIJ international*, 38(9):913–924, 1998.

[139] F Dobeš, H Hadraba, Z Chlup, A Dlouhỳ, M Vilémová, and J Matějíček. Compressive creep behavior of an oxide-dispersion-strengthened cocrfemnni high-entropy alloy. *Materials Science and Engineering: A*, 732:99–104, 2018.

[140] X Liu, H Yin, and Y Xu. Microstructure, mechanical and tribological properties of oxide dispersion strengthened high-entropy alloys. *Materials*, 10(11):1312, 2017.

[141] H Hadraba, Z Chlup, A Dlouhy, F Dobes, P Roupcova, M Vilemova, and J Matejicek. Oxide dispersion strengthened cocrfenimn high-entropy alloy. *Materials Science and Engineering: A*, 689:252–256, 2017.

[142] S Chung, B Lee, S Lee, C Do, and H Ryu. The effects of y pre-alloying on the in-situ dispersoids of ods cocrfemnini high-entropy alloy. *Journal of Materials Science & Technology*, 2021.

[143] Y Guo, M Li, P Li, C Chen, Q Zhan, Y Chang, and Y Zhang. Microstructure and mechanical properties of oxide dispersion strengthened feconi concentrated solid solution alloys. *Journal of Alloys and Compounds*, 820:153104, 2020.

[144] Y Guo, M Li, C Chen, P Li, W Li, Q Ji, Y Zhang, and Y Chang. Oxide dispersion strengthened feconi concentrated solid-solution alloys synthesized by mechanical alloying. *Intermetallics*, 117:106674, 2020.

[145] B Jia, X Liu, H Wang, Y Wu, and Z Lu. Microstructure and mechanical properties of feconicr high-entropy alloy strengthened by nano-y 2 o 3 dispersion. *Science China Technological Sciences*, 61(2):179–183, 2018.

[146] S Peng, Z Lu, and L Yu. Effects of y2o3/ti/zr addition on microstructure and hardness of ods-cocrfeni heas produced by mechanical alloying and spark plasma sintering. *Journal of Alloys and Compounds*, page 157940, 2020.

[147] ML Hamilton, DS Gelles, RJ Lobsinger, GD Johnson, WF Brown, MM Paxton, RJ Puigh, CR Eiholzer, C Martinez, and MA Blotter. Fabrication technological development of the oxide dispersion strengthened alloy ma957 for fast reactor applications. 3 2000.

[148] Y Li, T Nagasaka, T Muroga, A Kimura, and S Ukai. High-temperature mechanical properties and microstructure of 9cr oxide dispersion strengthened steel compared with rafms. *Fusion Engineering and Design*, 86(9):2495–2499, 2011. Proceedings of the 26th Symposium of Fusion Technology (SOFT-26).

[149] T Gräning, M Rieth, J Hoffmann, and A Möslang. Production, microstructure and mechanical properties of two different austenitic ods steels. *Journal of nuclear materials*, 487:348–361, 2017.

[150] DT Hoelzer, KA Unocic, MA Sokolov, and Z Feng. Joining of 14ywt and f82h by friction stir welding. *Journal of Nuclear Materials*, 442(1, Supplement 1):S529–S534, 2013.

[151] Z Zhou, S Sun, L Zou, Y Schneider, S Schmauder, and M Wang. Enhanced strength and high temperature resistance of 25cr20ni ods austenitic alloy through thermo-mechanical treatment and addition of mo. *Fusion Engineering and Design*, 138:175–182, 2019.

[152] M Wang, Z Zhou, Ho Sun, H Hu, and S Li. Microstructural observation and tensile properties of ods-304 austenitic steel. *Materials Science and Engineering: A*, 559:287–292, 2013.

[153] JRO Leo, S Pirfo Barroso, ME Fitzpatrick, M Wang, and Z Zhou. Microstructure, tensile and creep properties of an austenitic ods 316l steel. *Materials Science and Engineering: A*, 749:158–165, 2019.

[154] M Foex and J Traverse. Investigations about crystalline transformation in rare earths sesquioxides at high temperatures. *Rev. Int. Hautes Temp. Refract., 3: 429-53(Oct.-Dec. 1966).*, 1 1966.

[155] Z Jiao and GS Was. Novel features of radiation-induced segregation and radiation-induced precipitation in austenitic stainless steels. *Acta Materialia*, 59(3):1220–1238, 2011.

[156] TR Allen, JT Busby, GS Was, and EA Kenik. On the mechanism of radiation-induced segregation in austenitic fe–cr–ni alloys. *Journal of nuclear materials*, 255(1):44–58, 1998.

[157] GS Was, JP Wharry, B Frisbie, BD Wirth, D Morgan, JD Tucker, and TR Allen. Assessment of radiation-induced segregation mechanisms in austenitic and ferritic–martensitic alloys. *Journal of Nuclear Materials*, 411(1-3):41–50, 2011.

[158] DR Harries. Neutron irradiation-induced embrittlement in type 316 and other austenitic steels and alloys. *Journal of Nuclear Materials*, 82(1):2–21, 1979.

[159] R Bullough and MH Wood. Mechanisms of radiation induced creep and growth. *journal of Nuclear Materials*, 90(1-3):1–21, 1980.

[160] RS Barnes. Embrittlement of stainless steels and nickel-based alloys at high temperature induced by neutron radiation. *Nature*, 206(4991):1307–1310, 1965.

[161] K Krishan. Invited review article ordering of voids and gas bubbles in radiation environments. *Radiation Effects*, 66(3-4):121–155, 1982.

[162] GS Was. Irradiation-induced voids and bubbles. In *Fundamentals of Radiation Materials Science*, pages 379–484. Springer, 2017.

[163] Y Zhang, K Jin, H Xue, C Lu, RJ Olsen, LK Beland, MW Ullah, S Zhao, H Bei, DS Aidhy, et al. Influence of chemical disorder on energy dissipation and defect evolution in advanced alloys. *Journal of Materials Research*, 31(16):2363–2375, 2016.

[164] EJ Pickering, AW Carruthers, PJ Barron, SC Middleburgh, DEJ Armstrong, and AS Gandy. High-entropy alloys for advanced nuclear applications. *Entropy*, 23(1):98, 2021.

[165] Y Zhang, S Zhao, WJ Weber, K Nordlund, F Granberg, and F Djurabekova. Atomic-level heterogeneity and defect dynamics in concentrated solid-solution alloys. *Current Opinion in Solid State and Materials Science*, 21(5):221–237, 2017.

[166] MW Thompson. Defects and radiation damage in metals. *Defects and Radiation Damage in Metals*, 1974.

[167] GS Was. *Fundamentals of radiation materials science: metals and alloys*. springer, 2016.

[168] MR Gilbert, T Eade, T Rey, R Vale, C Bachmann, U Fischer, and NP Taylor. Waste implications from minor impurities in european demo materials. *Nuclear Fusion*, 59(7):076015, 2019.

[169] O Waseem and HJ Ryu. Powder metallurgy processing of a w x tativcr high-entropy alloy and its derivative alloys for fusion material applications. *Scientific reports*, 7(1):1–14, 2017.

[170] A Ayyagari, R Salloom, S Muskeri, and S Mukherjee. Low activation high entropy alloys for next generation nuclear applications. *Materialia*, 4:99–103, 2018.

[171] PJ Barron, AW Carruthers, JW Fellowes, NG Jones, H Dawson, and EJ Pickering. Towards v-based high-entropy alloys for nuclear fusion applications. *Scripta Materialia*, 176:12–16, 2020.

[172] AW Carruthers, BS Li, M Rigby, LC Raquet, R Mythili, C Ghosh, A Dasgupta, DEJ Armstrong, AS Gandy, and EJ Pickering. Novel reduced-activation tivcrfe based high entropy alloys. *Journal of Alloys and Compounds*, page 157399, 2020.

[173] M Sadeghilaridjani, A Ayyagari, S Muskeri, V Hasannaeimi, R Salloom, W Chen, and S Mukherjee. Ion irradiation response and mechanical behavior of reduced activity high entropy alloy. *Journal of Nuclear Materials*, 529:151955, 2020.

[174] M Moschetti, A Xu, B Schuh, A Hohenwarter, J-P Couzinié, JJ Kruzic, D Bhattacharyya, and B Gludovatz. On the room-temperature mechanical properties of an ion-irradiated tizrnbhfta refractory high entropy alloy. *Jom*, 72(1):130–138, 2020.

[175] OA Waseem and HJ Ryu. Helium ions irradiation analysis of w0. 5 (tativcr) 0.5 for application as a future fusion plasma-facing material. *Materials Chemistry and Physics*, page 124198, 2020.

[176] S Zhao. Defect properties in a vtacrw equiatomic high entropy alloy (hea) with the body centered cubic (bcc) structure. *Journal of Materials Science & Technology*, 44:133–139, 2020.

[177] CM Barr, GA Vetterick, KA Unocic, K Hattar, X Bai, and ML Taheri. Anisotropic radiation-induced segregation in 316l austenitic stainless steel with grain boundary character. *Acta Materialia*, 67:145–155, 2014.

[178] LE Rehn, PR Okamoto, DI Potter, and H Wiedersich. Effect of solute misfit and temperature on irradiation-induced segregation in binary ni alloys. *Journal of Nuclear Materials*, 74(2):242–251, 1978.

[179] Z Lu, RG Faulkner, G Was, and BD Wirth. Irradiation-induced grain boundary chromium microchemistry in high alloy ferritic steels. *Scripta Materialia*, 58(10):878–881, 2008.

[180] K Fukuya. Current understanding of radiation-induced degradation in light water reactor structural materials. *Journal of Nuclear Science and Technology*, 50(3):213–254, 2013.

[181] T Nagase, PD Rack, JH Noh, and T Egami. In-situ tem observation of structural changes in nano-crystalline cocrcufeni multicomponent high-entropy alloy (hea) under fast electron irradiation by high voltage electron microscopy (hvem). *Intermetallics*, 59:32–42, 2015.

[182] MR He, S Wang, S Shi, K Jin, H Bei, K Yasuda, S Matsumura, K Higashida, and IM Robertson. Mechanisms of radiation-induced segregation in crfeconi-based single-phase concentrated solid solution alloys. *Acta Materialia*, 126:182–193, 2017.

[183] T Yang, C Lu, G Velisa, K Jin, P Xiu, Y Zhang, H Bei, and L Wang. Influence of irradiation temperature on void swelling in nicofecrmn and nicofecrpd. *Scripta Materialia*, 158:57–61, 2019.

[184] C Lu, T Yang, K Jin, N Gao, P Xiu, Y Zhang, F Gao, H Bei, WJ Weber, K Sun, et al. Radiation-induced segregation on defect clusters in single-phase concentrated solid-solution alloys. *Acta Materialia*, 127:98–107, 2017.

[185] CM Barr, James E Nathaniel II, KA Unocic, J Liu, Y Zhang, Y Wang, and ML Taheri. Exploring radiation induced segregation mechanisms at grain boundaries in equiatomic cocrfenimn high entropy alloy under heavy ion irradiation. *Scripta Materialia*, 156:80–84, 2018.

[186] CM Barr, L Barnard, JE Nathaniel, K Hattar, KA Unocic, I Szlufarska, D Morgan, and ML Taheri. Grain boundary character dependence of radiation-induced segregation in a model ni–cr alloy. *Journal of Materials Research*, 30(9):1290–1299, 2015.

[187] M Vaidya, KG Pradeep, BS Murty, G Wilde, and SV Divinski. Bulk tracer diffusion in cocrfeni and cocrfemnni high entropy alloys. *Acta Materialia*, 146:211–224, 2018.

[188] NK Kumar, C Li, KJ Leonard, H Bei, and SJ Zinkle. Microstructural stability and mechanical behavior of fenimncr high entropy alloy under ion irradiation. *Acta Materialia*, 113:230–244, 2016.

[189] S Zhao, T Egami, GM Stocks, and Y Zhang. Effect of d electrons on defect properties in equiatomic nicocr and nicofecr concentrated solid solution alloys. *Physical Review Materials*, 2(1):013602, 2018.

[190] S Zhao, GM Stocks, and Y Zhang. Defect energetics of concentrated solid-solution alloys from ab initio calculations: Ni 0.5 co 0.5, ni 0.5 fe 0.5, ni 0.8 fe 0.2 and ni 0.8 cr 0.2. *Physical Chemistry Chemical Physics*, 18(34):24043–24056, 2016.

[191] JB Piochaud, TPC Klaver, G Adjanor, Pär Olsson, C Domain, and CS Becquart. First-principles study of point defects in an fcc fe-10ni-20cr model alloy. *Physical Review B*, 89(2):024101, 2014.

[192] JJ Holmes, RE Bobbins, and JL Brimhall. Effect of fast reactor irradiation on the tensile properties of 304 stainless steel. *Journal of Nuclear Materials*, 32(2):330–339, 1969.

[193] F Abe, T Noda, H Araki, M Narui, and H Kayano. Irradiation hardening and ductility loss of a low-activation 9cr-1v ferritic steel at low temperatures. *Journal of Nuclear Materials*, 166(3):265–277, 1989.

[194] MR He, S Wang, K Jin, H Bei, K Yasuda, S Matsumura, K Higashida, and IM Robertson. Enhanced damage resistance and novel defect structure of crfeconi under in situ electron irradiation. *Scripta Materialia*, 125:5–9, 2016.

[195] Q Ding, X Fu, D Chen, H Bei, B Gludovatz, J Li, Z Zhang, EP George, Q Yu, T Zhu, et al. Real-time nanoscale observation of deformation mechanisms in crconi-based medium-to high-entropy alloys at cryogenic temperatures. *Materials Today*, 25:21–27, 2019.

[196] T Yang, C Lu, K Jin, ML Crespillo, Y Zhang, H Bei, and L Wang. The effect of injected interstitials on void formation in self-ion irradiated nickel containing concentrated solid solution alloys. *Journal of Nuclear Materials*, 488:328–337, 2017.

[197] C Lu, K Jin, LK Béland, F Zhang, T Yang, L Qiao, Y Zhang, H Bei, HM Christen, RE Stoller, et al. Direct observation of defect range and evolution in ion-irradiated single crystalline ni and ni binary alloys. *Scientific reports*, 6:19994, 2016.

[198] J Gan, EP Simonen, SM Bruemmer, L Fournier, BH Sencer, and GS Was. The effect of oversized solute additions on the microstructure of 316ss irradiated with 5 mev ni++ ions or 3.2 mev protons. *Journal of nuclear materials*, 325(2-3):94–106, 2004.

[199] T Okita, T Sato, N Sekimura, T Iwai, and FA Garner. The synergistic influence of temperature and displacement rate on microstructural evolution of ion-irradiated fe–15cr–16ni model austenitic alloy. *Journal of nuclear materials*, 367:930–934, 2007.

[200] A Etienne, M Hernández-Mayoral, C Genevois, B Radiguet, and P Pareige. Dislocation loop evolution under ion irradiation in austenitic stainless steels. *Journal of nuclear materials*, 400(1):56–63, 2010.

[201] T Muroga, N Yoshida, and FA Garner. The influence of nickel content on microstructures of fe-cr-ni austenitic alloys irradiated with nickel ions. Technical report, Pacific Northwest Lab., 1990.

[202] SG McDonald and Anthony Taylor. Void swelling behavior of types 304 and 316 stainless steel irradiated with 4-mev ni+ ions. In *Effects of Radiation on Substructure and Mechanical Properties of Metals and Alloys*. ASTM International, 1973.

[203] H Jin, E Ko, S Lim, and J Kwon. Effects of helium and hydrogen on radiation-induced microstructural changes in austenitic stainless steel. *Nuclear Instruments and Methods in Physics Research Section B: Beam Interactions with Materials and Atoms*, 359:69–74, 2015.

[204] K Shiraishi, K Fukai, and E Yagi. Damage profiles in a stainless steel irradiated with ar and n ions. *Journal of nuclear materials*, 179:550–553, 1991.

[205] S Wood, JA Spitznagel, WJ Choyke, NJ Doyle, JN McGruer, and JR Townsend. Microstructural development in dual-ion-bombarded 316 stainless steel. In *Effects of Radiation on Materials*. ASTM International, 1981.

[206] Q Xu, H Watanabe, and N Yoshida. Microstructural evolution in fecrni alloy irradiated with ni ion under varying temperature. *Journal of nuclear materials*, 233:1057–1061, 1996.

[207] HF Huang, JJ Li, DH Li, RD Liu, GH Lei, Q Huang, and L Yan. Tem, xrd and nanoindentation characterization of xenon ion irradiation damage in austenitic stainless steels. *Journal of Nuclear Materials*, 454(1-3):168–172, 2014.

[208] TM Williams. The effect of soluble carbon on void swelling and low dose dislocation structures in type 316 austenitic stainless steel irradiated with 46.5 mev ni6+ ions. *Journal of Nuclear Materials*, 88(2-3):217–225, 1980.

[209] JA Hudson. Void formation in solution-treated aisi 316 and 321 stainless steels under 46.5 mev ni6+ irradiation. *Journal of Nuclear Materials*, 60(1):89–106, 1976.

[210] TM Williams. Interstitial loop nucleation and growth in solution-treated type 316 stainless steel irradiated to low doses with 22 mev c2+ and 46.5 mev ni6+ ions. *Journal of Nuclear Materials*, 79(1):28–42, 1979.

[211] BH Sencer and FA Garner. Compositional and temperature dependence of void swelling in model fe–cr base alloys irradiated in the ebr-ii fast reactor. *Journal of nuclear materials*, 283:164–168, 2000.

[212] FA Garner and MB Toloczko. Irradiation creep and void swelling of austenitic stainless steels at low displacement rates in light water energy systems. *Journal of nuclear materials*, 251:252–261, 1997.

[213] K Jin, H Bei, and Y Zhang. Ion irradiation induced defect evolution in ni and ni-based fcc equiatomic binary alloys. *Journal of Nuclear Materials*, 471:193–199, 2016.

[214] C Lu, T Yang, K Jin, G Velisa, P Xiu, Q Peng, F Gao, Y Zhang, H Bei, WJ Weber, et al. Irradiation effects of medium-entropy alloy nicocr with and without pre-indentation. *Journal of Nuclear Materials*, 524:60–66, 2019.

[215] Y Tong, G Velisa, S Zhao, W Guo, T Yang, K Jin, C Lu, H Bei, JYP Ko, DC Pagan, et al. Evolution of local lattice distortion under irradiation in medium-and high-entropy alloys. *Materialia*, 2:73–81, 2018.

[216] S Xia, MC Gao, T Yang, PK Liaw, and Y Zhang. Phase stability and microstructures of high entropy alloys ion irradiated to high doses. *Journal of Nuclear Materials*, 480:100–108, 2016.

[217] T Yang, S Xia, S Liu, C Wang, S Liu, Y Fang, Y Zhang, J Xue, S Yan, and Y Wang. Precipitation behavior of al x cocrfeni high entropy alloys under ion irradiation. *Scientific reports*, 6:32146, 2016.

[218] C Lu, T Yang, K Jin, G Velisa, P Xiu, M Song, Q Peng, F Gao, Y Zhang, H Bei, et al. Enhanced void swelling in nicofecrpd high-entropy alloy by indentation-induced dislocations. *Materials Research Letters*, 6(10):584–591, 2018.

[219] NH Packan and K Farrell. Radiation-induced swelling in an austenitic alloy: Observations and interpretation of the effects of helium. *Nuclear Technology-Fusion*, 3(3):392–404, 1983.

[220] T Yang. *The Effect of Principal Elements on Defect Evolution in Single-Phase Solid Solution Ni Alloys*. PhD thesis, 2018.

[221] D Chen, Y Tong, H Li, J Wang, YL Zhao, A Hu, and JJ Kai. Helium accumulation and bubble formation in feconicr alloy under high fluence he+ implantation. *Journal of Nuclear Materials*, 501:208–216, 2018.

[222] D Chen, S Zhao, J Sun, P Tai, Y Sheng, Y Zhao, G Yeli, W Lin, S Liu, W Kai, et al. Diffusion controlled helium bubble formation resistance of feconicr high-entropy alloy in the half-melting temperature regime. *Journal of Nuclear Materials*, 526:151747, 2019.

[223] Z Fan, S Zhao, K Jin, D Chen, YN Osetskiy, Y Wang, H Bei, KL More, and Y Zhang. Helium irradiated cavity formation and defect energetics in ni-based binary single-phase concentrated solid solution alloys. *Acta Materialia*, 164:283–292, 2019.

[224] WH Bragg and WL Bragg. The reflection of x-rays by crystals. *Proceedings of the Royal Society of London. Series A, Containing Papers of a Mathematical and Physical Character*, 88(605):428–438, 1913.

[225] S Khalili, V Soleimanian, and A Mokhtari. Developing a method for the evaluation of dislocation parameters from the rietveld refinement procedure. *Powder Diffraction*, 31(3):198, 2016.

[226] J Rodríguez-Carvajal. Fullprof. *CEA/Saclay, France*, 2001.

[227] JC Russ. *Fundamentals of energy dispersive X-ray analysis: Butterworths monographs in materials*. Butterworth-Heinemann, 2013.

[228] S Burgess, X Li, and J Holland. High spatial resolution energy dispersive x-ray spectrometry in the sem and the detection of light elements including lithium. *Microscopy and Analysis*, 6:S8–S13, 2013.

[229] I Barkshire, P Karduck, WP Rehbach, and S Richter. High-spatial-resolution low-energy electron beam x-ray microanalysis. *Microchimica Acta*, 132(2-4):113–128, 2000.

[230] J Liu. *High resolution structural analysis of irradiated zirconium alloys*. PhD thesis, University of Oxford, 2019.

[231] AJ Schwartz, M Kumar, BL Adams, and DP Field. *Electron backscatter diffraction in materials science*, volume 2. Springer, 2009.

[232] PW Trimby. Orientation mapping of nanostructured materials using transmission kikuchi diffraction in the scanning electron microscope. *Ultramicroscopy*, 120:16–24, 2012.

[233] DB Williams and CB Carter. The transmission electron microscope. In *Transmission electron microscopy*, pages 3–17. Springer, 1996.

[234] J Mayer, LA Giannuzzi, T Kamino, and J Michael. Tem sample preparation and fib-induced damage. *MRS bulletin*, 32(5):400–407, 2007.

[235] ML Jenkins and MA Kirk. *Characterisation of radiation damage by transmission electron microscopy*. CRC Press, 2000.

[236] J Schindelin, I Arganda-Carreras, E Frise, V Kaynig, M Longair, T Pietzsch, S Preibisch, C Rueden, S Saalfeld, B Schmid, et al. Fiji: an open-source platform for biological-image analysis. *Nature methods*, 9(7):676–682, 2012.

[237] J Haley. *TEM of neutron, proton and self-ion irradiation damage in FeCr alloys*. PhD thesis, University of Oxford, 2018.

[238] WC Oliver and GM Pharr. An improved technique for determining hardness and elastic modulus using load and displacement sensing indentation experiments. *Journal of materials research*, 7(6):1564–1583, 1992.

[239] GM Pharr, EG Herbert, and Y Gao. The indentation size effect: a critical examination of experimental observations and mechanistic interpretations. *Annual Review of Materials Research*, 40:271–292, 2010.

[240] ASTM Standard. E8. standard test method for tension testing of metallic materials. *West Conshohocken (USA): ASTM*, 2004.

[241] GS Was, Z Jiao, E Getto, K Sun, AM Monterrosa, SA Maloy, O Anderoglu, BH Sencer, and M Hackett. Emulation of reactor irradiation damage using ion beams. *Scripta Materialia*, 88:33–36, 2014.

[242] GS Was and Robert S Averback. Radiation damage using ion beams. In *Comprehensive Nuclear Materials*, pages 195–221. Elsevier Ltd, 2012.

[243] LK Mansur. Void swelling in metals and alloys under irradiation: an assessment of the theory. *Nuclear Technology*, 40(1):5–34, 1978.

[244] GS Was. Challenges to the use of ion irradiation for emulating reactor irradiation. *Journal of Materials Research*, 30(9):1158–1182, 2015.

[245] GS Was and T Allen. Intercomparison of microchemical evolution under various types of particle irradiation. *Journal of nuclear materials*, 205:332–338, 1993.

[246] SJ Zinkle and LL Snead. Opportunities and limitations for ion beams in radiation effects studies: Bridging critical gaps between charged particle and neutron irradiations. *Scripta Materialia*, 143:154–160, 2018.

[247] JF Ziegler, MD Ziegler, and JP Biersack. Srim–the stopping and range of ions in matter (2010). *Nuclear Instruments and Methods*

in Physics Research Section B: Beam Interactions with Materials and Atoms, 268(11-12):1818–1823, 2010.

[248] RE Stoller, MB Toloczko, GS Was, AG Certain, S Dwaraknath, and FA Garner. On the use of srim for computing radiation damage exposure. *Nuclear instruments and methods in physics research section B: beam interactions with materials and atoms*, 310:75–80, 2013.

[249] D Lingis, E Lagzdina, A Plukis, R Plukienė, and V Remeikis. Evaluation of the primary displacement damage in the neutron irradiated rbmk-1500 graphite. *Nuclear Instruments and Methods in Physics Research Section B: Beam Interactions with Materials and Atoms*, 436:9–17, 2018.

[250] LR Owen, EJ Pickering, HY Playford, Howard James Stone, MG Tucker, and Nicholas Gwilym Jones. An assessment of the lattice strain in the crmnfeconi high-entropy alloy. *Acta Materialia*, 122:11–18, 2017.

[251] C Suryanarayana and MG Norton. *X-ray diffraction: a practical approach*. Springer Science & Business Media, 2013.

[252] D Weygand, Y Bréchet, and J Lépinoux. Zener pinning and grain growth: a two-dimensional vertex computer simulation. *Acta Materialia*, 47(3):961–970, 1999.

[253] CA Williams, EA Marquis, A Cerezo, and GDW Smith. Nanoscale characterisation of ods–eurofer 97 steel: an atom-probe tomography study. *Journal of Nuclear Materials*, 400(1):37–45, 2010.

[254] S Chen, X Jin, and L Rong. Improving the strength and ductility of reduced activation ferritic/martensitic steel by cold-swaging and post-annealing. *Materials Science and Engineering: A*, 631:139–143, 2015.

[255] B Weiss and R Stickler. Phase instabilities during high temperature exposure of 316 austenitic stainless steel. *Metallurgical and Materials Transactions B*, 3(4):851–866, Apr 1972.

[256] Z Hong, A Morrison, H Zhang, S Roberts, and P Grant. Development of a novel melt spinning-based processing route for oxide

dispersion-strengthened steels. *Metallurgical and Materials Transactions A*, 49(2):604–612, 2018.

[257] V Maier-Kiener, B Schuh, EP George, H Clemens, and A Hohenwarter. Insights into the deformation behavior of the crmnfeconi high-entropy alloy revealed by elevated temperature nanoindentation. *Journal of Materials Research*, 32(14):2658–2667, 2017.

[258] WH Liu, Y Wu, JY He, TG Nieh, and ZP Lu. Grain growth and the hall–petch relationship in a high-entropy fecrnicomn alloy. *Scripta Materialia*, 68(7):526–529, 2013.

[259] AA Elmustafa and DS Stone. Indentation size effect in polycrystalline fcc metals. *Acta Materialia*, 50(14):3641–3650, 2002.

[260] A. DI Schino, I. Salvatori, and J. M. Kenny. Effects of martensite formation and austenite reversion on grain refining of aisi 304 stainless steel. *Journal of Materials Science*, 37(21):4561–4565, Nov 2002.

[261] S He, X Zeng, L Peng, X Gao, J Nie, and W Ding. Microstructure and strengthening mechanism of high strength mg–10gd–2y–0.5 zr alloy. *Journal of Alloys and Compounds*, 427(1-2):316–323, 2007.

[262] JE Bailey and PB Hirsch. The dislocation distribution, flow stress, and stored energy in cold-worked polycrystalline silver. *Philosophical Magazine*, 5(53):485–497, 1960.

[263] K Venkateswarlu, A Chandra Bose, and N Rameshbabu. X-ray peak broadening studies of nanocrystalline hydroxyapatite by williamson–hall analysis. *Physica B: Condensed Matter*, 405(20):4256–4261, 2010.

[264] T Gladman. Precipitation hardening in metals. *Materials science and technology*, 15(1):30–36, 1999.

[265] MA Delesse. Mechanical process to determine the composition of rocks. *CR Acad. Sci. Paris*, 25:544–545, 1847.

[266] J Shin, J Doh, J Yoon, D Lee, and J Kim. Effect of molybdenum on the microstructure and wear resistance of cobalt-base stellite hardfacing alloys. *Surface and Coatings Technology*, 166(2-3):117–126, 2003.

[267] G Liu. Applied stereology in materials science and engineering. *Journal of Microscopy*, 171(1):57–68, 1993.

[268] Behzad VF, Rui A, Paulo JT, Pedro MGP Moreira, and Abel S. Material characterization and damage assessment of an aa5352 aluminium alloy using digital image correlation. *The Journal of Strain Analysis for Engineering Design*, 55(1-2):3–19, 2020.

[269] Q Liu and N Hansen. Deformation microstructure and orientation of fcc crystals. *Physica status solidi (a)*, 149(1):187–199, 1995.

[270] M Yamasaki, M Sasaki, M Nishijima, K Hiraga, and Y Kawamura. Formation of 14h long period stacking ordered structure and profuse stacking faults in mg–zn–gd alloys during isothermal aging at high temperature. *Acta Materialia*, 55(20):6798–6805, 2007.

[271] G Casillas, AA Gazder, EV Pereloma, and AA Saleh. Evidencing extrinsic stacking faults in twinning-induced plasticity steel. *Materials Characterization*, 123:275–281, 2017.

[272] RE Smallman. *Modern physical metallurgy*. Elsevier, 2016.

[273] X Wu, YT Zhu, MW Chen, and E Ma. Twinning and stacking fault formation during tensile deformation of nanocrystalline ni. *Scripta Materialia*, 54(9):1685–1690, 2006.

[274] GS Was and PL Andresen. Irradiation assisted corrosion and stress corrosion cracking (iac/iascc) in nuclear reactor systems and components. In *Nuclear Corrosion Science and Engineering*, pages 131–185. Elsevier, 2012.

[275] H Oka, M Watanabe, H Kinoshita, T Shibayama, N Hashimoto, S Ohnuki, S Yamashita, and S Ohtsuka. In situ observation of damage structure in ods austenitic steel during electron irradiation. *Journal of nuclear materials*, 417(1-3):279–282, 2011.

[276] S Shi, MR He, K Jin, H Bei, and IM Robertson. Evolution of ion damage at 773k in ni-containing concentrated solid-solution alloys. *Journal of Nuclear Materials*, 501:132–142, 2018.

[277] C Abromeit. Aspects of simulation of neutron damage by ion irradiation. *Journal of nuclear materials*, 216:78–96, 1994.

[278] CD Hardie, CA Williams, S Xu, and SG Roberts. Effects of irradiation temperature and dose rate on the mechanical properties of self-ion implanted fe and fe–cr alloys. *Journal of nuclear materials*, 439(1-3):33–40, 2013.

[279] JL Seran and JM Dupouy. *The swelling of solution annealed 316 cladding in RAPSODIE and PHENIX*. ASTM International, 1982.

[280] GE Lucas. The evolution of mechanical property change in irradiated austenitic stainless steels. *Journal of Nuclear Materials*, 206(2-3):287–305, 1993.

[281] K Wang, Y Dai, and P Spätig. Deformation twinning in irradiated ferritic/martensitic steels. *Journal of Nuclear Materials*, 501:336–346, 2018.

[282] JI Cole and SM Bruemmer. Post-irradiation deformation characteristics of heavy-ion irradiated 304l ss. *Journal of nuclear materials*, 225:53–58, 1995.